

STUDY OF MIXED IONIC/ELECTRONIC CONDUCTORS (MIECS)
BASED ON π -CONJUGATED LIQUID CRYSTALS AND BLOCK
COPOLYMERS

A Dissertation

Presented to the Faculty of the Graduate School

of Cornell University

In Partial Fulfillment of the Requirements for the Degree of

Doctor of Philosophy

by

Ziwei Liu

May 2020

© 2020 Ziwei Liu

STUDY OF MIXED IONIC/ELECTRONIC CONDUCTORS (MIECS) BASED ON Π -CONJUGATED LIQUID CRYSTALS AND BLOCK COPOLYMERS

Ziwei Liu, Ph. D.

Cornell University 2020

Mixed ionic/electronic conductors (MIECs) are materials that conduct both ions and electronic charge carriers simultaneously. Generally, they belong to two distinct families: ceramics and conducting polymers with the latter exhibiting advantages such as easy wet synthesis, low cost processability, biocompatibility and mechanical flexibility over its ceramic counterpart. Conducting polymers, either with single ionic or electronic conductivity, have been extensively studied for their potential applications in energy storage, sensors, and so on. New materials with combined functionalities within the same molecule are expected to form interesting structures and exhibit intriguing properties. Nano/micro-segregation between immiscible components will lead to spatially confined self-assembly with unanticipated synergies including the potential to improve ionic and electronic transport properties.

Our goal has been to develop new materials with mixed ionic and electronic conductivity. A systematic study of design, synthesis and characterization of MIECs based on small dimension liquid crystals and large dimension block copolymers has been conducted. First, we synthesized linear structured coil-rod-coil liquid crystals with oligothiophene as a rigid building block for electronic conductivity and ion-doped ethylene oxide units as the flexible ionically-conducting phase. A variety of characterization methods were employed to study the structure and self-assembly behavior of our liquid crystal materials. Simultaneous ionic/electronic transport was for the first time characterized by electrochemical impedance spectroscopy (EIS) with LiTFSI and

F4TCNQ as ionic and electronic dopant, respectively. Apart from experiments, molecular dynamic (MD) simulations were adopted to guide molecular design and material properties. Based on simulation results, a series of liquid crystals with ternary amphiphilic structures was synthesized and investigated, leading to complex structures and unique charge transport response.

We also carried out the synthesis and study of P3HT-*b*-POEM rod-coil block copolymers. Without well-ordered phase separation between the two blocks, the incorporation of LiTFSI to the POEM phase resulted in enhanced molecular order as well as electronic doping of the P3HT block, leading to improved electronic conductivity with retained ionic conductivity. In order to achieve comparable mixed conductivity, a polymer with modified P3HT regioregularity and block ratio was investigated and showed a “crystallinity-conductivity” trade-off. The knowledge gained from those studies offers opportunities for further development of conducting polymers.

BIOGRAPHICAL SKETCH

Ziwei Liu was born and grew up in Shandong Province, P. R. China before her family moved to Beijing. She finished her undergraduate studies in College of Chemistry and Molecular Engineering (CCME) at Peking University. Ziwei came to U.S. in 2014 and enrolled in the Ph.D. program of the Department of Materials Science and Engineering, Cornell University. Under supervision of Prof. Christopher K. Ober, Ziwei's research focused on synthesis and characterization of mixed ionic/electronic conducting materials (MIECs) based on π -conjugated liquid crystal and block copolymer systems. After completing her Ph.D. degree in spring 2020, Ziwei set out to begin her career as researcher in industry.

ACKNOWLEDGEMENTS

First and foremost, I would like to express my deepest gratitude to my advisor Prof. Christopher K. Ober, who has been very patient and supportive through all the years of my PhD studies, and given me great opportunities to collaborate with excellent researchers as well as freedom to pursue independent work. His great personality and dedication to work have been truly inspirational to me. I am also very grateful to Prof. Barbara Baird and Prof. Lynden Archer for serving on my thesis committee and also Prof. Huili (Grace) Xing for serving as the department assigned committee for my A Exam. I would also like to give my special thanks to all my collaborators of the DMREF project: Prof. Fernando A. Escobedo, Dr. Mayank Misra, Dr. Christian Nowak and Yangyang Sun (School of Chemical Engineering, Cornell University); Prof. Paul F. Nealey, Prof. Shrayesh N. Patel and Dr. Ban Xuan Dong (institute for Molecular Engineering, University of Chicago); and Prof. Christine Luscombe and Jonathan Onorato (department of Materials Science and Engineering, University of Washington).

It has been a great privilege to spend five years in Prof. Ober's group and I would like to thank all group members for their help and support. In particular, I sincerely thank Dr. Hong Xu, Dr. Peter Ohlendorf, Dr. Wei-Liang Chen, and Dr. Roselynn Cordero for sharing their knowledge and experience and giving me great advice for my research. I would also like to thank people from Duffield 258 office, past and present, Dr. Katie Camera, Dr. Florian Kafer, Mufei Yu, Chengjian Shi, Dung-Yi Wu, Yuming Huang and Yinglu Wang for creating a good atmosphere inside and outside the lab. I would thank my dear friends Yiren Zhang and Hai Tran for their care and help in research and daily life.

I would like to thank my family in China, my parents, my grandpa, my aunt and my cousin for always standing behind me throughout my graduate studies. Your love and care are the driving

force for me to pursue my Ph.D. and I wish you could be proud of my achievements. I also want to thank my dear boyfriend Johan Bjorck for his love, care and understanding. I feel very lucky that we met each other here at Cornell.

TABLE OF CONTENTS

BIOGRAPHICAL SKETCH	iv
ACKNOWLEDGEMENTS	v
LIST OF ABBREVIATIONS	xi
LIST OF FIGURES	xiii
LIST OF TABLES	xv
Chapter One: Mixed ionic-electronic conducting (MIEC) materials	1
1.1 Introduction of polymer-based MIECs	1
1.2 Overview of Conducting polymers	3
1.2.1 PEDOT-PSS	3
1.2.2 P3HT-PEO	7
1.3 Liquid crystals with amphiphilic structures	8
1.3.1 Overview of liquid crystals	8
1.3.2 LC amphiphiles	10
1.4 Liquid crystals for conductivity applications	12
1.4.1 LCs for ionic conductivity	13
1.4.2 LCs for electronic conductivity	17
1.5 Conclusions	20
REFERENCES	22
Chapter Two: Self-Assembly Behavior of An Oligothiophene-Based Conjugated Liquid Crystal and Its Implication for Mixed Ionic-Electronic Conductivity Characteristics.....	27
2.1 Introduction.....	27
2.2 Experimental section.....	30
2.2.1 Materials	30
2.2.2 Materials preparation	30
2.2.3 Characterization methods.....	31
2.2.4 Synthetic procedures	33
2.3. Results and discussions	36

2.3.1 Synthesis of Liquid Crystalline Material 4T/PEO4.....	36
2.3.2 Thermal and Structural Properties of Bulk 4T/PEO4-LiTFSI Mixtures	37
2.3.3 Self-assembly Behavior of 4T/PEO4-LiTFSI Thin Film Measured by Temperature-dependent GIWAXS	42
2.3.4 Self-assembly Behavior of 4T/PEO4-LiTFSI Complexes Studied by Molecular Dynamics Simulation	47
2.3.5 Implication of 4T/PEO4-LiTFSI Self-assembly on Ion transport	51
2.3.6 Mixed ion/Electron conduction in 4T/PEO4.....	53
2.4 Conclusions.....	59
REFERENCES	61

Chapter Three: Study of the Structural Evolution of Amphiphilic Liquid Crystals from Binary System to Ternary Systems.....	65
3.1 Introduction.....	65
3.2 Experimental section.....	67
3.2.1 Materials	67
3.2.2 Characterization methods.....	68
3.2.3 Synthetic procedures	70
3.3 Results and discussion	80
3.3.1 Structural evolution of 4T/PEOn studied by simulation	80
3.3.2 Thermal properties and self-assembly behaviors of 4T/PEO5 compared to 4T/PEO4 ...	81
3.3.3 Study of linear amphiphiles 6T/PEO4 in its self-assembly behavior and ionic conduction characteristics.....	86
3.3.4 Synthesis and thermal properties of X-shaped bolaamphiphiles 4T/alkyl/PEO4	90
3.4 Conclusions.....	92
REFERENCES	95

Chapter Four: Study of self-assembly behavior and ionic conductivity of T-shaped facial amphiphilic liquid crystals	97
4.1 Introduction.....	97
4.2 Experimental Section	98

4.2.1 Materials	98
4.2.2 Characterization methods.....	99
4.2.3 Synthetic procedures of T-shaped facial amphiphilic LCs (5T/PEOn/alkyl)	101
4.3 Results and Discussion.....	110
4.3.1 Simulation of the self-assembly of 5T/PEOn/alkyl	110
4.3.2 Synthesis of 5T/PEOn/alkyl facial amphiphiles	112
4.3.3 Thermal properties of bulk 5T/PEOn/alkyl	112
4.3.4 Self-assembly behavior of 5T/PEOn/alkyl thin film.....	115
4.3.5 Ionic conductivity of 5T/PEOn/alkyl	118
4.4 Conclusions.....	121
REFERENCES	123

Chapter Five: Enhanced Electronic Conductivity of a Molecularly-Doped Poly(3-hexylthiophene)-Based Rod-Coil Block Copolymer via the Addition of an Ionic Salt LiTFSI. 124

5.1 Introduction.....	124
5.2 Experimental Section	126
5.2.1 Materials	126
5.2.2 Characterization	127
5.2.3 Synthetic procedures	129
5.3 Results and Discussion.....	135
5.3.1 Synthesis of regioregular P3HT-b-POEM	135
5.3.2 Structural control of P3HT-b-POEM via addition of LiTFSI	140
5.3.3 Improved molecular order and induced electronic doping of P3HT-b-POEM by the addition of LiTFSI	144
5.3.4 Further improvement of electrical performance via doping with F4TCNQ vapor	147
5.4 Conclusions.....	149
REFERENCES	151

Chapter Six: Paired Ionic-Electronic Conduction in Regioregularity (RR)-Controlled Self-Assembled P3HT-POEM Rod-Coil Block Copolymers 154

6.1 Introduction.....	154
6.2 Experimental Section	156
6.2.1 Materials	156
6.2.2 Characterizations.....	157
6.2.3 Synthetic procedures	158
6.3 Results and discussions	165
6.3.1 Synthesis of regioregularity (RR)-controlled P3HT block with alkyne end-functionalization	165
6.3.2 Synthesis and purification of P3HT-b-PEOMEMA copolymer	169
6.3.3 Self-assembly and phase separation of RR-controlled P3HT-b-PEOMEMA	176
6.4 Conclusions.....	177
REFERENCES	179
Chapter Seven: Conclusions	181

LIST OF ABBREVIATIONS

Abbreviation	Description
LC	Liquid crystal
MIECs	Mixed ionic-electronic conductors
PEDOT-PSS	Poly(3,4-ethylenedioxythiophene) with poly(4-styrenesulfonate) polymer blend
PEO	Poly(ethylene oxide)
PCE	Power-conversion efficiency
OFET	Organic field-effect transistors
OLED	Organic light emitting diodes
OECT	Organic electrochemical transistors
P3HT-PEO	Poly(3-hexylthiophene)- <i>b</i> -poly(ethylene oxide)
DSSC	Dye-sensitized solar cells
4T/PEO4	5,5''-di(2,5,8,11-tetraoxatridecan-13-yl)-2,2':5',2'':5'',2'''-quaterthiophene
LiTFSI	lithium bis(trifluoro-methanesulfonyl) imide
F4TCNQ	2,3,5,6-tetrafluoro-7,7,8,8-tetracyanoquinodimethane
NMR	Nuclear magnetic resonance
DSC	Differential scanning calorimetry
TGA	thermogravimetric analysis
POM	Polarized optical microscope
XRD	X-ray diffraction
FTIR	Fourier-transform infrared spectroscopy
GPC	Gel permeated chromatography
GIWAXS	Grazing-incidence wide angle X-ray scattering
GISAXS	Grazing-incidence small angle X-ray scattering
MD	Molecular dynamics
CG	Coarse-grained
OPLS-AA	Optimized potentials for liquid simulations-all atom force field
DFT	Density functional theory
GPGPU	General-purpose graphical processing units

PPPM	Particle-particle particle-mesh
FWHM	Full-width at half-maximum
EIS	Electrochemical impedance spectroscopy
ATRP	Atom transfer radical polymerization
NMP	Nitroxide-mediated radical polymerization
RAFT	Reversible addition-fragmentation chain-transfer polymerization
GRIM	Grignard metathesis polymerization
CuAAC	Copper-catalyzed alkyne-azide cycloaddition
P3HT-<i>b</i>-POEM	Poly(3-hexhythiophene)-poly(polyethylene glycol methyl ether methacrylate) block copolymer
P2VP	Poly(2-vinylpyridine)
P4VP	Poly(4-vinylpyridine)
PSS	Polystyrene sulfonate
RR	Regioregular/ Regioregularity

LIST OF FIGURES

Figure 1.1	Survey of ionic and/or electronic conductors comparing ionic and electronic conductivity	2
Figure 1.2	Chemical structure and conductivity of PEDOT-PSS	5
Figure 1.3	Schematic of polymer solar cells and OECTs	6
Figure 1.4	Liquid crystalline mesophases	9
Figure 1.5	Phase sequence of T-shaped bolaamphiphiles and facial amphiphiles with increasing size of lateral substituent.	13
Figure 1.6	1D, 2D and 3D charge transport channels of formed by liquid crystalline materials	13
Figure 1.7	Schematic illustration of rod-like liquid crystals forming 2D ion transport channels as electrolyte for lithium-ion batteries	16
Figure 1.8	Schematic illustration of rod-like liquid crystals forming 2D ion transport channels as electrolyte for DSSCs	17
Figure 1.9	FET with columnar/smectic LC semiconductors	19
Figure 2.1	DSC traces and POM images of 4T/PEO4-LiTFSI complexes	38
Figure 2.2	TGA of pristine 4T/PEO4 and LiTFSI	41
Figure 2.3	X-ray diffraction pattern of neat 4T/PEO4 compound at ambient temperature	41
Figure 2.4	Representative geometrically corrected GIWAXS patterns of 4T/PEO4-LiTFSI complex thin film at selected temperatures	44
Figure 2.5	Vertical linecuts of (00h) spot sequence for 4T/PEO4-LiTFSI complexes	46
Figure 2.6	Representative room-temperature GIWAXS patterns of 4T/PEO4-LiTFSI at higher blending ratio	47
Figure 2.7	Simulation steps to capture the AA structure of 4T/PEO4	50
Figure 2.8	Snapshots of 4T/PEO4-LiTFSI structures at three representative blending ratios	51

Figure 2.9	Ionic conductivities of LiTFSI-blended 4T/PEO4 thin film	52
Figure 2.10	Mixed ionic/electronic conductivity of 4T/PEO4-LiTFSI doped with F4TCNQ	56
Figure 3.1	Lindemann Parameter for 4T/PEO _n systems and Normalized Potential Energy between 4T and PEO _n as a function of temperature	82
Figure 3.2	Thermal and optical properties of 4T/PEO5	84
Figure 3.3	Temperature-dependent WAXS profiles of 4T/PEO5	85
Figure 3.4	GIWAXS patterns of 6T/PEO4-LiTFSI complex thin film	87
Figure 3.5	Ionic conductivity of 6T/PEO4 and 4T/PEO4	89
Figure 3.6	DSC and UV-vis of 4T bolaamphiphiles	92
Figure 4.1	Molecular structure of 5T/PEO _n /alkyl facial amphiphiles	111
Figure 4.2	DSC traces of 5T/PEO _n /alkyl molecules	114
Figure 4.3	POM images of 5T/PEO _n /alkyl molecules	115
Figure 4.4	Experimental and simulated GIWAXS patterns of 5T/PEO _n /alkyl molecules	118
Figure 4.5	Temperature-dependent WAXS patterns of 5T/PEO _n /alkyl molecules	119
Figure 4.6	Ionic conductivities of LiTFSI-blended 5T/PEO _n /alkyl thin film	120
Figure 5.1	NMR and GPC traces of P3HT- <i>b</i> -POEM copolymer	138
Figure 5.2	FTIR spectra P3HT- <i>b</i> -POEM copolymer	140
Figure 5.3	AFM phase images of P3HT- <i>b</i> -POEM-LiTFSI complex thin films	141
Figure 5.4	Self-assembly study of P3HT- <i>b</i> -POEM-LiTFSI complex thin films	143
Figure 5.5	Electronic doping effect of LiTFSI on P3HT- <i>b</i> -POEM	144
Figure 5.6	Electronic conductivity of P3HT- <i>b</i> -POEM-LiTFSI doped by F4TCNQ	149
Figure 6.1	Characterizations of RR-controlled P3HT-alkyne homopolymer	168

Figure 6.2	Structures of P3HT- <i>b</i> -PEOMEMA	169
Figure 6.3	GPC traces of P3HT- <i>b</i> -PEOMEMA with varying RR values and block ratios	171
Figure 6.4	¹ H NMR of ω-ethynyl-P3HT	173
Figure 6.5	P3HT- <i>b</i> -PEOMEMA copolymer dissolved in different solvents	174
Figure 6.6	Phase separation of P3HT- <i>b</i> -PEOMEMA copolymers	177

LIST OF TABLES

Table 2.1	Thermal Properties of 4T/PEO4-LiTFSI complexes	39
Table 3.1	3,3'-dialkyl(C _n H _{2n+1})-5,5'-dibromo-2,2'-bithiophene	90
Table 5.1	Molecular weight characterization of azido-POEM block by SEC	131
Table 6.1	Molecular weight of azido-PEOMEMA characterized by GPC	163
Table 6.2	Characteristics of RR-controlled P3HT blocks	167
Table 6.3	Characteristics of P3HT- <i>b</i> -PEOMEMA copolymers	170

Chapter One: Mixed ionic-electronic conducting (MIEC) materials

1.1 Introduction of polymer-based MIECs

Mixed ionic–electronic conductors (MIECs) are materials that exhibit conductivity of both ions and electronic charge carriers.^[1] Generally, MIECs belong to two distinct families, ceramics and conducting polymers^[2] as shown in **Figure 1.1**. Despite the extensive focus on ceramic MIECs,^[3–5] their polymer counterparts often exhibit unmatched advantages such as easier wet synthesis, lower cost and lower temperature processing, greater mechanical flexibility and biocompatibility, combining to make them promising and attractive for mass production and implementation on a large scale. Currently there are only a limited number of organic MIECs combining both ionic and electronic conducting functionalities within the same molecule. Paired ionic-electronic conducting polymers are believed to exhibit interesting structures that lead to intriguing properties. For example, charge transport, through the conjugated electronically conducting blocks, is greatly enhanced by the mere presence of an adjacent ionically charged segment.^[65] Such synergistic effects are of great interest.

Mixed ionic/electronic conducting materials have been used in a variety of devices including bioelectronics,^[6] batteries,^[7] and electrochemical capacitors, electrochromic displays,^[8] electromechanical actuators,^[9] with various requirements for chemical, electrical, thermal and mechanical properties. Moreover, the ability to precisely control the nanoscale architecture of ionically and electronically conducting domains can, in principle, enable design of materials for energy storage applications^[10–13] with not only high capacity, but also high charge-discharge rates, yielding high power. In bioelectronics, mixed conductors can be used as transducers of ionic signals from the biological world producing electronic signals that can be further amplified and

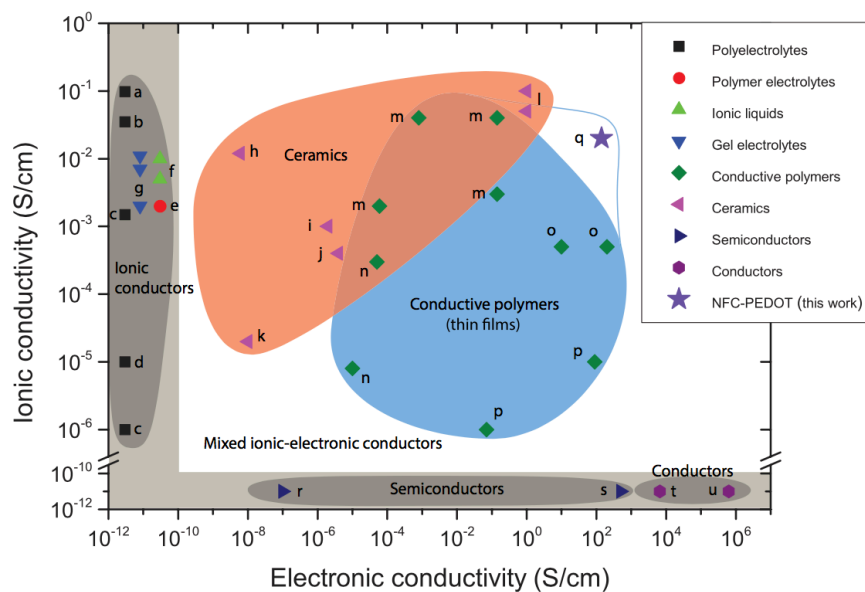


Figure 1.1 Survey of ionic and/or electronic conductors comparing ionic and electronic conductivity. (Reprint from *Adv. Sci.* 2016^[21]) The points in the graph represents the following materials: a: Nafion; b: poly(diallyldimethyl ammonium chloride)/poly(2,6-dimethyl-1,4-phenylene oxide); c: poly(4-styrenesulfonic acid); d: poly(ethylene oxide)/poly(acrylic acid)/ poly(ethylene oxide)/(poly(acrylic acid)/multiwalled carbon nanotubes); e: polyvinylidene fluoride/polyethylene oxid/propylene carbonate/ LiClO₄; f: (lithium bis(oxlate)borate and lithium tetrafluoroborate)/1-ethyl-3-methyl-imidazolium tetrafluoroborate; g: LiCF₃SO₃/poly(methyl methacrylate), LiClO₄/poly(methyl methacrylate), and LiClO₄/propylene carbonate/ethylene carbonate/ dimethylformamide/poly(acrylonitrile); h: Li₁₀GeP₂₂S₁₂; i: Ag₂HfS₃; j: Ag₂S; k: Li_{3.5}V_{0.5}Ge_{0.5}O₄; l: Ce_{0.8}Gd_{0.2}O_{2-d}-CoFe₂O₄; m: poly(3,4-ethylenedioxythiophene):polystyrene sulfonate and poly(3,4-ethylenedioxythiophene):polystyrene sulfonate/sodium polystyrene sulfonate; n: poly-[1-methyl-3-(pyrrol-1-ylmethyl)pyridinium perchlorate]; o: Polyaniline p: Polypyrrole; q: poly(3,4-ethylene-dioxythiophene):polystyrene sulfonate/nanofibrillated cellulose/dimethyl sulfoxide/polyethylene glycol (this work); r/s: GaAs; t: Nichrome; u: Ag.

processed using traditional electronics. Examples include conducting polymer electrodes^[14,15] and organic electrochemical transistors^[16,17] that record and stimulate brain activity, organic electronic ion pumps^[18,19] that deliver drugs with exquisite spatiotemporal control, as well as a variety of biosensors^[20,21] for health monitoring, drug screening, and toxicology. While of immense practical interest, these are very complex materials. Furthermore, such materials can be tailored to have surface chemistries that promote biocompatibility and stability over extended periods of time.

1.2 Overview of Conducting polymers

Electronically conducting polymers, such as polyaniline, polypyrrole, and polythiophene, are as a result of the conjugated π -system along their backbone. They exhibit good intrinsic conductivity in their doped state,^[22] low bandgaps,^[23] and relatively fast charge-discharge kinetics,^[24] making them promising materials for a variety of applications including solar cells, rechargeable batteries, organic electronics, electrochromic devices, sensors and so on.^[25–30] On the other hand, ionically conducting polymers among which poly(ethylene oxide) (PEO) and its derivatives^[31,32], because they contain both ether coordination sites enabling the dissociation of lithium salts and a flexible macromolecular backbone enabling ionic transport, are widely studied for applications in energy production, and storage and in sensing. However, single-phase MIECs can seldom fulfill all of the requirements for these diverse applications. To overcome this challenge, researchers have looked at composite materials consisting of separate ionic and electronic conducting phases.^[3]

1.2.1 PEDOT-PSS

Polymer-based MIECs come in several discrete architectures. The most common type currently is a blended architecture where a polymer that possesses electronic conductivity is combined with a polymer that possesses ionic conductivity. An example is a blend of poly(3,4-

ethylenedioxythiophene) with poly(4-styrenesulfonate), (PEDOT–PSS system, the structure of which is shown in **Figure 1.2(a)**) that has been to date the most successful combination in terms of both fundamental research^[33,34] and practical application^[35]. PEDOT has been found to exhibit a relatively high conductivity and appears to be the most stable conducting polymer currently available despite its poor solubility. PSS, as a polymer surfactant, helps to disperse and stabilize PEDOT in water and other solvents. The PEDOT-PSS polymer blends consist of positively charged conjugated PEDOT and negatively charged saturated PSS where the PEDOT chains are incorporated into a PSS matrix while PSS acts as a polyanionic counterion to neutralize the highly oxidized PEDOT.^[36] PEDOT-PSS possesses the outstanding advantages of good film-forming properties, high transparency in the visible range, excellent thermal stability, especially tunable and improved conductivity achieved by secondary doping.^[37] Systematic studies have found that the conductivity of PEDOT-PSS can be significantly enhanced by thermal and light treatment,^[38,39] or organic solvents, ionic liquids, surfactants, salts, zwitterions, and acids as summarized in **Figure 1.2(b)**. They have been applied a wide range of applications^[33,40], for example in antistatic coatings, as electrodes in light-emitting diodes (LEDs), photovoltaics (PV), memories, sensors, and as active material for electrochromic devices, field-effect transistors and circuits in general.^[41–46]

Here we give a brief introduction to the applications of conducting polymer-based MIECs with PEDOT-PSS as an example.

1.2.1.1 Polymer solar cells

Solar cells are devices which convert solar energy directly into electricity. So far, the most common material used for solar cells is silicon.^[48] Although silicon-based solar cells possess advantages such as high power-conversion efficiency (PCE), the energy intensive processing

techniques and the high cost of silicon make them expensive.^[49] Conducting polymer-based solar cells have received considerable attention in recent years and are widely recognized as promising alternatives to their inorganic counterparts. Despite the relatively low PCE compared to inorganic solar cells, polymer solar cells are inexpensive and solution processable. Moreover, their intrinsic flexibility enables large-area production.^[50,51] In addition to high absorption coefficient, their mechanical flexibility simplifies the coating and printing processes and allows the development of flexible devices, such as organic field-effect transistors (OFETs) and organic light-emitting diodes (OLEDs).^[52]

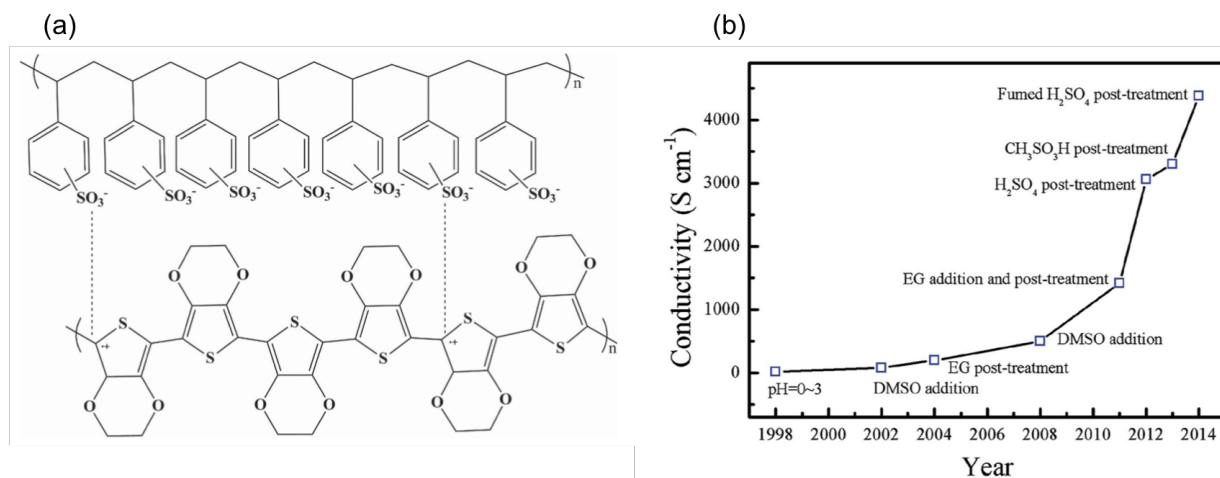


Figure 1.2 (a) Chemical structure, and (b) Timeline of conductivity values for PEDOT-PSS. (Reprint from *Adv. Electron. Mater.* 2015^[47])

The working principle of a polymer solar cell is depicted in **Figure 1.3(a)**. As a hole transport layer, PEDOT-PSS is spin-coated on top of the anode with another active layer sandwiched between the cathode and the hole transport layer to form the donor and acceptor. When the light-absorbing material absorbs photons and excites electrons from the ground state to the excited state, bound electron-hole pairs (excitons) are created and diffuse to the donor-acceptor interface where

they dissociate into free charge carriers after overcoming their binding energies. Photocurrent is generated when the free charge carriers move to the anode and cathode under internal electric fields.

Regardless the advantages that polymer solar cells exhibit, problems such as insufficient PCEs and device lifetime still limit commercialization of these materials.

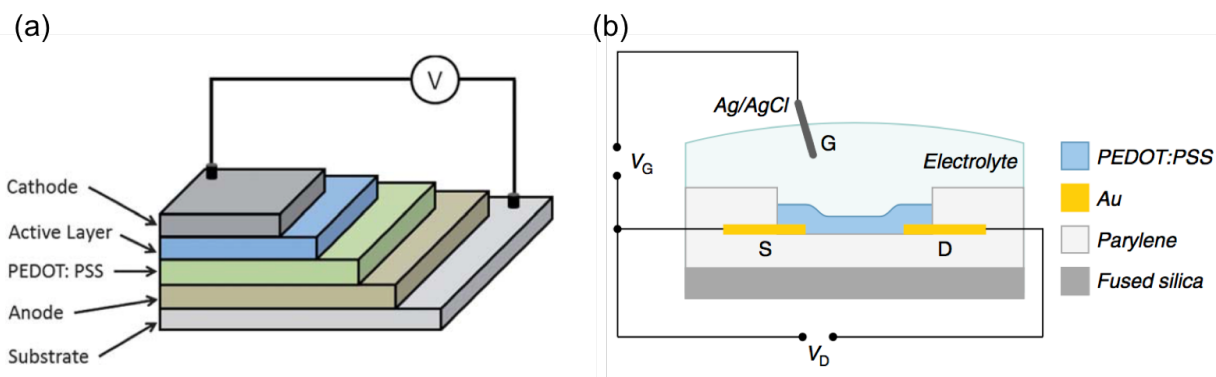


Figure 1.3 Schematic of (a) polymer solar cell (reprint from *Polym. Chem. 2011*^[53]), and (b) OEET (reprint from *Nat. Comm. 2013*^[54]).

1.2.1.2 Organic electrochemical transistors (OEET)

An organic electrochemical transistor (OEET) is a transistor in which the drain current is controlled by the injection of ions from an electrolyte into a semiconductor channel. Organic electrochemical transistors (OEETs) make effective use of ion injection from an electrolyte to modulate the bulk conductivity of an organic semiconductor channel.^[55] An OEET consists of an organic semi-conductor film, usually made of conducting polymers, in contact with an electrolyte. While the gate electrode establishes electrical contact to the electrolyte, the source and drain electrodes establish contact with the organic semiconductor film and define the channel through which holes or electrons flow from the source to the drain. PEDOT-PSS is the most widely used

material for OECTs. The p-type doped PEDOT leads to mobile holes hopping from chain to chain while PSS works as an acceptor in which the holes are compensated by the sulfonate anions (see **Figure 1.3(b)**). Various co-solvents, surfactants and processing methods have been investigated to maximize hole conductivity.

1.2.2 P3HT-PEO

Regardless its conducting characteristics, there remain some drawbacks of the PEDOT-PSS polymer blend such as indistinct morphology and poorly defined internal interfaces, both of which are critical to the behavior and interplay between the two conducting phases.^[56] Furthermore, their thermal stability is not comparable to block copolymers in which the two blocks are chemically linked. Therefore, developing a model material with well-defined ion channels would greatly aid in understanding combined ionic-electronic conductors and enable the creation of new, more effective materials.

Studies of mixed ionic-electronic conductors made from block copolymers have also been carried out in a few systems,^[57–62] from among which poly(3-hexylthiophene)-*b*-poly(ethylene oxide) (P3HT-*b*-PEO) has received the most attention. Conjugated P3HT is attractive as a stable hole conductor (p-type conductor) and has achieved electronic conductivity as high as 10 S/cm in the oxidized state.^[63] Coupling P3HT to ionic conductors allows for simultaneous ionic/electronic conduction^[64] in which the PEO block enables ion transport by loaded lithium salt while the P3HT enables electronic transport by dopants through an electrochemical oxidation. By using a combination of ac impedance spectroscopy and dc measurements, simultaneous ionic/electronic transport can be characterized. The ionic conductivity of P3HT-PEO-LiTFSI is lower than that of P3EO-LiTFSI due to the presence of non-ionically conducting P3HT microphases in the mixtures while its electronic conductivity is significantly higher than that of P3HT homopolymer. This kind

of material could serve as a more conductive binder and transporter of electronic charge and lithium ions of lithium battery electrodes compared to the current ones which require an inert polymer to bind the cathode particles, carbon additives for electronic conduction and a liquid electrolyte for lithium ion conduction. Balsara *et al.* showed that using a solid–state three-terminal cell that depends on the oxidation state, conductivity ranged from 10^{-7} S/cm at low oxidation up to 10^{-2} S/cm at higher oxidation levels.^[65] More importantly when fabricated into a battery, at the end of the discharge cycle the material turned insulator and could act to prevent overcharging of the battery.

1.3 Liquid crystals with amphiphilic structures

1.3.1 Overview of liquid crystals

Liquid crystals (LCs) can be considered as a state of matter which in a unique way combines order and mobility, and they are also described as ordered fluids.^[66–69] LCs can be divided into three categories: thermotropic, lyotropic and metallotropic based on whether the LC phases are dependent on temperature, concentration or the ratio between organic and inorganic molecules. In my thesis we focus on thermotropic liquid crystals.

LC phases usually occur in a distinct temperature range between the crystalline solid state (Cr) and the isotropic liquid state (Iso). The LC phases are also called mesophases. Among the many LC mesophases, nematic and smectic phases are most well-known and studied (see **Figure 1.4**). The nematic phase (N) is the least ordered, and the most fluid LC phase. The smectic phases (Sm, arranged in layered structures) have a periodicity in only one direction (the distance d between the layers) and these phases can be further classified according to the order in the layers.

Conventional LCs often have a rod-like shape (calamitic mesogens) or a disk-like shape (discotic mesogens). In both cases, the molecules can be described as cylinders, which represent the average

or effective shape of mesogens, with a high degree of structural anisotropy. The cylinders are free to rotate about their primary molecular axis in fluidic LC phases. By tuning the molecular shape and intermolecular interactions, the molecules can self-assemble into a range of LC nanostructures through spontaneous self-organization of the mesogenic molecules driven by different kinds of intermolecular interactions, including ion-ion interaction, ion-dipole interaction, van der Waals interaction, hydrogen bonding, and so on. During the self-organization process, nano-segregation/micro-segregation caused by differences within the mesomorphic molecules often plays a primary role. Compatible regions interact with one another in the mesophase, whereas incompatible segments segregate into distinct sub-phases. The relative size, shape, and volume fraction of the incompatible segments determine the interface curvature and strongly influence the mesophase morphology.

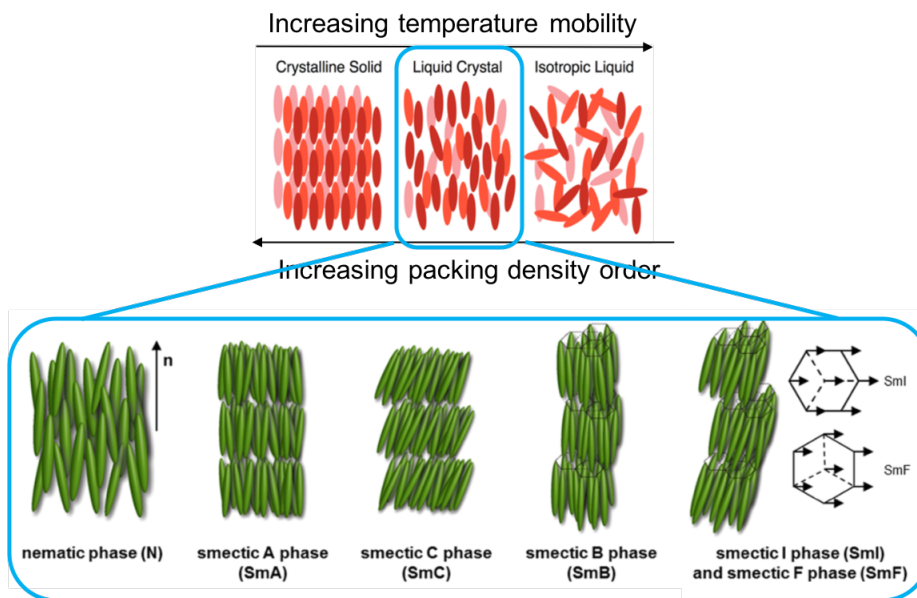


Figure 1.4 Liquid crystalline mesophases.

1.3.2 LC amphiphiles

The term amphiphile, coined by Paul Winsor more than 50 years ago, of hydrophilic and hydrophobic fractions in one molecular structure.^[70] Thermotropic LC materials are intrinsically amphiphilic, as they are usually composed of rigid and flexible segments.^[71] Self-assembly in such amphiphilic systems is based on the segregation of incompatible molecular segments into distinct subspaces^[72] to form positionally ordered LC phases. Depending on the number of incompatible components within the molecular structure, amphiphiles can be further divided into binary and tertiary systems. Binary amphiphiles organize into a series of mesophases with positional order in one (smectic LC phases), two (columnar LC phases) and three dimensions (cubic mesophases). The mesophase type is determined by the relative volume of the two incompatible parts and smectic phases (layer structures) with flat interfaces result only for molecules where the incompatible segments have comparable cross section area. The hydrophilic substituents are usually grafted to the termini of the rigid mesogenic molecules so that the tendency for parallel alignment of the rigid cores facilitates the segregation of hydrophilic and hydrophobic parts of the molecules and vice versa^[73] and therefore significantly stabilizes layered smectic structures. When the hydrophilic segments are laterally attached to the rod-like mesogenic molecules, the two organizing forces are thus perpendicularly directed and in competition to each other rather than both enhancing a predominant structure. In the former case, more interesting and complicated mesophases may be obtained.

By going from binary to tertiary amphiphiles, the complexity of the self-organized structures and also the diversity of the phase structures can be significantly enhanced with three distinct segments incompatible to each other. As a consequence, more topologies and phase structures can be

achieved. Here two specific structures will be introduced called bolaamphiphiles and facial amphiphiles.

1.3.2.1 Bolaamphiphiles

Bolaamphiphiles are composed of two polar head groups separated by one, two or three hydrophobic skeletons.^[74] In this chapter, bolaamphiphiles are referred to as a class of liquid crystals that, like block copolymers, can form ordered phase separated structures. Such molecules consist of three incompatible units: a rigid rod-like aromatic core, two hydrophilic terminal groups, and one or two lipophilic lateral chains. Depending on the number of lateral chains, bolaamphiphiles can be further divided into T-shaped^[75-77] (one lateral chain) and X-shaped^[78-80] (two lateral chains at opposite sides of the aromatic core). With appropriate structural design and under certain thermal conditions, these molecules form honeycomb cylinder arrays with a variety of geometries (see **Figure 1.5(a)**). Due to the strong competition between the tendency of the rods to align parallel to each other and the desire of the lateral chains to organize into their own subspaces, the layered smectic phase is distorted and destabilized. The rod-like cores organize into cylinder frameworks, held together by attractive interactions between the terminal groups located at the edges of the cylinder walls while the nonpolar lateral chains organize into extended columns, providing new thermotropic LC phases.^[81-84] In these structures, the length of the rigid core with respect to the volume provided by the lateral chain determines the number of rod-like cores organized in the circumference of the cylinders that are aligned parallel and fused side-by-side and edge-to-edge to give a close 2D periodic packing assigned as polygonal honeycomb ranging from tetragonal to hexagonal. Up to now, a variety of bolaamphiphiles with thiophene/phenyl groups as rigid core, glycerol terminal groups, and alkyl lateral chains have been synthesized by a leader in this field, the Tschierske group.

1.3.2.2 Facial amphiphiles

The term “facial amphiphilic” molecules was first introduced by Kahne *et al.*^[85] in 1992, defined as molecules with rigid structures containing separated hydrophilic and hydrophobic “faces” in the field of biology. In the LC field, facial amphiphiles are defined as a group of rod-like mesogens with alkyl chains at both termini and a polar group in the lateral position. Compared to bolaamphiphiles, the positions of hydrophilic and alkyl segments are switched.

A sequence of related polygonal cylinder phases with an inverted structure was also found for facial amphiphiles. The aromatic cores form cylinder shells enclosing columns containing the lateral polar chains, whereas the non-polar alkyl chains form separate columns located at the corners of the cylinders, running along the edges. Upon increasing the size of the polar lateral group, the smectic phase is gradually replaced by cylinder phases and eventually lamellae phases (see **Figure 1.5(b)**). In this way these alkyl chains interconnect the cylinder sides, leading to the formation of honeycomb structures.^[81] In addition, the terminal alkyl groups must be relatively long to enable their segregation from the aromatic cores. As a consequence, the cylinders of the facial amphiphiles have a much larger diameter compared to bolaamphiphiles.^[72]

1.4 Liquid crystals for conductivity applications

Liquid crystals have already had tremendous applications in industry fields such as LCs displays, LCs thermometers and LC polymers. Kevlar and 4-pentyl-4'-cyanobiphenyl (5CB) are among the most famous and successful LC molecules for high-strength fibers^[86] and flat-panel displays,^[87] respectively.

LC materials are also promising candidates for the efficient transport of ions and electrons. Their unique structural properties based on self-assembly into various functional nanostructures termed columnar, smectic and bicontinuous cubic phases can be used for the formation of confined 1D,

transport molecular moieties, usually alkyl groups, are immiscible with the functional parts and induce flexible properties and insulating functions, resulting in the formation of nanoscale channels. Such liquid crystal molecules can be treated as block copolymer analogues at smaller molecular dimensions. Moreover, they possess advantages in the preparation of flexible devices because they have the ability to form stable, soft and lightweight thin films, and in addition, they undergo simple and fast self-assembly and structural re-organization.^[100] In this section we will talk about the ionic and electronic conductivity separately and introduce some of their applications.

1.4.1 LCs for ionic conductivity

Nanosegregated ionic domains are desirable for ion transport in many materials including LCs. Both ionic salts, such as crown ethers,^[101] oligo(ethylene oxide)s,^[102] cyclic carbonates,^[89,93,94] diol moieties,^[103] and charged (cationic, anionic and zwitterionic) moieties, such as imidazolium,^[104,105] ammonium,^[106–109] and phosphonium^[109] units have been used to facilitate ion conductivity. Such LCs have been proposed for potential application as efficient and stable electrolytes for batteries^[89,90] and dye-sensitized solar cells (DSSCs)^[91–94]. Compared to currently-used organic liquids^[110] and gel electrolytes^[111,112] that are inherently suffering risks of leakage, evaporation or flammability, the LC electrolytes are more stable and less volatile. Yet they possess higher ionic conductivity, easier processability and better interfacial compatibility with electrode materials than their solid-state inorganic counterparts.^[113–115]

1.4.1.1 LCs for lithium-ion batteries

A lithium-ion battery is a type of rechargeable battery commonly used for portable electronics and electric vehicles. Lithium is the lightest of all metals with the greatest electrochemical potential and provides the largest energy density. However, lithium batteries failed

due to safety problems and people find lithium-ions much safer yet lower in energy density than lithium metal. In batteries lithium atoms are ionized and separated from their electrons, the ions move from the anodes (usually graphite) through an electrolyte to the cathodes (lithium cobalt oxide, LiCoO_2) where they recombine with during discharge, and back when charging.^[116] Lithium-ion batteries have a number of advantages. In addition to their high energy density (100-265 Wh/kg) and high cell voltage (3.6 V), they exhibit relatively low self-discharge and require low maintenance.

In published work by Kato, a rod-like LC molecule having a cyclic carbonate moiety attached to one terminal was used to form self-assembled, highly-mobile 2D ion-conductive pathways with lithium salts (see **Figure 1.7**).^[89] Sufficient electrochemical and thermal stability as well as efficient ion conductivity in the order of $10^{-4} \text{ S cm}^{-1}$ around 80 °C have been achieved.

1.4.1.2 Dye-sensitized solar cells (DSSCs)

DSSCs belong to the group of thin film solar cells. The modern version of DSSC was originally co-invented in 1988 by Brian O'Regan and Michael Gratzel,^[117] which is composed of a porous layer of titanium dioxide nanoparticles covered with a photosensitive dye that absorbs sunlight. The titanium dioxide is immersed under an electrolyte solution underneath a platinum-based catalyst. An anode (the TiO_2) and a cathode (the Pt) are placed on either side of a liquid conductor (the electrolyte).^[118] When light shines on the cell, the dye molecules are excited from their ground state to a higher energy state; the excited electrons are then injected into the conduction band of the TiO_2 electrode and transported to the current collector of the anode via diffusion processes. The oxidized dye molecule is again regenerated by electron donation from the

iodide in the electrolyte and in return, iodide is regenerated by reduction of triiodide on the cathode (see **Figure 1.8**).^[119]

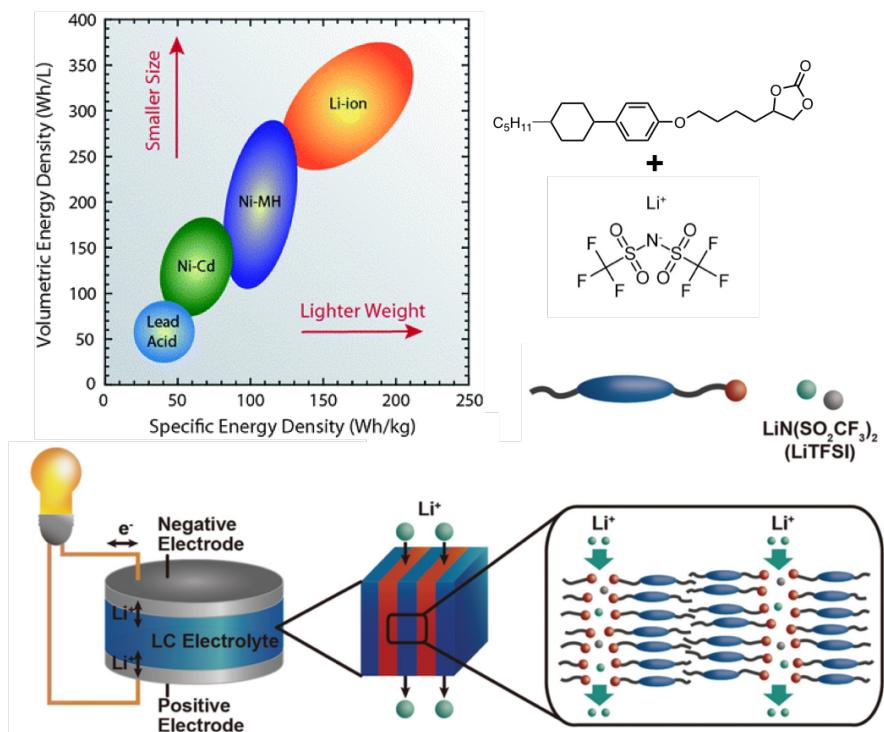


Figure 1.7 Schematic illustration of rod-like liquid crystals forming 2D ion transport channels as electrolyte for lithium-ion batteries. (Reprint from *Adv. Funct. Mater.* 2015^[89]).

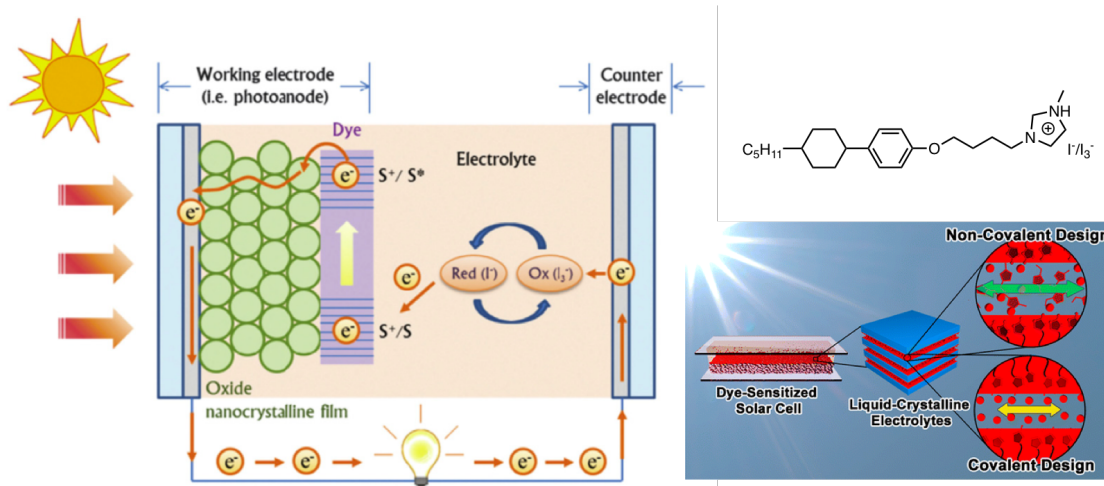


Figure 1.8 Schematic illustration of rod-like liquid crystals forming 2D ion transport channels as electrolyte for DSSCs. (Reprint from *Phys. Chem. Chem. Phys.* 2012^[131] and *Chem. Mater.* 2016^[94])

LC molecules have also been used as electrolyte materials in DSSCs. Kato *et al.* have designed mesogenic compounds which covalently bond I_2 -doped imidazolium moieties via alkyl or oligooxyethylene spacer, providing 2D ionic arrays.^[94] The presence of the oligooxyethylene spacer extends the temperature range of the SmA phase to lower temperature due to the induction of flexibility and suppression of crystallization. The diffusion coefficient of I_3^- is as high as $4.9 \times 10^{-9} \text{ cm}^2 \text{ s}^{-1}$ at 30 °C and the cell exhibits excellent long-term stability over 1000 h.

1.4.2 LCs for electronic conductivity

The π -stacking effect resulting from self-organization of the mesogenic component of an LC makes the molecules promising candidates for electron transport. π -Conjugated columnar and smectic LC molecules comprising rigid discotic and calamitic moieties have been extensively studied as organic LC semiconductors. Among all the common LC mesophases, the nematic phase is not usually considered suitable for fast charge transport because of the weak overlap of the π -

orbitals of adjacent molecules while columnar liquid crystals deserve particular attention because of their ability to form highly ordered one-dimensional structures for charge transportation.^[66,120] Smectic LCs have been developed owing to the formation of 2D charge-transport pathways upon the intermolecular π - π stacking and CH- π interactions between neighboring rod-like molecules. What's more, the fact that LC molecules are softer and may bend smoothly prevents the formation of sharp grain boundaries found in polycrystalline samples, rendering the pinning of charge carriers at grain boundaries less problematic.^[121]

LC semiconductors exhibit large anisotropic carrier transport comparable to that of amorphous and crystalline semiconductors in addition to their advantageous solution processability and film-forming ability, which makes them interesting for applications as flexible electronics. Oligothiophenes make up a promising class of organic semiconductors due to their unique and intriguing electronic, optical, and redox properties as well as their unique self-assembling properties on solid surfaces or in the bulk.^[122] Furthermore, the high polarizability of sulfur atoms in the thiophene rings leads to a stabilization of the conjugated chain and excellent charge transport properties. With respect to synthesis, thiophenes are ideal building blocks in transition metal-catalyzed cross-coupling reactions, such as Kumada-, Suzuki- and Stille-coupling, providing conjugated π -systems.

Liquid crystalline (LC) oligothiophenes have been recognized as a new type of self-organized semiconductor since they can form homogeneous thin films with high charge carrier mobilities. It has already been revealed that terthiophenes substituted with different alkyl chains at the terminal alpha-positions exhibit smectic phases whereas corresponding quaterthiophenes show smectic and nematic phases^[123] with hole/electron mobilities ranging from $\sim 10^{-4}$ to ~ 0.2 cm²V⁻¹s⁻¹. Examples

include organic field-effect transistors (OFETs),^[124–127] organic light emitting diodes (OLEDs)^[128,129] and so on.

1.4.2.1 LCs for field-effect transistors (FETs)

A FET is a type of transistor that uses an electric field to control the flow of current. It is made of three terminals: source, drain and gate. The FET controls the flow of electrons/holes from the source to drain via the application of a voltage to the gate, which affects the size and shape of a “conductive channel” between source and drain as well as altering the conductivity.^[130] LCs as promising semiconducting materials have been employed as the active layer in FET. The columnar and smectic LC semiconductors are uniaxially aligned parallel and perpendicular to the substrate (see **Figure 1.9**). In these materials, the charge carriers hop along the π -stacked region while the attachment of alkyl chains not only improves flexibility and solubility which compensates for the high melting points and low solubility resulted from extensive π -conjugated moieties, but their insulating effect also helps to achieve highly anisotropic conductivity.^[88]

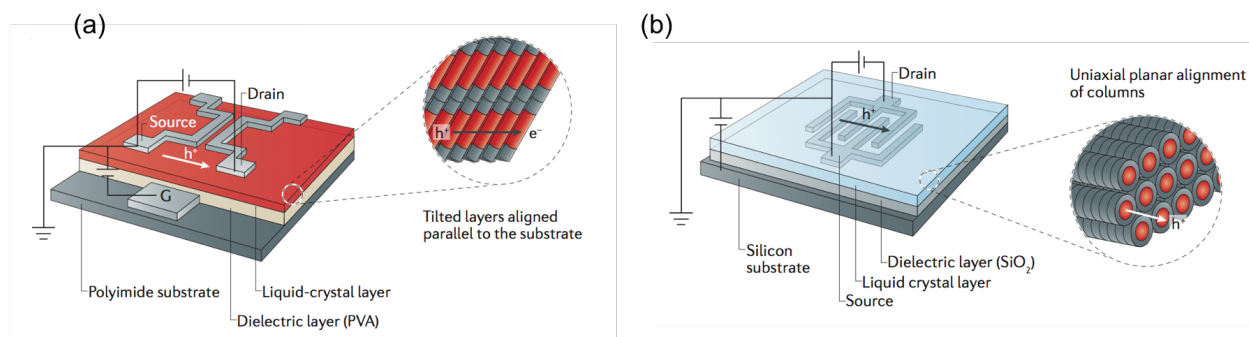


Figure 1.9 (a) Bottom-contact FET with columnar LC semiconductors. (b) Top-contact FET with smectic LC semiconductors. (Reprint from *Nature Reviews Materials* 2017^[88]).

1.5 Conclusions

Organic MIECs has shown great potential in forming unique architectures suitable for a variety of charge transport applications. Despite the great effort and achievement on separate organic ionic and electronic conductors, organic MIECs that combine both type of charge transporting unit in a single molecule remain limited. In order to enable rational design, and long-term gains in MIEC performance, the connection between ionic and electronic conductivity, and resulting morphology must be better understood. In this dissertation, I conducted a systematic study of the design, synthesis and characterization of MIECs based on 1) small dimension rod-coil liquid crystalline oligomers and 2) large dimension rod-coil block copolymers. I will identify not only the independent fundamentals of electronic and ionic conduction, but the effects of both conducting phases on each other and overall transport as well. I hope that our discovery about the fundamental principles of mixed ionic/electronic conduction could lead to new devices with potential applications in energy harvesting and storage, as well as robotic devices that combine sensing, actuation, computation, or communication capabilities and even multi-stimuli responsive “smart” materials.

Simulation and modelling studies of the molecular behavior of liquid crystals and block copolymers have become increasingly important for the design of assembled nanostructures. The relationship between molecular and self-assembled structures is well known based on experimental results; however, it remains difficult to predict the properties of nanostructured liquid crystals and block copolymers based on their molecular structures. An iterative study consisting of both simulation and experiments was carried out in which simulations have guided structural design

and synthesis of new materials while the experimental results have helped to modify simulation parameters.

REFERENCES

- [1] I. Riess, *Solid State Ionics* **2003**, *157*, 1.
- [2] A. Malti, J. Edberg, H. Granberg, Z. U. Khan, J. W. Andreasen, X. Liu, D. Zhao, H. Zhang, Y. Yao, J. W. Brill, I. Engquist, M. Fahlman, L. Wågberg, X. Crispin, M. Berggren, *Adv. Sci.* **2016**, *3*, 1500305.
- [3] Y. Lin, S. Fang, D. Su, K. S. Brinkman, F. Chen, *Nat Commun* **2015**, *6*, 6824.
- [4] O. Yu. Posudievsky, O. A. Kozarenko, I. E. Kotenko, O. P. Boiko, A. G. Shkavro, V. G. Koshechko, V. D. Pokhodenko, *Theor Exp Chem* **2014**, *50*, 197.
- [5] N. M. Kocherginsky, Z. Wang, *Synthetic Metals* **2006**, *156*, 1065.
- [6] J. Rivnay, R. M. Owens, G. G. Malliaras, *Chem. Mater.* **2014**, *26*, 679.
- [7] H. D. Abruña, Y. Kiya, J. C. Henderson, *Physics Today* **2008**, *61*, 43.
- [8] R. J. Mortimer, A. L. Dyer, J. R. Reynolds, *Displays* **2006**, *27*, 2.
- [9] E. Smela, *MRS Bull.* **2008**, *33*, 197.
- [10] S. E. Burkhardt, M. A. Lowe, S. Conte, W. Zhou, H. Qian, G. G. Rodríguez-Calero, J. Gao, R. G. Hennig, H. D. Abruña, *Energy Environ. Sci.* **2012**, *5*, 7176.
- [11] S. I. Cho, S. B. Lee, *Acc. Chem. Res.* **2008**, *41*, 699.
- [12] S. Conte, G. G. Rodríguez-Calero, S. E. Burkhardt, M. A. Lowe, H. D. Abruña, *RSC Adv.* **2013**, *3*, 1957.
- [13] J. Roncali, *J. Mater. Chem.* **1999**, *9*, 1875.
- [14] G. G. Wallace, S. E. Moulton, G. M. Clark, *Science* **2009**, *324*, 185.
- [15] D. Khodagholy, J. N. Gelinas, T. Thesen, W. Doyle, O. Devinsky, G. G. Malliaras, G. Buzsáki, *Nat Neurosci* **2015**, *18*, 310.
- [16] D. Khodagholy, T. Doublet, P. Quilichini, M. Gurfinkel, P. Leleux, A. Ghestem, E. Ismailova, T. Hervé, S. Sanaur, C. Bernard, G. G. Malliaras, *Nat Commun* **2013**, *4*, 1575.
- [17] J. Rivnay, P. Leleux, M. Ferro, M. Sessolo, A. Williamson, D. A. Koutsouras, D. Khodagholy, M. Ramuz, X. Strakosas, R. M. Owens, C. Benar, J.-M. Badier, C. Bernard, G. G. Malliaras, *Sci. Adv.* **2015**, *1*, e1400251.
- [18] D. T. Simon, S. Kurup, K. C. Larsson, R. Hori, K. Tybrandt, M. Goiny, E. W. H. Jager, M. Berggren, B. Canlon, A. Richter-Dahlfors, *Nature Mater* **2009**, *8*, 742.
- [19] A. Jonsson, Z. Song, D. Nilsson, B. A. Meyerson, D. T. Simon, B. Linderoth, M. Berggren, *Sci. Adv.* **2015**, *1*, e1500039.
- [20] X. Strakosas, M. Bongo, R. M. Owens, *J. Appl. Polym. Sci.* **2015**, *132*, 41735.
- [21] P. Lin, F. Yan, *Adv. Mater.* **2012**, *24*, 34.
- [22] M. Mastragostino, C. Arbizzani, F. Soavi, *Journal of Power Sources* **2001**, *97–98*, 812.
- [23] K. Lota, V. Khomenko, E. Frackowiak, *Journal of Physics and Chemistry of Solids* **2004**, *65*, 295.
- [24] K. S. Ryu, Y.-G. Lee, Y.-S. Hong, Y. J. Park, X. Wu, K. M. Kim, M. G. Kang, N.-G. Park, S. H. Chang, *Electrochimica Acta* **2004**, *50*, 843.
- [25] A. N. Aleshin, *Adv. Mater.* **2006**, *18*, 17.
- [26] S. Virji, J. Huang, R. B. Kaner, B. H. Weiller, *Nano Lett.* **2004**, *4*, 491.
- [27] J. Huang, S. Virji, B. H. Weiller, R. B. Kaner, *J. Am. Chem. Soc.* **2003**, *125*, 314.
- [28] H. Peng, L. Zhang, C. Soeller, J. Travas-Sejdic, *Biomaterials* **2009**, *30*, 2132.
- [29] R. J. Tseng, J. Huang, J. Ouyang, R. B. Kaner, Yang, *Nano Lett.* **2005**, *5*, 1077.
- [30] N. Oyama, T. Tatsuma, T. Sato, T. Sotomura, *Nature* **1995**, *373*, 598.
- [31] M. Armand, *Solid State Ionics* **1994**, *69*, 309.

- [32] D. Baril, *Solid State Ionics* **1997**, *94*, 35.
- [33] L. ^aBert^o Groenendaal, F. Jonas, D. Freitag, H. Pielartzik, J. R. Reynolds, 14.
- [34] R. Yue, J. Xu, *Synthetic Metals* **2012**, *162*, 912.
- [35] K. Sun, S. Zhang, P. Li, Y. Xia, X. Zhang, D. Du, F. H. Isikgor, J. Ouyang, *J Mater Sci: Mater Electron* **2015**, *26*, 4438.
- [36] L. Lindell, A. Burquel, F. L. E. Jakobsson, V. Lemaure, M. Berggren, R. Lazzaroni, J. Cornil, W. R. Salaneck, X. Crispin, *Chem. Mater.* **2006**, *18*, 4246.
- [37] J. Ouyang, *Displays* **2013**, *34*, 423.
- [38] S. K. M. Jönsson, J. Birgersson, X. Crispin, G. Greczynski, W. Osikowicz, A. W. Denier van der Gon, W. R. Salaneck, M. Fahlman, *Synthetic Metals* **2003**, *139*, 1.
- [39] A. Moujoud, S. H. Oh, H. S. Shin, H. J. Kim, *phys. stat. sol. (a)* **2010**, *207*, 1704.
- [40] S. Kirchmeyer, K. Reuter, *J. Mater. Chem.* **2005**, *15*, 2077.
- [41] M. M. de Kok, M. Buechel, S. I. E. Vulto, P. van de Weijer, E. A. Meulenkaamp, S. H. P. M. de Winter, A. J. G. Mank, H. J. M. Vorstenbosch, C. H. L. Weijtens, V. van Elsbergen, *phys. stat. sol. (a)* **2004**, *201*, 1342.
- [42] C.-J. Ko, Y.-K. Lin, F.-C. Chen, C.-W. Chu, *Appl. Phys. Lett.* **4**.
- [43] F. Verbakel, S. C. J. Meskers, R. A. J. Janssen, *Chemistry of Materials* **2006**, *18*, 2707.
- [44] S. C. J. Meskers, J. K. J. van Duren, R. A. J. Janssen, F. Louwet, L. Groenendaal, *Adv. Mater.* **2003**, *15*, 613.
- [45] B. Yoo, A. Dodabalapur, D. C. Lee, T. Hanrath, B. A. Korgel, *Appl. Phys. Lett.* **2007**, *90*, 072106.
- [46] B. Chen, T. Cui, Y. Liu, K. Varahramyan, *Solid-State Electronics* **2003**, *47*, 841.
- [47] H. Shi, C. Liu, Q. Jiang, J. Xu, *Adv. Electron. Mater.* **2015**, *1*, 1500017.
- [48] A. Shah, *Science* **1999**, *285*, 692.
- [49] A. Goetzberger, C. Hebling, H.-W. Schock, *Materials Science and Engineering: R: Reports* **2003**, *40*, 1.
- [50] S. Günes, H. Neugebauer, N. S. Sariciftci, *Chem. Rev.* **2007**, *107*, 1324.
- [51] B. C. Thompson, J. M. J. Fréchet, *Angew. Chem. Int. Ed.* **2008**, *47*, 58.
- [52] R. H. Friend, R. W. Gymer, A. B. Holmes, J. H. Burroughes, R. N. Marks, C. Taliani, D. D. C. Bradley, D. A. D. Santos, J. L. Brédas, M. Lögdlund, W. R. Salaneck, *Nature* **1999**, *397*, 121.
- [53] J.-T. Chen, C.-S. Hsu, *Polym. Chem.* **2011**, *2*, 2707.
- [54] D. Khodagholy, J. Rivnay, M. Sessolo, M. Gurfinkel, P. Leleux, L. H. Jimison, E. Stavrinidou, T. Herve, S. Sanaur, R. M. Owens, G. G. Malliaras, *Nat Commun* **2013**, *4*, 2133.
- [55] J. Rivnay, S. Inal, A. Salleo, R. M. Owens, M. Berggren, G. G. Malliaras, *Nat Rev Mater* **2018**, *3*, 17086.
- [56] J. Zhou, D. H. Anjum, L. Chen, X. Xu, I. A. Ventura, L. Jiang, G. Lubineau, *J. Mater. Chem. C* **2014**, *2*, 9903.
- [57] N. Costantini, G. Wegner, M. Mierzwa, T. Pakula, *Macromol. Chem. Phys.* **2005**, *206*, 1345.
- [58] D. Witker, M. D. Curtis, *Journal of Power Sources* **2006**, *156*, 525.
- [59] X. Ren, *J. Electrochem. Soc.* **1992**, *139*, 2097.
- [60] X. Ren, P. G. Pickup, *Faraday Trans.* **1993**, *89*, 321.
- [61] J. Plochanski, *Solid State Ionics* **2000**, *127*, 337.

- [62] Z. Siroma, J. Hagiwara, K. Yasuda, M. Inaba, A. Tasaka, *Journal of Electroanalytical Chemistry* **2010**, 648, 92.
- [63] J. S. Liu, E. Sheina, T. Kowalewski, R. D. McCullough, *Angew. Chem., Int. Ed.* **2002**, 329.
- [64] A. E. Javier, S. N. Patel, D. T. Hallinan, V. Srinivasan, N. P. Balsara, *Angewandte Chemie International Edition* **2011**, 50, 9848.
- [65] S. N. Patel, A. E. Javier, G. M. Stone, S. A. Mullin, N. P. Balsara, *ACS Nano* **2012**, 6, 1589.
- [66] T. Kato, N. Mizoshita, K. Kishimoto, *Angewandte Chemie International Edition* **2006**, 45, 38.
- [67] C. Tschierske, *Angewandte Chemie International Edition* **2013**, 52, 8828.
- [68] S. Sergeev, W. Pisula, Y. H. Geerts, *Chemical Society Reviews* **2007**, 36, 1902.
- [69] T. Kato, *Science* **2002**, 295, 2414.
- [70] M. Fariya, A. Jain, V. Dhawan, S. Shah, M. S. Nagarsenker, 9.
- [71] C. Tschierske, *J. Mater. Chem.* **1998**, 8, 1485.
- [72] C. Tschierske, *Chemical Society Reviews* **2007**, 36, 1930.
- [73] C. Tschierske, F. Hildebrandt, J. A. Schröter, J. H. Wendorff, R. Festag, M. Wittenberg, *Adv. Mater.* **1997**, 9, 564.
- [74] J.-H. Fuhrhop, T. Wang, *Chemical Reviews* **2004**, 104, 2901.
- [75] X. Cheng, X. Dong, R. Huang, X. Zeng, G. Ungar, M. Prehm, C. Tschierske, *Chemistry of Materials* **2008**, 20, 4729.
- [76] M. Prehm, F. Liu, U. Baumeister, X. Zeng, G. Ungar, C. Tschierske, *Angewandte Chemie International Edition* **2007**, 46, 7972.
- [77] B. Glettner, F. Liu, X. Zeng, M. Prehm, U. Baumeister, G. Ungar, C. Tschierske, *Angewandte Chemie International Edition* **2008**, 47, 6080.
- [78] X. Cheng, X. Dong, G. Wei, M. Prehm, C. Tschierske, *Angewandte Chemie International Edition* **2009**, 48, 8014.
- [79] H. Gao, Y. Ye, L. Kong, X. Cheng, M. Prehm, H. Ebert, C. Tschierske, *Soft Matter* **2012**, 8, 10921.
- [80] M. Prehm, G. Götz, P. Bäuerle, F. Liu, X. Zeng, G. Ungar, C. Tschierske, *Angewandte Chemie* **2007**, 119, 8002.
- [81] B. Chen, U. Baumeister, S. Diele, M. K. Das, X. Zeng, G. Ungar, C. Tschierske, *J. Am. Chem. Soc.* **2004**, 126, 8608.
- [82] B. Chen, U. Baumeister, G. Pelzl, M. K. Das, X. Zeng, G. Ungar, C. Tschierske, *J. Am. Chem. Soc.* **2005**, 127, 16578.
- [83] X. Cheng, M. Prehm, M. K. Das, J. Kain, U. Baumeister, S. Diele, D. Leine, A. Blume, C. Tschierske, *Journal of the American Chemical Society* **2003**, 125, 10977.
- [84] X. Cheng, M. K. Das, U. Baumeister, S. Diele, C. Tschierske, *J. Am. Chem. Soc.* **2004**, 126, 12930.
- [85] Y. Cheng, D. M. Ho, C. R. Gottlieb, D. Kahne, *J. Am. Chem. Soc.* **1992**, 114, 7319.
- [86] C. K. Ober, J. I. Jin, R. W. Lenz, *Adv. Polym. Sci.* **1985**, 59.
- [87] G. W. Gray, K. J. Harrison, J. A. Nash, *Electron. Lett.* **1973**, 9, 130.
- [88] T. Kato, M. Yoshio, T. Ichikawa, B. Soberats, H. Ohno, M. Funahashi, *Nature Reviews Materials* **2017**, 2, 17001.
- [89] J. Sakuda, E. Hosono, M. Yoshio, T. Ichikawa, T. Matsumoto, H. Ohno, H. Zhou, T. Kato, *Advanced Functional Materials* **2015**, 25, 1206.
- [90] R. L. Kerr, J. P. Edwards, S. C. Jones, B. J. Elliott, D. L. Gin, *Polym J* **2016**, 48, 635.

- [91] N. Yamanaka, R. Kawano, W. Kubo, T. Kitamura, Y. Wada, M. Watanabe, S. Yanagida, *Chemical Communications* **2005**, 740.
- [92] R. D. Costa, F. Werner, X. Wang, P. Grönninger, S. Feihl, F. T. U. Kohler, P. Wasserscheid, S. Hibler, R. Beranek, K. Meyer, D. M. Guldi, *Advanced Energy Materials* **2013**, *3*, 657.
- [93] D. Högberg, B. Soberats, S. Uchida, M. Yoshio, L. Kloo, H. Segawa, T. Kato, *Chemistry of Materials* **2014**, *26*, 6496.
- [94] D. Högberg, B. Soberats, R. Yatagai, S. Uchida, M. Yoshio, L. Kloo, H. Segawa, T. Kato, *Chemistry of Materials* **2016**, *28*, 6493.
- [95] U. Beginn, G. Zipp, A. Mourran, P. Walther, M. Möller, **2000**, *12*, 513.
- [96] M. Henmi, K. Nakatsuji, T. Ichikawa, H. Tomioka, T. Sakamoto, M. Yoshio, T. Kato, *Adv. Mater.* **2012**, *24*, 2238.
- [97] M. Zhou, P. R. Nemade, X. Lu, X. Zeng, E. S. Hatakeyama, R. D. Noble, D. L. Gin, *J. Am. Chem. Soc.* **2007**, *129*, 9574.
- [98] Y. Sagara, T. Kato, *Nature Chem* **2009**, *1*, 605.
- [99] T. Kato, *Angewandte Chemie International Edition* **2010**, *49*, 7847.
- [100] B. X. Dong, Z. Liu, M. Misra, J. Strzalka, J. Niklas, O. G. Poluektov, F. A. Escobedo, C. K. Ober, P. F. Nealey, S. N. Patel, *Nature Communications* **2019**, submitted.
- [101] C. F. van Nostrum, S. J. Picken, A.-J. Schouten, R. J. M. Nolte, *J. Am. Chem. Soc.* **1995**, *117*, 9957.
- [102] T. Ohtake, K. Ito, N. Nishina, H. Kihara, H. Ohno, T. Kato, *Polymer Journal* **1999**, *31*, 1155.
- [103] H. Shimura, M. Yoshio, K. Hoshino, T. Mukai, H. Ohno, T. Kato, *Journal of the American Chemical Society* **2008**, *130*, 1759.
- [104] M. Yoshio, T. Mukai, H. Ohno, T. Kato, *Journal of the American Chemical Society* **2004**, *126*, 994.
- [105] M. Yoshio, T. Kagata, K. Hoshino, T. Mukai, H. Ohno, T. Kato, *Journal of the American Chemical Society* **2006**, *128*, 5570.
- [106] T. Ichikawa, M. Yoshio, A. Hamasaki, T. Mukai, H. Ohno, T. Kato, *Journal of the American Chemical Society* **2007**, *129*, 10662.
- [107] A. E. Frise, T. Ichikawa, M. Yoshio, H. Ohno, S. V. Dvinskikh, T. Kato, I. Furó, *Chem. Commun.* **2010**, *46*, 728.
- [108] T. Ichikawa, M. Yoshio, A. Hamasaki, J. Kagimoto, H. Ohno, T. Kato, *Journal of the American Chemical Society* **2011**, *133*, 2163.
- [109] T. Ichikawa, M. Yoshio, A. Hamasaki, S. Taguchi, F. Liu, X. Zeng, G. Ungar, H. Ohno, T. Kato, *Journal of the American Chemical Society* **2012**, *134*, 2634.
- [110] K. Xu, *Chemical Reviews* **2004**, *104*, 4303.
- [111] J. Y. Song, Y. Y. Wang, C. C. Wan, *Journal of Power Sources* **1999**, *77*, 183.
- [112] A. Manuel Stephan, *European Polymer Journal* **2006**, *42*, 21.
- [113] N. Kamaya, K. Homma, Y. Yamakawa, M. Hirayama, R. Kanno, M. Yonemura, T. Kamiyama, Y. Kato, S. Hama, K. Kawamoto, A. Mitsui, *Nature Mater* **2011**, *10*, 682.
- [114] T. Minami, A. Hayashi, M. Tatsumisago, *Solid State Ionics* **2006**, *177*, 2715.
- [115] P. Knauth, *Solid State Ionics* **2009**, *180*, 911.
- [116] Lithium-ion battery. *Wikipedia* **2019**.
- [117] B. O'Regan, M. Gratzel, **1991**, 353, 4.
- [118] A. Pandikumar, S.-P. Lim, S. Jayabal, N. M. Huang, H. N. Lim, R. Ramaraj, *Renewable and Sustainable Energy Reviews* **2016**, *60*, 408.

- [119] Dye-sensitized solar cell. *Wikipedia* **2019**.
- [120] T. Yasuda, T. Shimizu, F. Liu, G. Ungar, T. Kato, *J. Am. Chem. Soc.* **2011**, *133*, 13437.
- [121] W. Pisula, M. Zorn, J. Y. Chang, K. Müllen, R. Zentel, *Macromolecular Rapid Communications* **2009**, *30*, 1179.
- [122] A. Mishra, C.-Q. Ma, P. Bäuerle, *Chem. Rev.* **2009**, *109*, 1141.
- [123] R. Azumi, G. Giitz, A. OrganischeChemieII, U. Ulm, 2.
- [124] F. Garnier, R. Hajlaoui, A. Yassar, P. Srivastava, **1994**, 265, 4.
- [125] H. Sirringhaus, T. Kawase, R. H. Friend, T. Shimoda, M. Inbasekaran, W. Wu, E. P. Woo, **2000**, *290*, 5.
- [126] B. S. Ong, Y. Wu, P. Liu, S. Gardner, *J. Am. Chem. Soc.* **2004**, *126*, 3378.
- [127] C. Waldauf, P. Schilinsky, M. Perisutti, J. Hauch, C. J. Brabec, *Adv. Mater.* **2003**, *15*, 2084.
- [128] D. Fichou, *J. Mater. Chem.* **2000**, *10*, 571.
- [129] U. Mitschke, P. Bäuerle, *J. Mater. Chem.* **2000**, *10*, 1471.
- [130] Field-effect transistor. *Wikipedia* **2019**.
- [131] Q. Zhang, D. Myers, J. Lan, S. A. Jenekhe, G. Cao, *Phys. Chem. Chem. Phys.* **2012**, *14*, 14982.

Chapter Two: Self-Assembly Behavior of An Oligothiophene-Based Conjugated Liquid Crystal and Its Implication for Mixed Ionic-Electronic Conductivity Characteristics¹

2.1 Introduction

Liquid crystals (LCs) are thermodynamically stable phases with an intermediate degree of order between the isotropic melt (amorphous) and the crystal (perfectly regular).^[1-3] In LC phases, the molecules exhibit lower order and density than in the crystalline phase, but they are easier to align homogeneously and spontaneously over large areas.^[3] Ordered self-assembled molecules can induce enhanced properties and functions,^[4] thus enabling specific applications in a wide variety of advanced technologies.^[5,6] The idea of using LCs for ion^[7-10] and electron^[5,6,11,12] transport has attracted much attention in recent decades. The spontaneous phase segregation between immiscible parts^[5,6,13-15] enables the use of LCs as anisotropic ion conductors, making them promising candidates for energy devices. Moreover, their properties of fast assembly and easy processability^[16] excel those of traditional electrolytes. By tuning the molecular shape and intermolecular interactions, mesogenic molecules can self-assemble into a range of LC nanostructures such as columnar, smectic or bicontinuous cubic phases, providing 1D,^[17-19] 2D,^[20-24] and 3D^[7,25-28] ion transport pathways. These molecules have been proposed for potential application as efficient and stable electrolytes for batteries and dye-sensitized solar cells.^[10,29-33] 1D and 2D channels formed by discotic and rod-like LCs, respectively, are mostly studied.

In general, ion conducting LCs consist of polar or ionic groups such as cyclic carbonates,^[10,32,33] poly(ethylene oxide)s (PEOs),^[20,21,35,36] or cationic and anionic moieties attached to rod-like or

¹ This work is published as two papers: (1) Z. Liu, B. X. Dong, M. Misra, Y. Sun, J. Strzalka, S. N. Patel, F. A. Escobedo, P. F. Nealey, C. K. Ober, *Adv. Funct. Mater.* **2019**, *29*, 1805220^[51] and (2) B. X. Dong, Z. Liu, M. Misra, J. Strzalka, J. Niklas, O. G. Poluektov, F. A. Escobedo, C. K. Ober, P. F. Nealey, S. N. Patel, *ACS Nano* **2019**, *13*, 7665.^[52] Dr. Ban X. Dong helped with GIWAXS and conductivity measurements. Dr. Mayank Misra performed MD simulations.

wedge-shaped moieties to achieve columnar and smectic structures.^[37] The 2D arrangement of smectics is believed to be more tolerant with regard to defects than 1D ordered columns and provides more directions for ion transport therefore results in an improved performance.^[3] Despite large amount of recent work focusing on ionic conduction achieved by small ionic or cyclic carbonate moieties, PEO remains a popular component for LCs. Extensive studies have shown that PEO possesses excellent solvating capability for a wide range of lithium salts, and inherently high ionic conductivity and facile processability.^[38] In these molecules, PEO moieties are usually attached to mesogenic fragments so that the coexistence of ion-conducting and non-conducting phases induces better phase segregation and ions are transported through segmental motion of PEO fragments.

Phase segregation and self-assembly provide additional functionality and stability to LC materials. Generally, segregation is favored in molecules with well-defined intramolecular contrast, such as distinct rigid and flexible segments. Apart from specific intermolecular interactions such as hydrogen bonding and ionic interactions that play key roles in the formation of complex structures, π - π stacking interaction is also considered one of the very important non-covalent interactions as driving force for molecules to achieve hierarchical self-assembly.^[39,40] Abundant evidence from the columnar stacking of discotic LC molecules suggests that self-assembly through strong π - π stacking could be an effective approach to 1D nanostructures for planar, rigid organic molecules,^[6,41] and it could also be effective to obtain 2D nanostructures with calamitic molecules. π - π stacking has in fact been observed in many oligothiophenes and their derivatives.^[42-48] Experimental measurements indicate that π - π interaction plays an important role in the control of the solid-state and self-assembled structures of thiophene oligomers and polymers.^[49,50]

To this end, we report the synthesis and characterization of a coil-rod-coil π -conjugated LC compound (4T/PEO4) consisting of oligothiophene and ethylene oxide moieties. The rigid rod mesogen consists of four thiophene rings whereas the flexible tetra(ethylene oxide) segments on both ends of the mesogen core function as ion transport domains. Oligothiophene moieties, commonly used in flexible electronics, were chosen to endow electronic transport properties to the compound for a promising mixed ionic/electronic conducting material. Using both grazing incidence wide-angle X-ray scattering (GIWAXS) and molecular dynamics (MD) simulation, we show that the compound exhibits ordered smectic phases in the absence and presence of lithium bis(trifluoro-methanesulfonyl)imide (LiTFSI) at concentration $r = [\text{Li}^+]/[\text{EO}]$ up to 0.2. Temperature-dependent GIWAXS and MD simulations indicated the π - π interaction among mesogens also plays a key role in controlling LC self-assembly. Further, ionic conductivity is measured by electrochemical impedance spectroscopy for different doping ratios and temperature ranging from 25 °C to 130 °C. Our results provide important new insights into self-assembly behavior of this class of π -conjugated LCs and their morphology-ion transport relationship. Later in this chapter, mixed conduction of 4T/PEO4 was further investigated with its electronic conductivity realized by exposing the samples to vapor of 2,3,5,6-tetrafluoro-7,7,8,8-tetracyanoquinodimethane (F4TCNQ), a method known to introduce electronic dopants into organic semiconductors without disrupting the morphology of the host material. The optimum ion transport is observed at low LiTFSI concentration where 4T/PEO4 adopts smectic morphology, and the highest electronic conductivity is seen at $r = 0.10$ where favorable electronic percolation pathways exist. This work is published as two papers: (1) Z. Liu, B. X. Dong, M. Misra, Y. Sun, J. Strzalka, S. N. Patel, F. A. Escobedo, P. F. Nealey, C. K. Ober, *Adv. Funct. Mater.* **2019**, *29*, 1805220^[51] and (2) B. X. Dong, Z. Liu, M. Misra, J. Strzalka, J. Niklas, O. G. Poluektov, F. A.

Escobedo, C. K. Ober, P. F. Nealey, S. N. Patel, *ACS Nano* **2019**, *13*, 7665.^[52] Dr. Ban X. Dong helped with GIWAXS and conductivity measurements. Dr. Mayank Misra performed MD simulations.

2.2 Experimental section

2.2.1 Materials

N-bromosuccinimide (NBS), 2-thiopheneethanol were purchased from AK Scientific, Inc. Sodium hydroxide (NaOH), p-toluenesulfonyl chloride, triethylene glycol monomethyl ether, [1,3-Bis(diphenylphosphino)propane]dichloronickel(II) (Ni(dppp)Cl₂), and isopropylmagnesium chloride solution (*i*-PrMgCl, 2.0 M in THF), bis(trifluoromethane)sulfonimide lithium salt (LiTFSI, battery grade) were purchased from Sigma-Aldrich. 5,5'-dibromo-2,2'-bithiophene was purchased from One Click Chemistry. Organic solvent such as hexane, ethyl acetate (EtOAc), tetrahydrofuran (THF) and methanol (MeOH) was purchased from Fisher. All reagents and solvents were used as received unless otherwise noted. Anhydrous THF was freshly distilled from sodium and benzophenone prior to use. NBS was recrystallized in water and stored in refrigerator before use.

2.2.2 Materials preparation

Solutions of 4T/PEO4 and LiTFSI were prepared separately by dissolving the materials in anhydrous THF at a concentration of 10 mg/mL each and fully shaken using a vortexer before mixing. 4T/PEO4 and LiTFSI solution were then mixed at the appropriate ratios to achieve the concentrations $r = [\text{Li}^+]/[\text{EO}]$. Differential scanning calorimetry (DSC), polarized optical microscope (POM) images, and X-ray diffraction (XRD) were taken on bulk 4T/PEO4-LiTFSI complexes prepared by slow evaporation of the mixed 4T/PEO4-LiTFSI solution at 80 °C followed by drying under vacuum for 24h at 80 °C.

Small-angle X-ray scattering (SAXS), grazing incidence wide-angle X-ray scattering (GIWAXS), and ion conductivity measurements were performed on 4T/PEO4 thin films spin-cast from the mixed solution at 1000 rpm for 2 min. The film thickness of all thin film samples is ca. 80 nm as confirmed by spectroscopic ellipsometry.

2.2.3 Characterization methods

2.2.3.1 Nuclear magnetic resonance (NMR)

^1H and ^{13}C NMR spectra were recorded on a Varian INOVA 400 and a MERCURY 300 spectrometers. Chemical shifts were quoted relative to the residual protons of the deuterated solvents CDCl_3 ($\delta = 7.26$ for ^1H and $\delta = 77.36$ for ^{13}C). The multiplicity was characterized by the following abbreviations: s-singlet, d-doublet, t-triplet, q-quartet, m-multiplet.

2.2.3.2 Differential scanning calorimetry (DSC)

DSC measurements were performed on a Q 2000 from TA Instruments at a scanning rate of $10\text{ }^\circ\text{C}/\text{min}$ within temperature range from -90 to $250\text{ }^\circ\text{C}$. The phase transition temperatures were determined as the peak positions in the DSC traces due to broadness of the transition peaks.

2.2.3.3 Polarized optical microscope (POM)

An Olympus BX51 polarizing optical microscope equipped with a Mettler FP 82 HT hot stage were used for visual observation of optical textures at different temperatures.

2.2.3.4 X-ray diffraction (XRD) and Small-angle X-ray Scattering (SAXS)

XRD patterns were obtained using Bruker D8 Advance ECO powder diffractometer with $\text{Cu K}\alpha$ radiation $\lambda = 1.54\text{ \AA}$. SAXS patterns were obtained using Rigaku SmartLab X-ray diffractometer with $\text{Cu K}\alpha$ radiation $\lambda = 1.54\text{ \AA}$.

2.2.3.5 Grazing- incidence wide-angle X-ray scattering (GIWAXS)

Temperature dependence GIWAXS measurements were performed at beamline 8-ID-E of the Advanced Photon Source, Argonne National Laboratory with 10.86 keV ($\lambda = 1.1416 \text{ \AA}$) synchrotron radiation. The temperature of the samples was varied from room temperature up to 130°C using a Linkam HFSX350-GI stage. Samples were measured inside a low vacuum chamber (10^{-3} mbar) to minimize concerns about radiation damages, samples' moisture uptake and extraneous scattering from ambient air. The measurement time was chosen to be 3 second per frame. For each sample, 3 data sets were taken from 3 adjacent spots on the sample and then summed in order to enhance the signal-to-noise ratio. The samples were tilted at an angle of incidence of 0.14° with respect to the incoming beam, which is above the estimated critical angle of sample (ca. 0.13°) but below the critical angle of the Si substrates (ca. 0.17°) in order to probe the whole film thickness. The scattering signal was recorded with a Pilatus 1MF pixel array detector (pixel size = 172 \mu m) positioned 228 mm from the sample. Each data set was stored as a 981×1043 32-bit tiff image with 20-bit dynamic range. The Pilatus detector has rows of inactive pixels at the border between detector modules. In order to fill these gaps, after each measurement the detector was moved to a new vertical direction and the measurement on each spot was repeated, then the gaps were filled by combining the data from two detector positions. The signals were reshaped and output as intensity maps in q_z vs q_r ($= \sqrt{q_x^2 + q_y^2}$) space. We also performed detector non-uniformity, detection efficiency, the polarization effect and solid-angle variation for each image. All the GIWAXS data processing and extraction were executed using the GIXSGUI package for MATLAB.^[53]

Peak shape analysis was performed on wedge cuts taken with an angular breadth of 2° . Each wedge cut was first fit to an empirical baseline function to enable the subtraction of the background intensity and amorphous scattering. The background-subtracted wedge cut was then fit to a Voigt

function to extract the peak position and the full width at half-maximum (FWHM) of the reflections of interest. More details of peak shape analysis can be found elsewhere.^[54]

2.2.3.6 Conductivity Measurements

Electrochemical Impedance Spectroscopy (EIS) conductivity measurements were performed on samples fabricated on top of custom-built interdigitated gold electrode devices (IDE) using a Gamry 600+ Potentiostat inside a nitrogen-filled glovebox. Prior to EIS measurement, the excess amount of materials on the electrode pads was scraped away to make electrical connection from the Potentiostat to the sample. The electrical connection was made using two probe manipulators (Semiprobe Inc.). The EIS characterization was performed from 1 MHz to 0.1 Hz with an oscillatory peak potential of 50 mV. EIS measurement was carried out at different temperature controlled by a miniature benchtop heater controller (Omega Engineering Inc.). The collected impedance data were then fit to the appropriate equivalent circuit in order to extract the sample ionic resistance R_{ion} and then ionic conductivity according to the following equation:^[55]

$$\sigma = \frac{1}{R} \frac{d}{l(N-1)h}$$

l - the length of gold electrode, 1000 μm

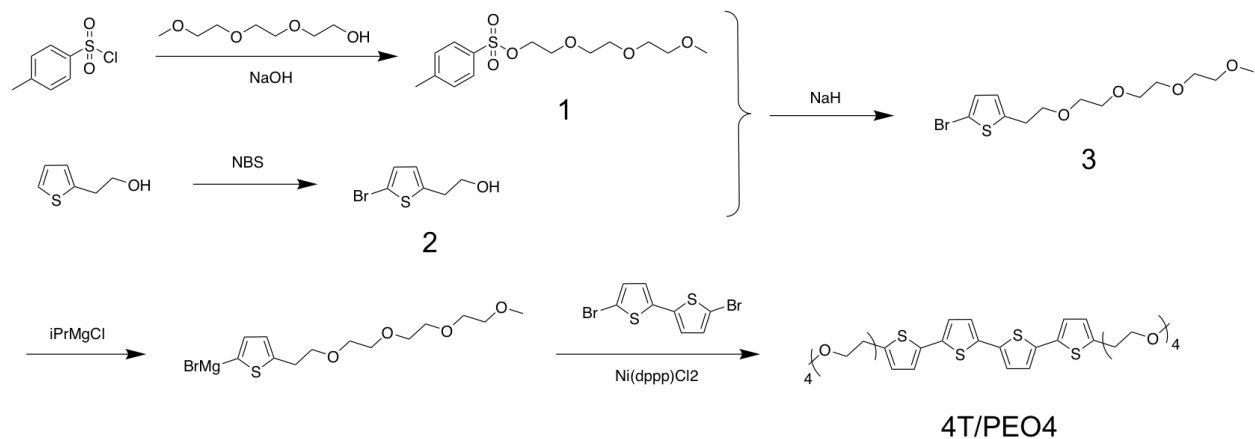
d -distance between adjacent electrode teeth, 8 μm

N -number of gold electrodes, 160

R - ion resistance

h - total thickness of the sample, 80 nm

2.2.4 Synthetic procedures



Scheme 2.1 Synthetic procedure of 4T/PEO4.

Synthesis of 2-(2-(2-methoxyethoxy)ethyl) 4-methylbenzenesulfonate (1)

To a 500mL round bottom flask with a magnetic bar was added triethylene glycol monomethyl ether (100 mmol, 1.0 eq) dissolved in 70 mL THF. Sodium hydroxide (350 mmol, 3.5 eq) was dissolved in 70 mL H₂O and then added slowly to the flask. After the reaction mixture was cooled down to 0 °C in an ice bath, p-toluenesulfonyl chloride dissolved in 50 mL THF was added dropwise to the mixture under vigorous stirring. The reaction mixture was stirred at 0 °C for 2 h, and then at room temperature for 12 h. After completion of the reaction as indicated by TLC, the reaction mixture was poured to 5 wt% hydrochloric acid aqueous solution, and the product was extracted with dichloromethane (30 mL × 3). The organic layer was then washed successively with saturated sodium bicarbonate solution (50 mL × 3) and water (50 mL × 3) and dried over anhydrous magnesium sulfate. After solvent evaporation the product was obtained as a slight yellow liquid without further purification, yield 97%.

¹H-NMR (400MHz, CDCl₃, δ): 7.80 (d, J=8 Hz, 2H; Ar H), 7.34 (d, J=8 Hz, 2H; Ar H), 4.15 (t, J=4 Hz, 2H; CH₂), 3.68 (t, J=4 Hz, 2H; CH₂), 3.62-3.58 (m, 6H; CH₂), 3.53-3.50 (m, 2H; CH₂), 3.36 (s, 3H; CH₃), 2.44 (s, 3H; CH₃) ppm.

Synthesis of 5-bromo-2-thiopheneethanol (2)

2-thiopheneethanol (50 mmol, 1.0 eq) was dissolved in 100 mL THF and cooled down to 0 °C in an ice bath. Recrystallized NBS (50 mmol, 1.0 eq) was added to the solution portionwise. The reaction was stirred at 0 °C for 1h, and then at room temperature for 5h before quenched with 10wt% sodium hydroxide aqueous solution. The crude product was extracted with ethyl acetate (30 mL × 3) and the combined organic layer washed with water (50 mL × 3), then dried over magnesium sulfate. The solvent was evaporated, and the product was purified by column chromatography on silica gel with hexane: EtOAc =5:1 (v/v) as eluent to give **2** as a yellow liquid (41.6 mmol) in 83% yield.

¹H-NMR (400MHz, CDCl₃, δ): 6.90 (d, J=4 Hz, 1H; Th H), 6.64 (d, J=4 Hz, 1H; Th H), 3.83 (q, J=4 Hz, 2H; CH₂), 3.00 (t, J=8 Hz, 2H; CH₂), 1.61 (t, 1H, OH) ppm.

Synthesis of 13-(5-bromothiophen-2-yl)-2,5,8,11-tetraoxatridecane (3)

To a dry round bottom flask was added sodium hydride (60 wt% in mineral oil, 80 mmol, 2.0 eq), and 100 mL anhydrous THF. The reaction mixture was stirred under Argon atmosphere at room temperature for 30 min. **2** (40 mmol, 1.0 eq) was then added dropwise via a syringe and the mixture was stirred vigorously at room temperature for 1h. **1** (48 mmol, 1.2 eq) was added to the reaction mixture slowly and stirred at room temperature overnight. After completion of the reaction as indicated by TLC, the reaction mixture was quenched with 200 mL H₂O and vigorously stirred for 30 min. The crude product was extracted with ethyl acetate (50 mL × 3) and then washed with water (80 mL × 3). The solvent was evaporated after dried over magnesium sulfate, and the crude product was purified by column chromatography on silica gel with hexane: EtOAc =1:1 (v/v) as eluent to give **3** as a yellow liquid (31 mmol) in 77.5% yield.

¹H-NMR (400MHz, CDCl₃, δ): 6.85 (d, J=4 Hz, 1H; Th H), 6.60 (d, J=4 Hz, 1H; Th H), 3.66-3.63 (m, 12H; CH₂), 3.56-3.54 (m, 2H, CH₂), 3.38 (s, 3H; CH₃), 3.01 (t, J=4 Hz, 2H; CH₂) ppm.

Synthesis of 5,5'''-di(2,5,8,11-tetraoxatridecan-13-yl)-2,2':5',2'':5'',2'''-quaterthiophene (4T/PEO4)

To a dry 100 mL 3-neck flask filled with Argon was added **3** (9 mmol, 3.0 eq) dissolved in 10 mL anhydrous THF. Isopropyl magnesium chloride (2.0 M in THF, 9.6 mmol, 3.2 eq) was added dropwise. The mixture was refluxed at 65 °C for 3.5 h and was transferred to a second 3-neck flask with 5,5'-dibromo-2,2'-bithiophene (3 mmol, 1.0 eq) and Ni(dppp)Cl₂ (0.15 mmol, 0.05 eq) under Argon atmosphere through cannula. The reaction mixture was refluxed at 65 °C for 20h, before being quenched with 5 wt% hydrochloric acid aqueous solution. With remaining catalyst filtered, the crude product was extracted with ethyl acetate (30 mL × 3) and washed successively with saturated aqueous sodium bicarbonate (30 mL × 3) and H₂O (30 mL × 3). The solution was evaporated after dried over magnesium sulfate and the product was purified with by column chromatography on silica gel with EtOAc: methanol =50:1 (v/v) to give a red viscous liquid. Solid was precipitated out by addition of methanol and filtered to give 4T/PEO4 as a dark red wax (0.90 mmol) in 30% yield.

¹H-NMR (CDCl₃, 400MHz, δ): 7.04 (dd, J₁=12 Hz, J₂=4 Hz, 4H; Th H), 6.99 (d, J=4 Hz, 2H, Th H), 6.76 (d, J=4 Hz, 2H, Th H), 3.72 (t, J=8 Hz, 4H; CH₂), 3.67-3.64 (m, 20H; CH₂), 3.56-3.53 (m, 4H; CH₂) 3.37 (s, 6H; CH₃), 3.08 (t, J=8 Hz, 4H; CH₂) ppm.

2.3. Results and discussions

2.3.1 Synthesis of Liquid Crystalline Material 4T/PEO4

A quaterthiophene-based π -conjugated LC compound designated 4T/PEO4, has been designed and synthesized as shown in **Scheme 2.1**. In this molecule, the terminal PEO4 segments are directly attached to both ends of a quaterthiophene (4T) core without any linker, in order to maximize the volume ratio and ion transport function of PEO moieties. The synthesis of compound 4T/PEO4 was accomplished via two-fold Kumada cross-coupling of 5,5'-dibromo-2,2'-bithiophene with three equivalents of the corresponding brominated thiophene-PEO4 precursors in the presence of Ni(dppp)Cl₂ as catalyst.

2.3.2 Thermal and Structural Properties of Bulk 4T/PEO4-LiTFSI Mixtures

The thermal properties of the compound 4T/PEO4 were analyzed by differential scanning calorimetry (DSC). Optical textures of the substances exhibiting LC phases were obtained by polarized optical microscopy (POM). Here we investigate the structure of 4T/PEO4 blended with LiTFSI which has good thermal stability, high ion dissociation rate and high ionic conductivity.^[56] Specifically we choose to study 4T/PEO4-LiTFSI complexes with 3 different blending ratios $r = [\text{Li}^+]/[\text{EO}] = 0$ (neat sample), 0.01 and 0.05. We notice that higher blending concentration r results in a more complex structure due to the strong interaction of LiTFSI with the LC molecules and is the subject of a separate investigation.

Figure 2.1(a) presents the DSC traces from the 1st cooling scans and the subsequent 2nd heating scans obtained for the three samples $r = 0, 0.01, \text{ and } 0.05$. The doping ratio r was set between 0 and 0.05 because ionic conductivity in polyether derivatives generally shows a maximum in the vicinity of 0.05 mol of ions to ethylene oxide unit.^[20] The thermogravimetric analysis (TGA) results shown **Figure 2.2** suggest that both 4T/PEO4 and LiTFSI remain stable within the DSC temperature range. All three samples exhibit stable LC mesophases at room temperature. Pristine compound 4T/PEO4 ($r = 0$) shows a pronounced transition during both cooling and heating

processes. The blended complexes, on the other hand, exhibit more complicated thermal behaviors, including multiple phases observed from the small shoulder peak around the transition temperature as well as a monotropic transition in the heating process for $r = 0.05$. A sharp transition temperature

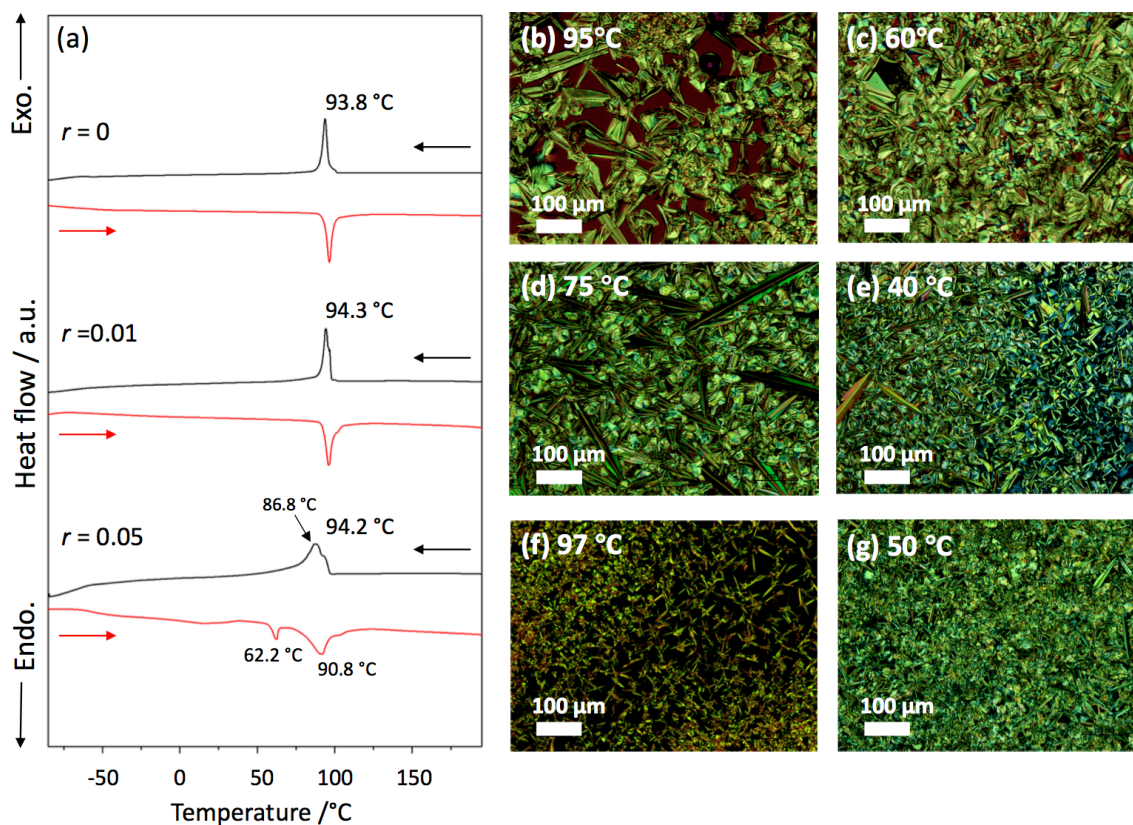


Figure 2.1. DSC traces ($10\text{ }^{\circ}\text{C min}^{-1}$) and POM images of 4T/PEO4 -LiTFSI complexes: (a) 1st cooling scans (indicated by black arrows) and 2nd subsequent heating scans (indicated by red arrows) of 4T/PEO-LiTFSI complexes ($r = 0$, $r = 0.01$, $r = 0.05$), (b) POM image of pristine 4T/PEO4 ($r = 0$) on cooling from isotropic melt at 95°C and (c) 60°C, (d) POM image of 4T/PEO4-LiTFSI complex ($r = 0.01$) on cooling from isotropic melt at 75°C and (e) 40°C, (f) POM image of 4T/PEO4-LiTFSI complex ($r = 0.05$) on cooling from isotropic melt at 97°C and (g) 50°C. (scale bar: 100 μm). (Reprint from *Adv. Funct. Mater.* 2019^[51]).

appears around 94 °C for all three samples (93.8 °C for $r = 0$, 94.3 °C for $r = 0.01$, and 94.2 °C for $r = 0.05$) suggesting that the addition of LiTFSI doesn't change the structure and phase of 4T/PEO4. What cannot be neglected, however, is the broadening of the transition peak and the appearance of a shoulder peak (86.8 °C) for sample $r = 0.05$, which suggests that an even more complicated phase shows up and overwhelms the original smectic phase. A higher doping ratio was not adopted due to the possibility that the incorporation of large TFSI anions are antagonistic to an ordered phase and may disturb the in-plane packing of thiophenes in the smectic layer and therefore destabilize the LC structures.^[10] More details about the thermal properties of 4T/PEO4-LiTFSI complexes are listed below in **Table 2.1**.

Table 2.1 Thermal Properties of 4T/PEO4-LiTFSI complexes

Complex	Thermal properties						
	1 st cooling			2 nd heating			
$r = 0$	Iso	93.8 (21.4)	Sm	Sm	93.6 (22.7)	Iso	
$r = 0.01$	Iso	94.3 (23.0)	Sm	Sm	96.3 (24.8)	Iso	
$r = 0.05$	Iso	86.8 (14.7)	Sm	Sm	62.2 (2.28)	90.8 (8.58)	Iso

Transition temperatures (°C) are given as the maximum of the peaks detected by DSC measurements on the 1st cooling and 2nd heating at a scanning rate of 10 °C min⁻¹. The transition enthalpies (kJ mol⁻¹) are in parentheses. Sm: smectic. Iso: isotropic liquid.

The POM images provide a clearer picture towards the process of the phase transition. The bulk material is placed between a piece of glass microscope slide and cover slip. The sample is heated to above the transition temperature at a heating rate of 10 °C min⁻¹, the same as the DSC scan rate. A film of several microns thick is formed between the microscope slide and cover slip when the

sample optically turns black under the polarized light microscope, signifying an isotropic melt. In **Figure 2.1(b)**, the formation of a batonnet texture, typical for a smectic phase, is observed for pristine 4T/PEO4 compound when cooled from isotropic melt at 95 °C. Such a texture is maintained until the sample is cooled down to 60 °C (see **Figure 2.1(c)**) where the texture becomes more uniform, suggesting that the compound has formed a smectic phase. The two blended complexes, on the other hand, exhibit more complicated phase transitions during the cooling process. The complex with $r = 0.01$ also shows a batonnet texture at the beginning of the cooling process, which is then taken over by two coexisting mesophases as shown in **Figure 2.1(d)**. The coexistence of different textures suggests the possibility of multiple mesophases whose transition temperatures are so close that the transition peaks have overlapped, consistent with DSC measurement. As temperature further decreases, the batonnet texture fades while the other more ordered phase becomes the majority at ambient temperature (see **Figure 2.1(e)**). The complex with $r = 0.05$ shows a similar trend to the one with $r = 0.01$. An obvious batonnet texture at the isotropic–smectic transition was observed as shown in **Figure 2.1(f)**, which then also experiences coexistence with and replacement by a higher ordered phase as temperature decreases (see **Figure 2.1(g)**). At room temperature the complex exhibits a less ordered smectic phase compared to that with $r = 0.01$. Such phenomena can be attributed to the higher doping ratio of LiTFSI that slightly disturbs π - π stacking of oligothiophene thus reducing the degree of chain alignment within the materials.

X-ray diffraction (XRD) was carried out to examine the mesomorphic phase structures of compound 4T/PEO4 and its blended complexes with LiTFSI. **Figure 2.3** shows the representative XRD pattern for compound 4T/PEO4 as a bulk material at ambient temperature. The 4 diffraction peaks indexed as (001), (002), (003) and (004) indicate a layer spacing of ca. 3.5 nm in the smectic

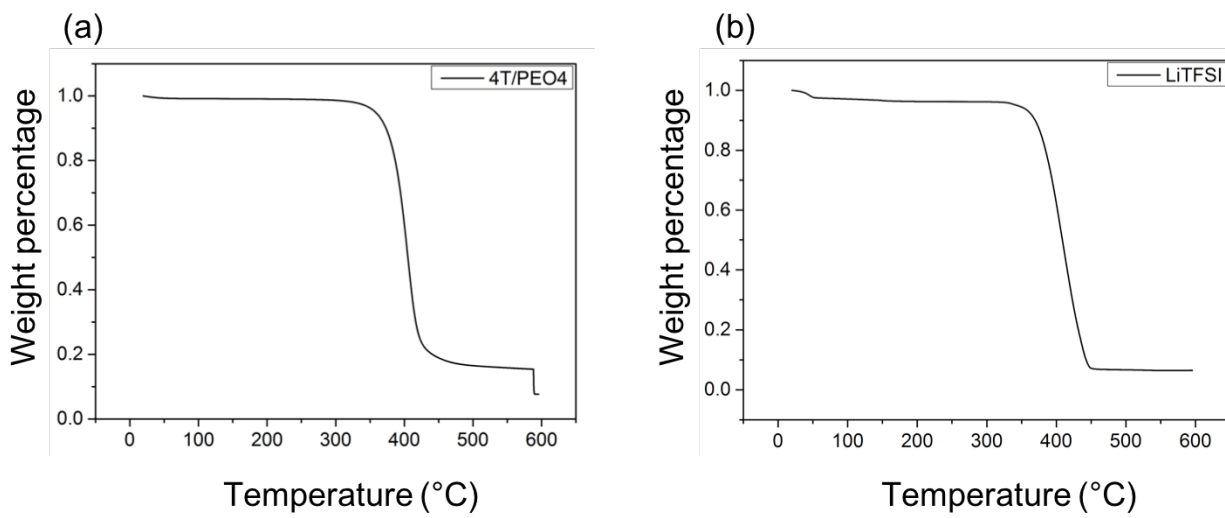


Figure 2.2. TGA of (a) pristine 4T/PEO4, and (b) pristine LiTFSI. (Reprint from *Adv. Funct. Mater.* 2019^[51]).

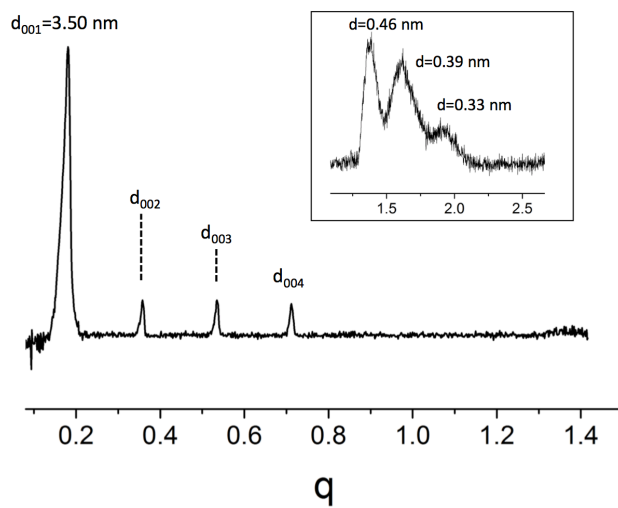


Figure 2.3. X-ray diffraction pattern of neat 4T/PEO4 compound (bulk) shows smectic phase at ambient temperature. (Reprint from *Adv. Funct. Mater.* 2019^[51]).

phase. The broad peaks in the wide-angle region reflect the molecular arrangement inside each layer with intermolecular distances from 0.33 nm to 0.46 nm. We assigned these peaks to the π - π stacking of 4T units as they are within the expected range of π - π stacking distance.^[57,58] This result not only supports the existence of an ordered smectic structure with fixed layer distance, but also suggests π stacking between oligothiophene segments might play a role in maintaining such structure, in accordance with the POM images. Later we will show that this conclusion is further supported by MD simulation and GIWAXS measurement.

2.3.3 Self-assembly Behavior of 4T/PEO4-LiTFSI Thin Film Measured by Temperature-dependent GIWAXS

To gain more insight into the self-assembly behaviors of 4T/PEO4, we performed temperature-dependent GIWAXS measurement on ca. 80 nm thin film samples of 4T/PEO4-LiTFSI complexes. The experiments were carried out at different temperatures ranging from 25 °C to 123 °C to capture the phase transition behavior of 4T/PEO4 revealed by DSC. The samples were equilibrated at each temperature for ca. 20 min. **Figure 2.4** shows exemplary GIWAXS patterns of the three samples ($r = 0, 0.01, 0.05$) at selected temperatures: as-cast sample at 25 °C, high temperature 123 °C and annealed sample at 25 °C after cooling back from the first heating cycle. At each selected temperature, the GIWAXS patterns of the 3 samples appear qualitatively similar. As shown in **Figure 2.4(a)**, for pristine 4T/PEO4 thin film $r = 0$ at 25 °C, we observe narrow and well-defined diffraction peaks ($00h$) in the out-of-plane direction up to the 4th order. This is evidence of a smectic morphology in which the layers are oriented parallel to the substrate with a layer distance of ca. 3.42 nm, in good agreement with XRD results shown in **Figure 2.3**. This observation demonstrates that different fabrication methods do not affect LC structures and molecular

alignment for this material. While this smectic morphology is retained in both LiTFSI-blended samples at 25 °C, we observe an increase in the layer spacing distance from 3.42 to 3.48 nm upon introduction of LiTFSI at $r = 0.05$. This observation provides indirect evidence that addition of LiTFSI swells the PEO domains, similar to previous studies on block copolymer-salt and LC-salt complexes.^[59,60] Interestingly, together with the smectic ordering peaks, we also observe two strong elongated peaks near $q_r \sim 1.3 - 1.5 \text{ \AA}^{-1}$ denoted as A and B and other elongated peaks at higher q in **Figure 2.4(a)**, (d) and (g). The A and B peaks originate from the π -stacking interaction of the adjacent 4T units whereas the other elongated peaks are the higher order peaks of A and B. Later we will show that this conclusion is further supported by molecular dynamics simulations. The elongation of these peaks most likely originates from the strong in-plane but rather weak out-of-plane interaction of the π - π stacking units. In other words, the 4T units interact exclusively with other 4T units within the same 2D smectic layer.

As the sample is heated above the transition temperature, the π - π diffraction peaks become notably weak in $r = 0$ sample shown in **Figure 2.4(b)**, and not observable in $r = 0.01$ and $r = 0.05$ samples (see **Figure 2.4(e)** and (h)). Coinciding with the weakening/disappearing of the π - π interaction peaks, we observe a substantial broadening of the $(00h)$ diffraction peaks, indicating a significant loss of smectic ordering above the transition temperature. Our results thus unambiguously indicate that the π - π interaction of the 4T units plays a significant role in controlling the layered structures of 4T/PEO4. Here, it is important to note that at high temperature, all samples are not completely disordered and still maintain weakly layered structures. Upon cooling from above the transition temperature, partial recovery of the ordered smectic phases as well as some new diffraction features are observed as shown in **Figure 2.4(c)**, (f) and (i). Any unmelt molecules remaining after the heating process act as nucleation sites upon cooling and lead to LC phases with different

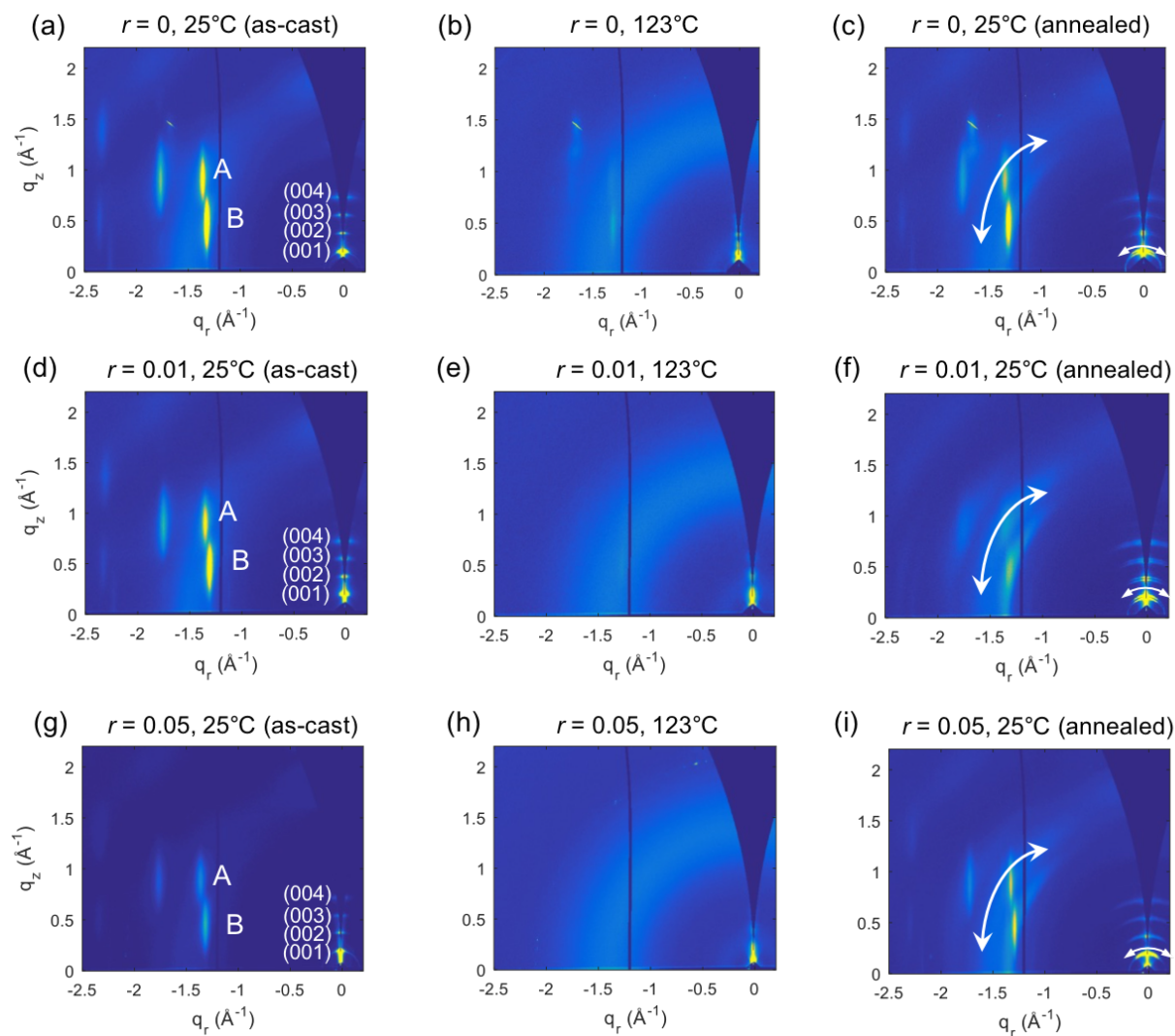


Figure 2.4. Representative geometrically corrected GIWAXS patterns of 4T/PEO4-LiTFSI complex thin film at selected temperatures during heating and cooling processes $r = 0$ (a-c), $r = 0.01$ (d-f) and $r = 0.05$ (g-i). Thin film of pristine 4T/PEO4 compound ($r = 0$) at (a) 25 °C (as-cast), (b) 123 °C (during heating), and (c) 25 °C (after annealed). Thin film of 4T/PEO4-LiTFSI complex ($r = 0.01$) at (d) 25 °C (as-cast), (e) 123 °C (during heating), and (f) 25 °C (after annealed). Thin film of 4T/PEO4-LiTFSI complex ($r = 0.05$) at (g) 25 °C (as-cast), (h) 123 °C (during heating), and (i) 25 °C (after annealed). All samples were annealed at each temperature for 20 min to reach equilibrium. The arrows in (c), (f), (i) indicate the peak broadening along the azimuthal direction. (Reprint from *Adv. Funct. Mater.* 2019^[51]).

configurations. In particular, we observe a broadening along the azimuthal direction of both π - π stacking peaks and $(00h)$ peaks (indicated by the arrows), which is similar to previous reports of oligothiophene/low molecular weight polythiophene thin films.^[61,62] The broadening of the azimuthal breadth of the $(00h)$ and π - π stacking peaks for all samples indicates disordering of the 4T units, which induces misalignment of the smectic domains. This observation provides further evidence that π - π interaction dictates the molecular ordering of 4T/PEO4. Such phenomenon indicates that thermal annealing of 4T/PEO4-LiTFSI complexes has led to poor molecular alignment compared to as-cast samples, which could be attributed to insufficient annealing time, surface chemistry between silicon wafer and 4T/PEO4, etc.

To show the temperature dependence of the structure in a more quantitative manner, we show in **Figure 2.5** the vertical linecuts from the GIWAXS patterns of the three samples at all temperatures during the heating and cooling processes. The linecuts of all three complexes below the transition temperature during both the heating and cooling processes consist of sharp diffraction peaks at $q/q^* = 2, 3, \text{ and } 4$ representing $(002), (003) \text{ and } (004)$, again confirming a well-ordered smectic morphology at room temperature. As temperature increases, all the samples undergo an order-disorder transition, indicated by the broadening of the scattering peaks in the vicinity of 100°C , where a smectic–isotropic transition takes place shown by optical microscope. It is worth mentioning that there is a subtle difference among the transition temperatures for each sample, with $106 - 114^\circ\text{C}$ for pristine 4T/PEO4, $96 - 106^\circ\text{C}$ for $r = 0.01$ sample and $87 - 96^\circ\text{C}$ for $r = 0.05$ sample. The decrease in transition temperature with increasing blend ratio is in good agreement with DSC measurements.

As mentioned above, the π - π stacking interaction between 4T units has made the LC phases of 4T/PEO4 much more complicated than the commonly observed smectic A (SmA) or smectic C

(SmC) phases. Highly ordered smectic phases such as SmF, SmG, SmI, SmJ, etc. with a long molecular axis are not only tilted with respect to layer surface, but also towards one side or one apex have been identified after SmC phases.^[63] With GIWAXS patterns closely resembling the intermediate tilted phase of a fatty acid monolayer,^[64] we conclude that the smectic phase the 4T/PEO4 exhibits belongs to is a highly ordered smectic phase.

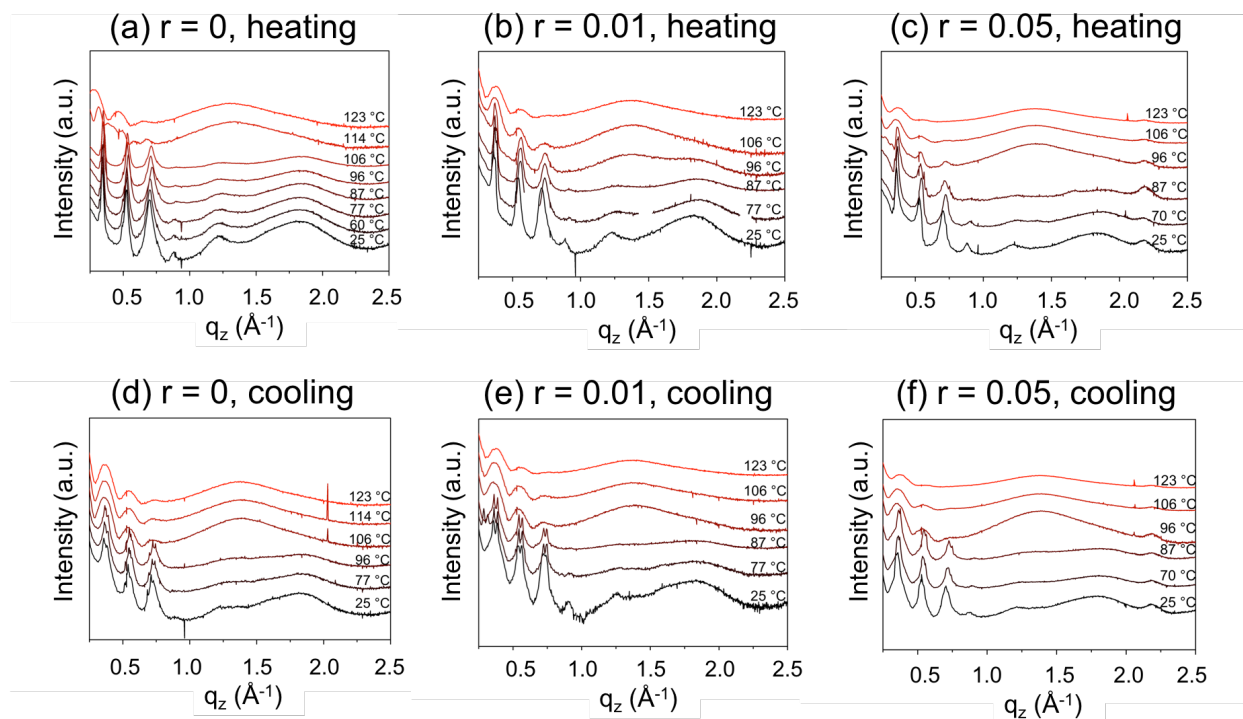


Figure 2.5. Vertical linecuts of (00h) spot sequence for 4T/PEO4-LiTFSI complexes at different temperatures for $r = 0$ (a, d), $r = 0.01$ (b, e) and $r = 0.05$ (c, f) during each heating and cooling processes. The curves are vertically translated for better comparison. (Reprint from *Adv. Funct. Mate.* 2019^[51]).

Further study on the evolution of 4T/PEO4 morphology upon addition of LiTFSI at even higher blending ratios ($r = 0.1, 0.2$) was conducted by GIWAXS at room temperature, as shown in **Figure 2.6**. For $r = 0.1$, we observe a significant change in the structure of the sample compared to the neat and lower salt concentration samples. The GIWAXS image of the $r = 0.1$ sample reveals a

different diffraction pattern indicative of a more ordered 4T/PEO4-LiTFSI structure. The appearance of extra diffraction peaks in this sample might indicate either a more periodic arrangement between 4T and PEO domains and/or an increase in crystallinity upon interacting with LiTFSI. Moreover, we do not observe the peak elongation of the off-axis reflections along the vertical direction as seen in the $r = 0$ or 0.05 samples, suggesting a better 3D registration between 4T units along π - π interaction direction across the whole film thickness. At even higher blending ratio $r = 0.2$, the smectic peaks in the out-of-plane direction significantly broadens and the signature π - π interacting peaks at higher q disappears, indicating that the LC structure of 4T/PEO4 is lost due to the excessive amount of LiTFSI.

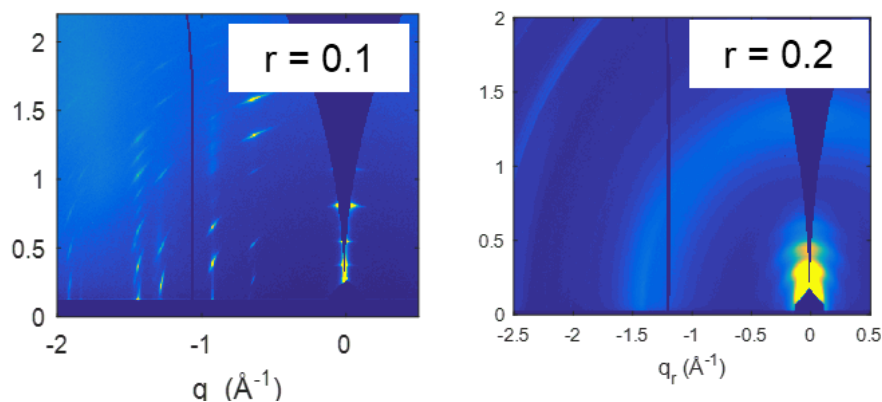


Figure 2.6. Representative room-temperature GIWAXS patterns of 4T/PEO4-LiTFSI at $r = [\text{Li}^+]/[\text{EO}] = 0.1$ (left) and 0.2 (right). (Reprint from *ACS Nano* 2019^[52]).

2.3.4 Self-assembly Behavior of 4T/PEO4-LiTFSI Complexes Studied by Molecular Dynamics Simulation

To provide complementary insights to the experimental results, we employ all-atom (AA) molecular dynamics (MD) simulations to study the self-assembly behavior of 4T/PEO4 as a function of temperature. More details can be found in our published work.

Our attempts to directly self-assemble this system from the melt state via AA simulations proved ineffective due to the considerable computational challenges associated with the slow kinetics of this process. To circumvent this limitation, we used a suitably calibrated coarse-grained (CG) model, an approach that has been proven effective in describing the self-assembly of similar systems.^[65,66] For 4T/PEO4, our CG model represents each thiophene ring by a single spherical bead,^[67] and multiple aliphatic segments by a single bead depending on the specific chemistry as shown in **Figure 2.7(a)**.^[68] The CG simulation started from an amorphous 400-molecule system, equilibrated for 5 ns at 625 °C, a high enough temperature to ensure complete isotropization. The amorphous system was then cooled at a constant rate of 50 °C per ns to 27 °C, and then equilibrated at the final temperature for 10 ns. In agreement with XRD results of the bulk material and GIWAXS results of thin films, the final equilibrated structure obtained is smectic, where 4T units are tilted at an angle $25 \pm 3^\circ$ to the layer stacking direction. The self-assembled CG structure at 27 °C provides a good initial guess for generating the LC AA structure. We used a reverse coarse-grained technique to replace the CG beads with their atomistic representation as implemented by Marrink *et al.*^[69] The resulting AA system was relaxed at 27 °C for 10 ns. Note that the equilibrated AA structure (**Figure 2.7(a)**) provides information on the thiophene ring packing not available in the CG model.

Figure 2.7(b) shows a representative arrangement of 6 adjacent 4T units within a smectic layer at 27 °C. We observe that the 4T units self-assemble into a typical herringbone packing comparable to the $P2_1/c$ crystal structure of pure 4T reported by Campione *et al.*,^[70] indicating that the 4T self-assembly drives the ordering of the smectic structure of 4T/PEO4. Unlike the CG smectic phase, the AA structure does not reveal any ordering in the PEO domains, showing instead that PEO chains from adjacent layers tend to interdigitate.

To compare the simulated structure to GIWAXS results, we calculate the structure factor^[71] for the thiophene rings, $S(\mathbf{q}) = |\sum_n \exp(i\mathbf{q} \cdot \mathbf{r}_n)|^2$, where \mathbf{r}_n is the center of mass of each non-hydrogen atom in thiophene ring. The two-dimensional $S(\mathbf{q})$ shown in **Figure 2.7(c)** results from averaging the q_x and q_y components along circles of constant $q_r = \sqrt{q_x^2 + q_y^2}$. The simulated GIWAXS pattern shows key similarity to the experimental one shown in **Figure 2.4(a)**: (i) the $(00h)$ peaks identify a smectic structure with calculated layer thickness of 3.41 nm, and (ii) the two peaks originating from the herringbone structure denoted as A and B. In **Figure 2.7(b)**, these two peaks represent the alignment between the homo-tilts with 0.39 nm spacing and hetero-tilts with 0.44 nm spacing in the herringbone packing, respectively (the spacing is the mean distance between thiophene ring centers of mass).

To simulate the morphological change of 4T/PEO4 with temperature, we heat the system from 37 °C to 187 °C in 10 °C increments. At each temperature the system is annealed for 10 ns in attempt to achieve equilibrium before taking the next step. **Figure 2.7(d)** and (e) show the arrangement of 4T units and the corresponding GIWAXS patterns at $T = 127^\circ\text{C}$ which is above the disordering transition temperature of 4T/PEO4. At $T = 127^\circ\text{C}$, the top-view of the 4T units shows a considerable twisting/bending compared to that at 27°C , leading to a significant loss of the π - π interaction between the 4T units. Accordingly, the simulated GIWAXS pattern in **Figure 2.7(e)** shows no evidence of π - π stacking peaks (with only weaker smectic $(00h)$ peaks persisting), which is again in agreement with our experimental results.

The morphology of 4T/PEO4 blended with LiTFSI at different blending ratios was also studied by MD simulation as shown in **Figure 2.8**. For $r \leq 0.05$, the diffraction patterns of 4T/PEO4-LiTFSI are qualitatively similar to the neat samples, indicating that the smectic morphology of 4T/PEO4 is maintained. For $r = 0.1$, we observe 4T/PEO4 fragments acquiring enough translational entropy

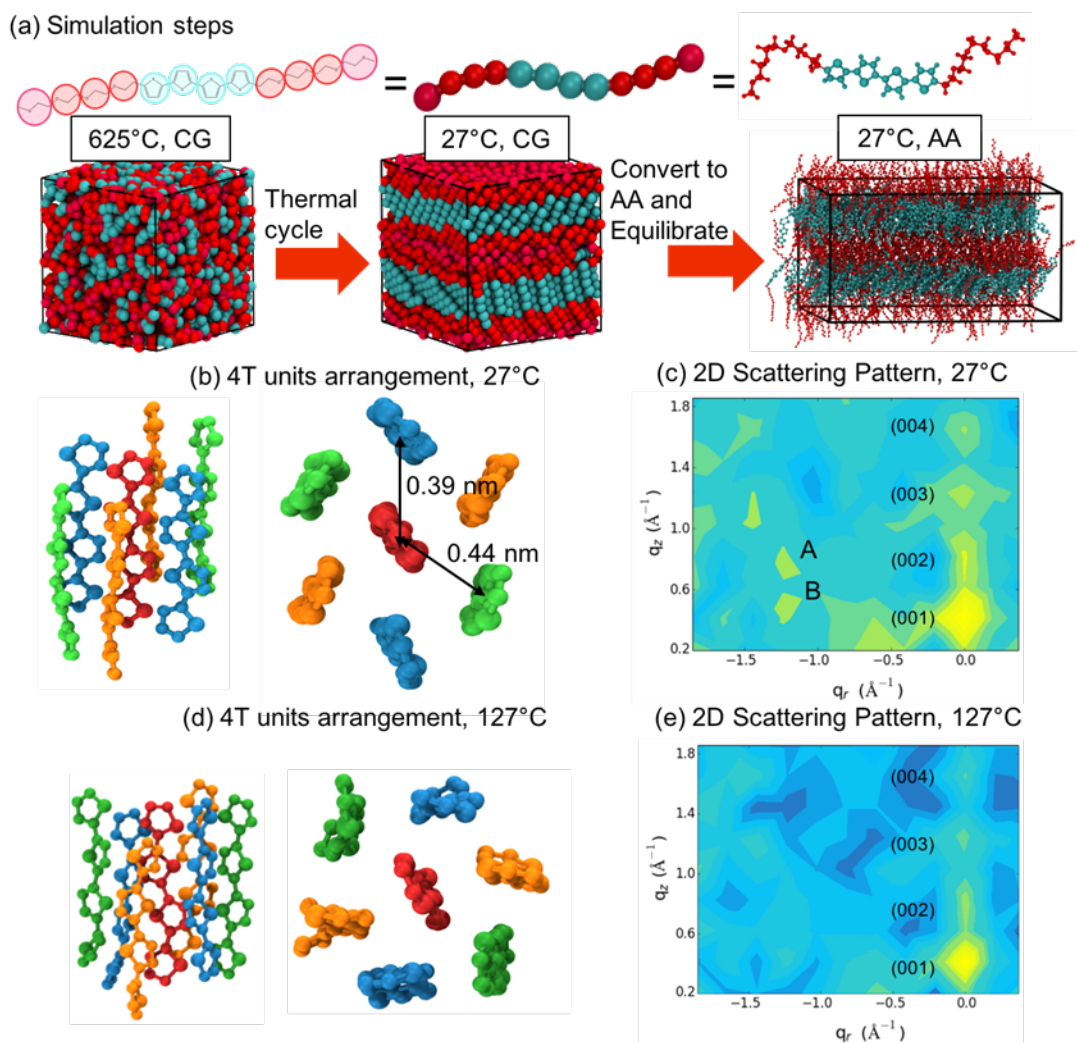


Figure 2.7 (a) Simulation steps to capture the AA structure of 4T/PEO4 at 27°C. The thiophene rings are shown in cyan, the PEO units are shown in red, and hydrogens are omitted for clarity. Herringbone packing of the thiophene units at (b) 27 °C and (d) 127 °C is shown in perpendicular and parallel views to the thiophene principal axis, with 4T units given different colors and PEO4 chains omitted for clarity. (c) and (e) represent average two-dimensional structure factor of the thiophene rings at 27 °C and 127 °C, respectively. (Reprint from *Adv. Funct. Mater.* 2019^[51]).

to break apart from the herringbone arrangement of 4T and penetrating the PEO phase, and thus connecting the smectic layers. At very high salt concentration $r = 0.2$, a complete loss of LC structure due to excessive amount of LiTFSI was observed in the corresponding snapshots.

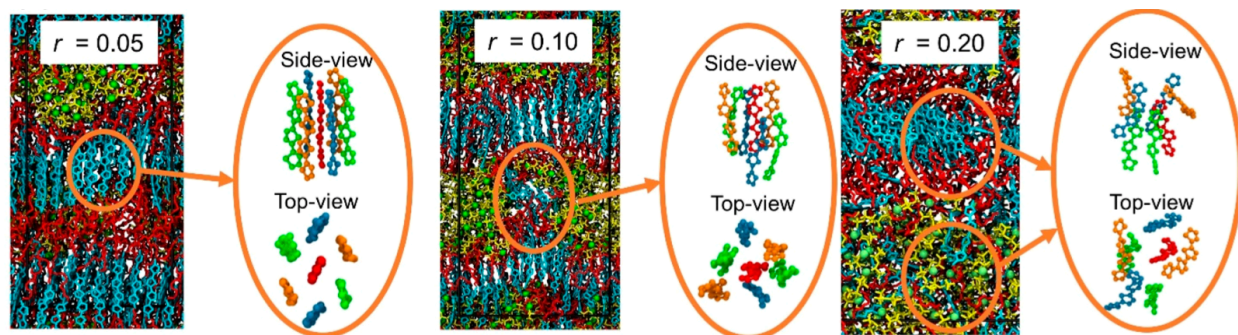


Figure 2.8 Snapshots of 4T/PEO4-LiTFSI structures at three representative blending ratios of $r = 0.05$ (left), 0.10 (middle) and 0.20 (right) from MD simulation with the top-view and side-view 4T unit arrangements. (Reprint from *ACS Nano* 2019^[52]).

2.3.5 Implication of 4T/PEO4-LiTFSI Self-assembly on Ion transport

The ionic conductivity of 4T/PEO4-LiTFSI thin films is measured by electrochemical impedance spectroscopy (EIS) using interdigitated gold electrodes devices (IDEs) as shown in **Figure 2.9(a)**. IDEs are used in order to enhance signal-to-noise ratio in highly resistive thin films.^[55,72] Due to the geometry of IDE, the ionic conductivity reported in our work is in-plane conductivity, or conductivity in the direction parallel to the substrate. In fact, in the smectic phases the 4T/PEO4-LiTFSI complexes exhibit homeotropic alignment, indicating the formation of 2D ion-conductive pathways parallel to the surface of substrate. **Figure 2.9(b)** depicts the temperature-dependent ionic conductivity of the two samples $r = 0.01$ and $r = 0.05$ during heating and cooling cycles as the well-ordered smectic morphology of 4T/PEO4 at these two blending ratios is not disrupted. In the complexes, ions propagate through segmental motion of PEO chains. For both samples, the

conductivity appears qualitatively similar, consistent with similar temperature-dependent morphology suggested by GIWAXS measurement above. From $r = 0.01$ to 0.05 , we observe a significant improvement in conductivity due to the increase in ionic carrier concentration. During the first heating cycle below the transition temperature, the ionic conductivity monotonically increases with temperature, consistent with thermally activated ionic transport behavior of electrolytes.^[73]

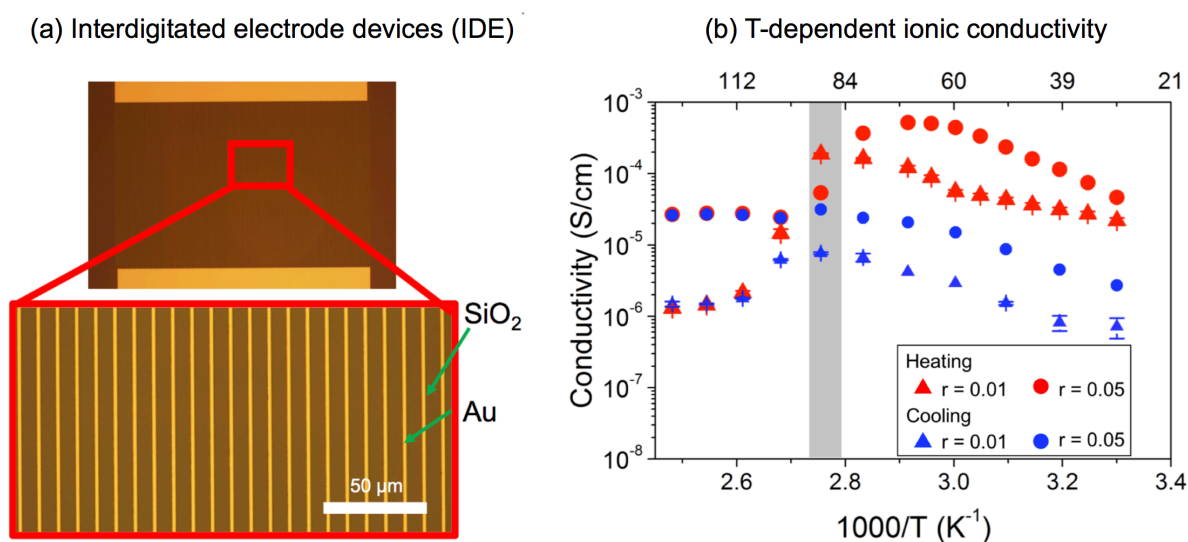


Figure 2.9 (a) Optical microscope image of an interdigitated gold electrode device (IDE) used for ionic conductivity measurement, (b) Ionic conductivities of LiTFSI-blended 4T/PEO4 thin film at $r = 0.01$ and $r = 0.05$ as a function of temperature during heating and cooling processes. The gray-shaded area indicates the order-disorder transition regime. (Reprint from *Adv. Funct. Mater.* 2019^[51]).

The maximum conductivity is ca. 1.9×10^{-4} S/cm for $r = 0.01$ sample (at 90°C), and 5.2×10^{-4} S/cm for $r = 0.05$ sample (at 70°C), which are comparable or even superior to those of nanosegregated ionic LCs.^[17,18,26,59,74–76] 2D lamellar system also has more flexibility in device design in which allows the transport of lithium ions within the layers along more directions

compared to 1D cylindrical structures. What's more, these conductivity values from our material are achieved at relatively lower temperatures, endowing more practicality and processability to 4T/PEO4. We believe that the high ionic conductivity of 4T/PEO4-LiTFSI thin films originates from the formation of the highly ordered smectic layers and thus efficient 2D transport pathways in the direction parallel to the device substrate as suggested by GIWAXS measurements. However, at around 100 °C where the order-disorder transition takes place, as indicated by the gray-shaded area in **Figure 2.9(b)**, we observe a substantial drop in ionic conductivity. This is most likely because the layered structures and ion transport channels are disturbed at this temperature as indicated by the significant broadening of the (*00h*) layering peaks in GIWAXS measurement. This behavior has already been reported for a number of columnar and smectic ionic LCs.^[18,26,59,74–76] Finally, upon cooling the samples from above the transition temperature to room temperature, the ionic conductivity does not recover to its initial value, which is also consistent with GIWAXS measurements suggesting that the conductivity loss is caused by the misalignment of the smectic layers due to local and partial crystallization of 4T/PEO4 upon cooling as well as larger grain size obtained due to shrunken layer structure and expanded π - π stacking. Furthermore, the same measurements were run for another two cycles afterwards, and the data followed exactly the second trend where the ionic conductivity before and after heating/cooling treatment remains the same. This behavior suggests that the LC mesophases and molecular alignments are stable.

2.3.6 Mixed ion/Electron conduction in 4T/PEO4

4T is formally a semiconducting material and insulating in its pristine state. To enable and modulate electronic conduction in 4T/PEO4 and 4T/PEO4-LiTFSI requires the incorporation of molecular dopants. Specifically, the small molecule electron acceptor F4TCNQ has been shown

to be a suitable dopant molecule for 4T.^[77] Note that different strategies of solution mixing and sequential doping have been employed to introduce molecular dopants into conjugated organic semiconductors.^[78–80] Motivated to understand how controlling the underlying self-assembled structure with LiTFSI influences the charge transport properties, we choose to follow the sequential doping method where one first casts a thin film and then infiltrates F4TCNQ from the vapor phase using different exposure times as illustrated in **Figure 2.10(a)**. Previous reports have shown that vapor doping of polymeric semiconductors with F4TCNQ leads to homogenous doping through the thickness of the thin film and minimal disruption of the underlying self-assembled structure.^[79–81] For our 4T/PEO4 $r = 0$ and $r = 0.1$ thin films, GIWAXS experiments reveal that vapor doping does not lead to significant disruption to the underlying self-assembled structure as indicated by similar GIWAXS patterns before and after vapor doping with F4TCNQ. At room temperature, the intrinsic electronic conductivity of pristine 4T/PEO4 without F4TCNQ was $(4.9 \pm 1.5) \times 10^{-7}$ S/cm as determined by DC method. The intrinsic electronic conductivity without F4TCNQ of 4T/PEO4-LiTFSI samples was below 2×10^{-8} S/cm for all values of r . These values of intrinsic electronic conductivity are sufficiently low thus enable the measurement of ionic conductivity using EIS method.

Figure 2.10(b) depicts Nyquist impedance plots of the $r = 0.1$ sample at different F4TCNQ doping times. As frequently observed for ion conducting materials, the Nyquist plot of the sample without F4TCNQ shows a semicircle at high frequencies and a capacitive tail at low frequencies, indicative of dominating ion conducting behavior. Upon introducing vapor F4TCNQ to the sample for 3 min, the Nyquist impedance data drastically changes. The observation of two semicircles in the Nyquist plot together with the absence of the capacitive tail at low frequency indicates the presence of both ionic and electronic transport.^[82] At 30 min of F4TCNQ doping, the Nyquist impedance data

becomes a single semicircle with significantly reduced radius, indicating that the electronic conductivity has increased considerably compared to ionic conductivity. The ionic and electronic resistance values were calculated for F4TCNQ-doped 4T/PEO4-LiTFSI samples by fitting the EIS data to the appropriate equivalent circuits showed in the inset of each Nyquist plot in Figure 5b. The rationale for the equivalent circuit selection and conductivity calculation is reported elsewhere^[82] and also detailed in Supporting Information. We note for all samples, the electronic conductivity can be measured using either EIS or DC method, both yield excellent agreement, suggesting the accuracy of the model fit in our EIS data.

Shown in **Figure 2.10(c)** is the room temperature electronic conductivity of the two samples as a function of F4TCNQ doping time. As expected, vapor doping F4TCNQ leads to an increase in lateral thin film electronic conductivity for both samples. The neat $r = 0$ sample shows more than an order-of-magnitude increase in electronic conductivity from $(1.3 \pm 0.89) \times 10^{-5}$ S/cm to $(3.2 \pm 0.54) \times 10^{-4}$ S/cm after 25 min of doping. The $r = 0.1$ sample initially has lower conductivity than the 4T/PEO4 sample but exhibits a larger increase in conductivity from $(1.3 \pm 0.16) \times 10^{-7}$ to $(3.1 \pm 0.45) \times 10^{-3}$ S/cm after 25 min of doping. Near the optimal doping time, the maximum electronic conductivity of $(3.1 \pm 0.45) \times 10^{-3}$ S/cm in the $r = 0.1$ sample is nearly an order-of-magnitude higher than the maximum electronic conductivity of the $r = 0$ sample. Moreover, electronic conductivity of the $r = 0.1$ sample is superior to the maximum conductivity of 4T co-deposited with F4TCNQ reported by Mendez and Heimel *et al*^[77] as marked by the dashed line in **Figure 2.10(c)**. Such improvement most likely arises from the difference in the underlying self-assembled structure as suggested by the structural changes observed in GIWAXS and MD simulation results discussed earlier.

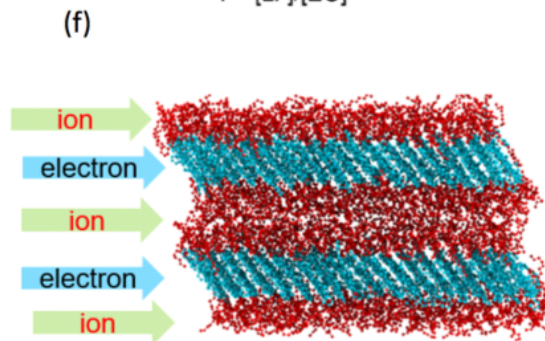
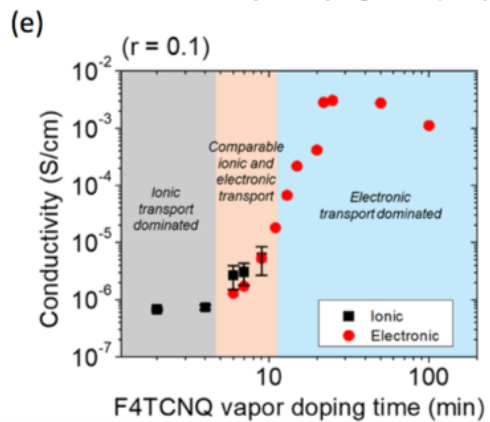
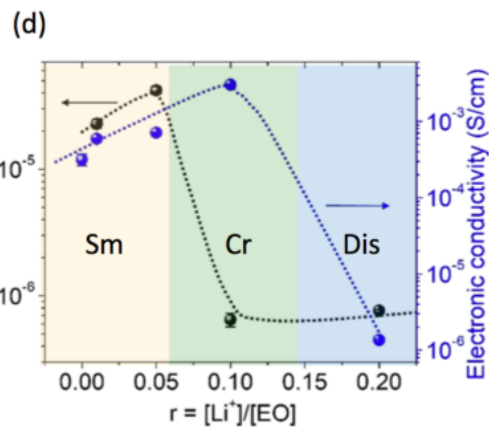
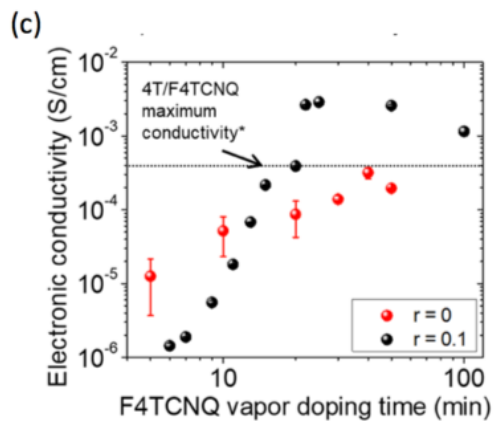
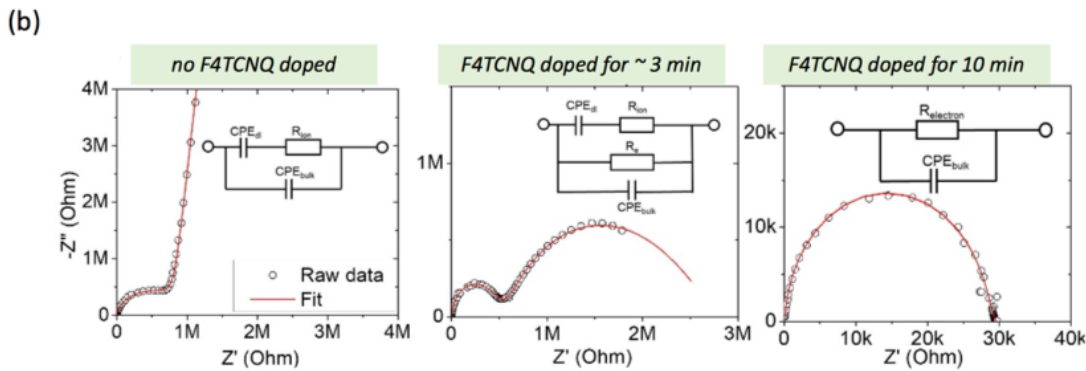
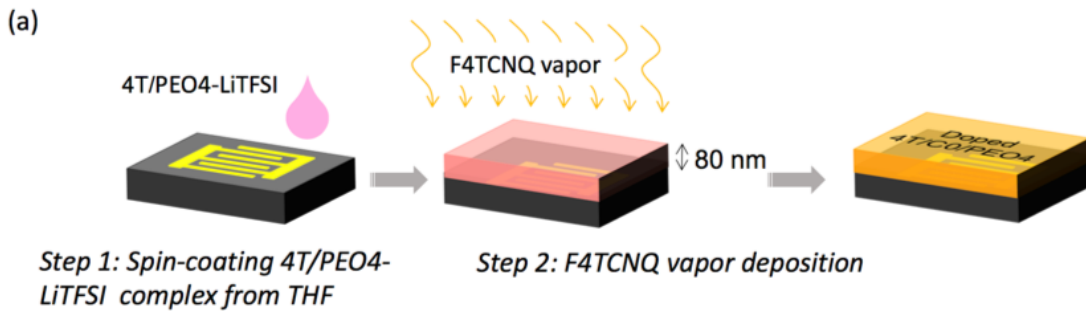


Figure 2.10 (a) Schematic representation for F4TCNQ vapor doping procedure of 4T/PEO4-LiTFSI thin film. (b) Nyquist plots of the $r = 0.1$ sample at different F4TCNQ doping time. The inset of each plot represents the simplified equivalent circuit used to fit the impedance data. (c) Electronic conductivity of $r = 0$ and $r = 0.10$ samples as a function of F4TCNQ doping time. The dashed line represents the maximum 4T/F4TCNQ electronic conductivity reported by Mendes and Heimel *et al.* (d) Ionic conductivity and maximum electronic conductivity upon introducing F4TCNQ. (e) Schematic representation of mixed ionic/electronic conduction in 2D smectic morphology. (Reprint from *ACS Nano* 2019^[52]).

It is evident that the underlying self-assembled structure with the addition of LiTFSI plays a vital role in dictating charge transport properties. Thus, we expand and characterize the electronic and ionic conduction characteristics of all LiTFSI concentrations from $r = 0$ to $r = 0.20$ after vapor doping with F4TCNQ, and the ionic conductivity of 4T/PEO4-LiTFSI without F4TCNQ as well as the maximum electronic conductivity of 4T/PEO4-LiTFSI upon introducing F4TCNQ was summarized in **Figure 2.10(d)**. The room temperature ionic conductivity of 4T/PEO4-LiTFSI is relatively high for $r = 0.01$ [$(2.3 \pm 0.2) \times 10^{-5}$ S/cm] and $r = 0.05$ [$(4.2 \pm 0.3) \times 10^{-5}$ S/cm] samples due to the ordered smectic morphology of 4T/PEO4. The stable smectic morphology and high ionic conductivity up to $r = 0.05$ in 4T/PEO4 are similar to other reports by Ohtake *et al.* where the authors found that lithium salt-complexed rod-coil-rod LCs exhibited stabilized mesophase with high ionic conductivity.^[83,84] However, at $r = 0.10$ and $r = 0.20$ where the smectic layer ordering is disrupted, we found a significant drop in ionic conductivity for both concentrations. While the drop in ionic conductivity at high concentrations could originate from ion-pair formation and the reduction in segmental mobility that arises from transient cross-linking between Li^+ and EO units,^[85] we partially attribute the decrease in ionic conductivity to the disruption of the smectic ordering that hinders the ionic conduction pathways within the samples. On the other hand, the electronic conductivity remains relatively constant for $r \leq 0.05$ where 4T/PEO4 adopts a smectic morphology but increases by an order of magnitude at $r = 0.1$, as was shown earlier. At $r = 0.2$ the electronic conductivity significantly drops, which is also consistent with the poorly ordered structure suggested by both GIWAXS and MD simulations.

Finally **Figure 2.10(e)** summarizes the evolution of ionic and electronic conductivity of the $r = 0.1$ sample as a function of F4TCNQ vapor doping time. The charge transport processes can be divided into three stages: The early stage where ionic transport dominates (gray-shaded area), the

intermediate stage where ionic and electronic transports are comparable (orange-shaded area) and the late stage where the electronic transport dominates (blue-shade area). Here, we would like to note that at the late stage, we believe that ionic conduction still remains. However, the EIS response only captures the lower resistance electronic transport contribution as we are using electronically reversible and ion-blocking Au metal electrodes.^[82] Our results clearly indicate that 4T/PEO4-LiTFSI samples still maintain their ion conducting functionality upon doping with F4TCNQ.

2.4 Conclusions

In summary, we have performed a systematic study on the structure and self-assembly of newly-synthesized conjugated LC compound 4T/PEO4 as well as its mixed ionic/electronic conduction characteristics upon blending with LiTFSI and doping with F4TCNQ molecular dopants. Using GIWAXS in combination with MC simulation, we found out the morphology transition of 4T/PEO4-LiTFSI from a smectic morphology at $r \leq 0.05$ to a more ordered structure with better percolation between 4T units at $r = 0.1$ before losing its ordered structure at $r = 0.2$. At low LiTFSI blending ratio ($r \leq 0.05$) the compounds exhibited a highly ordered smectic phase due to segregation between immiscible aromatic and aliphatic segments as well as π - π stacking of thiophene rings, forming efficient 2D channels for ion transport. EIS measurements on 4T/PEO4-LiTFSI samples showed remarkable ion transport behavior with the highest conductivity of 5.2×10^{-4} S/cm at 70°C and $r = 0.05$. Temperature-dependent GIWAXS measurements and molecular dynamic simulations indicated that upon heating the samples from ambient temperature to above the isotropization temperature, a significant loss in π - π interaction and smectic order was observed, which led to a significant drop in ionic conductivity due to disruption of the ordered smectic phase and ion transport pathways. Additionally, the conductivity became lower than the initial state upon

cooling to ambient temperature due to the disruption of 2D ion transport channels. The electronic conductivity upon doping with vapor F4TCNQ were showed to increase from $r = 0$ to 0.10 due to the improvement of percolation pathways for electronic transports, whereas the $r = 0.20$ sample exhibited the lowest electronic conductivity because of the disordered structure.

The results presented in this work provide several important contributions to the rational design of electronic and ionic transporting LC materials. First, we introduce a new design strategy of using LC multiblock-oligomers that provide both electro-active and ion-active properties. Second, we describe for the first time a detailed connection between processing, self-assembly and ionic/electronic transport behavior in LCs systems. In addition, we show how the use of LC materials introduces new opportunities in elucidating molecular doping mechanisms, which could significantly help in advancing the field of organic semiconductors. What's more important, for the first time, modeling has played an important role in guiding the design and understanding the self-assembly behaviors of the conducting material. We believe that the method using simulation to interpret experimental data is an elegant approach toward understanding the self-assembly and transport behavior of soft materials in general. Our results open the door to additional, more detailed studies of the interconnection among LC self-assembly, electronic properties of 4T/PEO4 (and related molecules), and molecular doping; work along these lines are currently under way. By utilizing the ease of synthesis, straightforward self-assembly and less intensive computational calculation, we showed that LCs could be use as material testbeds to understand mixed conduction behavior of soft materials in general.

REFERENCES

- [1] G. W. Gray, J. W. G. Goodby, *Smectic Liquid Crystals- Textures and Structures*; Lenard Hill: Glasgow, UK, 1984.
- [2] D. Demus, J. Goodby, G. W. Gray, H. W. Spiess, V. Vill, *Handbook of Liquid Crystals*; Wiley VCH: Weinheim, Germany, 1998.
- [3] W. Pisula, M. Zorn, J. Y. Chang, K. Müllen, R. Zentel, *Macromolecular Rapid Communications* **2009**, *30*, 1179.
- [4] I. W. Hamley, *Angewandte Chemie International Edition* **2003**, *42*, 1692.
- [5] T. Kato, N. Mizoshita, K. Kishimoto, *Angewandte Chemie International Edition* **2006**, *45*, 38.
- [6] T. Kato, *Science* **2002**, *295*, 2414.
- [7] R. L. Kerr, S. A. Miller, R. K. Shoemaker, B. J. Elliott, D. L. Gin, *Journal of the American Chemical Society* **2009**, *131*, 15972.
- [8] T. Kato, *Angewandte Chemie International Edition* **2010**, *49*, 7847.
- [9] B. R. Wiesenaus, D. L. Gin, *Polymer journal* **2012**, *44*, 461.
- [10] J. Sakuda, E. Hosono, M. Yoshio, T. Ichikawa, T. Matsumoto, H. Ohno, H. Zhou, T. Kato, *Advanced Functional Materials* **2015**, *25*, 1206.
- [11] S. Sergeev, W. Pisula, Y. H. Geerts, *Chemical Society Reviews* **2007**, *36*, 1902.
- [12] M. O'Neill, S. M. Kelly, *Advanced Materials* **2011**, *23*, 566.
- [13] C. Tschierske, *J. Mater. Chem.* **2011**, *11*, 2647.
- [14] G. H. Mehl, *Angewandte Chemie International Edition* **2005**, *44*, 672.
- [15] C. Tschierske, *Annual Reports Section "C" (Physical Chemistry)* **2001**, *97*, 191.
- [16] C. Ruiz, E. M. García-Frutos, G. Henrich, B. Gómez-Lor, *The Journal of Physical Chemistry Letters* **2012**, *3*, 1428.
- [17] H. Shimura, M. Yoshio, A. Hamasaki, T. Mukai, H. Ohno, T. Kato, *Advanced Materials* **2009**, *21*, 1591.
- [18] M. Yoshio, T. Mukai, H. Ohno, T. Kato, *Journal of the American Chemical Society* **2004**, *126*, 994.
- [19] B. Soberats, M. Yoshio, T. Ichikawa, X. Zeng, H. Ohno, G. Ungar, T. Kato, *Journal of the American Chemical Society* **2015**, *137*, 13212.
- [20] T. Ohtake, K. Ito, N. Nishina, H. Kihara, H. Ohno, T. Kato, *Polymer Journal* **1999**, *31*, 1155.
- [21] T. Ohtake, Y. Takamitsu, K. Ito-Akita, K. Kanie, M. Yoshizawa, T. Kato, *Macromolecules* **2000**, *33*, 8109.
- [22] K. Kishimoto, T. Suzawa, T. Yokota, T. Mukai, H. Ohno, T. Kato, *Journal of the American Chemical Society* **2005**, *127*, 15618.
- [23] Y. Iinuma, K. Kishimoto, Y. Sagara, M. Yoshio, T. Mukai, I. Kobayashi, H. Ohno, T. Kato, *Macromolecules* **2007**, *40*, 4874.
- [24] M. Yoshio, T. Mukai, K. Kanie, M. Yoshizawa, H. Ohno, T. Kato, *Chemistry Letters* **2002**, *31*, 320.
- [25] T. Ichikawa, M. Yoshio, A. Hamasaki, S. Taguchi, F. Liu, X. Zeng, G. Ungar, H. Ohno, T. Kato, *Journal of the American Chemical Society* **2012**, *134*, 2634.
- [26] T. Ichikawa, M. Yoshio, A. Hamasaki, T. Mukai, H. Ohno, T. Kato, *Journal of the American Chemical Society* **2007**, *129*, 10662.
- [27] A. E. Frise, T. Ichikawa, M. Yoshio, H. Ohno, S. V. Dvinskikh, T. Kato, I. Furó, *Chem. Commun.* **2010**, *46*, 728.

- [28] T. Ichikawa, M. Yoshio, A. Hamasaki, J. Kagimoto, H. Ohno, T. Kato, *Journal of the American Chemical Society* **2011**, *133*, 2163.
- [29] R. D. Costa, F. Werner, X. Wang, P. Grönninger, S. Feihl, F. T. U. Kohler, P. Wasserscheid, S. Hibler, R. Beranek, K. Meyer, D. M. Guldi, *Advanced Energy Materials* **2013**, *3*, 657.
- [30] A. Abate, A. Petrozza, G. Cavallo, G. Lanzani, F. Matteucci, D. W. Bruce, N. Houbenov, P. Metrangolo, G. Resnati, *Journal of Materials Chemistry A* **2013**, *1*, 6572.
- [31] N. Yamanaka, R. Kawano, W. Kubo, N. Masaki, T. Kitamura, Y. Wada, M. Watanabe, S. Yanagida, *The Journal of Physical Chemistry B* **2007**, *111*, 4763.
- [32] D. Högberg, B. Soberats, S. Uchida, M. Yoshio, L. Kloo, H. Segawa, T. Kato, *Chemistry of Materials* **2014**, *26*, 6496.
- [33] D. Högberg, B. Soberats, R. Yatagai, S. Uchida, M. Yoshio, L. Kloo, H. Segawa, T. Kato, *Chemistry of Materials* **2016**, *28*, 6493.
- [34] T. Kato, M. Yoshio, T. Ichikawa, B. Soberats, H. Ohno, M. Funahashi, *Nature Reviews Materials* **2017**, *2*, 17001.
- [35] V. Percec, *J. CHEM. SOC. PERKIN TRANS.* **1994**, *16*, 31.
- [36] K. Hoshino, K. Kanie, T. Ohtake, T. Mukai, M. Yoshizawa, S. Ujiie, H. Ohno, T. Kato, *Macromolecular Chemistry and Physics* **2002**, *203*, 1547.
- [37] K. Goossens, K. Lava, C. W. Bielawski, K. Binnemans, *Chemical Reviews* **2016**, *116*, 4643.
- [38] M. Yoshizawa, T. Mukai, T. Ohtake, K. Kanie, T. Kato, H. Ohno, *Solid state ionics* **2002**, *154*, 779.
- [39] F. J. M. Hoeben, P. Jonkheijm, E. W. Meijer, A. P. H. J. Schenning, *Chemical Reviews* **2005**, *105*, 1491.
- [40] J. A. A. W. Elemans, A. E. Rowan, R. J. M. Nolte, *J. Mater. Chem.* **2003**, *13*, 2661.
- [41] T.-Q. Nguyen, R. Martel, P. Avouris, M. L. Bushey, L. Brus, C. Nuckolls, *Journal of the American Chemical Society* **2004**, *126*, 5234.
- [42] L. L. Miller, K. R. Mann, *Accounts of Chemical Research* **1996**, *29*, 417.
- [43] D. D. Graf, J. P. Campbell, L. L. Miller, K. R. Mann, *Journal of the American Chemical Society* **1996**, *118*, 5480.
- [44] D. D. Graf, R. G. Duan, J. P. Campbell, L. L. Miller, K. R. Mann, *Journal of the American Chemical Society* **1997**, *119*, 5888.
- [45] X.-C. Li, H. Sirringhaus, F. Garnier, A. B. Holmes, S. C. Moratti, N. Feeder, W. Clegg, S. J. Teat, R. H. Friend, *Journal of the American Chemical Society* **1998**, *120*, 2206.
- [46] G. Barbarella, M. Zambianchi, A. Bongini, L. Antolini, *Advanced Materials* **1992**, *4*, 282.
- [47] G. Barbarella, M. Zambianchi, L. Antolini, P. Ostojka, P. Maccagnani, A. Bongini, E. A. Marseglia, E. Tedesco, G. Gigli, R. Cingolani, *Journal of the American Chemical Society* **1999**, *121*, 8920.
- [48] G. Barbarella, M. Zambianchi, A. Bongini, L. Antolini, *Advanced Materials* **1993**, *5*, 834.
- [49] S. Tsuzuki, K. Honda, R. Azumi, *Journal of the American Chemical Society* **2002**, *124*, 12200.
- [50] H. Sirringhaus, P. J. Brown, R. H. Friend, M. M. Nielsen, K. Bechgaard, B. M. W. Langeveld-Voss, A. J. H. Spiering, R. A. J. Janssen, E. W. Meijer, P. Herwig, **1999**, *401*, 4.
- [51] Z. Liu, B. X. Dong, M. Misra, Y. Sun, J. Strzalka, S. N. Patel, F. A. Escobedo, P. F. Nealey, C. K. Ober, *Advanced Functional Materials* **2019**, *29*, 1805220.
- [52] B. X. Dong, Z. Liu, M. Misra, J. Strzalka, J. Niklas, O. G. Poluektov, F. A. Escobedo, C. K. Ober, P. F. Nealey, S. N. Patel, *ACS Nano* **2019**, *13*, 7665.
- [53] Z. Jiang, *Journal of Applied Crystallography* **2015**, *48*, 917.

- [54] B. X. Dong, J. Strzalka, Z. Jiang, H. Li, G. E. Stein, P. F. Green, *ACS Applied Materials & Interfaces* **2017**, *9*, 44799.
- [55] D. K. Paul, R. McCreery, K. Karan, *Journal of the Electrochemical Society* **2014**, *161*, F1395.
- [56] K. Xu, *Chemical Reviews* **2004**, *104*, 4303.
- [57] C. Janiak, *Journal of the Chemical Society, Dalton Transactions* **2000**, 3885.
- [58] S. Alvarez, *Dalton Transactions* **2013**, *42*, 8617.
- [59] A. Eisele, K. Kyriakos, R. Bhandary, M. Schönhoff, C. M. Papadakis, B. Rieger, *Journal of Materials Chemistry A* **2015**, *3*, 2942.
- [60] M. Singh, O. Odusanya, G. M. Wilmes, H. B. Eitouni, E. D. Gomez, A. J. Patel, V. L. Chen, M. J. Park, P. Fragouli, H. Iatrou, N. Hadjichristidis, D. Cookson, N. P. Balsara, *Macromolecules* **2007**, *40*, 4578.
- [61] B. X. Dong, M. Smith, J. Strzalka, H. Li, A. J. McNeil, G. E. Stein, P. F. Green, *Journal of Polymer Science Part B: Polymer Physics* **2018**, *56*, 652.
- [62] S. Himmelberger, D. T. Duong, J. E. Northrup, J. Rivnay, F. P. V. Koch, B. S. Beckingham, N. Stingelin, R. A. Segalman, S. C. B. Mannsfeld, A. Salleo, *Advanced Functional Materials* **2015**, *25*, 2616.
- [63] S. Z. D. Cheng, Y. Yoon, A. Zhang, E. P. Savitski, J.-Y. Park, V. Percec, P. Chu, *Macromolecular Rapid Communications* **1995**, *16*, 533.
- [64] V. M. Kaganer, I. R. Peterson, R. M. Kenn, M. C. Shih, M. Durbin, P. Dutta, *The Journal of Chemical Physics* **1995**, *102*, 9412.
- [65] Y. Sun, P. Padmanabhan, M. Misra, F. A. Escobedo, *Soft Matter* **2017**, *13*, 8542.
- [66] A. J. Crane, F. J. Martínez-Veracochea, F. A. Escobedo, E. A. Müller, *Soft Matter* **2008**, *4*, 1820.
- [67] H. S. Marsh, E. Jankowski, A. Jayaraman, *Macromolecules* **2014**, *47*, 2736.
- [68] H. Lee, A. H. de Vries, S.-J. Marrink, R. W. Pastor, *The Journal of Physical Chemistry B* **2009**, *113*, 13186.
- [69] J. J. Uusitalo, H. I. Ingólfsson, P. Akhshi, D. P. Tieleman, S. J. Marrink, *Journal of Chemical Theory and Computation* **2015**, *11*, 3932.
- [70] M. Campione, S. Tavazzi, M. Moret, W. Porzio, *Journal of Applied Physics* **2007**, *101*, 083512.
- [71] J.-P. Hansen, I. R. McDonald, *Theory of Simple Liquids: with Application to Soft Matter*; 4th ed.; Academic Press, 2013.
- [72] C. G. Arges, Y. Kambe, H. S. Suh, L. E. Ocola, P. F. Nealey, *Chemistry of Materials* **2016**, *28*, 1377.
- [73] S. Lascaud, M. Perrier, A. Vallee, S. Besner, J. Prud'homme, M. Armand, *Macromolecules* **1994**, *27*, 7469.
- [74] H. Shimura, M. Yoshio, K. Hoshino, T. Mukai, H. Ohno, T. Kato, *Journal of the American Chemical Society* **2008**, *130*, 1759.
- [75] M. Yoshio, T. Kagata, K. Hoshino, T. Mukai, H. Ohno, T. Kato, *Journal of the American Chemical Society* **2006**, *128*, 5570.
- [76] S. Yazaki, Y. Kamikawa, M. Yoshio, A. Hamasaki, T. Mukai, H. Ohno, T. Kato, *Chemistry Letters* **2008**, *37*, 538.
- [77] H. Méndez, G. Heimel, S. Winkler, J. Frisch, A. Opitz, K. Sauer, B. Wegner, M. Oehzelt, C. Röthel, S. Duhm, D. Töbrens, N. Koch, I. Salzmann, *Nature Communications* **2015**, *6*, 8560.

- [78] D. T. Scholes, P. Y. Yee, J. R. Lindemuth, H. Kang, J. Onorato, R. Ghosh, C. K. Luscombe, F. C. Spano, S. H. Tolbert, B. J. Schwartz, *Advanced Functional Materials* **2017**, *27*.
- [79] S. N. Patel, A. M. Glauddell, K. A. Peterson, E. M. Thomas, K. A. O'Hara, E. Lim, M. L. Chabiny, *Science Advances* **2017**, *3*, e1700434.
- [80] J. Hynynen, D. Kiefer, L. Yu, R. Kroon, R. Munir, A. Amassian, M. Kemerink, C. Müller, *Macromolecules* **2017**, *50*, 8140.
- [81] K. Kang, S. Watanabe, K. Broch, A. Sepe, A. Brown, I. Nasrallah, M. Nikolka, Z. Fei, M. Heeney, D. Matsumoto, K. Marumoto, H. Tanaka, S. Kuroda, H. Sirringhaus, *Nature Materials* **2016**, *15*, 896.
- [82] S. N. Patel, A. E. Javier, G. M. Stone, S. A. Mullin, N. P. Balsara, *ACS Nano* **2012**, *6*, 1589.
- [83] T. Ohtake, M. Ogasawara, K. Ito-Akita, N. Nishina, S. Ujiie, H. Ohno, T. Kato, *Chemistry of Materials* **2000**, *12*, 782.
- [84] T. Ohtake, K. Ito, N. Nishina, H. Kihara, H. Ohno, T. Kato, *Polymer Journal* **1999**, *31*, 1155.
- [85] S. Lascaud, M. Perrier, A. Vallee, S. Besner, J. Prud'homme, M. Armand, *Macromolecules* **1994**, *27*, 7469.

Chapter Three: Study of the Structural Evolution of Amphiphilic Liquid Crystals from Binary System to Ternary Systems²

3.1 Introduction

In the prior chapter, the structure and self-assembly behavior of 4T/PEO4 were studied by GIWAXS together with molecular dynamic simulations. We observed that these 4T/PEO4 molecules self-assemble into a smectic morphology where the 4T cores packed in a crystalline order similar to pure 4T whereas the PEO4 tails formed intercalating layers. These results suggest that in this class of block oligomers the core thiophene rings determine molecular packing, while the capping linear oligomers have thermally mobile, relaxed conformations. Treated as smaller molecular-scale block systems, the π -conjugated LCs exhibit typical self-assembly behavior similar to larger molecular-scale (higher molecular weight) block copolymers. The stiffness asymmetry results in an increase in the Flory-Huggins parameter in comparison with coil-coil type diblock molecules. As a consequence, phase separation of rod-coil diblock copolymers can occur at lower molecular weights with much smaller domain size than for coil-coil diblock copolymers. The ratio between two blocks could dramatically affect the physical properties of the materials as well as the self-assembly behavior.

To further investigate the disruptive effect of PEO on the ordered packing of 4T due to its low melting point and less congruent packing compared to alkyl chains,^[1] similar coil-rod-coil triblock oligomer with fixed quaterthiophene cores and varying numbers of ethylene oxide units (4T/PEO5) is studied experimentally and computationally. As for the rigid segments, sexithiophene (6T) cores are of great interest as they provide even larger and more stable conjugated systems suitable for

² Part of this work (structure-thermal stability relationship of 4T/PEOn) is published as: M. Misra, Z. Liu, B. X. Dong, S. N. Patel, P. F. Nealey, C. K. Ober, F. A. Escobedo, *ACS Macro Lett.* **2020**, *9*, 295.^[33] Ziwei Liu synthesized the material 4T/PEO5 and characterized its thermal and optical property. Mayank Misra did MD simulation, and Ban Dong did temperature-dependent WAXS measurement.

electron transport with carrier mobility in the range of $\sim 10^{-3}$ to $\sim 10^{-4}$ $\text{cm}^2 \text{Vs}^{-1}$, one to two orders of magnitude than those polythiophene-based FET.^[2,3] Therefore, binary-structured amphiphilic LC (6T/PEO4) is also studied. Finally, the volume/length ratio between structure-charge conduction relationship, as a consequence, is also worth investigating in order to figure out the optimal ratio for mixed ionic/electronic conduction. This part work has been published on *ACS Macro Lett.* as “Thermal stability of π -conjugated n-ethylene-glycol-terminated quaterthiophene oligomers: a computational and experimental study” co-authored with Dr. Mayank Misra and Dr. Ban Dong.^[33] Ziwei Liu synthesized the material 4T/PEO5 and characterized its thermal and optical property with DSC, TGA, POM and UV-Vis spectroscopy. Mayank Misra performed MD simulation, and Ban Dong did temperature-dependent WAXS measurement.

Later in this chapter, our horizon of understanding the structure-property relationship of LCs is further broadened from traditional binary systems to ternary ones with a third non-polar alkyl component introduced to the current structure. The three components: oligothiophene, ethylene oxide units and the alkyl segments are incompatible from one another and tend to self-organize into distinct subspaces, leading to more complicated and ordered structure for the formation of potential efficient charge transport channels. X-shaped boalamphiphilic LCs in which ethylene oxide units are attached to both the termini of rigid oligothiophene core with two alkyl segments of different lengths laterally attached to opposite sides of oligothiophene are aimed at developing more self-assembly structures and exploring their thermal and conducting property as a functional of structural evolution. Despite that quantitative research about the self-assembly of mesophase evolution has been done by Tschierske group,^[4-14] not many researchers have ever tried to study the charge transport property based on materials with such unique structures. In our work, a series of X-shaped bolaamphiphiles with combined ionic and electronic conducting functional groups

were established. These π -conjugated compounds consist of oligothiophene which provides π - π stacking and potential electronic conducting function, ethylene oxide moieties as ion transport domains, and alkyl segments to improve flexibility and solubility as well as introducing more incompatibility to the system. However, no evident LC characteristics were detected with these bolaamphiphile structures, which could be attributed to insufficient intramolecular and intermolecular forces for the formation of ordered columnar morphology while the π - π stacking interaction between adjacent oligothiophene units is also disrupted by the alkyl chains.

3.2 Experimental section

3.2.1 Materials

N-bromosuccinimide (NBS), 2-thiopheneethanol, 2-hexylthiophene, 2-thiopheneboronic acid pinacol ester, 3-hexylthiophene, 3-decylthiophene, 3-dodecylthiophene, and 2-bromo-3-methylthiophene were purchased from AK Scientific, Inc. Sodium hydroxide (NaOH), p-toluenesulfonyl chloride, 2-[2-(2-methoxyethoxy)ethoxy]-ethanol, [1,3-Bis(diphenylphosphino)propane]dichloronickel(II) (Ni(dppp)Cl₂), bis(benzonitrile)palladium(II) chloride (Pd(PhCN)₂Cl₂), silver nitrate (AgNO₃), potassium fluoride (KF) and isopropylmagnesium chloride solution (*i*-PrMgCl, 2.0 M in THF) were purchased from Sigma-Aldrich. 5,5'-dibromo-2,2'-bithiophene was purchased from One Click Chemistry. Potassium carbonate (K₂CO₃) and organic solvent such as hexane, ethyl acetate (EtOAc), tetrahydrofuran (THF), methanol (MeOH) and anhydrous dimethylsulfoxide (DMSO) were purchased from Fisher. 1,2-dimethoxyethane (DME) was purchased from Honeywell. All reagents and solvents were used as received unless otherwise noted. Anhydrous THF was freshly distilled from sodium and benzophenone prior to use. NBS was recrystallized in water and stored in refrigerator before use.

3.2.2 Characterization methods

3.2.2.1 Nuclear Magnetic resonance (NMR)

^1H and ^{13}C NMR spectra were recorded on a Varian INOVA 400 and a MERCURY 300 spectrometers. Chemical shifts were quoted relative to the residual protons of the deuterated solvents CDCl_3 ($\delta = 7.26$ for ^1H and $\delta = 77.36$ for ^{13}C). The multiplicity was characterized by the following abbreviations: s-singlet, d-doublet, t-triplet, q-quartet, m-multiplet.

3.2.2.2 Differential Scanning Calorimetry (DSC)

DSC measurements were performed on a Q 2000 from TA Instruments at a scanning rate of $10\text{ }^\circ\text{C min}^{-1}$ within temperature range from -90 to $250\text{ }^\circ\text{C}$. The phase transition temperatures were determined as the peak positions in the DSC traces due to broadness of the transition peaks.

3.2.2.3 Polarized Optical Microscope (POM)

An Olympus BX51 polarizing optical microscope equipped with a Mettler FP 82 HT hot stage was used for visual observation of optical textures at different temperatures.

3.2.2.4 Ultraviolet-visible spectroscopy (UV-Vis)

UV-Vis measurements were conducted on a Shimadzu UV-Vis-NIR Spectrometer with absorption range from 200-700 nm. For solution state measurement, samples were dissolved in dry THF at concentration of $20\text{ }\mu\text{M}$. For solid-state thin film measurement, samples were dissolved in THF at a concentration of 20 mM and drop-cast on a piece of glass slide.

3.2.2.5 Grazing-Incidence Wide-Angle X-Ray Scattering (GIWAXS)

Temperature- dependent GIWAXS measurements were performed at beamline 8-ID-E of the Advanced Photon Source, Argonne National Laboratory with 10.86 keV ($\lambda = 1.1416 \text{ \AA}$) synchrotron radiation. The temperature of the samples was varied from room temperature up to 130 °C using a Linkam HFSX350-GI stage. Samples were measured inside a low vacuum chamber (10^{-3} mbar) to minimize concerns about radiation damages, samples' moisture uptake, and extraneous scattering from ambient air. The measurement time was chosen to be 3 s frame⁻¹. For each sample, three data sets were taken from three adjacent spots on the sample and then summed in order to enhance the signal-to-noise ratio. The samples were tilted at an angle of incidence of 0.14° with respect to the incoming beam, which is above the estimated critical angle of sample ($\approx 0.13^\circ$) but below the critical angle of the Si substrates ($\approx 0.17^\circ$) in order to probe the whole film thickness. The scattering signal was recorded with a Pilatus 1MF pixel array detector (pixel size = 172 μm) positioned 228 mm from the sample. Each data set was stored as a 981 \times 1043 32-bit tiff image with 20-bit dynamic range. The Pilatus detector has rows of inactive pixels at the border between detector modules. In order to fill these gaps, after each measurement the detector was moved to a new vertical direction and the measurement on each spot was repeated, then the gaps were filled by combining the data from two detector positions. The signals were reshaped and output as intensity maps in q_z versus q_r ($=\sqrt{q_x^2 + q_y^2}$) space. We also performed detector nonuniformity, detection efficiency, the polarization effect, and solid- angle variation for each image. All the GIWAXS data processing and extraction were executed using the GIXSGUI package for MATLAB.

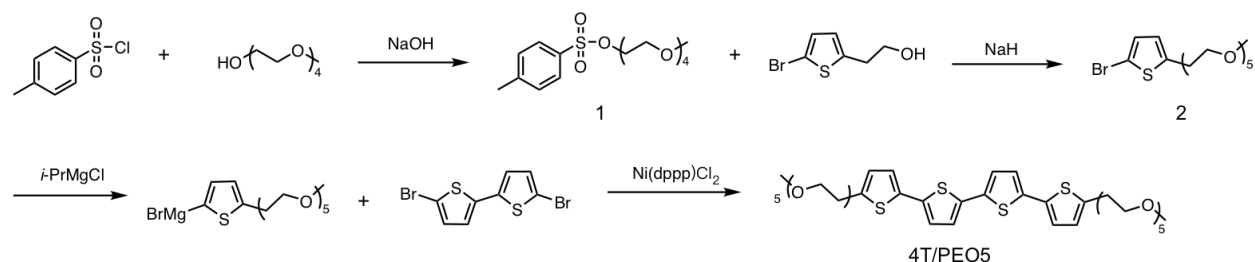
Peak shape analysis was performed on wedge cuts taken with an angular breadth of 2°. Each wedge cut was first fit to an empirical baseline function to enable the subtraction of the background intensity and amorphous scattering. The background-subtracted wedge cut was then fit to a Voigt

function to extract the peak position and the FWHM of the reflections of interest. More details of peak shape analysis can be found elsewhere.

3.2.3 Synthetic procedures

3.2.3.1 Synthesis of linear amphiphiles 4T/PEO5

The synthesis of 4T/PEO5 followed the same procedure of 4T/PEO4 as mentioned in the last chapter in which a two-fold Kumada-coupling reaction was the key step. The synthetic procedure is shown in **Scheme 3.1**. The final product is red solid with more viscosity and fluidity compared to 4T/PEO4 visually.



Scheme 3.1 Synthetic procedure of 4T/PEO5 via Kumada coupling.

Synthesis of 2,5,8,11-tetraoxatridecan-13-yl 4-methylbenzenesulfonate (1)

To a 500mL round bottom flask with a magnetic bar was added 2-[2-(2-methoxyethoxy)ethoxy]-ethanol ether (100 mmol, 1.0 eq) dissolved in 70 mL THF. Sodium hydroxide (350 mmol, 3.5 eq) was dissolved in 70 mL H₂O and then added slowly to the flask. After the reaction mixture was cooled down to 0 °C in an ice bath, p-toluenesulfonyl chloride dissolved in 50 mL THF was added dropwise to the mixture under vigorous stirring. The reaction mixture was stirred at 0 °C for 2 h, and then at room temperature overnight. After completion of the reaction as indicated by TLC, the

reaction mixture was poured to 5 wt% hydrochloric acid aqueous solution, and the product was extracted with dichloromethane (30 mL × 3). The organic layer was then washed successively with saturated sodium bicarbonate solution (50 mL × 3) and water (50 mL × 3) and dried over anhydrous magnesium sulfate. After solvent evaporation the product was obtained as a slight yellow liquid without further purification, yield 90%.

¹H NMR (400MHz, CDCl₃, δ): 7.80 (d, J=8 Hz, 2H; Ar H), 7.34 (d, J=8 Hz, 2H; Ar H), 4.15 (t, J=4 Hz, 2H; CH₂), 3.68 (t, J=4 Hz, 2H; CH₂), 3.62-3.58 (m, 10H; CH₂), 3.53-3.50 (m, 2H; CH₂), 3.36 (s, 3H; CH₃), 2.44 (s, 3H; CH₃).

Synthesis of 16-(5-bromothiophen-2-yl)-2,5,8,11,14-pentaoxahexadecane (**2**)

To a dry round bottom flask was added sodium hydride (60 wt% in mineral oil, 30 mmol, 2.0 eq), and 100 mL anhydrous THF. The reaction mixture was stirred under Argon atmosphere at room temperature for 30 min. 5-bromo-2-thiopheneethanol (15 mmol, 1.0 eq) was then added dropwise via a syringe and the mixture was stirred vigorously at room temperature for 1h. **1** (18 mmol, 1.2 eq) was added to the reaction mixture slowly and stirred at room temperature overnight. After completion of the reaction as indicated by TLC, the reaction mixture was quenched with 100 mL H₂O and vigorously stirred for 30 min. The crude product was extracted with ethyl acetate (30 mL × 3) and the collected organic layer was washed with water (30 mL × 3). The crude product was purified after dried over anhydrous magnesium sulfate by column chromatography on silica gel with hexane: EtOAc =1:1 (v/v) as eluent to give **2** as a yellow liquid (9 mmol) in 60% yield.

¹H NMR (400MHz, CDCl₃, δ): 6.85 (d, J=4 Hz, 1H; Th H), 6.60 (d, J=4Hz, 1H; Th H), 3.65 (m, 16H; CH₂), 3.54 (m, 2H; Th-CH₂-CH₂), 3.37 (s, 3H; CH₃), 3.01 (t, J=8 Hz, 2H; Th-CH₂).

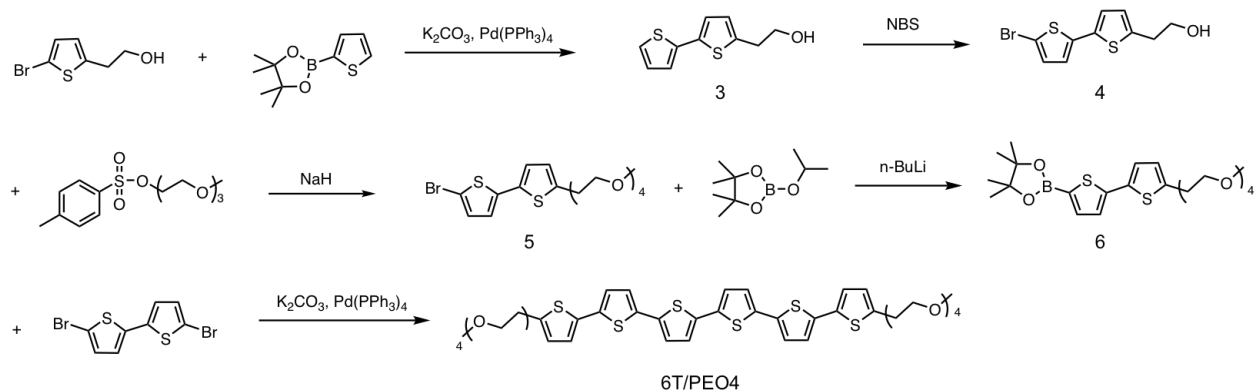
Synthesis of 4T/PEO5

To a dry 100 mL 3-neck flask filled with Argon was added **2** (6 mmol, 3.0 eq) dissolved in 15 mL anhydrous THF. Isopropyl magnesium chloride (2.0 M in THF, 6.4 mmol, 3.2 eq) was added dropwise. The mixture was refluxed at 65 °C for 3.5 h and was transferred to a second 3-neck flask with 5,5'-dibromo-2,2'-bithiophene (2 mmol, 1.0 eq) and Ni(dppp)Cl₂ (0.1 mmol, 0.05 eq) under Argon atmosphere through cannula. The reaction mixture was refluxed at 65 °C for 20h, before being quenched with 5 wt% hydrochloric acid aqueous solution. With remaining catalyst filtered, the crude product was extracted with ethyl acetate (30 mL × 3) and washed successively with saturated aqueous sodium bicarbonate (30 mL × 3) and H₂O (30 mL × 3). The solution was evaporated after dried over magnesium sulfate and the product was purified with by column chromatography on silica gel with EtOAc: methanol =50:1 (v/v) to give a red viscous liquid (0.60 mmol) in 30% yield.

¹H NMR (CDCl₃, 400MHz, δ): 7.04 (d, J=4 Hz, 2H; Th H), 6.99 (m, 4H; Th H), 6.76 (d, J=4 Hz, 2H; Th H), 3.66 (m, 32H; CH₂), 3.54 (m, 4H; CH₂), 3.37 (s, 6H; CH₃), 3.08 (t, J=8 Hz, 4H; CH₂).

3.2.3.2 Synthesis of linear amphiphiles 6T/PEO4

As for the synthesis of 6T/PEO4, two-fold Suzuki coupling reaction was adopted with Pd(PPh₃)₄ as catalyst instead of Kumada coupling as the latter one generated homo-coupled 4T/PEO4 as major product. The synthetic procedure of 6T/PEO4 is shown in **Scheme 3.2** and the final product is a wax-like solid in dark red color.



Scheme 3.2 Synthetic procedure of 6T/PEO4 via Suzuki coupling.

Synthesis of (2,2'-bithiophene)-5-ethanol (**3**)

To a 200 mL 3-neck flask equipped with a condenser was charged 5-bromo-2-thiopheneethanol (36 mmol, 1.0 eq), 2-thiopheneboronic acid pinacol ester (43.5 mmol, 1.2 eq), and K_2CO_3 (108 mmol, 3.0 eq). The flask was purged with Argon for 25 min before $Pd(PPh_3)_4$ (0.36 mmol, 0.01 eq) catalyst was added to the flask and the reactant was purged with Argon for another 25 min. To another round-bottom flask was added mixed solvent of 1,2-dimethoxyethane (120 mL) and water (30 mL). The solvent was bubbled with Argon for 30 min before canula transferred to the 3-neck flask under Argon. The reaction was refluxed at 85 °C for 16 h followed by opening to air. 1,2-dimethoxyethane was evaporated first and the crude product was extracted with EtOAc (30 mL \times 3) and then washed with water (30 mL \times 3), dried over anhydrous magnesium sulfate and concentrated. The product was further purified via column chromatography with hexane: EtOAc = 5:1 (v/v) as eluent to give **3** as a dark red liquid (28.2 mmol) in 78% yield.

1H NMR ($CDCl_3$, 400MHz, δ): 7.19 (d, $J=4$ Hz, 1H; Th H), 7.12 (d, $J=4$ Hz, 1H; Th H), 7.02 (d, $J=4$ Hz, 1H; Th H), 7.00 (m, 1H; Th H), 6.79 (d, $J=4$ Hz, 1H; Th H), 3.89 (q, $J=6.28$ Hz, 2H; CH_2), 3.06 (t, $J=6.16$ Hz, 2H; CH_2), 1.55 (s, 1H; OH).

Synthesis of 5'-bromo-(2,2'-bithiophene)-5-ethanol (**4**)

3 (28.2 mmol, 1.0 eq) was dissolved in 100 mL THF and cooled down to 0 °C in an ice bath. NBS (29 mmol, 1.03 eq) was added to the solution portionwise. The reaction was stirred at 0 °C for 1h, and then at room temperature for 5h before quenched with 10wt% sodium hydroxide aqueous solution. The crude product was extracted with ethyl acetate (30 mL × 3) and the combined organic layer washed with water (50 mL × 3), then dried over magnesium sulfate. The solvent was evaporated, and the product was purified by column chromatography on silica gel with hexane: EtOAc =5:1 (v/v) as eluent to give **4** as a dark red liquid (21 mmol) in 74% yield.

¹H NMR (CDCl₃, 400MHz, δ): 6.96-6.94 (m, 2H; Th H), 6.86 (d, J=4 Hz, 1H; Th H), 6.78 (d, J=4 Hz, 1H; Th H), 3.89 (q, J=6 Hz, 2H; CH₂), 3.05 (t, J=6 Hz, 2H; CH₂), 1.55 (s, 1H; OH).

Synthesis of 5-bromo-5'-PEO4-2,2'-bithiophene (**5**)

To a dry round bottom flask was added sodium hydride (60 wt% in mineral oil, 32 mmol, 2.0 eq), and 60 mL anhydrous THF. The reaction mixture was stirred under Argon atmosphere at room temperature for 30 min. **4** (16 mmol, 1.0 eq) was dissolved in 5 mL anhydrous THF and added dropwise to the flask. The mixture was stirred vigorously at room temperature for 4h. **PEO3-tosylate** (19.2 mmol, 1.2 eq, synthesis can be found in chapter 2) was added dropwise to the reaction mixture and stirred at room temperature overnight. After completion of the reaction as indicated by TLC, the reaction mixture was quenched with 200 mL H₂O and vigorously stirred for 30 min. The crude product was extracted with ethyl acetate (30 mL × 3) and then washed with water (30 mL × 3). The solvent was evaporated after dried over magnesium sulfate, and the crude

product was purified by column chromatography on silica gel with hexane: EtOAc =1:1 (v/v) as eluent to give **5** as a dark red liquid (11.2 mmol) in 70% yield.

¹H NMR (CDCl₃, 400MHz, δ): 6.94 (d, J=4 Hz, 1H; Th H), 6.92 (d, J=4 Hz, 1H; Th H), 6.84 (d, J=4 Hz, 1H; Th H), 6.74 (d, J=4 Hz, 1H; Th H), 3.66 (m, 12H; CH₂), 3.55 (m, 2H; CH₂), 3.37 (s, 3H; CH₃), 3.06 (t, J=8 Hz, 2H; CH₂).

Synthesis of 5-boronic acid pinacol ester-5'-PEO4-2,2'-bithiophene (**6**)

5 (6.48 mmol, 1.0 eq), 2-isopropoxy-4,4,5,5-tetramethyl-1,3,2-dioxaborolane (12.96 mmol, 2.0 eq) was dissolved in 30 mL anhydrous THF under Argon atmosphere. The reaction mixture was cooled down to -78 °C in acetone/dry ice bath while n-butyllithium solution (1.6 M in hexane, 4.86 mL, 1.2 eq) was added dropwise via a syringe. The reaction mixture was stirred at -78 °C for 40 min then at room temperature overnight, followed by quenched with water. The crude product was extracted with EtOAc (30 mL × 3) and then washed with water (30 mL × 3). The solvent was evaporated after dried over magnesium sulfate, and the crude product was purified by column chromatography on silica gel with hexane: EtOAc =1:2 (v/v) as eluent to give **6** as a dark red liquid (3.93 mmol) in 61% yield.

¹H NMR (CDCl₃, 400MHz, δ): 6.94 (d, J=4 Hz, 1H; Th H), 6.92 (d, J=4 Hz, 1H; Th H), 6.84 (d, J=4 Hz, 1H; Th H), 3.66 (m, 12H; CH₂), 3.55 (m, 2H; CH₂), 3.37 (s, 3H; CH₃), 3.06 (t, J=8 Hz, 2H; CH₂), 1.27 (s, 5H; CH₃), 1.24 (s, 7H; CH₃).

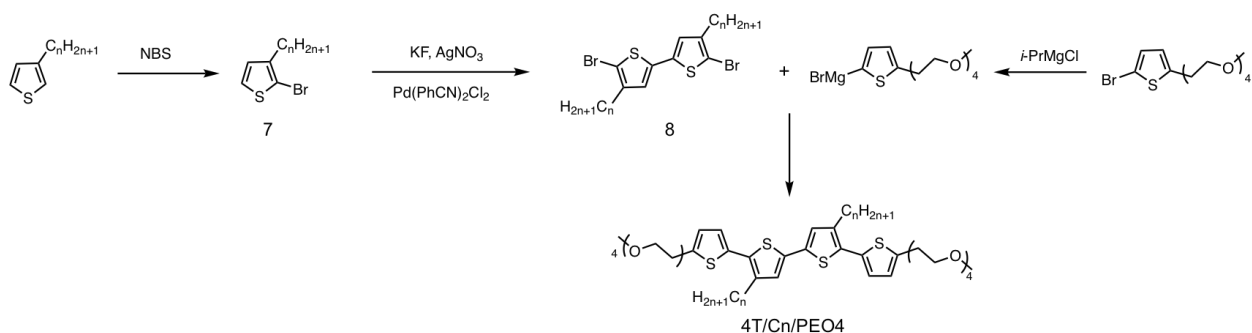
Synthesis of 6T/PEO4

To a 100 mL 3-neck flask equipped with a condenser was charged 5,5'-dibromo-2,2'-bithiophene (0.7 mmol, 1.0 eq), **6** (2.1 mmol, 3.0 eq) and K₂CO₃ (4.2 mmol, 6.0 eq). The flask was purged with

Argon for 25 min before Pd(PPh₃)₄ (0.014 mmol, 0.02 eq) catalyst was added to the flask and the reactant was purged with Argon for another 25 min. To another round-bottom flask was added a mixed solvent of 1,2-dimethoxyethane (40 mL) and water (10 mL). The solvent was bubbled with Argon for 30 min before canula transferred to the 3-neck flask under Argon. The reaction was refluxed at 85 °C for 16 h followed by opening to air. 1,2-dimethoxyethane was evaporated first and the crude product was extracted with EtOAc (30 mL × 3) and then washed with water (30 mL × 3), dried over anhydrous magnesium sulfate and concentrated. The product was further purified via column chromatography with EtOAc: MeOH = 20:1 (v/v) as eluent to give 6T/PEO4 as a dark red wax-like solid (0.11 mmol) in 16% yield which was precipitated out in MeOH.

¹H NMR (CDCl₃, 400MHz, δ): 7.06-7.04 (m, 3H; Th H), 7.01-6.97 (m, 6H; Th H), 6.91 (d, J=4Hz, 1H; Th H), 6.76 (d, J=3.54Hz, 2H; Th H), 3.73 (t, J=6.7Hz, 4H; CH₂), 3.67 (m, 20H; CH₂), 3.54 (m, 4H; CH₂), 3.37 (s, 6H; CH₃), 3.08 (t, J=6.74Hz, 4H; CH₂).

3.2.3.3 Synthesis of X-shaped bolaamphiphilic LCs



Scheme 3.3 Synthetic procedures of X-shaped bolaamphiphiles 4T/alkyl/PEO4.

Synthesis of 2-bromo-3-alkylthiophene (7)

3-alkylthiophene (1.0 eq, 25 mmol) was dissolved in 50 mL THF in a round-bottom flask and cooled down to 0°C in ice bath. NBS (1.05 eq, 26.25 mmol) was added portionwise to the flask in 30 min. The reaction mixture was stirred at 0°C for 30 min and then at room temperature overnight. The reaction was quenched with NaOH solution and extracted with EtOAc (30 mL × 3). The organic layer was collected, washed with water (30 mL × 3), dried over MgSO₄ and concentrated. The crude product was further purified by column chromatography with pure hexane as eluent to give **7** as colorless liquid.

2-bromo-3-hexylthiophene (n = 6, yield 92%), ¹H NMR (CDCl₃, 300MHz, δ): 7.19 (d, J=6Hz, 1H; Th H), 6.80 (d, J=6Hz, 1H; Th H), 2.56 (t, J=7.56Hz, 2H; Th-CH₂), 1.57 (m, 2H; Th-CH₂-CH₂), 1.31 (m, 6H; (CH₂)₃), 0.89 (t, J=6Hz, 3H; CH₃).

2-bromo-3-decylthiophene (n = 10, yield 90%), ¹H NMR (d-Acetone, 400MHz, δ): 7.44 (d, J=5.6Hz, 1H; Th H), 6.94 (d, J=8Hz, 1H; Th H), 2.58 (t, J=8Hz, 2H; Th-CH₂), 1.59 (m, 2H; Th-CH₂-CH₂), 1.28 (m, 14H; (CH₂)₇), 0.87 (t, J=6.82Hz, 3H; CH₃).

2-bromo-3-dodecylthiophene (n = 12, yield 85%), ¹H NMR (d-Acetone, 400MHz, δ): 7.44 (d, J=4Hz, 1H; Th H), 6.94 (d, J=8Hz, 1H; Th H), 2.58 (t, J=8Hz, 2H; Th-CH₂), 1.59 (m, 2H; Th-CH₂-CH₂), 1.28 (m, 18H; (CH₂)₉), 0.88 (t, J=6.82Hz, 3H; CH₃).

2-bromo-3-tetradecylthiophene (n = 14, yield 92%), ¹H NMR (CDCl₃, 400MHz, δ): 7.19 (d, J=8Hz, 1H; Th H), 6.80 (d, J=8Hz, 1H; Th H), 2.55 (t, J=8Hz, 2H; Th-CH₂), 1.57 (m, 2H; Th-CH₂-CH₂), 1.26 (m, 22H; (CH₂)₁₁), 0.88 (t, J=6.82Hz, 3H; CH₃).

Synthesis of 3,3'-dialkyl-5,5'-dibromo-2,2'-bithiophene (**8**)

To a Schlenk flask was charged KF (4.0 eq, 20 mmol), AgNO₃ (4.0 eq, 20 mmol) and Pd(PhCN)₂Cl₂ (0.1 eq, 0.5 mmol) with a stir bar covered by alumina foil. The flask was degassed

and refilled with Argon for 5 times. To another round bottom flask was charged 2-bromo-3-alkylthiophene (1.0 eq, 5.0 mmol) and 40 mL anhydrous DMSO. The solution was purged with Argon for 30min before canula transferred to the Schlenk flask and vigorously stirred at 80 °C overnight. The reaction was quenched by opening to air and the reaction mixture was filtered under vacuum. The filtrate was then extracted with EtOAc (30 mL × 3), the collected organic layer was washed with water (30 mL × 3) followed by dried over MgSO₄ and concentrated. The crude product was purified by column chromatography with pure hexane as eluent to give **8** as yellow solid.

3,3'-dimethyl-5,5'-dibromo-2,2'-bithiophene (n = 1, yield 54.6 %), ¹H NMR (CDCl₃, 300MHz, δ): 6.76 (s, 2H; Th H), 2.17 (s, 6H; CH₃).

3,3'-dihexyl-5,5'-dibromo-2,2'-bithiophene (n = 6, yield 51%), ¹H-NMR (CDCl₃, 400MHz, δ): 6.77 (s, 2H; Th H), 2.52 (t, J=10.24Hz, 4H; Th-CH₂), 1.55 (m, 4H; Th-CH₂-CH₂), 1.31 (m, 12H; (CH₂)₃), 0.89 (t, J=8Hz, 6H; CH₃).

3,3'-didecyl-5,5'-dibromo-2,2'-bithiophene (n = 10, yield 48%), ¹H-NMR (CDCl₃, 400MHz, δ): 6.77 (s, 2H; Th H), 2.52 (t, J=8Hz, 4H; Th-CH₂), 1.55 (m, 4H; Th-CH₂-CH₂), 1.26 (m, 28H; (CH₂)₇), 0.89 (t, J=6.66Hz, 6H; CH₃).

3,3'-didodecyl-5,5'-dibromo-2,2'-bithiophene (n = 12, yield 38%), ¹H-NMR (CDCl₃, 400MHz, δ): 6.77 (s, 2H; Th H), 2.51 (t, J=7.72Hz, 4H; Th-CH₂), 1.55 (m, 4H; Th-CH₂-CH₂), 1.26 (m, 32H; (CH₂)₈), 0.88 (t, J=8Hz, 6H; CH₃).

3,3'-ditetradecyl-5,5'-dibromo-2,2'-bithiophene (n = 14, yield 42%), ¹H-NMR (CDCl₃, 400MHz, δ): 6.77 (s, 2H; Th H), 2.51 (t, J=7.72Hz, 4H; Th-CH₂), 1.55 (m, 4H; Th-CH₂-CH₂), 1.26 (m, 36H; (CH₂)₉), 0.88 (t, J=8Hz, 6H; CH₃).

Synthesis of 4T/Cn/PEO4

To a dry 100 mL 3-neck flask filled with Argon was added **2-bromo-5-PEO4-thiophene** (3 mmol, 3.0 eq) dissolved in 15 mL anhydrous THF. Isopropyl magnesium chloride (2.0 M in THF, 3.2 mmol, 3.2 eq) was added dropwise. The mixture was refluxed at 65 °C for 3.5 h and was transferred to a second 3-neck flask with **8** (1 mmol, 1.0 eq) and Ni(dppp)Cl₂ (0.05 mmol, 0.05 eq) under Argon atmosphere through cannula. The reaction mixture was refluxed at 65 °C for 20h, before being quenched with 5 wt% hydrochloric acid aqueous solution. With remaining catalyst filtered, the crude product was extracted with ethyl acetate (30 mL × 3) and washed successively with saturated aqueous sodium bicarbonate (30 mL × 3) and H₂O (30 mL × 3). The solution was evaporated after dried over magnesium sulfate and the product was purified with by column chromatography on silica gel with EtOAc: methanol =50:1 (v/v) to give a red liquid as final product.

4T/methyl/PEO4 (n = 1, yield 25%), ¹H NMR (400 MHz, CDCl₃, δ): 6.95 (d, J=4Hz, 2H; Th H), 6.90 (s, 2H; Th H), 6.80 (d, J=4Hz, 2H; Th H), 3.73 (t, J=5.48Hz, 4H; CH₂), 3.66 (m, 20H; CH₂), 3.54 (m, 4H; CH₂), 3.37 (s, 6H; CH₃), 3.05 (t, J=6.82Hz, 4H; CH₂), 2.34 (s, 6H; CH₃).

4T/hexyl/PEO4 (n = 6, yield 17%), ¹H NMR (400 MHz, CDCl₃, δ): 6.95 (s, 2H; Th H), 6.93 (d, J=4Hz, 2H; Th H), 6.80 (d, J=4Hz, 2H; Th H), 3.74 (t, J=8Hz, 4H; CH₂), 3.67 (m, 20H; CH₂), 3.54 (m, 4H; CH₂), 3.37 (s, 6H; CH₃), 3.10 (t, J=8Hz, 4H; CH₂), 2.70 (t, J=8Hz, 4H; CH₂), 1.62 (m, 4H; CH₂), 1.30 (m, 12H; CH₂), 0.89 (t, J=6.66Hz, 6H; CH₃).

4T/decyl/PEO4 (n = 10, yield 38.6%), ¹H NMR (400MHz, CDCl₃, δ): 6.95 (s, 2H; Th H), 6.93 (d, J=4Hz, 2H; Th H), 6.80 (d, J=4Hz, 2H; Th H), 3.74 (t, J=6.9Hz, 4H; CH₂), 3.67 (m, 20H; CH₂), 3.54 (m, 4H; CH₂), 3.37 (s, 6H; CH₃), 3.10 (t, J=7.02Hz, 4H; CH₂), 2.69 (t, J=8Hz, 4H; CH₂), 1.62 (m, 4H; CH₂), 1.26 (m, 28H; CH₂), 0.89 (t, J=6.8Hz, 6H; CH₃).

4T/dodecyl/PEO4 ($n = 12$, yield 23.6%), $^1\text{H NMR}$ (400MHz, CDCl_3 , δ): 6.95 (s, 2H; Th H), 6.93 (d, $J=4\text{Hz}$, 2H; Th H), 6.80 (d, $J=4\text{Hz}$, 2H; Th H), 3.74 (t, $J=6.84\text{Hz}$, 4H; CH_2), 3.67 (m, 20H; CH_2), 3.54 (m, 4H; CH_2), 3.37 (s, 6H; CH_3), 3.10 (t, $J=6.68\text{Hz}$, 4H; CH_2), 2.69 (t, $J=7.98\text{Hz}$, 4H; CH_2), 1.63 (m, 4H; CH_2), 1.26 (m, 36H; CH_2), 0.89 (t, $J=6.84\text{Hz}$, 6H; CH_3).

4T/tetradecyl/PEO4 ($n = 14$, yield 16%), $^1\text{H NMR}$ (400MHz, CDCl_3 , δ): 6.95 (s, 2H; Th H), 6.93 (d, $J=4\text{Hz}$, 2H; Th H), 6.80 (d, $J=4\text{Hz}$, 2H; Th H), 3.74 (t, $J=6.72\text{Hz}$, 4H; CH_2), 3.67 (m, 20H; CH_2), 3.54 (m, 4H; CH_2), 3.37 (s, 6H; CH_3), 3.10 (t, $J=6.24\text{Hz}$, 4H; CH_2), 2.69 (t, $J=7.92\text{Hz}$, 4H; CH_2), 1.63 (m, 4H; CH_2), 1.26 (m, 44H; CH_2), 0.89 (t, $J=6.96\text{Hz}$, 6H; CH_3).

3.3 Results and discussion

3.3.1 Structural evolution of 4T/PEOn studied by simulation

It has been a long-standing assumption that oligothiophenes with terminal thiophene rings containing functionalized end-capping chains at their α -positions would behave either like liquid crystals or like block copolymers depending on molecular weight.^[15–18] In our submitted work, MD simulations were employed to predict that PEO units would have a more disruptive effect on the ordered packing of 4T due to their lower melting points and less congruent packing than alkyl chains with comparable molecular weight. Lindemann Parameter^[19] (δ_L), defined as the ratio of the root mean square fluctuation in atomic positions about the equilibrium lattice positions and the nearest neighbor distance (p), was calculated in order to capture the melting and disordering of the smectic layer of thiophene rings with varying PEO chain lengths. As shown in **Figure 3.1(a)**, the critical value of δ_L for 4T/PEOn materials is around 5-10%, resulting in a melting point of 400 K, 380 K, 350 K, and 310 K for $n = 3, 4, 5$, and 6, respectively. Moreover, the potential energy (U) between 4T segments ($U_{4\text{T}-4\text{T}}$), PEO segments ($U_{\text{PEOn-PEOn}}$), and between 4T and PEO (U_{cross})

were also tracked to better understand how the melting behavior of 4T/PEO n oligomers correlates with the intermolecular interactions. As expected, all these energetic terms increase (more positive) with temperature for all the systems as the intermolecular attractions tend to weaken. The slope of the U_{4T-4T} component as a function of temperature remains constant while the slope of $U_{PEO_n-PEO_n}$ does show slight changes. The normalized “segmental” cross potential energy U_{cross} for all the systems at different temperatures was shown in **Figure 3.1(b)**. A sudden change in the slope or a break in the curves was observed at 400 K, 380 K, 350 K, and 310 K for $n = 3, 4, 5,$ and $6,$ respectively. While these changes become fainter as n increases, they can be seen as indicative of a significant structural re-arrangement involving the 4T-PEO n interactions the system. Note that the melting temperature predicted using Lindemann Parameter (shown in **Figure 3.1(a)**) are consistent with the temperatures where the change in the slope occurs in the 4T-PEO n potential energy.

3.3.2 Thermal properties and self-assembly behaviors of 4T/PEO5 compared to 4T/PEO4

To experimentally verify that the simulation results captured the correct trend in melting behavior with n , experiments were conducted on 4T/PEO5 system in comparison to 4T/PEO4. We choose 4T/PEO5 for experimental characterization in addition to 4T/PEO4 since simulation predicted at 300K 4T/PEO n undergoes order-disorder transition from $n = 4$ to $n = 5$. At room temperature (near 300K), 4T/PEO5 appears as a sticky substance of dark red color while 4T/PEO4 remains in the solid state. The TGA curves (**Figure 3.2(c)**) suggest that both compounds remain thermally stable below 473 K, which is within the DSC temperature range (183 K – 473 K) as shown in the heating cycle in **Figure 3.2(a)**. A broader transition peak centered near 340 K is observed (indicated by the shaded areas) for 4T/PEO5. Such observations are consistent with the simulation trends in **Figure 3.1** where longer PEO chains result in lower melting point. As can be seen in

Figure 3.2(b), fan-shaped textures, typical of smectic phases were also observed for 4T/PEO5 under POM below the melting temperature while black while featureless image was observed above the melting point, which further supports that the transition temperature detected by DSC and simulation is indeed an LC order-disorder transition.

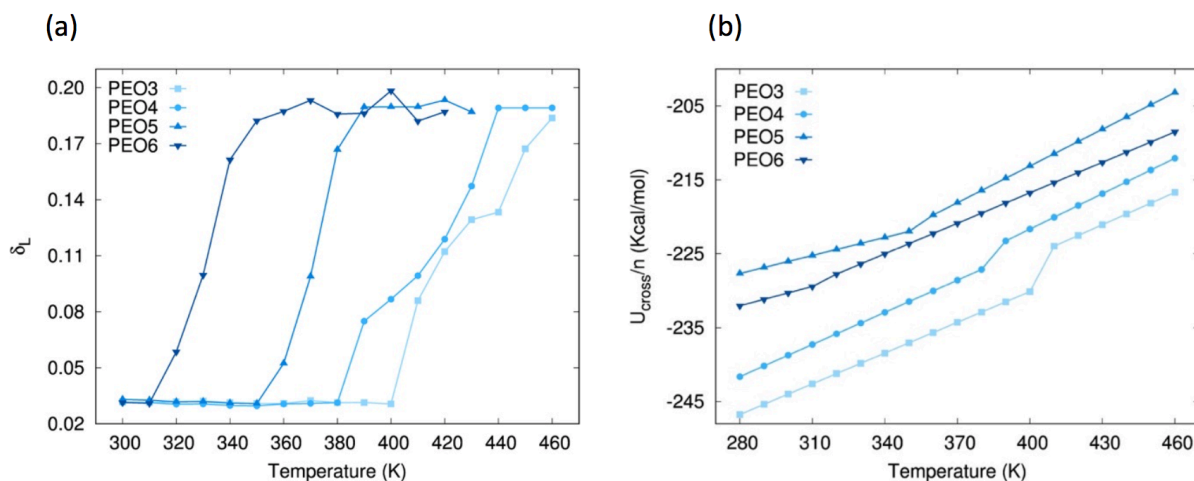


Figure 3.1 (a) Effect of temperature on the Lindemann Parameter for 4T/PEOn systems. (b) Normalized Potential Energy between 4T and PEOn as a function of temperature. (Reprint from *ACS Macro Lett.* 2020^[33]).

Figure 3.2(d) depicts the UV-Vis absorption spectra of pristine 4T/PEO4 and 4T/PEO5 in both THF solution and drop-cast thin film states at room temperature. In solution state both compounds exhibit characteristic π - π^* absorption peak λ_{max} at 402 nm with free molecular movement, indicating that the elongation of attached PEO segments did not significantly affect the conformation of quaterthiophene in good solvent.^[20] For drop-cast thin films (without annealing), a λ_{max} blue-shift is observed (even though a red-shift was supposed to show up due to increased planarity of packed molecules in thin film state) for both compounds and the absorption peaks shift

to 372 nm for 4T/PEO4 and 358 nm for 4T/PEO5, respectively, with the appearance of two vibronic “shoulder” peaks as indicated by the arrows (absent in the solution samples) which were attributed to the absorption of strong interchain π - π interaction, suggesting the formation of π -stacked aggregates within both thin film samples.^[21] Note that the absorption peaks appear at a smaller wavelength for 4T/PEO5 than for 4T/PEO4, indicative of a more ordered π - π stacking between adjacent 4T cores with shorter PEO chains in thin film state. This observation aligns well with the simulation results and further supports the contention that longer PEO chains tend to loosen up the smectic structure.

To further verify that π - π interaction controls the self-assembly behavior of 4T/PEO n systems, we employed T-dependent WAXS experiments to investigate both the π - π interaction and smectic ordering of 4T/PEO4 and 4T/PEO5. Shown in **Figure 3.3**(a) and (b) are the WAXS profiles at varying temperatures of 4T/PEO4 and 4T/PEO5, respectively. Consistent with simulation results described above, at room temperature (293K), both 4T/PEO4 and 4T/PEO5 adopt a smectic morphology with characteristic smectic diffraction peaks ($00h$) in the out-of-plane direction, corresponding to the smectic domain spacing of 3.64 nm in 4T/PEO4 and 4.06 nm in 4T/PEO5. In addition, two π - π interacting peaks denoted as A and B at higher q which correlate to the herringbone hetero- and homo-tilt alignment as proven in our prior studies^[22,23] were also observed for both compounds. Upon heating, the WAXS diffraction intensity of both smectic and π - π interacting peaks in 4T/PEO4 remains almost unchanged until the intensity substantially decreases above 393K, indicating the order-disorder transition. In contrast, the peak intensity of 4T/PEO5 shows an earlier but more gradual change, suggesting a slower and/or broader order-disorder transition compared to 4T/PEO4.

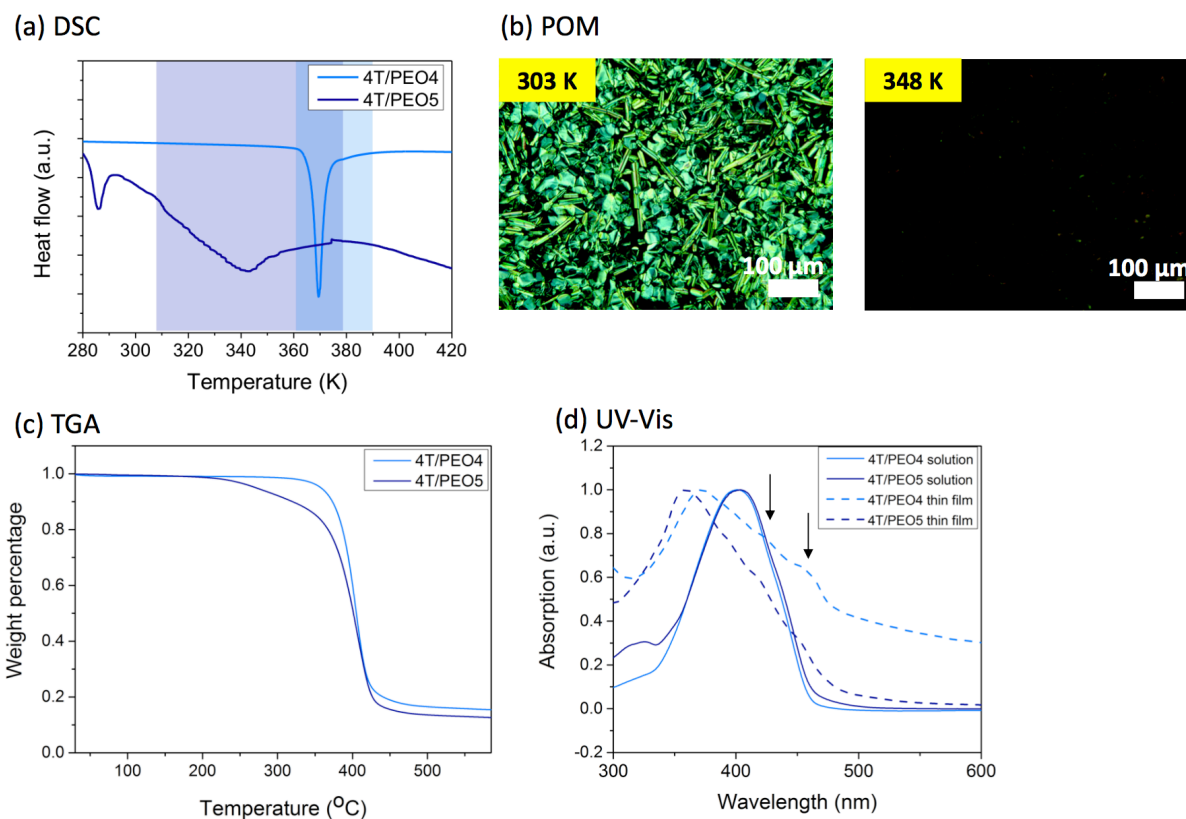


Figure 3.2. (a) DSC traces of 4T/PEO4 and 4T/PEO5 as a function of temperature with scanning rate 10 K/min during the second heating scan. (b) POM images of 4T/PEO5 below (left) and above (right) order-disorder transition temperature. (c) TGA traces of 4T/PEO4 and 4T/PEO5 with heating rate 10 K/min. (d) UV-Vis spectra of 4T/PEO4 and 4T/PEO5 samples in solution and thin film state. (Reprint from *ACS Macro Lett.* 2020^[33])

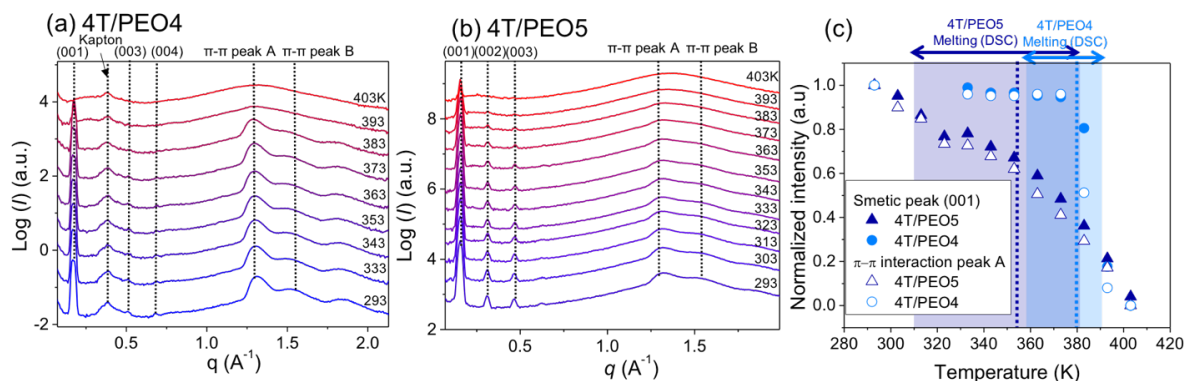


Figure 3.3 Temperature-dependent WAXS profiles of (a) 4T/PEO4 and (b) 4T/PEO5 from 293K to 403K. Note that there exist background scattering peaks from Kapton tape in 4T/PEO4 sample. c) Evolution of the normalized intensity of the smectic peak (001) and the π - π interacting peaks of 4T/PEO4 and 4T/PEO5 as a function of temperature. The shaded red and black areas indicate the melting transition range by DSC and dotted black line indicates the transition temperature prediction from simulations. (Reprint from ACS Macro Lett. 2020^[33])

To quantify the trend observed in **Figure 3.3** (a) and (b), we show in **Figure 3.3**(c) the (001) and π - π interacting peaks intensity, normalized by the peak intensity at the lowest temperature of 293 K. Similar to the qualitative observation in **Figure 3.3** (a) and (b), the intensity of the smectic and π - π interacting peaks in 4T/PEO4 remains almost constant until 383K before suddenly dropping at higher temperature, whereas the peak intensity of 4T/PEO5 sample shows a more gradual drop with temperature. The drop-in intensity of both samples occurs within the temperature ranges measured by DSC as indicated by the shaded areas in **Figure 3.2**(a). Importantly, for each sample the temperature dependent peak intensity of both smectic and π - π interacting peaks follows almost identical trends. This observation is consistent with the assessment from simulations that the π - π interacting of the 4T units control the self-assembly behavior of the 4T/PEO_n systems. We note that for 4T/PEO5, besides the smectic-disorder transition, we observed a sharper transition near 285K, which our WAXS experiment indicates to be a smectic-smectic transition.

3.3.3 Study of linear amphiphiles 6T/PEO4 in its self-assembly behavior and ionic conduction characteristics

As for synthesis of 6T/PEO4 binary system with sexithiophene core and two PEO4 chains at both ends, Suzuki coupling was adopted instead of Kumada coupling since the latter one usually generated homo-coupled products. Moreover, Suzuki coupling possesses the following advantages: 1) mild reaction conditions; 2) commercial availability of many boronic acid; and 3) starting materials tolerate a wide variety of functional groups and they are unaffected by water. The mechanism of Suzuki coupling is analogous to the catalytic cycle for the other cross-coupling reactions with four distinct steps: oxidative addition, anion exchange, transmetallation and reductive elimination.

To further investigate the self-assembly behaviors of 6T/PEO4, the same GIWAXS measurements were conducted on spin-coated thin film samples on silicon substrate in the presence and absence of LiTFSI at room temperature, as shown in **Figure 3.4(a)** and (b). The two samples exhibit qualitatively similar patterns with narrow and well-defined diffraction peaks ($00h$) in the out-of-plane direction, representing a smectic morphology with layer distance of 3.50 nm, as well as multiple elongated peaks at larger q_z (1.5-2.0 Å) denoted as A, B, and C, representing different π - π stacking interactions between adjacent oligothiophene units based on our experience with 4T/PEO4 in Chapter One. Such similarity between pristine and blended 6T/PEO4 indicates that the 0.05 molar fraction between Li^+ ion and ethylene oxide units is a safe blending ratio which doesn't overly disrupt the smectic morphology. Compared to 4T/PEO4, 6T/PEO4 exhibits a larger layer distance (~ 3.52 nm) due to longer molecular structures. The value can be calculated from the vertical linecut shown in **Figure 3.4(c)** where the diffraction peaks of 6T/PEO4 exhibit at relatively

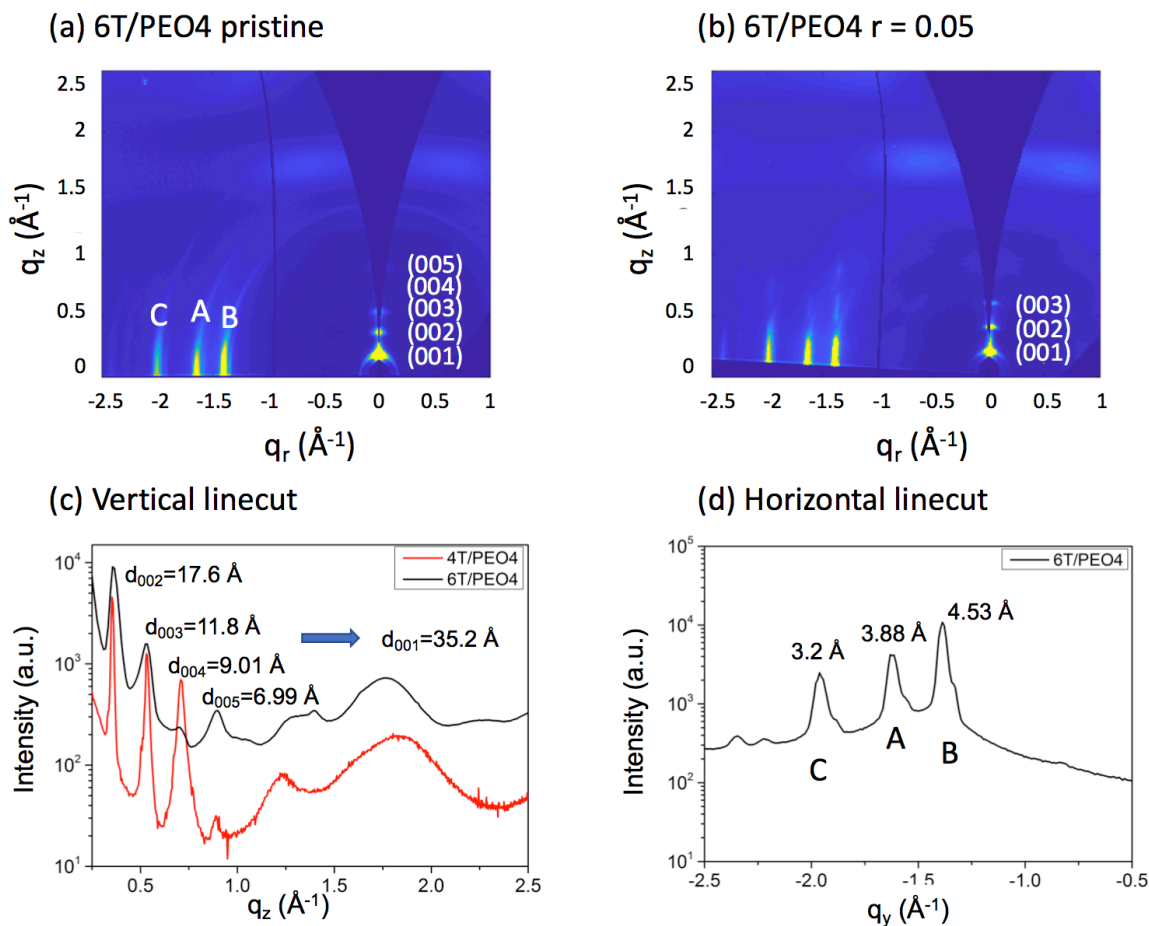


Figure 3.4 GIWAXS patterns of 6T/PEO4-LiTFSI complex thin film at room temperature (a) $r = 0$, (b) $r = 0.05$. (c) Vertical linecuts of pristine 6T/PEO4 thin film. (d) Horizontal linecuts of pristine 6T/PEO4 thin film.

smaller q_z compared to those of 4T/PEO4, representing larger layer spacing. However, the smectic peaks of 6T/PEO4 seem broader, suggesting a more “disordered” structure. Upon blended with LiTFSI, a slight decrease in the layer distance instead of increase was observed from 3.52 nm to 3.43 nm, opposite to the PEO domain swelling that was observed for 4T/PEO4. Moreover, all the π -stacking peaks for 6T/PEO4 lie in the plane of the layer with q_z equal 0, suggesting untilted molecules in the phase, which is in contrast to NNN-tilted phase observed in 4T/PEO4.^[24] Shown

in **Figure 3.4(d)** is the horizontal linecut representing the in-plane π - π interaction where the peak of 6T/PEO4 exhibits at a larger q_r than that of 4T/PEO4, indicating shorter π -stacking distance between adjacent sexithiophene units as a result of larger conjugated system, which in return could have increased the LC density on silicon wafer and led to untilted molecule orientation even though the peaks are also broader. The π -stacking distances for peak A, B, and C are calculated as 3.88 Å, 4.53Å, and 3.2Å, respectively. Peak C is believed to be higher order of peak B as $\frac{4.53 \text{ Å}}{3.2 \text{ Å}} = 1.415 = \sqrt{2}$.

The ionic conductivity of 6T/PEO4-LiTFSI ($r = 0.05$) thin film as a function of temperature is measured by EIS using the same method mentioned before. In-plane conductivity parallel to the surface is measured as a result of the homeotropic alignment of 6T/PEO4-LiTFSI complex. The phase transition of 6T/PEO4 occurring in the vicinity of 180 °C characterized by DSC renders the material more tolerable with high temperature, and stable smectic morphology is maintained within the testing temperature range from 20-140 °C. A homogeneous increase in conductivity is observed during heating, consistent with thermally activated ionic transport behavior of electrolyte, and maximum conductivity $\approx 1.0 \times 10^{-3}$ S/cm is reached at high temperature 140°C, higher than that of 4T/PEO4 as shown in **Figure 3.5(a)**. In **Figure 3.5(b)**, the measured ionic conductivity is normalized by the volume fraction of PEO in the temperature range from 20-70 °C before phase transition of 4T/PEO4 takes place. To our surprise, the corrected ionic conductivity of 6T/PEO4 is about 2.5 times lower than that of 4T/PEO4. 6T/PEO4 possessing the same PEO segments and even denser packing leaves the most plausible explanation to interfacial chemistry. The broadening of the smectic peaks of 6T/PEO4 (shown in **Figure 3.4(c)**) could be considered as evidence of interfacial mixing between the oligothiophene and PEO domains, which impairs an effective ion conduction pathway.

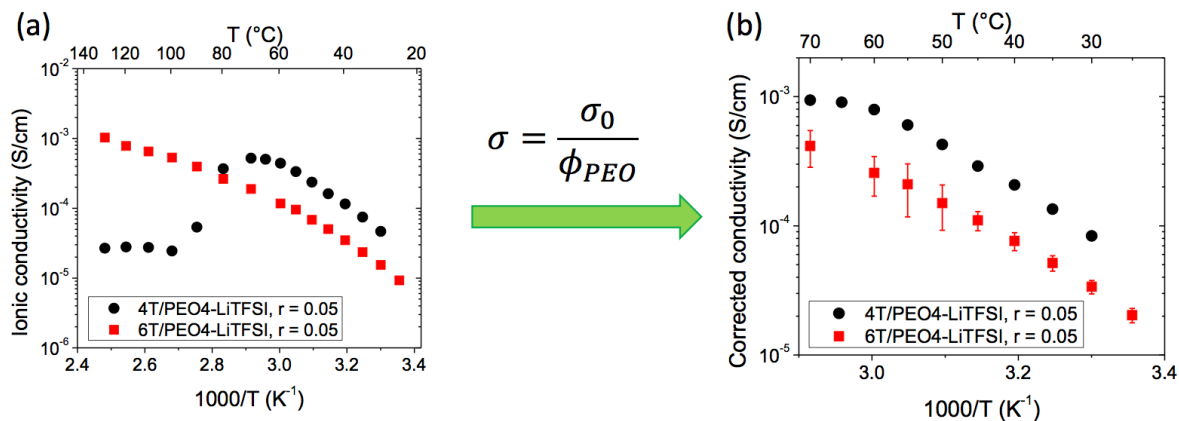
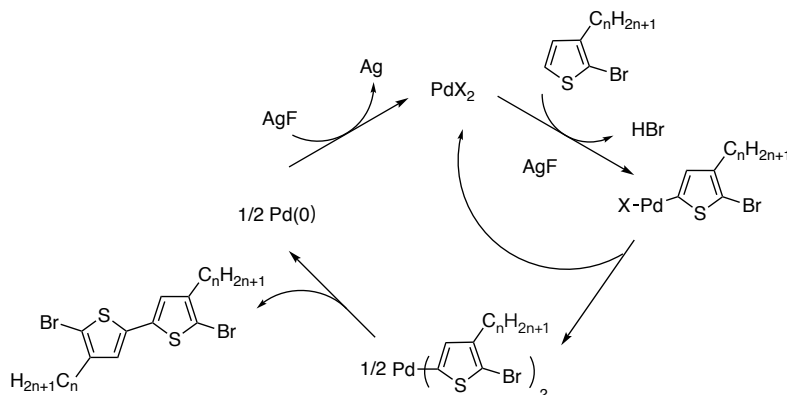


Figure 3.5 (a) Ionic conductivity of 6T/PEO4 and 4T/PEO4 with LiTFSI blending ratio $r = 0.05$ as a function of temperature during heating process. (b) normalized ionic conductivity of 6T/PEO4 and 4T/PEO4 within temperature range from 20-70 °C.

Another possible reason involves the structure-activation energy relationship. The ionic conductivity due to movement of Li⁺ ions inside the channels depends on lattice parameter. While it has been observed that ionic conductivity is higher for materials with longer lattice parameters, other factors such as size of the cavities in which Li⁺ resides, and the strength of the Li-lattice oxygen bonds, also play an important role in ionic conductivity. Despite the lack of computational support, the relationship between structure and the activation energy involved in the motion of Li⁺ ions along the conduction channels of 4T/PEO4 and 6T/PEO4 can be extrapolated from its inorganic counterpart, the NASICON materials.^[32] It has been demonstrated that in such inorganic materials the activation energy decreases with increasing lattice parameter until it becomes constant. Comparing 4T/PEO4 and 6T/PEO4, the relatively lower activation energy of 6T/PEO4 resulted from larger layer spacing of longer oligothiophene component, could provide less power

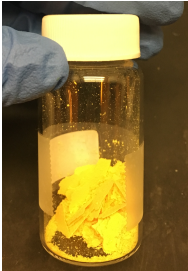
for Li⁺ ions to move along the conduction channel, leading to lower ionic conductivity. MD simulation results, however, are still in need for further investigation.

3.3.4 Synthesis and thermal properties of X-shaped bolaamphiphiles 4T/alkyl/PEO4



Scheme 3.4 Mechanism of homocoupling for synthesis of bithiophene core.

Table 3.1 3,3'-dialkyl(C_nH_{2n+1})-5,5'-dibromo-2,2'-bithiophene

n = 1	n = 6	n = 10	n = 12	n = 14
Yield 54%	Yield 51%	Yield 48%	Yield 38%	Yield 42%
				

The synthetic procedures of 4T/alkyl/PEO4, which are a ternary system consisting of a quaterthiophene unit terminated with PEO4 chains at both ends and laterally substituted with two linear alkyl segments with varying lengths remain similar to that of linear 4T/PEO4. The terminal PEO4 segments are attached to the terminal thiophene ring via etherification whereas the

bithiophene core with two alkyl lateral chains on both sides were synthesized independently via a catalytic C-H homocoupling reaction of 2-bromo-3-alkylthiophene at 5-position^[25,26] as shown in **Scheme 3.4**. AgF serves as an effective promotor in forming the intermediate through a specific interaction with the palladium catalyst as well as an oxidizing agent of the formed Pd(0) species also to regenerate the Pd(II) catalyst. A series of bithiophene cores with varying alkyl chain lengths have been synthesized as listed below in **Table 3.1**, most of them are yellow powders except 3,3'-dihexyl-5,5'-dibromo-2,2'-bithiophene which is yellow liquid. Note that most of the lateral alkyl chains possess even numbers from 6 -14 except for a methyl group, because of the odd-even effect discovered by Kato^[27] that in liquid crystals based on spacers with an even number of carbon atoms show liquid crystallinity over wider temperature ranges and higher ion conductivities as compared to liquid crystals based on spacers with an odd number of carbon atoms.

The thermal properties of 4T bolaamphiphile series were characterized by DSC as shown in **Figure 3.6(a)**. No evident phase transition was observed from 4T/methyl/PEO4 to 4T/decyl/PEO4. Compared to the glycerol end-groups which are used in most bolaamphiphile structures to provide strong hydrogen-bonding (15-60 kcal/mol^[28]) for assembly of π -conjugated rods into polygonal honeycombs, the PEO segments used in our experiments, even though still quite hydrophilic, could only provide van der Waals force (0.4-4.0 kJ/mol \approx 1.7-17 kcal/mol, 1 kcal=4.184 kJ), one order of magnitude smaller than H-bonding. As a result, the intermolecular force is not strong enough for the interconnection of the π -conjugated rods. Moreover, the addition of lateral alkyl chains further disrupted the π - π stacking and prevented the formation of self-assembly. As a consequence, the expected cylindrical structures for this ternary system is not achieved. However, as we further increase the lateral chain length to 12 and 14 carbons, endothermic and exothermic peaks were observed during the second heating and first cooling scans, respectively, at low temperature below

0 °C. This feature is probably because the lateral chains are long and flexible enough to segregate into its own subspace to fill in the gap between the quaterthiophene and PEO domains. However, since all the compounds exhibit liquid state at room temperature, no featured POM images were obtained. The UV-vis spectra of 4T/alkyl/PEO4 series compared with 4T/PEO4 in THF solution are shown in **Figure 3.6(b)**. Since PEO chains and alkyl segments are not UV-active within 200-700 nm wavelength range, the absorption peaks observed around 400 nm are attributed to the oligothiophene units. Compared to linear 4T/PEO4 with λ_{max} at 401.5 nm, the λ_{max} of 4T/alkyl/PEO4 bolaamphiphiles blue-shifted to 390.4 nm for 4T/methyl/PEO4 with shorter lateral chains and 385.0 nm for the other structures with relatively longer lateral chains, indicating that the well-ordered packing of quaterthiophene units was disrupted by addition of lateral chains.

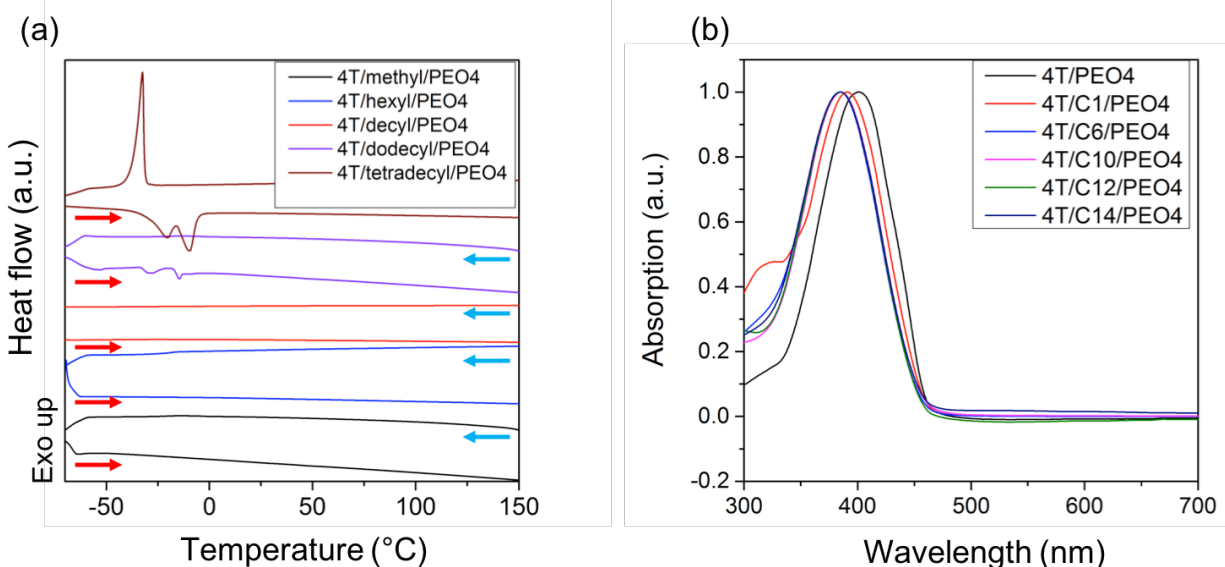


Figure 3.6 (a) DSC traces (10 K min⁻¹) of 4T bolamphiphiles in bulk phase. (b) UV-Vis spectra of 4T bolamphiphiles together with 4T/PEO4 in THF solution (20 μM).

3.4 Conclusions

In summary, the knowledge and experience obtained from 4T/PEO4 has been successfully applied to other LC materials in order to further investigate the structure-property relationship. The volume ratio between oligothiophene and PEO moieties are varied for optimization of structural design in which MD simulations has played an important role. For the PEO chain length in structure 4T/PEOn, the smectic morphology of 4T/PEOn observed by simulation is primarily driven by the crystal structure of thiophene packing, while the PEO segments at the end serve largely as space fillers between the ordered thiophene cores. This results in a nano-segregated two-domain structure where the oligothiophene domain is highly ordered and (nearly) crystalline while the PEO domain is less ordered and remains liquid-like. As the length of the capping PEO segments increases, their associated increase in configurational entropy drives a tendency toward “liquidity” or disorder that eventually becomes comparable to the energetic attractive forces which keep the ordered packing of the thiophene rings. This increased mobility of the PEO “jiggles” the thiophene rings towards states of higher translational entropy and thus to the destabilization of their ordered packing. Because the ordered morphology is primarily governed by thiophene packing, to a first approximation the conformational behavior of the capping chains can be computationally studied independently (as grafted chains in a bilayer) to efficiently identify trends with chain length, temperature or other parameters. Experimental results on the thermal and structural properties and self-assembly behaviors of 4T/PEO5 sample have provided a great match to the simulation prediction.

In the case of 6T/PEO4, the effect of larger conjugated segments on LC structure and conducting characteristics was also studied. Despite of similar molecular structure and self-assembly behavior, 6T/PEO4 exhibit relatively lower ionic conductivity compared to 4T/PEO4. Simulation is needed for future study about the interfacial chemistry between the ionic and electronic conducting

domains as well as activation energy. Finally, the study of LC structure-property relationship was further expanded to X-shaped bolaamphiphiles with introduction of alkyl lateral chains attached to oligothiophene core, which renders more flexibility and solubility to the compounds while impairs the π -stacking interaction between adjacent thiophene units, leading to the disappearance of LC characteristics. However, evident phase transition peaks were detected by DSC when the alkyl chains are long enough with the number of carbon atoms larger than 12, in good agreement with the structural evolution of bolaamphiphiles based on the volume ratio between different components. We assume that the incorporation of alkyl lateral chains could render the LC morphology from smectic phase to columnar phase, while more details needs to be provided by simulation and X-ray diffraction. Moreover, it has been demonstrated that (semi)perfluorinated lateral chains have distinct effects to influence the self-organization of bolaamphiphilic structures^[29–31] with the following advantages: first the perfluorinated segments are incompatible with hydrogenated molecular parts and also with polar segments, the effect of which increases segregation and stabilizes mesophases. Second, perfluorinated chains have significantly larger volume than alkyl chains. Finally, such chains have preferred conformation (helical), different from those adopted by alkyl chains. This also gives us ideas about how to further improve LC structure design and come up with better functional materials.

REFERENCES

- [1] M. Ashizawa, T. Niimura, Y. Yu, K. Tsuboi, H. Matsumoto, R. Yamada, S. Kawauchi, A. Tanioka, T. Mori, *Tetrahedron* **2012**, *68*, 2790.
- [2] A. Tsumura, H. Koezuka, T. Ando, *Synthetic Metals* **1988**, *25*, 11.
- [3] A. Assadi, C. Svensson, M. Willander, O. Inganäs, *Appl. Phys. Lett.* **1988**, *53*, 195.
- [4] X. Cheng, X. Dong, R. Huang, X. Zeng, G. Ungar, M. Prehm, C. Tschierske, *Chemistry of Materials* **2008**, *20*, 4729.
- [5] X. Cheng, X. Dong, G. Wei, M. Prehm, C. Tschierske, *Angewandte Chemie International Edition* **2009**, *48*, 8014.
- [6] H. Gao, Y. Ye, L. Kong, X. Cheng, M. Prehm, H. Ebert, C. Tschierske, *Soft Matter* **2012**, *8*, 10921.
- [7] M. Prehm, G. Götz, P. Bäuerle, F. Liu, X. Zeng, G. Ungar, C. Tschierske, *Angewandte Chemie* **2007**, *119*, 8002.
- [8] G. Ungar, C. Tschierske, V. Abetz, R. Holyst, M. A. Bates, F. Liu, M. Prehm, R. Kieffer, X. Zeng, M. Walker, B. Glettner, A. Zywockinski, *Advanced Functional Materials* **2011**, *21*, 1296.
- [9] M. Prehm, F. Liu, U. Baumeister, X. Zeng, G. Ungar, C. Tschierske, *Angewandte Chemie International Edition* **2007**, *46*, 7972.
- [10] B. Glettner, F. Liu, X. Zeng, M. Prehm, U. Baumeister, G. Ungar, C. Tschierske, *Angewandte Chemie International Edition* **2008**, *47*, 6080.
- [11] X. Cheng, M. K. Das, U. Baumeister, S. Diele, C. Tschierske, *Journal of the American Chemical Society* **2004**, *126*, 12930.
- [12] X. Cheng, H. Gao, X. Tan, X. Yang, M. Prehm, H. Ebert, C. Tschierske, *Chemical Science* **2013**, *4*, 3317.
- [13] W. Bu, H. Gao, X. Tan, X. Dong, X. Cheng, M. Prehm, C. Tschierske, *Chem. Commun.* **2013**, *49*, 1756.
- [14] X. Cheng, M. Prehm, M. K. Das, J. Kain, U. Baumeister, S. Diele, D. Leine, A. Blume, C. Tschierske, *Journal of the American Chemical Society* **2003**, *125*, 10977.
- [15] K. Sasaki, Y. Shibata, M. Lu, Y. Yoshida, R. Azumi, Y. Ueda, *Advances in Materials Physics and Chemistry* **2013**, *03*, 185.
- [16] Y. Sun, P. Padmanabhan, M. Misra, F. A. Escobedo, *Soft Matter* **2017**, *13*, 8542.
- [17] L. Zhang, N. S. Colella, B. P. Cherniawski, S. C. B. Mannsfeld, A. L. Briseno, *ACS Applied Materials & Interfaces* **2014**, *6*, 5327.
- [18] T. P. Kaloni, P. K. Giesbrecht, G. Schreckenbach, M. S. Freund, *Chemistry of Materials* **2017**, *29*, 10248.
- [19] F. A. Lindemann, *Phys. Z.* **1910**, *11*, 609.
- [20] M. G. Mohamed, C.-C. Cheng, Y.-C. Lin, C.-W. Huang, F.-H. Lu, F.-C. Chang, S.-W. Kuo, *RSC Adv.* **2014**, *4*, 21830.
- [21] J. Li, X. Li, D. Ni, J. Wang, G. Tu, J. Zhu, *J. Appl. Polym. Sci.* **2014**, *131*, 41186.
- [22] B. X. Dong, Z. Liu, M. Misra, J. Strzalka, J. Niklas, O. G. Poluektov, F. A. Escobedo, C. K. Ober, P. F. Nealey, S. N. Patel, *ACS Nano* **2019**, *13*, 7665.
- [23] Z. Liu, B. X. Dong, M. Misra, Y. Sun, J. Strzalka, S. N. Patel, F. A. Escobedo, P. F. Nealey, C. K. Ober, *Advanced Functional Materials* **2018**, *1805220*, 1.
- [24] V. M. Kaganer, H. Möhwald, P. Dutta, *Rev. Mod. Phys.* **1999**, *71*, 779.

- [25] K. Masui, H. Ikegami, A. Mori, *Journal of the American Chemical Society* **2004**, *126*, 5074.
- [26] M. Takahashi, K. Masui, H. Sekiguchi, N. Kobayashi, A. Mori, M. Funahashi, N. Tamaoki, *Journal of the American Chemical Society* **2006**, *128*, 10930.
- [27] Y. Mizumura, D. Högberg, K. Arai, J. Sakuda, B. Soberats, M. Yoshio, T. Kato, *BCSJ* **2019**, *92*, 1226.
- [28] S. J. Grabowski, *J. Phys. Org. Chem.* **2004**, *17*, 18.
- [29] X. H. Cheng, S. Diele, C. Tschierske, *Angew. Chem. Int. Ed.*, **2000**, *39*, 592.
- [30] V. Percec, G. Johansson, G. Ungar, J. Zhou, *J. Am. Chem. Soc.* **1996**, *118*, 9855.
- [31] X. Cheng, M. K. Das, S. Diele, C. Tschierske, *Langmuir* **2002**, *18*, 6521.
- [32] A. Martinez-Juarez, C. Pecharroman, J. Iglesias, J. Rogo, *J. Phys. Chem B* **1998**, *102*, 372.
- [33] M. Misra, Z. Liu, B. X. Dong, S. N. Patel, P. F. Nealey, C. K. Ober, F. A. Escobedo, *ACS Macro Lett.* **2020**, *9*, 295.

Chapter Four: Study of self-assembly behavior and ionic conductivity of T-shaped facial amphiphilic liquid crystals³

4.1 Introduction

Liquid crystals are ordered fluids in which the simultaneous phase-segregation of incompatible components results in positional and orientational long-range order. Facial amphiphiles are a specific group of liquid crystals, which consist in our study of three distinct and incompatible units: a rod-like mesogenic core, alkyl chains attached to both termini of the core and a polar segment in the lateral position. A variety of nanostructures including smectic phases, polygonal cylinder phases and lamellar phases are therefore generated depending on the volume fraction of each component.^[1] Compared to the conventional linear binary amphiphiles in our previous work,^[2] the complexity of the self-organized structures as well as the phase diversity of the ternary amphiphiles are significantly enhanced. When one further considers that the anisometric shape and amphiphilic structures are perpendicular to each other,^[3] this opens new opportunities for their use as sophisticated functional materials. A series of facial amphiphile molecules has been synthesized and studied by Tschierske et al.^[4-8] in which phenylene groups (terminated by lipophilic alkyl chains) were used as a rod-like, conjugated core while a polar unit was laterally attached to it. To the best of our knowledge, no researcher has ever investigated their conductivity properties and instead only focused on structural evolution.

Liquid crystals which have already been of tremendous interest for industrial applications,^[9,10] have recently become promising candidates in the field of energy storage and generation for efficient transport of ions and electrons,^[11] such as lithium-ion batteries, dye-sensitized solar cells,

³ A manuscript of this work is being prepared for submission to *Advanced Science* with authorship: Z. Liu, Y. Sun, B. X. Dong, S. N. Patel, P. F. Nealey, F. A. Escobedo, C. K. Ober. Ziwei Liu synthesized all the 5T facial amphiphile molecules and characterized their thermal and optical property. Yangyang Sun performed all the simulation work. Ban Dong did GIWAXS and ionic conductivity measurement.

field-effect transistors, and electroluminescent devices, with a majority of them possessing linear structures. To this end, we combined the unique structure and self-assembly of T-shaped facial amphiphiles with ionic/electronic conductivity by using oligothiophene as a mesogenic core with potential electronic conductivity and PEO lateral chains for ion conduction. A simulation-guided experimental study of the self-assembly behavior and ionic conductivity was conducted on a series of T-shaped amphiphilic LC molecules consisting of a pentathiophene as rigid core, terminated by two linear alkyl chains, and a PEO chain attached to the lateral position of the rigid core. The length of PEO chains is varied according to simulation guidance to manipulate the self-assembly of the LC molecule from a smectic phase, in which the shorter PEO chains assemble into small clusters and form layer structures together with thiophene units, to columnar phase, in which the longer PEO chains percolate through the thiophene units and alkyl units forming larger domains. The thermotropic liquid crystalline behavior of these compounds was investigated by polarized optical microscopy (POM), differential scanning calorimetry (DSC), and wide-angle X-ray scattering (WAXS/GIWAXS). The ionic conductivity increased by more than 5 orders of magnitude with increasing PEO chain length at LiTFSI blending ratio $r = 0.05$ while the electronic conductivity was disrupted by the PEO clusters. Manuscript of this work in preparation for submission to *Advanced Science* co-authored with Yangyang Sun and Ban Dong. Ziwei Liu synthesized all the 5T facial amphiphile molecules and characterized their thermal and optical property. Yangyang Sun performed all the simulation work. Ban Dong did GIWAXS and ionic conductivity measurement.

4.2 Experimental Section

4.2.1 Materials

N-bromosuccinimide (NBS), 2-hexylthiophene, 3-thiopheneethanol, 2-thiopheneboronic acid pinacol ester were purchased from AK Scientific, Inc. 2-isopropoxy-4,4,5,5-tetramethyl-1,3,2-dioxaborolane, n-butyllithium solution (1.6 M in hexane), poly(ethylene glycol) methyl ether (MW ~ 550), 1-bromodecane, tetrakis(triphenylphosphine)palladium(0) (Pd(PPh₃)₄) were purchased from Sigma-Aldrich. Potassium carbonate (K₂CO₃) and organic solvent such as hexane, ethyl acetate (EtOAc), tetrahydrofuran (THF), and methanol (MeOH) were purchased from Fisher. 1,2-dimethoxyethane (DME) was purchased from Honeywell. All reagents and solvents were used as received unless otherwise noted. Anhydrous THF was freshly distilled from sodium and benzophenone prior to use. NBS was recrystallized in water and stored in refrigerator before use.

4.2.2 Characterization methods

4.2.2.1 Nuclear magnetic resonance (NMR)

¹H and ¹³C NMR spectra were recorded on a Varian INOVA 400 and a MERCURY 300 spectrometer, respectively. Chemical shifts were quoted relative to the residual protons of the deuterated solvents CDCl₃ ($\delta = 7.26$ for ¹H and $\delta = 77.36$ for ¹³C). The multiplicity was characterized by the following abbreviations: s-singlet, d-doublet, t-triplet, q-quartet, m-multiplet.

4.2.2.2 Differential Scanning Calorimetry (DSC)

DSC measurements were performed on a Q 2000 from TA Instruments at a scanning rate of 10 °C min⁻¹ within temperature range from -90 to 200 °C. The phase transition temperatures were determined as the peak positions in the DSC traces due to broadness of the transition peaks.

4.2.2.3 Polarized Optical Microscope (POM)

An Olympus BX51 polarizing optical microscope equipped with a Mettler FP 82 HT hot stage was used for visual observation of optical textures at different temperatures.

4.2.2.4 Wide-Angle X-Ray Scattering (WAXS)

WAXS patterns were obtained using Rigaku SmartLab X-ray diffractometer with Cu K α radiation $\lambda = 1.54 \text{ \AA}$ with thin film samples spin-coated on silicon wafer at different temperatures.

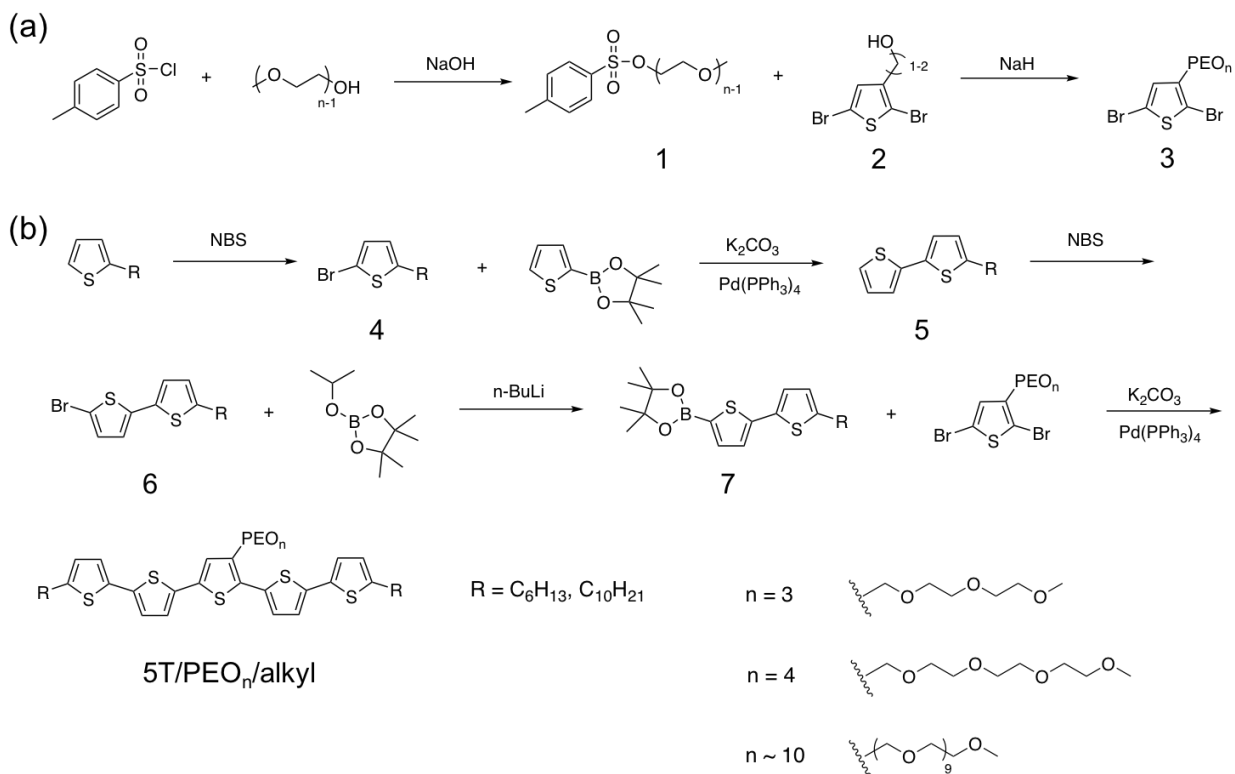
4.2.2.5 Grazing-Incidence Wide-Angle X-Ray Scattering (GIWAXS)

Temperature- dependent GIWAXS measurements were performed at beamline 8-ID-E of the Advanced Photon Source, Argonne National Laboratory with 10.86 keV ($\lambda = 1.1416 \text{ \AA}$) synchrotron radiation. The temperature of the samples was varied from room temperature up to 130 °C using a Linkam HFSX350-GI stage. Samples were measured inside a low vacuum chamber (10^{-3} mbar) to minimize concerns about radiation damages, samples' moisture uptake, and extraneous scattering from ambient air. The measurement time was chosen to be 3 s frame $^{-1}$. For each sample, three data sets were taken from three adjacent spots on the sample and then summed in order to enhance the signal-to-noise ratio. The samples were tilted at an angle of incidence of 0.14° with respect to the incoming beam, which is above the estimated critical angle of sample ($\approx 0.13^\circ$) but below the critical angle of the Si substrates ($\approx 0.17^\circ$) in order to probe the whole film thickness. The scattering signal was recorded with a Pilatus 1MF pixel array detector (pixel size = 172 μm) positioned 228 mm from the sample. Each data set was stored as a 981 \times 1043 32-bit tiff image with 20-bit dynamic range. The Pilatus detector has rows of inactive pixels at the border between detector modules. In order to fill these gaps, after each measurement the detector was moved to a new vertical direction and the measurement on each spot was repeated, then the gaps were filled by combining the data from two detector positions. The signals were reshaped and

output as intensity maps in q_z versus q_r ($=\sqrt{q_x^2 + q_y^2}$) space. We also performed detector nonuniformity, detection efficiency, the polarization effect, and solid-angle variation for each image. All the GIWAXS data processing and extraction were executed using the GIXSGUI package for MATLAB.

Peak shape analysis was performed on wedge cuts taken with an angular breadth of 2° . Each wedge cut was first fit to an empirical baseline function to enable the subtraction of the background intensity and amorphous scattering. The background-subtracted wedge cut was then fit to a Voigt function to extract the peak position and the FWHM of the reflections of interest. More details of peak shape analysis can be found elsewhere.

4.2.3 Synthetic procedures of T-shaped facial amphiphilic LCs (5T/PEO_n/alkyl)



Scheme 4.1 Synthesis of (a) 2,5-dibromo-3-PEO_n-thiophene, (b) 5T/PEO_n/alkyl facial amphiphiles.

Synthesis of PEO_{n-1}-tosylate (**1**)

PEO₃-tosylate (n=4) was synthesized according to our previous work. The synthetic procedure of PEO₉-tosylate (n=10) is described here: To a 500mL round bottom flask with a magnetic bar was added poly(ethylene glycol) methyl ether (MW ~ 550, 20 mmol, 1.0 eq) dissolved in 30 mL THF. Sodium hydroxide (70 mmol, 3.5 eq) was dissolved in 20 mL H₂O and then added slowly to the flask. After the reaction mixture was cooled down to 0 °C in an ice bath, p-toluenesulfonyl chloride (24 mmol, 1.2 eq) dissolved in another 30 mL THF was added dropwise to the mixture under vigorous stirring. The reaction mixture was stirred at 0 °C for 2 h, and then at room temperature for 12 h. After completion of the reaction as indicated by TLC, the reaction mixture was poured to 5 wt% hydrochloric acid aqueous solution, and the product was extracted with dichloromethane (30 mL × 3). The organic layer was then washed successively with saturated sodium bicarbonate solution (50 mL × 3) and water (50 mL × 3) and dried over anhydrous magnesium sulfate. After solvent evaporation the product was obtained as a slight yellow liquid without further purification in yield 50%.

¹H NMR (300 MHz, CDCl₃, δ): 7.80 (d, J=9Hz, 2H; Ar H), 7.35 (d, J=9Hz, 2H; Ar H), 4.14 (t, J=4.83Hz, 2H; CH₂), 3.63 (m, 52H, (CH₂)_n), 3.55 (m, 2H; CH₂), 3.37 (s, 3H; CH₃), 2.44 (s, 3H; CH₃).

Synthesis of 2,5-dibromo-3-thiophenemethanol/ 2,5-dibromo-3-thiopheneethanol (**2**)

2-thiophenemethanol (or 2-thiopheneethanol) (20 mmol, 1.0 eq) was dissolved in 100 mL THF and cooled down to 0 °C in an ice bath. NBS (50 mmol, 2.5 eq) was added to the solution portionwise. The reaction was stirred at 0 °C for 1h, and then at room temperature for 5h before quenched with 10wt% sodium hydroxide aqueous solution. The crude product was extracted with

ethyl acetate (30 mL × 3) and the combined organic layer washed with water (50 mL × 3), then dried over magnesium sulfate. The solvent was evaporated, and the product was purified by column chromatography on silica gel with hexane: EtOAc =5:1 (v/v) as eluent to give **2** as dark red liquid.

2,5-dibromo-3-thiopheneethanol (yield 83.7%), ¹H NMR (400 MHz, CDCl₃, δ): 6.87 (s, 1H; Th H), 3.82 (t, J=8.60Hz, 2H; CH₂), 2.80 (t, J=8.62Hz, 2H; CH₂).

2,5-dibromo-3-thiophenemethanol (yield 82.3%), ¹H NMR (400 MHz, CDCl₃, δ): 7.02 (s, 1H; Th H), 4.55 (d, J=6.04Hz, 2H; CH₂).

Synthesis of Synthesis of 2,5-dibromo-3-PEO_n-thiophene (**3**)

To a dry round bottom flask was added sodium hydride (60 wt% in mineral oil, 20 mmol, 2.0 eq), and 30 mL anhydrous THF. The reaction mixture was stirred under Argon atmosphere at room temperature for 30 min. **2** (10 mmol, 1.0 eq) was then added dropwise via a syringe and the mixture was stirred vigorously at room temperature for 1h. **1** (12 mmol, 1.2 eq) was added to the reaction mixture slowly and stirred at room temperature overnight. After completion of the reaction as indicated by TLC, the reaction mixture was quenched with 60 mL H₂O and vigorously stirred for 30 min. The crude product was extracted with ethyl acetate (30 mL × 3) and then washed with water (50 mL × 3). The solvent was evaporated after dried over magnesium sulfate, and the crude product was purified by column chromatography on silica gel with hexane: EtOAc =1:1 (v/v) as eluent to give **3** as a yellow liquid.

n=4, (2,5-dibromo-3-PEO₄-thiophene, yield 65%), ¹H NMR (400 MHz, CDCl₃, δ): 7.01 (s, 1H; Th H), 3.68 (m, 12H; CH₂), 3.58 (m, 2H; CH₂), 3.39 (s, 3H; CH₃).

n~10, (2,5-dibromo-3-PEO10-thiophene, yield 35%), ¹H NMR (300 MHz, CDCl₃, δ): 6.98 (s, 1H; Th H), 3.63 (m, 56H; (CH₂)_n), 3.54 (m, 2H; CH₂), 3.37 (s, 3H; CH₃).

Synthesis of 2-decylthiophene

To a dry flask was charged thiophene (40 mmol, 1.0 eq) dissolved in 30 mL anhydrous THF under Argon atmosphere. The flask was cooled to -78 °C in a dry ice/acetone bath and n-butyllithium solution (38 mmol, 0.95 eq) was added dropwise via a syringe under vigorous stirring. The reaction mixture was stirred at -78 °C for 30 min before warming up to room temperature. 1-bromodecane was added to the flask in one shot and the reaction was refluxed at 50 °C overnight. The reaction was quenched with water and the crude product was extracted with ethyl acetate (30 mL × 3), washed with pure water (50 mL × 3), dried over magnesium sulfate and concentrated by rotavap. Pure product was collected via vacuum distillation (9 Torr, 180 °C) as colorless liquid in 60 % yield.

¹H NMR (400 MHz, CDCl₃, δ): 7.11 (d, J=4Hz, 1H; Th H), 6.92 (m, 1H; Th H), 6.78 (d, J=4Hz, 1H; Th H), 2.82 (t, J=7.68Hz, 2H; CH₂), 1.67 (quintet, 7.51, 2H; CH₂), 1.26 (m, 14H; (CH₂)₇), 0.88 (t, J=6.96Hz, 3H; CH₃).

¹³C NMR (300 MHz, CDCl₃, δ): 146.24, 126.96, 124.21, 123.03, 32.25, 30.27, 29.95, 19.72, 29.49, 29.13, 28.53, 23.04, 14.48.

Synthesis of 2-bromo-5-alkylthiophene (4)

2-alkylthiophene (40 mmol, 1.0 eq) was dissolved in 100 mL THF and cooled down to 0 °C in an ice bath. NBS (40 mmol, 1.0 eq) was added to the solution portionwise. The reaction was stirred at 0°C for 1h, and then at room temperature for 5h before quenched by 10 wt% sodium hydroxide

solution. The mixture was extracted with ethyl acetate (30 mL × 3), the collected organic layer was washed with water (50 mL × 3), then dried over magnesium sulfate. After the solvent was evaporated via rotavap, and the crude product was purified by column chromatography on with pure hexane as eluent to give **4** as colorless liquid.

2-bromo-5-hexylthiophene, yield 90%, ¹H NMR (400 MHz, CDCl₃, δ): 6.84 (d, J=4Hz, 1H; Th H), 6.53 (d, J=4Hz, 1H; Th H), 2.73 (t, J=7.75Hz, 2H; Th-CH₂), 1.62 (quintet, J=7.37Hz, 2H; Th-CH₂-CH₂), 1.30 (m, 6H; (CH₂)₃), 0.89 (t, J=6.84, 3H; CH₃).

2-bromo-5-decylthiophene, yield 78.6%, ¹H NMR (400 MHz, CDCl₃, δ): 6.84 (d, 1H, J=4 Hz; Th H), 6.53 (d, 1H, J=4 Hz; Th H), 2.73 (t, 2H, J=4 Hz; Th-CH₂), 1.62 (quint, 2H, J=4 Hz; Th-CH₂-CH₂), 1.26 (m, 14H; CH₂), 0.89 (t, 3H, J=8 Hz; CH₃).

¹³C NMR (300 MHz, CDCl₃, δ): 147.99, 129.69, 124.66, 108.86, 32.25, 31.81, 30.68, 29.93, 29.88, 29.67, 29.32, 23.04, 14.49.

Synthesis of 5-alkyl-2,2'-bithiophene (**5**)

To a 3-neck round bottom flask with a condenser were added **4** (35 mmol, 1.0 eq), 2-thiopheneboronic acid pinacol ester (42 mmol, 1.2 eq) and K₂CO₃ (105 mmol, 3.0 eq) under Argon atmosphere. Pd(PPh₃)₄ (0.35 mmol, 0.01 eq) was added and the flask was purged Argon for 30 min. DME/H₂O mixed solvent (120 mL:30 mL, v/v) was bubbled with Argon for 40 min then transferred to the 3-neck flask via canula. The reaction mixture was refluxed at 80 °C overnight. The reaction was quenched by opening to air. The crude product was extracted with ethyl acetate (40 mL × 3), then the combined organic layer was washed with water (50 mL × 3) and dried over magnesium sulfate. The product was purified by column chromatography on silica gel with pure hexane as eluent to give **5** as a colorless liquid.

5-hexyl-2,2'-bithiophene, yield 82%, ¹H NMR (CDCl₃, 400 MHz, δ): 7.17 (dd, J₁=5.12 Hz, J₂=1.08 Hz, 1H; Th H), 7.10 (dd, J₁=3.52Hz, J₂=1Hz, 1H; Th H), 7.00-6.98 (m, 2H; Th H), 6.68 (d, J=3.56Hz, 1H; Th H), 2.79 (t, J=7.56Hz, 2H; Th-Th-CH₂), 1.68 (quintet, J=7.5 Hz, 2H; Th-Th-CH₂-CH₂), 1.38-1.21 (m, 6H; (CH₂)₃), 0.90 (t, J=6.90Hz, 3H; CH₃).

5-decyl-2,2'-bithiophene, yield 77%, ¹H NMR (CDCl₃, 400 MHz, δ): 7.17 (dd, J₁=4 Hz, J₂=1.08 Hz, 1H; Th H), 7.10 (dd, J₁=4 Hz, J₂=0.96 Hz, 1H; Th H), 7.00-6.98 (m, 2H; Th H), 6.68 (d, J=4 Hz, 1H; Th H), 2.78 (t, J=8 Hz, 2H; Th-CH₂), 1.68 (quint, J=8 Hz, 2H; Th-CH₂-CH₂), 1.26 (m, 14H; (CH₂)₇), 0.88 (t, 3H, J=8 Hz; CH₃).

¹³C NMR (300 MHz, CDCl₃, δ): 145.17, 135.05, 134.08, 128.00, 125.03, 124.03, 123.70, 123.30, 32.25, 31.96, 30.49, 29.95, 29.71, 29.43, 23.04, 14.49.

Synthesis of 5-bromo-5'-alkyl-2,2'-bithiophene (**6**)

5 (20 mmol, 1.0 eq) was dissolved in 100 mL THF and cooled down to 0 °C in an ice bath. NBS (21 mmol, 1.05 eq) was added to the solution portionwise. The reaction was stirred at 0°C for 1h, and then room temperature for 6h before quenched with 10 wt% sodium hydroxide aqueous solution. The crude product was extracted with EtOAc (30 mL × 3), and the combined organic layer was washed with water (50 mL × 3) and dried over MgSO₄. The solvent was evaporated, and the crude product was purified by column chromatography on silica gel with pure hexane as eluent to give **6** as a white solid.

5-bromo-5'-hexyl-2,2'-bithiophene, yield 74%, ¹H NMR (CDCl₃, 400 MHz, δ): 6.94 (d, J=4Hz, 1H; Th H), 6.92 (d, J=4Hz, 1H; Th H), 6.83 (d, J=4Hz, 1H; Th H), 6.67 (d, J=4Hz, 1H; Th H), 2.78 (t, J=8Hz, 2H; Th-Th-CH₂), 1.67 (quintet, J=7.46Hz, 2H; Th-Th-CH₂-CH₂), 1.39-1.30 (m, 6H; (CH₂)₃), 0.89 (t, J=8Hz, 3H; CH₃).

5-bromo-5'-decyl-2,2'-bithiophene, yield 80%, ¹H NMR (CDCl₃, 400 MHz, δ): 6.94 (d, J=4 Hz, 1H; Th H), 6.91 (d, J=3.52 Hz, 1H; Th H), 6.83 (d, J=4 Hz, 1H; Th H), 6.67 (quintet, J=4 Hz, 1H; Th H), 2.77 (t, J=8 Hz, 2H; Th-CH₂), 1.67 (quintet, J=7.44 Hz, 2H; Th-CH₂-CH₂), 1.26 (m, 14H; (CH₂)₇), 0.88 (t, J=8 Hz, 3H; CH₃).

¹³C NMR (300 MHz, CDCl₃, δ): 149.09, 146.30, 142.39, 139.80, 134.05, 130.80, 124.02, 123.34, 32.35, 31.93, 30.48, 29.94, 29.89, 29.67, 29.41, 23.04, 14.48.

Synthesis of 1-(5'-(4,4,5,5-tetramethyl-1,3,2-dioxaborolan-2-yl)-[2,2'-bithiophen]-5-yl)hexan-1-one (**7**)

To a round bottom flask were dissolved **6** (10 mmol, 1.0 eq) and 2-isopropoxy-4,4,5,5-tetramethyl-1,3,2-dioxaborolane (20 mmol, 2.0 eq) in anhydrous THF (50mL). The solution was purged Argon for 30min before cooling down to -78 °C in a dry ice/acetone bath. n-Butyllithium solution (12 mmol, 1.2 eq) was added dropwise via a syringe under vigorous stirring. The reaction mixture was stirred at -78 °C for 30 min then room temperature for overnight. 10% HCl was used to quench the reaction, and crude product was extracted with ethyl acetate (30 mL × 3), washed with pure water (50 mL × 3) and then dried over magnesium sulfate. Column chromatography was used to purify the product with hexane/ethyl acetate (20:1, v/v) as eluent to give **7** as a blue liquid.

5-(5'-(4,4,5,5-tetramethyl-1,3,2-dioxaborolan-2-yl)-5'-hexyl-2,2'-bithiophene (yield 52%),¹H NMR (CDCl₃, 400 MHz, δ): 7.50 (d, J=4Hz, 1H; Th H), 7.16 (d, J=4Hz, 1H; Th H), 7.04 (d, J=3.56Hz, 1H; Th H), 6.68 (d, J=4Hz, 1H; Th H), 2.78 (t, J= 7.76Hz, 2H; Th-CH₂), 1.67 (quintet, J=8Hz, 2H; Th-CH₂-CH₂), 1.34 (s, 12H; (CH₃)₄), 1.32-1.28 (m, 6H; (CH₂)₃), 0.88 (t, J=8Hz, 3H; CH₂-CH₃)

5-(5'-(4,4,5,5-tetramethyl-1,3,2-dioxaborolan-2-yl)-5'-decyl-2,2'-bithiophene (yield 45%), ¹H NMR (CDCl₃, 400 MHz, δ): 7.50 (d, J=3.6Hz, 1H; Th H), 7.16 (d, J=4Hz, 1H; Th H), 7.05 (d, J=3.56Hz, 1H; Th H), 6.68 (d, J=4Hz, 1H; Th H), 1.67 (quintet, J=8Hz, 2H; Th-CH₂-CH₂), 1.35 (s, 12H; (CH₃)₄), 1.26-1.24 (m, 14H; (CH₂)₇), 0.88 (t, J=8Hz, 3H; CH₂-CH₃).

¹³C NMR (300 MHz, CDCl₃, δ): 146.12, 144.75, 137.89, 134.61, 124.86, 124.07, 84.10, 82.82, 31.90, 31.59, 30.17, 29.60, 29.35, 29.08, 26.21, 24.76, 22.69, 14.14.

Synthesis 5T/PEO_n/alkyl

To a 3-neck round bottom flask was added **7** (4.48 mmol, 2.8 eq), **3** (1.6 mmol, 1.0 eq) and K₂CO₃ (9.6 mmol, 6.0 eq). The flask was purged with Argon for 30 min before Pd(PPh₃)₄ (0.032 mmol, 0.02 eq) was added. The flask was purged with Argon for another 30 min. A mixed solvent of DME/H₂O (40 mL/10 mL, v/v) was purged with Argon for 1 h before canula transferred to the 3-neck flask. The reaction was refluxed at 80 °C overnight. The crude product was extracted with ethyl acetate (30 mL× 3) and the combined organic layer was washed with pure water (30 mL× 3) and then dried over MgSO₄. Column chromatography was used to purify the product with hexane/ethyl acetate (3:1, v/v) as eluent to give the final product as a yellow solid (for PEO3 and PEO4) after precipitated with methanol, filtered and dried in vacuum oven or dark red liquid (for PEO10).

5T/PEO3/hexyl, yield 10%, ¹H NMR (CDCl₃, 400 MHz, δ): 7.18 (s, 1H; Th H), 7.11 (d, J=4Hz, 1H; Th H), 7.05 (t, J=3.32Hz, 2H; Th H), 7.00 (q, J=4Hz, 3H; Th H), 6.69 (m, 2H; Th H), 4.61 (s, 2H; Th-CH₂), 3.72 (s, 4H; Th-CH₂O-(CH₂)₂), 3.68-3.66 (m, 2H; Th-CH₂O-(CH₂)₂O-CH₂) 3.58-3.55 (m, 2H; Th-CH₂O-(CH₂)₂O-CH₂-CH₂), 3.38 (s, 3H; Th-CH₂O-(CH₂)₂O-(CH₂)₂O-CH₃), 2.79

(t, J=8Hz, 4H; 2(Th-CH₂)), 1.68 (quintet, J=8Hz, 4H; 2(Th-CH₂-CH₂)), 1.38-1.31 (m, 12H; 2(CH₂-CH₂-CH₂)), 0.90 (t, J=8Hz, 6H; 2(CH₃)).

¹³C NMR (300 MHz, CDCl₃, δ): 145.85, 145.75, 137.08, 132.82, 127.17, 126.34, 124.95, 124.87, 124.34, 123.58, 123.44, 70.60, 70.00, 69.52, 68.67, 66.95, 66.25, 65.68, 63.52, 31.56, 30.20, 28.75, 22.58, 14.10.

5T/PEO4/hexyl, yield 12%, ¹H NMR (CDCl₃, 400 MHz, δ): 7.04 (m, 4H; Th H), 6.98 (m, 3H; Th H), 6.68 (m, 2H; Th H), 3.74 (t, J=6.92Hz, 2H; CH₂), 3.66-3.60 (m, 10H; CH₂), 3.52 (m, 2H; CH₂), 3.35 (s, 3H; CH₃), 3.05 (t, J=7.04Hz, 2H; CH₂), 2.79 (t, J=7.24Hz, 4H; 2CH₂); 1.68 (quintet, J=7.71Hz, 4H; 2CH₂), 1.31 (m, 12H; 2(CH₂-CH₂-CH₂)), 0.90 (t, J=6.4Hz, 6H; 2CH₃).

5T/PEO3/decyl, yield 39%, ¹H NMR (CDCl₃, 400 MHz, δ): 7.18 (s, 1H; Th H), 7.11 (d, J=4Hz, 1H; Th H), 7.04 (t, J=3.5Hz, 2H; Th H), 6.99 (q, J=4Hz, 3H; Th H), 6.69 (t, J=2.96Hz, 2H; Th H), 4.61 (s, 2H; Th-CH₂), 3.72 (s, 4H; Th-CH₂O-(CH₂)₂), 3.68-3.66 (m, 2H; Th-CH₂O-(CH₂)₂O-CH₂), 3.58-3.55 (m, 2H; Th-CH₂O-(CH₂)₂O-CH₂-CH₂), 3.38 (s, 3H; Th-CH₂O-(CH₂)₂O-(CH₂)₂O-CH₃), 2.79 (t, J=8Hz, 4H; 2(Th-CH₂)), 1.68 (quintet, J=8Hz, 4H; 2(Th-CH₂-CH₂)), 1.34-1.27 (m, 28H; 2((CH₂)₇)), 0.88 (t, J=6.74Hz, 6H; 2(CH₃)).

¹³C NMR (300 MHz, CDCl₃, δ): 145.99, 145.89, 138.65, 137.22, 135.80, 135.32, 135.04, 134.50, 134.37, 133.18, 132.96, 72.09, 70.74, 69.66, 67.08, 61.20, 59.25, 32.05, 31.75, 30.35, 29.75.

5T/PEO10/hexyl, yield , ¹H NMR (CDCl₃, 300 MHz, δ): 7.17 (s, 1H; Th H), 7.09 (m, 1H; Th H), 7.05-7.03 (m, 2H; Th H), 6.99 (m, 3H; Th H), 6.68 (m, 2H; Th H), 3.64 (m, 56H; CH₂), 3.37 (s,

3H; CH₃), 2.79 (t, J=7.66Hz, 4H; 2CH₂), 1.68 (quintet, J=7.24Hz, 4H; 2CH₂), 1.33 (m, 12H; CH₂), 0.89 (t, J=6.40Hz, 6H; 2CH₃).

4.3 Results and Discussion

4.3.1 Simulation of self-assembly of 5T/PEO_n/alkyl

A coarse-grained (CG) model was developed to speed up the search for an ordered phase for 5T/PEO_n/Alkyl. In this model, each thiophene ring is represented by a single spherical bead (blue beads in **Figure 4.1(a)**), and three heavy atoms in the alkyl and PEO segment are represented by a single bead with different types (purple and red beads in **Figure 4.1(a)**). We parameterized the pair potential to match the experimental saturated liquid densities over a wide range of temperatures, as well as the bonded potential to match the bond and angle distribution from all-atom (AA) simulations using a relative entropy framework. Further details of the mapping procedure and the force field parameters can be found in our manuscript.

A series of simulations were performed for varying lengths of PEO lateral chains and alkyl segments, while the length of the oligothiophene unit is fixed. The Isobaric-isothermal ensemble was employed via the LAMMPS molecular dynamics (MD) simulation package using a Nosé-Hoover thermostat and barostat with cubic boxes and periodic boundary conditions. VMD was used for visualizations. The simulations were started at high temperature $T = 500$ K under the pressure of $P = 1.0$ atm to reach a well-equilibrated isotropic state. The system was then gradually cooled down at constant pressure to allow molecules to spontaneously form LC phases. For each simulation run, we first decreased the temperature by $\Delta T = 10$ K over a period of $t = 2$ ns, and then equilibrated the system at the new temperature for $t = 20$ ns. The final configuration of the equilibration part was used as input for the next simulation run at a lower temperature. We

collected equilibrium configurations for each temperature to analyze the phase morphology. An integration step of $\Delta t = 1$ fs was used.

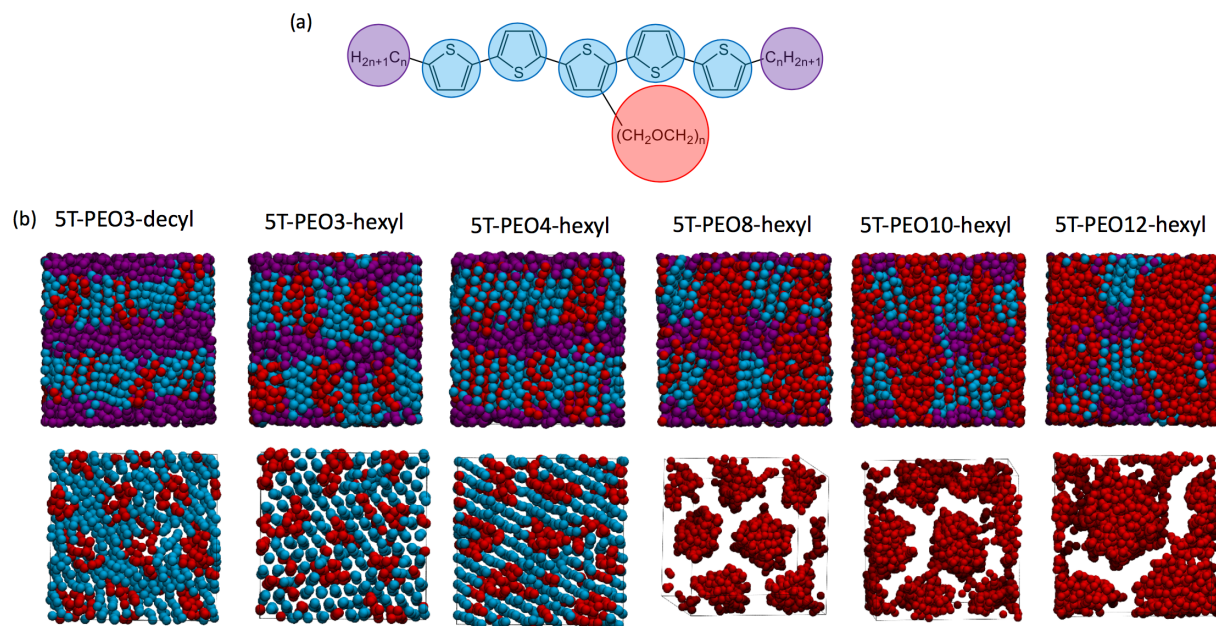


Figure 4.1 (a) Molecular structure of 5T/PEO_n/alkyl facial amphiphiles, the thiophene rings are shown in blue, the PEO chains are shown in red, and alkyl segments are shown in purple. (b) CG models of 5T/PEO_n/alkyl facial amphiphiles with varying lengths of PEO chains and alkyl segments (top: side view; bottom: top view).

By varying the length of PEO lateral chains and alkyl segments, different ordered phases were discovered as shown in **Figure 4.1**(b). The molecule with relatively shorter PEO chains (e.g. 5T/PEO3/decyl) was found to self-assemble into a lamellar phase in which the alkyl segment itself forms one layer, while the thiophene units and PEO segments together form adjacent two-component layer in which the PEO segments form small clusters scattered in the oligothiophene packing structure. The volume of alkyl segments only influences the thickness of the alkyl layer and shows little effect on the structure of thiophene and PEO. From **Figure 4.1**(b), 5T/PEO3/decyl and 5T/PEO3/hexyl exhibit similar structures from both top view and side view. With increasing

PEO chain length (e.g. 5T/PEO10/hexyl), however, the molecule was found to form a columnar phase where the PEO chains self-assemble into continuous cylinder structures and percolate into the thiophene and alkyl phase, while the other two segments fill the gap between adjacent cylinders. Such structural evolution from discontinuous clusters to continuous cylinders of PEO domains renders the molecules promising candidates for ion transport, especially with longer PEO chain length.

4.3.2 Synthesis of 5T/PEO_n/alkyl facial amphiphiles

A series of pentathiophene (5T)-based π -conjugated LCs have been synthesized as shown in **Scheme 4.1**. The terminal alkyl segments, either hexyl or decyl segments, are directly attached to both ends of the 5T core, with PEO chains of different chain lengths from 3 units to approximate 10 units of ethylene oxide laterally attached to the central thiophene ring, forming a T-shaped structure. The synthesis of the compounds was accomplished via two-fold Suzuki coupling reaction with Pd(PPh₃)₄ as catalyst. Lateral chains PEO3 and PEO4 possess an exact number of ethylene oxide units while PEO10 is a mixture PEO chains with average numbers of unit 10 due to easier synthesis given that 5T/PEO_n/hexyl molecules with *n* ranging from 8-12 exhibit similar cylindrical phases. Moreover, different lateral chain chemistry was involved with PEO chains attached to the central thiophene via either methylene linkage (for PEO3 and PEO10) or an ethylene linkage (for PEO4) which, fortunately, doesn't show much difference during the simulation process. Those compounds with shorter PEO chains (PEO3 and PEO4) are yellow powders at room temperature while that with PEO10 remains dark red liquid.

4.3.3 Thermal properties of bulk 5T/PEO_n/alkyl

The thermal properties of the compounds 5T/PEOn/alkyl were characterized by differential scanning calorimetry (DSC) and the optical textures of the substances exhibiting LC phases were obtained by polarized optical microscopy (POM) at room temperature. The DSC traces in **Figure 4.2(a)** show the first cooling scans and second heating scans obtained for all four samples in their pristine states with transition temperatures and heating capacities listed by the transition peaks. All samples, except 5T/PEO10/hexyl, exhibit stable LC mesophases at room temperature. Compound 5T/PEO3/hexyl exhibits phase transition during both cooling (31 °C) and heating (48 °C) processes. 5T/PEO4/hexyl, with one more unit of ethylene oxide, shows phase transition at lower temperature (20 °C during cooling and 35°C during heating), while 5T/PEO3/decyl with longer alkyl segments shows phase transitions at higher temperature (55 °C during cooling and 68 °C during heating). 5T/PEO10/hexyl, with extremely long PEO lateral chains, doesn't show any LC mesophase within room temperature range and its phase transition takes place at -36 °C during cooling and 4 °C during heating with evident peak broadening which is probably due to the mixture of PEO chains with varying lengths. We conclude for the structure-thermal relationship that while both PEO lateral chains and terminal alkyl segments introduce flexibility and enhance solubility for the pentathiophene core, increasing the volume fraction of PEO chains reduces the transition temperature between the LC and isotropic states while longer alkyl segments lead to higher transition temperatures. Later this structure-property evolution is further investigated by MD simulation in subsequent sections. LiTFSI is chosen as the ion source for ionic conductivity studies of 5T facial amphiphiles, thus the thermal properties of LiTFSI-blended 5T/PEOn/alkyl complexes are also studied at a preferred blending ratio $r = \frac{[Li^+]}{[EO]} = 0.05$ defined as the molar fraction between Li⁺ and ethylene oxide units. The detailed DSC traces are shown in **Figure 4.2(b)** and (c) with 5T/PEO3/hexyl-LiTFSI and 5T/PEO3/decyl-LiTFSI complexes as examples. Not

surprisingly, for both samples only one transition peak was observed during the first heating scan and no other phase transitions were observed afterwards, irrespective of the heating rate. This is probably because the addition of lithium salt suppressed crystallization and rendered the order-disorder transition harder to detect by DSC. Similar phenomena were also observed for temperature-dependent WAXS measurement and conductivity characterization in the following sections.

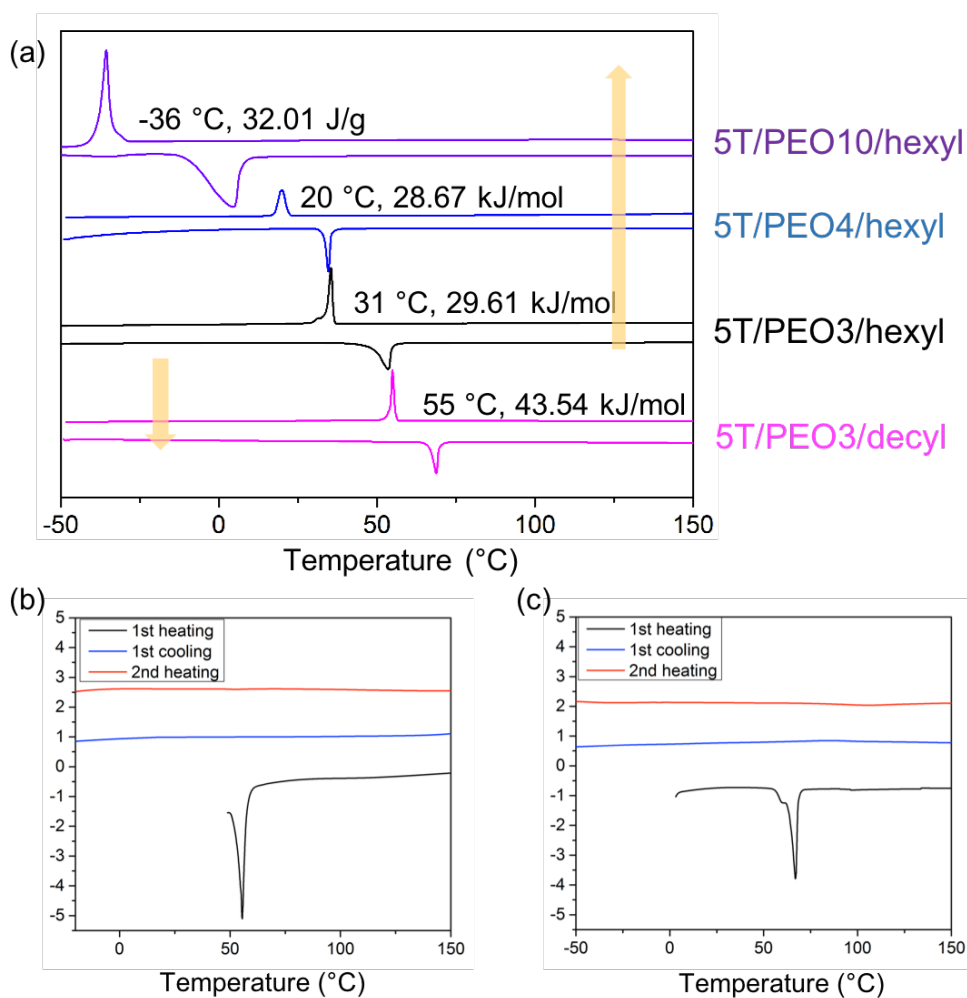


Figure 4.2 DSC traces ($10\text{ }^{\circ}\text{C min}^{-1}$) of (a) pristine 5T/PEO_n/alkyl molecules, (b) 5T/PEO3/hexyl-LiTFSI complex ($r = 0.05$), and (c) 5T/PEO3/decyl-LiTFSI complex ($r = 0.05$).

POM images were taken at 20 °C for all samples except 5T/PEO10/hexyl whose order-disorder phase transition takes place below room temperature. The bulk material is placed between a glass microscope slide and cover slip and treated in the same method as mentioned in our previous work. As shown in **Figure 4.3**, more crystalline features in addition to the birefringent batonnet textures, such as the needle-shaped character, were detected as well for these T-shaped facial amphiphiles compared to traditional liquid crystal structures due to potential crystallinity of PEO lateral chains and pentathiophene conjugated units. These materials are therefore believed to be highly ordered liquid crystals or defect rich, “condis” crystals. The definition of their specific LC phases, however, remains unclear and will be the subject of a separate investigation.

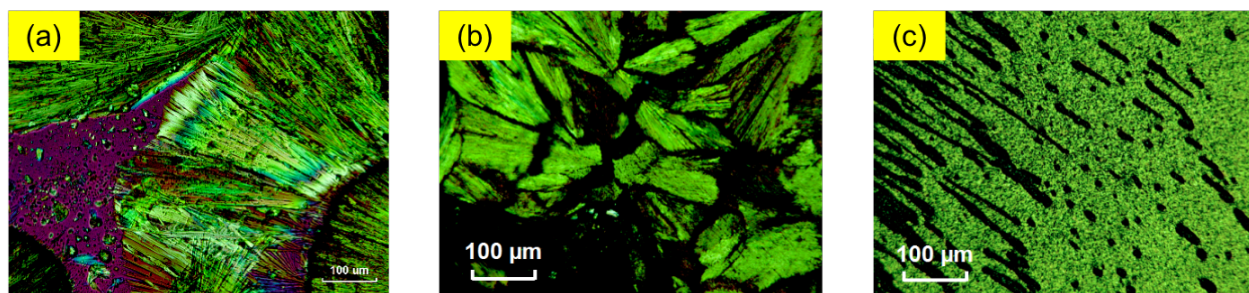


Figure 4.3 POM images of pristine (a) 5T/PEO3/hexyl, (b) 5T/PEO3/decyl, (c) 5T/PEO4/hexyl in their bulk phases at room temperature.

4.3.4 Self-assembly behavior of 5T/PEO_n/alkyl thin film

Room-temperature GIWAXS and temperature-dependent WAXS measurements were adopted to further investigate the self-assembly behaviors of 5T facial amphiphiles in thin film state both in the absence and presence of LiTFSI. GIWAXS was only conducted on the three samples with shorter PEO chains (PEO3 and PEO4). Their patterns (as shown in **Figure 4.4**(a), (b), (c)) appear qualitatively similar in their pristine states with negligible difference which may result from the different volume fractions of PEO and alkyl domains. Generally the peaks can be divided into three groups: the narrow diffraction peaks ($00h$) in the out-of-plane direction indicating a layer

structure parallel to the substrate, the relatively weak peaks at $q_r \sim 0.5$ representing PEO clusters in each layer, and elongated peaks at $q_r \sim 1.5$ indicative of π - π stacking interaction between adjacent 5T units which played a key role in creating the highly ordered smectic phase.

To provide more insight to the self-assembly behaviors obtained from GIWAXS characterization, the all-atom (AA) simulation was also conducted to introduce some useful chemical details, which is not captured by the CG model, (e.g. the thiophene ring). The force field of the AA model was developed in our previous study and the OPLS-AA force field was used to define any missing potential parameters. To avoid ineffective self-assembly using AA simulation, its initial ordered configuration was produced from the CG simulation using the reverse coarse-grained algorithm (RCG). The *NPT* ensemble was then employed to equilibrate the system. An integration step of $\Delta t = 1$ fs was used.

The AA configurations were used to calculate the structure factor of the thiophene rings by applying equation

$$S(\mathbf{q}) = \frac{(\sum_j \cos(\mathbf{q} \cdot \mathbf{r}_j))^2 + (\sum_j \sin(\mathbf{q} \cdot \mathbf{r}_j))^2}{N} \quad (1)$$

where \mathbf{q} is the wave vector, the \mathbf{r}_j represents all position vectors of the heavy atoms (i.e., non-hydrogen atom) in each thiophene ring, and N is the number of such atoms. The wave vector, \mathbf{q} , is restricted to integer numbers of wavelengths within the simulation box, namely, $\mathbf{q} = 2\pi (h/L_x, k/L_y, l/L_z)$. To obtain the 2D $S(\mathbf{q})$, the data was regrouped by q_z and $q_r = \sqrt{q_x^2 + q_y^2}$, and the maximum value of $S(\mathbf{q})$ for each group with constant (q_r, q_z) was used on the plot.

The simulated GIWAXS patterns show some similarities with experimental results. Since all thiophene segments in the ordered phase show directional order, their direction, \vec{n} , (calculated from P_2 order parameter) can be used as reference vector to study peaks in the GIWAXS. As we know, each point in the $S(\mathbf{q})$ plot can be denoted as the miller index (h, l, k) , which represents a

family of parallel lattice planes orthogonal to the vector $\vec{n}_{hkl} = h\vec{x} + k\vec{y} + l\vec{z}$. In the cubic box, the spacing d between adjacent lattice planes is $d_{hkl} = \frac{L_{box}}{\sqrt{h^2+l^2+l^2}}$, where L_{box} is the length of the unit cell. This spacing can help us measure certain distances in the ordered phase along \vec{n}_{hkl} . The relationship between \vec{n} and \vec{n}_{hkl} can be used to identify some spatial arrangement. For example, \vec{n} and \vec{n}_{hkl} being perpendicular to each other indicates some ordered feature within the PEO-thiophene layer. Similarly, if they are parallel, the ordered feature across layers will be identified. Here, we consider \vec{n} and \vec{n}_{hkl} are perpendicular if the dot product of their unit vector is smaller than 0.2; and they are parallel if the dot product is larger than 0.8. Based on this criterion, the diffraction peaks (00k) is parallel to the direction, indicating the layer structure in the out-of-plane. The diffraction peaks in both region 1 and 2 (see **Figure 4.4(a), (d)**) are perpendicular to the direction, indicating the in-plane order. The spacing in the region 1 is around 4.5 Å corresponding to the π - π stacking of thiophenes while the spacing in the region 2 is around 14 Å corresponding to the distance between different PEO clusters.

To show the temperature dependence of 5T facial amphiphile structures in a more quantitative manner, WAXS measurements were conducted during the heating process in addition to GIWAXS patterns and shown in **Figure 4.5**. Started from room temperature, we observe sharp peaks at both $q < 0.5$ and $q \sim 1.5$, representing layered structure and π - π interaction between thiophene rings respectively, for molecules with shorter PEO chains. For 5T/PEO10/hexyl, the WAXS measurement was conducted at lower temperature range between -70 °C and 20 °C in which we observe strong π -stacking peak whereas the layer scattering peaks are not very well-ordered at low temperature, indicating a different morphology of PEO percolation into thiophene and alkyl domains. As temperature increases, all samples undergo an order-disorder transition, indicated by the sudden broadening of scattering peaks in the vicinity of (a) 100 °C for 5T/PEO3/decyl, (b)

80 °C for 5T/PEO3/hexyl, (c) 50 °C for 5T/PEO4/hexyl, and (d) 10 °C for 5T/PEO10/hexyl, in good agreement with the DSC results shown in **Figure 4.2(a)**. Above those phase transition temperatures, samples (a), (b), and (c) are not completely disordered and still maintain weak layered structures while the π - π interaction is disrupted by the mobile PEO clusters. On the other hand, 5T/PEO10/hexyl with longer PEO chains becomes completely disordered.

4.3.5 Ionic conductivity of 5T/PEOn/alkyl

The ionic conductivity of the 5T/PEOn/alkyl-LiTFSI complex in the thin film state was measured by EIS with interdigitated gold electrodes devices (IDEs)^[12,13] as a function of temperature ranging from 0 °C to 140 °C through a heating process in order to capture the order-disorder transition revealed by DSC. LiTFSI is blended to each molecule at a ratio $r = 0.05$. Despite similar molecular structures, the length of PEO chains strongly influences the molecular morphology and as a result

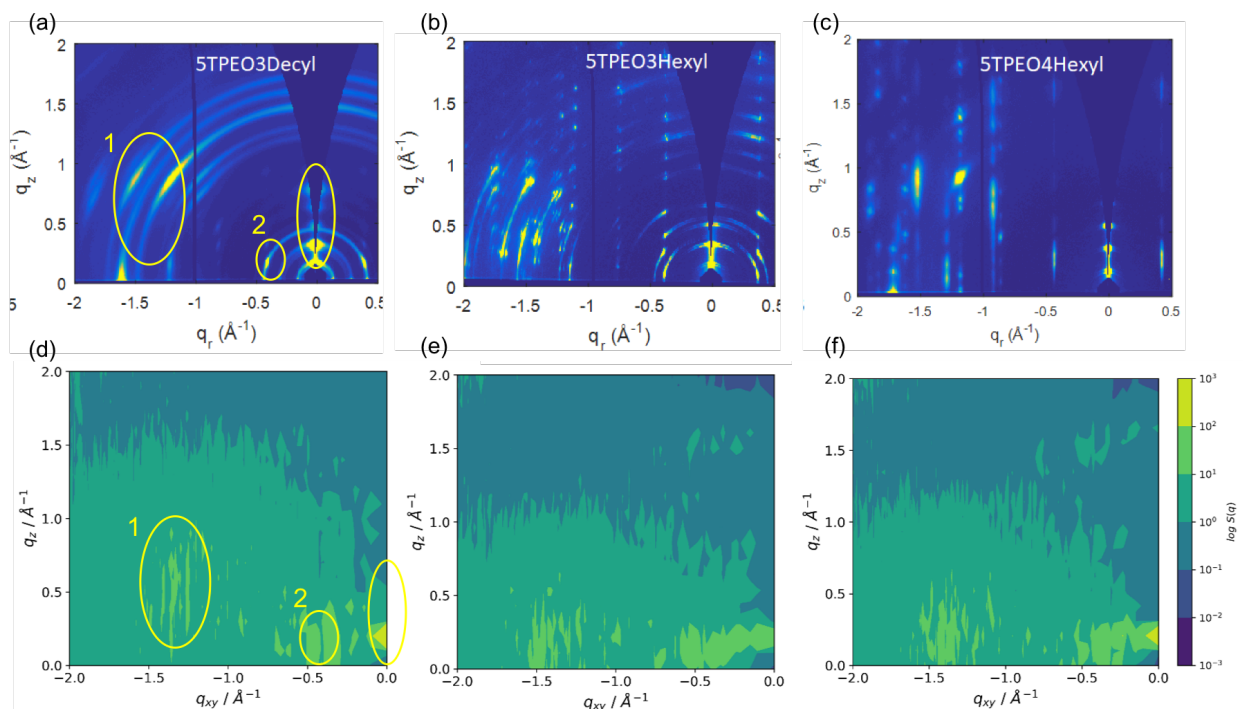


Figure 4.4 Experimental (top) and simulated (bottom) GIWAXS patterns of pristine (a) (e) 5T/PEO3hexyl, (b) (d) 5T/PEO3/hexyl, and (c) (f) 5T/PEO4/hexyl in thin film state at room temperature. (*The X-axis q_r in (a), (b), (c) and q_{xy} in (d), (e), (f) are the same)

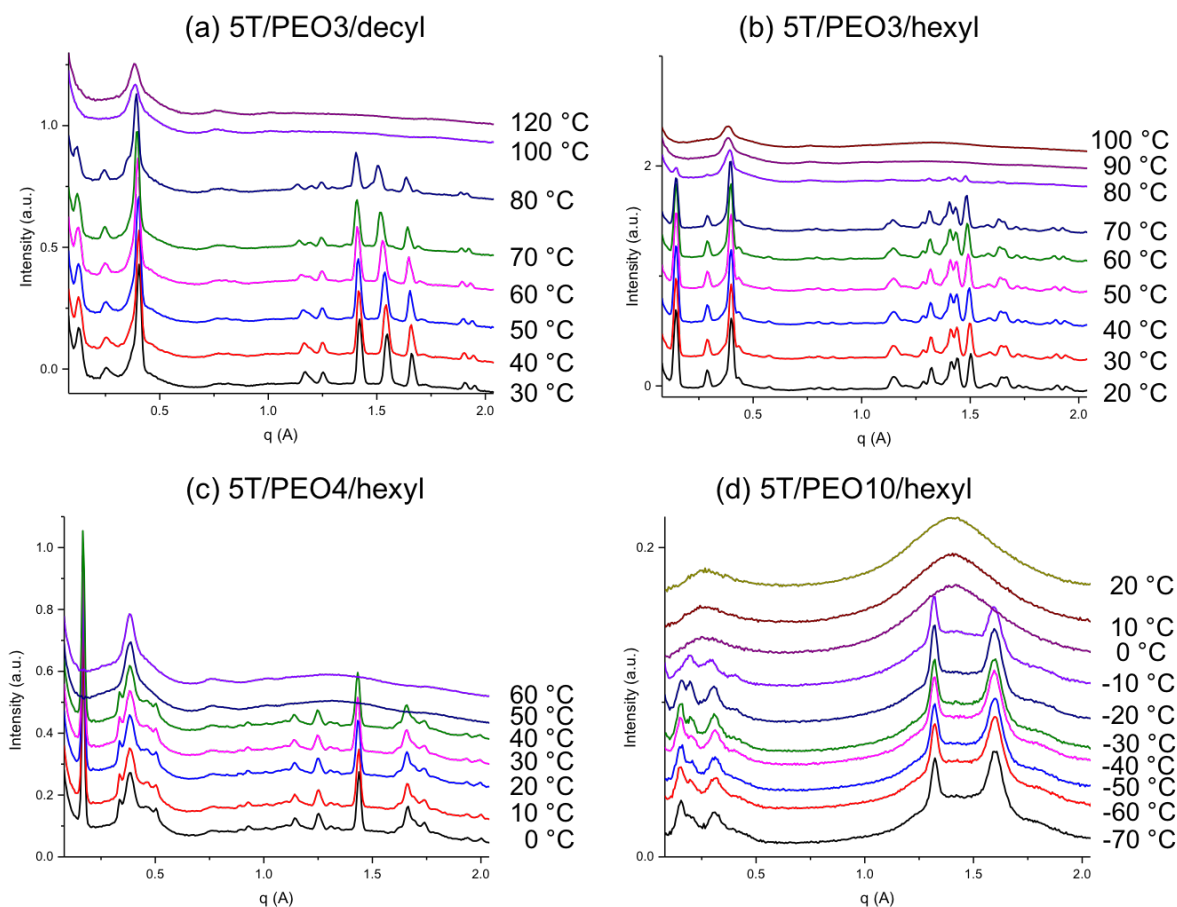


Figure 4.5 Temperature-dependent WAXS patterns of pristine (a) 5T/PEO3/decyl, (b) 5T/PEO3/hexyl, (c) 5T/PEO4/hexyl, and (d) 5T/PEO10/hexyl.

the ionic conductivity characteristics. When PEO lateral chains are relatively smaller than oligothiophene and alkyl domains, such as PEO3 and PEO4, they are not capable of self-assembling into their own subspace, instead they form small clusters in the same layer with 5T while the 5T units and terminal alkyl segments segregate into layer structures according to MD simulation results. The layer thickness of alkyl segments is based on chain length and longer alkyl segments (such as decyl groups) result in larger layer thickness than hexyl segments. The ionic conductivity based on a charge hopping mechanism among PEO clusters, is therefore lower since it is more difficult for ions to penetrate through thicker layers. When the PEO chain length is

further increased (PEO10) to be comparable with the other two components, PEO units percolate into the other two domains and columnar structures are generated leading to more efficient ion transport for practical applications. For both cases, the ion transport channels are parallel to the substrate according to molecular orientation. The promising electronic conductivity of oligothiophene in this case, however, is significantly disrupted by PEO domains.

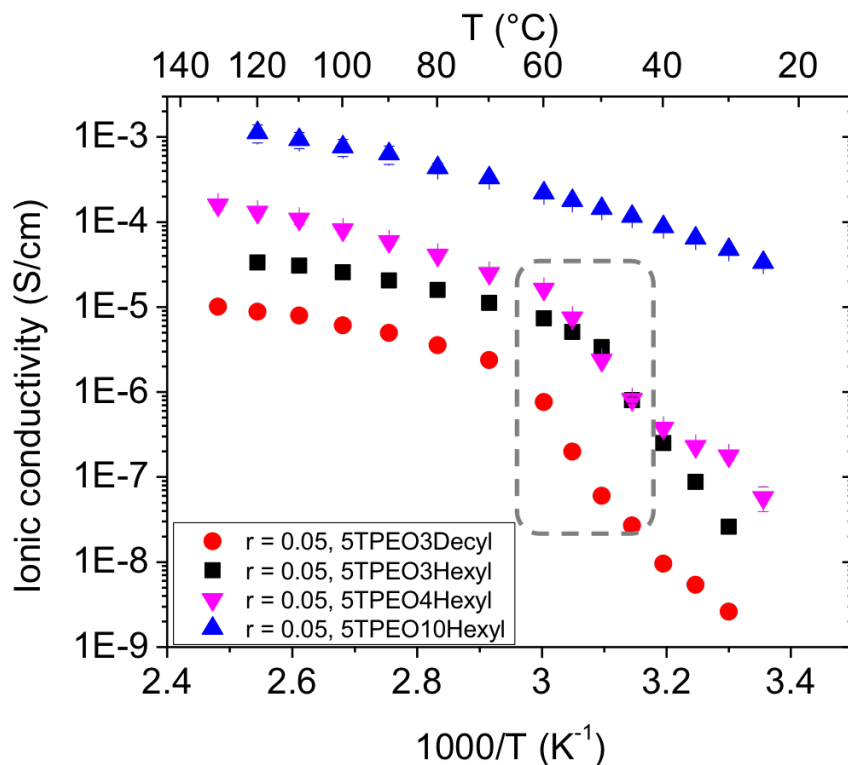


Figure 4.6 Ionic conductivity of LiTFSI-blended 5T/PEO_n/alkyl thin film samples at $r = 0.05$ as a function of temperature during the heating process. The circled area indicates the order-disorder transition regime.

Figure 4.6 depicts the temperature-dependent ionic conductivity of the four samples. All of them exhibit a monotonic increase with temperature in the current temperature range. For samples with shorter PEO chain length, such as PEO3 and PEO4, the conductivity exhibits qualitatively similar patterns with PEO4 resulting in relatively higher conductivity (10^{-8} S/cm) whereas decyl groups lead to decreased conductivity (10^{-9} S/cm) at room temperature. However, the conductivity is

actually quite low due to inefficient charge transport through small PEO clusters. When temperature reaches the order-disorder transition, indicated by the circled area, a discontinuous increase in conductivity is observed because the highly ordered LC structure is disrupted by mobile PEO clusters which forms continuous a domain leading to a different charge transport mechanism. As a consequence, a significant conductivity increase is observed and 5T/PEO4/hexyl with one more unit of ethylene oxide achieves maximum observed conductivity around 1.5×10^{-4} S/cm at 130 °C, comparable to our previous work with the linear structure, 4T/PEO4.

5T/PEO10/hexyl already exhibits disordered structure at room temperature with no more phase transition and therefore the conductivity increases homogeneously with temperature in a moving molecule mechanism. The maximum conductivity (10^{-3} S/cm) is achieved at 130 °C, which is even superior to those of nanosegregated ionic LCs.

4.4 Conclusions

In summary, we have performed a simulation-guided-experimental study of the self-assembly behavior and ionic conductivity of a series of newly synthesized conjugated LC materials with T-shaped facial amphiphile structures. The compounds exhibit increased crystallinity compared to our previous work due to enhanced incompatibility among oligothiophene, PEO and alkyl components as well as strong π - π interaction between adjacent thiophene units. Structure and property evolution based on the relative volume fraction of PEO lateral chains and alkyl terminal segments were also studied with shorter PEO segments that lead to small clusters immersed in the layers of 5T and longer PEO segments that percolate into 5T and alkyl domains resulting in a columnar phase. The length of alkyl chains also determines the layer thickness. The structures and self-assembly behaviors were further investigated with GIWAXS, temperature-dependent WAXS

and MD simulations. EIS measurements of 5T/PEO_n/alkyl achieved maximum conductivity as high as 10⁻³ S/cm with 5T/PEO10/hexyl at 130 °C under a moving molecule mechanism, superior to our previous results with 4T/PEO4.

The combination of T-shaped facial amphiphile structures and conducting functionalities proved to be successful in achieving complex structures with confined charge transport channels. Oligothiophene, not only provides π - π interaction as the skeleton for the formation of layer structures, is also known for its intriguing electronic, optical and redox properties as promising candidate for flexible electronics, despite the observation that the transport properties in 5T/PEO_n/alkyl were disturbed by PEO clusters. With adjusted structural design, this kind of material family will have significant potential for providing columnar simultaneous ionic/electronic conductivity in the future.

REFERENCES

- [1] C. Tschierske, *Chemical Society Reviews* **2007**, *36*, 1930.
- [2] Z. Liu, B. X. Dong, M. Misra, Y. Sun, J. Strzalka, S. N. Patel, F. A. Escobedo, P. F. Nealey, C. K. Ober, *Adv. Funct. Mater.* **2019**, *29*, 1805220.
- [3] C. Tschierske, F. Hildebrandt, J. A. Schröter, J. H. Wendorff, R. Festag, M. Wittenberg, *Adv. Mater.* **1997**, *9*, 564.
- [4] F. Hildebrandt, J. A. Schröter, C. Tschierske, R. Festag, R. Kleppinger, J. H. Wendorff, *Angew. Chem. Int. Ed. Engl.* **1995**, *34*, 1631.
- [5] B. Chen, X. B. Zeng, U. Baumeister, S. Diele, G. Ungar, C. Tschierske, *Angew. Chem. Int. Ed.* **2004**, *43*, 4621.
- [6] J. A. Schröter, C. Tschierske, M. Wittenberg, J. H. Wendorff, *Angew. Chem. Int. Ed. Engl.* **1997**, *36*, 1119.
- [7] J. A. Schröter, C. Tschierske, M. Wittenberg, J. H. Wendorff, *J. Am. Chem. Soc.* **1998**, *120*, 10669.
- [8] B. Chen, U. Baumeister, G. Pelzl, M. K. Das, X. Zeng, G. Ungar, C. Tschierske, *J. Am. Chem. Soc.* **2005**, *127*, 16578.
- [9] G. W. Gray, K. J. Harrison, J. A. Nash, *Electron. Lett.* **1973**, *9*, 130.
- [10] C. K. Ober, J. I. Jin, R. W. Lenz, *Adv. Polym. Sci.* **1984**, *59*, 103.
- [11] B. X. Dong, Z. Liu, M. Misra, J. Strzalka, J. Niklas, O. G. Poluektov, F. A. Escobedo, C. K. Ober, P. F. Nealey, S. N. Patel, *ACS Nano* **2019**, *13*, 7665.
- [12] D. K. Paul, R. McCreery, K. Karan, *Journal of the Electrochemical Society* **2014**, *161*, F1395.
- [13] C. G. Arges, Y. Kambe, H. S. Suh, L. E. Ocola, P. F. Nealey, *Chemistry of Materials* **2016**, *28*, 1377.

Chapter Five: Enhanced Electronic Conductivity of A Molecularly-Doped Poly(3-hexylthiophene)-Based Rod-Coil Block Copolymer via the Addition of An Ionic Salt LiTFSI⁴

5.1 Introduction

Π -conjugated polymers are very promising conducting and semiconducting materials for the next generation of electronic and optical devices. Their unique charge transport properties are based on delocalization of π -electrons across adjacent aligned polymer chains. To date poly(3-alkynethiophenes) (P3ATs) have become the most studied semiconducting polymers for organic electronics applications including solar cells, field effect transistors, pLEDs and chemical sensors, in which the polythiophene backbone has been found to be both highly conductive and environmentally and thermally stable, while a flexible side chain at the 3-position improves the solubility as well as tunes the electronic properties of the polymer.

Block copolymers are well-known for their microphase separation behavior to facilitate well-organized, self-assembled nanostructures, such as lamellae and cylindrical morphologies, which could provide large interfacial areas between domains consisting of different blocks.^[1] Conjugated block copolymers (BCPs) have received immense interest over the past few years because of their unique structure as well as their potential in many applications.^[2-6] The motivation of such material lies in the incorporation of a functional conducting block in equilibrium ordered nanostructures. Despite the unique optical and electronic properties of conjugated polymers, the extension of π orbitals also endows rigidity to polymer backbone thus introducing additional geometric

⁴ A manuscript of this work is in preparation for submission to *Macromolecules* with authorship as: B. X. Dong, Z. Liu, J. Onorato, S. N. Patel, C. Luscombe, C. K. Ober, P. F. Nealey. Jonathan Onorato synthesized all-regioregular P3HT block, Ziwei Liu synthesized POEM block via ATRP and P3HT-*b*-POEM copolymer via click reaction, and characterized the polymers with NMR, GPC, FTIR and AFM. Ban Dong studied block copolymer molecular doping with LiTFSI and F4TCNQ, performed GIWAXS/GISAXS, UV-Vis and conductivity measurements.

constraints for phase separation, which can limit the processability and mechanical properties of this material and lead to limited commercial applications.^[2] A flexible coil block linked to the rigid conjugated block, however, could mitigate such constraints and provide more flexibility for facilitating nanoscale phase separation^[7] as well as modifying solubility.^[8,9] Compared to polymer blends, the structures created with block copolymers are more thermally stable.^[10] Moreover, the self-assembled morphology of rod-coil BCPs may result in additional electronic processes such as exciton confinement and interfacial effect.^[11] Furthermore, the microphase separation of rod-coil BCPs provides the possibility to create highly ordered heterojunction structures for efficient charge generation as well as a bicontinuous domain for charge transport, the size of which is controlled by block length.

Doping has become a popular method for conjugated polymers to modulate carrier concentration and control electrical conductivity, which is critical for performance enhancement of many optoelectronic devices. For instance, doping has been shown to facilitate trap-filling in field-effect transistors (OFETs), and improve charge injection and collection in organic photovoltaics (OPVs) and organic light-emitting diodes (OLEDs).^[12-16] During the process, electrons transfer either from the host polymer to molecular dopant in the case of *p*-type doping or from the molecular dopant to the host polymer in the case of *n*-type doping. Typically, incorporating molecular dopants into the polymer affects not only carrier concentration but also the polymer structures, making it difficult to predict the change in electronic conductivity.^[17] Sequential doping methods where the polymer films is exposed to the dopant in either vapor or solution phase^[18-24] are shown to give superior electronic conductivity largely compared to solution processing where polymers and dopants are co-processed from solution^[25,26] due to the preservation of the underlying structure of the conjugated polymers.

To this end, we synthesized and studied the conducting performance of block copolymer poly(3-hexylthiophene)-*b*-poly (oligo-oxyethylene methacrylate) (P3HT-*b*-POEM) upon co-processing with lithium bis(trifluoromethanesulfonyl)imide (LiTFSI) and doped with molecular dopant 2,3,5,6-tetrafluoro-7,7,8,8-tetracyanoquinodimethane (F4TCNQ) via vapor deposition. The incorporation of a POEM block has two functions here: first, to tune the mechanical properties of P3HT by providing flexibility and enhancing solubility; second, to endow additional ionic conductivity to the material. In this chapter, we focus on the first characteristic. We find that while the electronic conducting performance of P3HT-*b*-POEM is lower than the homopolymer P3HT, co-processing P3HT-*b*-POEM with LiTFSI greatly improves its molecular order and thus electrical conductivity, which is further improved upon exposure to F4TCNQ vapor. A maximum conductivity around 31 S/cm has been achieved at the intermediate LiTFSI blending concentration of $r = [\text{Li}^+]/[\text{EO}] = 0.02$. We rationalize the improvement in molecular order of P3HT-*b*-POEM by the interaction between block copolymer chains and LiTFSI solution, which leads to the formation of aggregates in solution and thus higher order in thin film state. A manuscript of this work is in preparation for submission to *Macromolecules* co-authored with Ban Dong, Jonathan Onorato, *et al.* Jonathan Onorato synthesized all-regioregular P3HT block, Ziwei Liu synthesized the POEM block and P3HT-*b*-POEM block copolymer and characterized polymer properties via NMR, GPC, FTIR and AFM. Ban Dong studied block copolymer molecular doping with LiTFSI and F4TCNQ, and performed GIWAXS/GISAXS, UV-Vis and conductivity measurements.

5.2 Experimental Section

5.2.1 Materials

2-Bromoethanol, 2,2'-bipyridyl (bpy), α -bromoisobutyryl bromide, di(ethylene glycol)methyl ether methacrylate, sodium azide (NaN_3), copper (I) bromide (Cu(I)Br), copper (I) iodide (Cu(I)I), lithium bis(trifluoromethanesulfonyl)imide (LiTFSI, battery grade), 2,3,5,6-Tetrafluoro-7,7,8,8-tetracyanoquinodimethane (F4TCNQ), tetrabutylammonium fluoride solution (TBAF, 1.0 M in THF), *N,N,N',N'',N'''*-pentamethyldiethylenetriamine (PMDETA), isopropylmagnesium chloride solution (2.0 M in THF) were purchased from Sigma-Aldrich. Organic solvents such as acetone, hexane, ethyl acetate (EtOAc), methanol (MeOH), ethanol (EtOH), tetrahydrofuran (THF), chloroform (CHCl_3), and acetonitrile (MeCN) were purchased from Fisher. 2-bromo-3-hexyl-5-iodothiophene was purchased from Tokyo Chemical Industries (TCI) and filtered through a small silica plug with hexanes prior to use to remove copper inhibitor. Di(ethylene glycol)methyl ether methacrylate monomer was inhibitor-removed and stored at $-20\text{ }^\circ\text{C}$ freezer before polymerization. Cu(I)Br was purified with acetic acid and methanol, followed by dried in vacuum and stored in desiccator at room temperature. Anhydrous tetrahydrofuran (THF) was either freshly distilled from sodium and benzophenone prior to use or purified using a DriSolv solvent purification system.

5.2.2 Characterization

5.2.2.1 Nuclear magnetic resonance (NMR)

^1H and ^{13}C NMR spectra were recorded on a Varian INOVA 400 and a Bruker AV 500 spectrometer, respectively at room temperature. Chemical shifts were quoted relative to the residual protons of the deuterated solvents CDCl_3 ($\delta = 7.26$ for ^1H and $\delta = 77.36$ for ^{13}C). The multiplicity was characterized by the following abbreviations: s-singlet, d-doublet, t-triplet, q-quartet, m-multiplet.

5.2.2.2 GEL Permeation Chromatography (GPC)

GPC was performed on a Waters ambient-temperature GPC instrument equipped with a Waters 410 differential refractive index detector and a Waters 486 UV-Vis detector. GPC was performed at a flow rate of 1.0 mL/min with THF as the eluent at 40 °C and the elution times were converted to molecular weights using a calibration curve based on low dispersity polystyrene (PS) standards.

5.2.2.3 Fourier transform infrared spectroscopy (FTIR)

FTIR spectra of polymers were recorded under vacuum on a Bruker Vertex V80V Vacuum FTIR spectrometer with an attenuated total reflection (ATR) mode at a resolution of 4 cm⁻¹.

5.2.2.4 UV-vis absorption spectroscopy

The UV–vis absorption spectroscopy measurements were performed using a Shimadzu UV-3600 Plus UV-VIS-NIR Dual Beam Spectrophotometer at the Soft Matter Characterization Facility (SMCF) at the University of Chicago. Absorption spectra of thin films were performed on sample deposited atop quartz substrates whereas solution absorption spectra were obtained by using quartz cell having very short optical pathlength of ca. 20 μm.

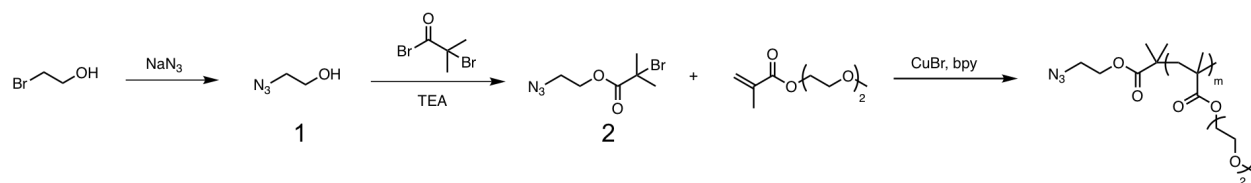
5.2.2.5 Grazing incidence wide-angle X-Ray scattering (GIWAXS) and small-angle X-ray scattering (GISAXS)

GIWAXS/GISAXS measurements were performed at beamline 8-ID-E of the Advanced Photon Source, Argonne National Laboratory with 10.86 keV ($\lambda = 0.11416$ nm) synchrotron radiation. Samples were enclosed and measured inside a low vacuum chamber (10⁻³ mbar) to minimize concerns about radiation damage as well as to prevent extraneous scattering from ambient air. The

measurement time was chosen to be 10 s per frame. For each sample, 3 data sets were taken from 3 adjacent spots on the sample and then summed in order to enhance the signal-to-noise ratio. In our work, the samples were tilted at an angle of incidence of 0.14° with respect to the incoming beam. This angle was chosen to be above the estimated critical angle of sample (*ca.* 0.13°) but below the critical angle of the Si substrates (*ca.* 0.17°). The scattering signal was recorded with a Pilatus 1MF pixel array detector (pixel size = $172\ \mu\text{m}$) positioned either 228 mm (GIWAXS) or 2185 mm (GISAXS) from the sample. Each data set was stored as a 981×1043 32-bit tiff image with 20-bit dynamic range. The Pilatus detector has rows of inactive pixels at the border between detector modules. In order to fill these gaps, after each measurement the detector was moved to a new vertical direction and the measurement on each spot was repeated, then the gaps were filled by combining the data from two detector positions. Each image was also subjected to detector nonuniformity, detection efficiency, the polarization effect and solid-angle variation correction. Vertical line-cuts were performed as a function of intensity along the q_z direction. All the data processing and extraction were executed using the GIXSGUI package for MATLAB.

5.2.3 Synthetic procedures

5.2.3.1 Synthesis of azido end-functionalized POEM block with varying molecular chain lengths via Atom Transfer Radical Polymerization (ATRP)



Scheme 5.1 Synthetic procedures of azido-POEM via ATRP.

Synthesis of 2-azidoethanol (1)

2-Bromoethanol (5.45 g, 40 mmol) was dissolved in 20 ml acetone. A solution of 20 ml sodium azide (7.83 g, 120 mmol) in deionized water was slowly added. The resulting solution was refluxed at 65 °C for 26 h. After the completion of reaction, acetone was removed via evaporation and the residue was extracted with ethyl acetate (30 mL ×3). The organic phase was collected and washed with water (40 mL ×3), dried over anhydrous magnesium sulfate, and concentrated under the reduced pressure. The crude product was obtained as colorless oil in 57.5 % yield without further purification.

¹H NMR (400 MHz, CDCl₃): δ 3.77 (t, 2H, CH₂), 3.43 (t, 2H, CH₂). ¹³C NMR (400 MHz, CDCl₃): δ 61.47, 53.50.

Synthesis of **2-azidoethyl 2-bromoisobutyrate** (ABIB-initiator, **2**)

The ATRP initiator was synthesized according to previous procedure.^[27] **1** (1.30 g, 15.0 mmol) was dissolved in 30 mL anhydrous THF with triethylamine (1.97 g, 19.5 mmol). The solution was cooled to 0 °C followed by dropwise addition of 2-bromo-2-methylpropanoyl bromide (5.17 g, 22.5 mmol) over 30 min. Temperature was maintained at 0 °C for a further 2 hours before subsequently reaching room temperature and left to stand overnight. After the completion of reaction, THF was removed *in vacuo* and the residue was extracted with ethyl acetate (30 mL ×3). The organic phase was washed with saturated NaHCO₃ solution (20 mL ×3), and water (20 mL ×3) successively, dried over anhydrous magnesium sulfate, then filtered and concentrated under the reduced pressure. The crude product was further purified by silica gel chromatography with hexane: EtOAc = 20:1 (v/v) as eluent to give **2** as yellow oily liquid in 77.7% yield.

¹H NMR (400 MHz, CDCl₃): δ 4.34 (t, 2H, -CH₂O-), 3.52 (t, 2H, -CH₂N₃), 1.96 (s, 6H, -CH₃).

Synthesis of azido end-functionalized POEM block

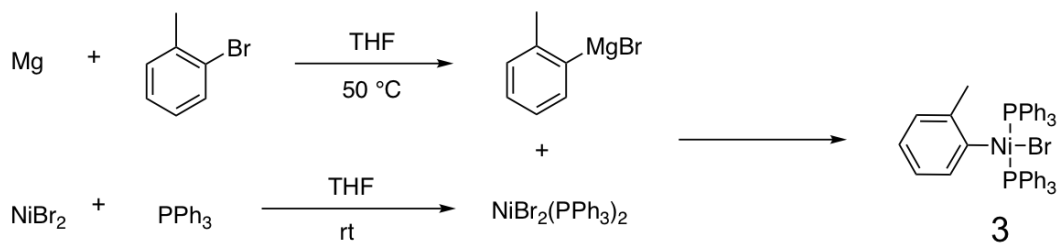
A series of POEM block have been synthesized with varying molar fraction between monomer and initiator. Here we only show one example with monomer/initiator ratio $[M]_0/[I]_0 = 130:1$. To a Schlenk flask was charged Cu(I)Br (0.016 g, 0.104 mmol) and 2,2'-Bipyridyl (0.033 g, 0.208 mmol). The solids were degassed and refilled with Argon for five cycles. In another round-bottom flask **2** (0.0245 g, 0.104 mmol), di(ethylene glycol)methyl ether methacrylate (2.56 g, 13.52 mmol) were dissolved in 5 mL EtOH and bubbled with Argon for 30 min. The solution was canula transferred to the Schlenk flask and stirred at 40 °C for 20 h under Argon. After the completion of polymerization, the reaction mixture was diluted in 20 mL ethanol and passed through a short column of neutral Al₂O₃ to remove remaining copper catalyst. The crude product was concentrated and further purified via dialysis in 10K MWCO membrane in EtOH bath for 24 h (8 h × 3) to yield colorless liquid product after dried in vacuum. The molecular weight and Đ were determined by SEC. The results are shown in **Table 5.1** below.

Table 5.1 Molecular weight characterization of azido-POEM block by GPC

$[M]_0/[I]_0$	M_n (g/mol)	M_w (g/mol)	Đ	DP
130:1	23.5 k	27.0 k	1.15	124
100:1	19.3 k	22.2 k	1.15	101
80:1	11.5 k	12.8 k	1.11	60
50:1	10.8 k	11.6 k	1.08	54

5.2.3.2 Synthesis of regioregular P3HT block via Grignard Metathesis (GRIM) polymerization

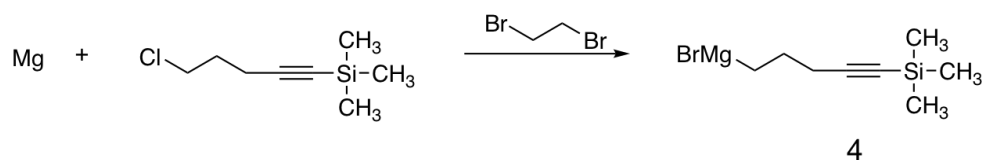
Synthesis of chloro(tolyl)(PPh₃)₂Nickel(II) (**3**)



Scheme 5.2 Synthetic procedure of catalyst precursors for P3HT block.

The catalyst precursor was synthesized according to a modified literature procedure^[28], as shown in Scheme 5.2. All glassware was dried in an air oven prior to use. To a 3-neck flask, a condenser and stir bar were added, then NiBr₂ (2.185 g, 10 mmol) and PPh₃ (5.245 g, 20 mmol) were added, and degassed under vacuum for 30 min. Anhydrous THF (15 mL) was then added, and the reaction was refluxed for 2 h, resulting in a dark green solution forming. Simultaneously, another 3-neck flask was prepared with an addition funnel and stir bar. To this flask, Mg (turnings, 0.2917 g, 12 mmol) were added, and activated through the application of flame and high vacuum. In some cases, a small amount of catalytic iodine crystal (~1 mg) was added to activate the Mg. To a separate flask, a solution of 2-bromotoluene (1.710 g, 10 mmol) was prepared in anhydrous THF (10 mL). After stirring, this solution was added to the addition funnel of the Mg flask and was then added dropwise to the Mg turnings. After addition, the reaction was allowed to stir for 1 h. Following stirring, this solution was dropwise added to the NiBr₂ reaction flask and allowed to stir for 20 minutes. The following steps should be performed quickly, to minimize air exposure of the catalyst precursor, though it is relatively stable under air. The reaction was quenched by precipitating into 250 mL of MeOH. The catalyst was collected by filtration, and the filtrate was washed with methanol until the solvent runs clean, resulting in a yellow-orange powder. The catalyst was then dried in a vacuum oven overnight and stored in a desiccator.

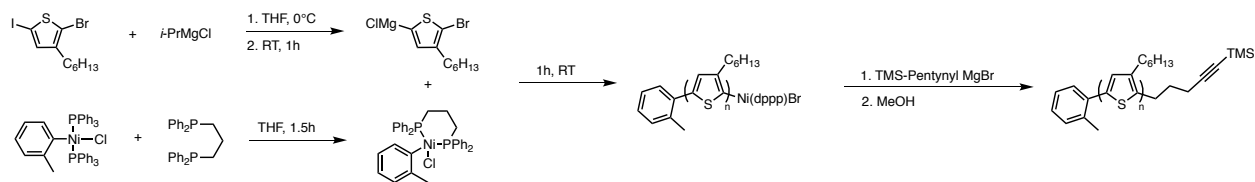
^{31}P NMR (202 MHz, CDCl_3): δ 22 (s, 2P).



Scheme 5.3 Synthetic procedure of (5-magnesio-1-pentynyl)trimethylsilane.

Synthesis of (5-magnesio-1-pentynyl)trimethylsilane (4)

To a dried round bottom flask, Mg (turnings, 87.5 mg, 3.6 mmol) were added, and activated with flame under high vacuum. Anhydrous THF (1.3 mL) was added to the reaction, and then the reaction was heated to 50 °C. 2 drops of 1,2-dibromoethane were added to ensure activation of the magnesium. To a vial, (5-chloro-1-pentynyl)trimethylsilane (0.536 mL, 3 mmol) was added, along with anhydrous THF (1.3 mL) and additional 1,2-dibromoethane (0.026 mL, 0.3 mmol), then mixed. This mixture was then added dropwise to the Mg over 1 h, and the reaction was allowed to stir overnight. The reaction mixture was used without purification in the following reaction.



Scheme 5.4 Synthetic procedures of TMS end-functionalized P3HT

Synthesis of P3HT-TMS

Regioregular P3HT was synthesized following a literature procedure with slight modifications.^[28]

All steps were performed under nitrogen using standard Schlenk techniques. To a Schlenk flask

1,3-bis(diphenylphosphino)propane (44.906 mg, 0.108 mmol) and chloro(tolyl)(PPh₃)₂Nickel(II) (41.072 mg, 0.0544 mmol) were added, and degassed under vacuum for 30 min. The flask was returned to nitrogen, then anhydrous THF (5 mL) was added, and the flask was allowed to stir for 2 h.

To a separate flask, 2-bromo-3-hexyl-5-iodothiophene (1.090 g, 5 mmol) was added, then degassed under vacuum for 30 min. Then, THF (50 mL) was added, the flask was cooled to 0 °C, and *i*-PrMgCl (2.475 mL, 4.95 mmol, 2.0 M in THF) was added dropwise over 10 min. The flask was then allowed to warm to RT and stirred for 1 h. Following stirring, the catalyst flask contents were added to the monomer flask, initiating the polymerization. Polymerization was allowed to continue for 1 h, then the polymerization was quenched with the addition of (5-magnesio-1-pentynyl)trimethylsilane solution (1.565 mL, 1.80 mmol, 1.15 M in THF), which was allowed to stir for 5 min. The polymer was then precipitated into excess MeOH and collected by filtration. The polymer was then dissolved in CHCl₃ and precipitated into MeOH two more times. The polymer was then collected and dried under vacuum, then stored under nitrogen. The molecular weight was measured as 15 kg/mol by ¹H NMR with 100% regioregularity.

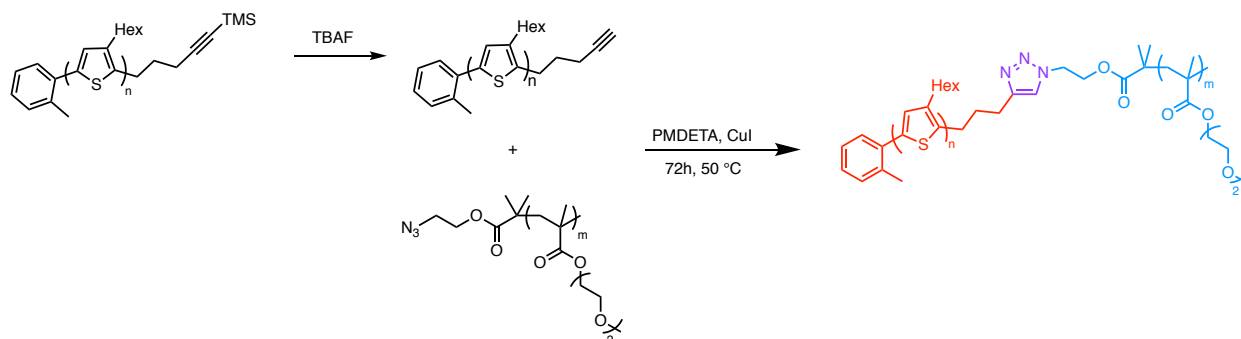
5.2.3.3 Synthesis of P3HT-*b*-POEM copolymer via copper-catalyzed alkyl-azide cycloaddition (CuAAC)

The synthetic procedure of P3HT-*b*-POEM copolymer consists of two steps:

Step 1: Deprotection of P3HT-TMS

P3HT-TMS homopolymer (0.11 g, ~ 0.007 mmol) was dissolved in 15 mL anhydrous THF under Argon atmosphere. TBAF (1.0 M in THF, 0.5 mL) was added in one shot and the reaction mixture was stirred at 50 °C for 4 h. THF was then evaporated and the deprotected P3HT-alkyne block was

precipitated in cold methanol and filtered for three times. The polymer was collected after being dried in a vacuum oven.



Scheme 5.5 Synthetic procedure of P3HT-*b*-POEM via CuAAC “click” reaction.

Step 2: Copper-catalyzed “click” reaction for P3HT-*b*-POEM

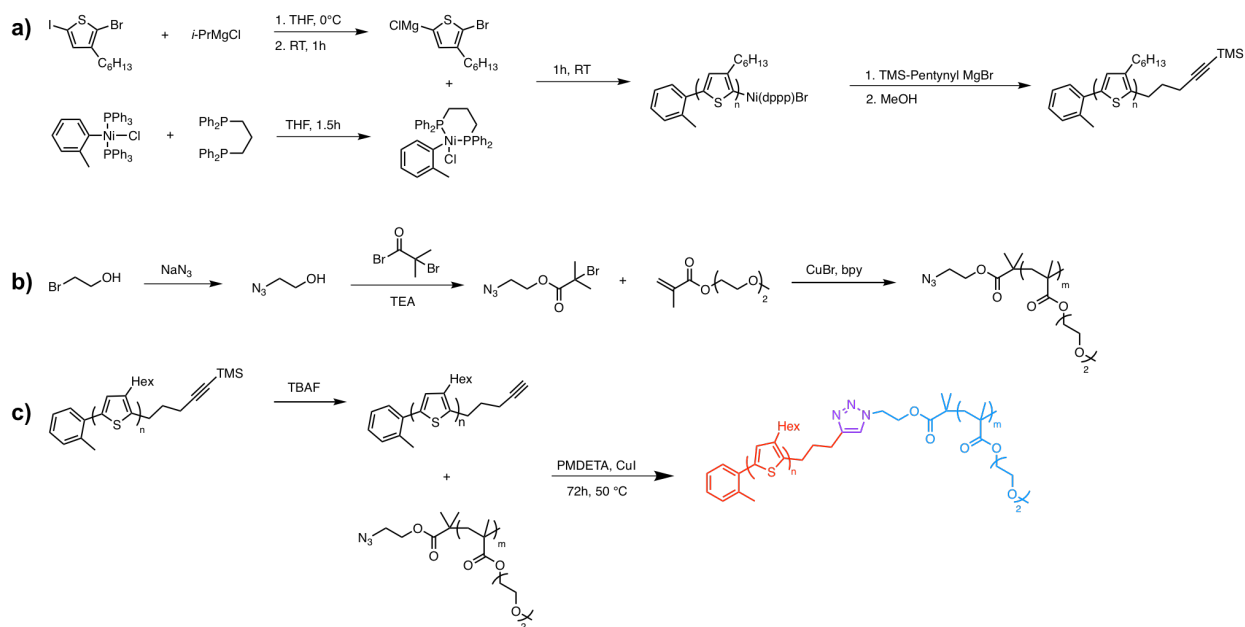
The deprotected P3HT-alkyne (0.11 g, ~ 0.007 mmol) and azido-POEM (DP) (0.5 g, ~ 0.021 mmol) were dissolved in 20 mL anhydrous THF under Argon atmosphere. PMDETA (0.07 mmol) and CuI (0.07 mmol) were added and the reaction was stirred at 50 °C for 72 h. Then, to the block copolymer solution chloroform was added and the solution was passed through a short column of neutral Al₂O₃ and concentrated. The final product was precipitated in methanol and filtered several times followed by drying in vacuum oven to yield a purple solid.

5.3 Results and Discussion

5.3.1 Synthesis of regioregular P3HT-*b*-POEM

Regioregularity (RR), defined as the percentage of head-to-tail (H-T) linkage of side chains along a polymer backbone, has been identified as a key parameter for determining the degree of crystallization of polymers^[29] and their optoelectrical properties. A polymer containing largely H-

T couplings is identified as regioregular while a polymer that contains all possible couplings is regiorandom. The regioregular polymers have attracted more interest than their regiorandom analogues. The three aspects of regioregular P3HT, i.e. conformational ordering along the backbone, π -stacking of flat polymer chains, and lamellar stacking between chains, produce long and highly crystalline fibrils, leading to excellent electrical properties of these materials, such as high conductivity and mobility.^[30–32] On the contrary, the loss of regioregularity due to multiple head-to-head (HH) and tail-to-tail (TT) couplings leads to sterically twisted structures in the polymer backbone, giving rise to a loss of π -conjugation and resulting in destruction of high conductivity and other desirable properties. For example, mobilities of regioregular poly(3-hexylthiophene) (rrP3HT) are as high as $0.2 \text{ cm}^2/(\text{V s})$, while those of regiorandom P3HT are $\sim 10^{-5} \text{ cm}^2/(\text{V s})$.



Scheme 5.6 Synthetic procedures of (a) regioregular P3HT-TMS block *via* Kumada Catalyst Transfer Polymerization, (b) α -azido-POEM block *via* ATRP, (c) P3HT-*b*-POEM copolymer *via* copper(I)-catalyzed azide–alkyne cycloaddition (CuAAC).

Generally, the synthetic strategies for preparation of rod-coil BCPs can be divided into two categories: “growing from” and “grafting to” as a two-stage synthesis approach is commonly used for combination of two different polymerization techniques. In the “growing-from” approach, the rigid block is first synthesized and then used as a macroinitiator to generate the coil block via living polymerization, such as ATRP,^[3,33,34] RAFT,^[4] ROMP^[35] or anionic polymerization.^[36] However, the subsequent second block is usually small due to slow kinetics and the dispersity broadening with increasing molecular weight.^[37] In the “grafting to” approach, both rod and coil blocks with complementary functional end-groups are synthesized independently and subsequently tethered together by a coupling reaction, such as etherification or “click” chemistry.^[38–40] In this case, not only can the two building blocks be well defined and characterized before coupling, more options of the coil block with a large variety of chemical structures and molecular weights could be introduced to the block copolymer system.

The rod-coil P3HT-b-POEM block copolymer was obtained *via* a “grafting-to” method by convenient and versatile CuAAC “click” chemistry. Such a synthetic approach has been demonstrated to be particularly effective for synthesis in organic semiconductors and electronics, providing pure and stable materials, offering high efficiency and quantitative yield, and enabling precise control of the resulting block copolymer.^[40] For the precursor homopolymers, the α -azido-POEM was obtained by ATRP with 2-azidopropyl 2-bromoisobutyrate (ABIB) as initiator synthesized in a two-step reaction following published procedures^[41] with good yield and purity. The α -azido-POEM samples were prepared by ATRP of di(ethylene glycol)methyl ether methacrylate at 40 °C in the presence of Cu(I)Br/bipyridyl as catalyst and ligand. The initial ratios between monomer and initiator were varied (130:1, 100:1, 80:1, 50:1) in order to achieve different

chain lengths. Alkynyl-terminated 100% regioregular P3HT was synthesized *via* GRIM following literature procedures^[28] as shown in **Scheme 5.6**.

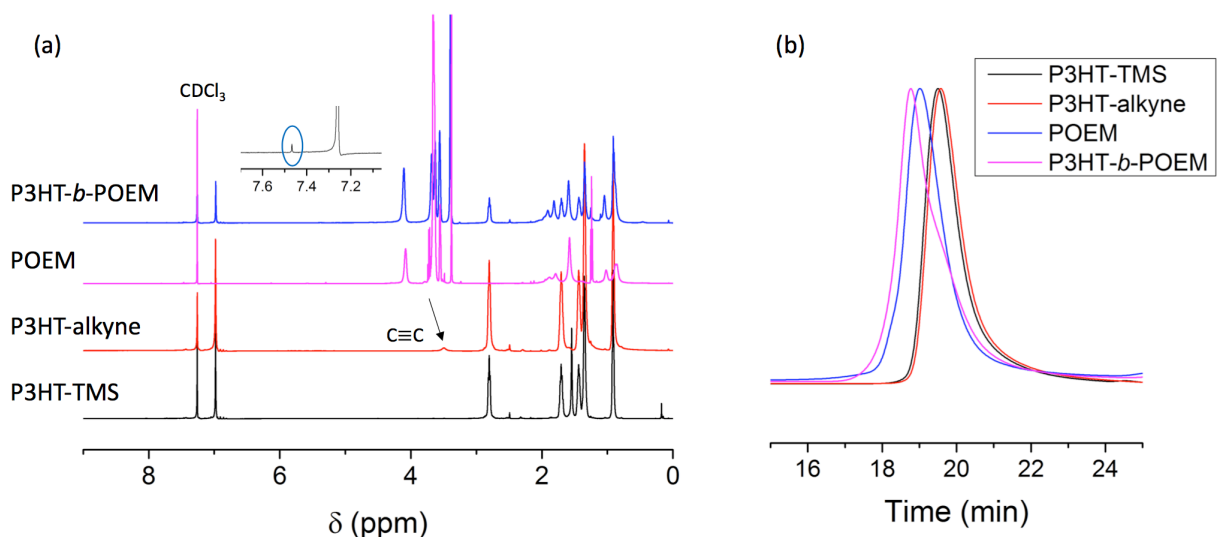


Figure 5.1 (a) NMR spectra (500 MHz, CDCl₃) and (b) GPC traces (THF, polystyrene standards) of P3HT and POEM homopolymers and P3HT-*b*-POEM copolymer.

NMR spectra helped us to identify the characteristic functional groups of each polymer chain, as shown in **Figure 5.1(a)**. For the P3HT block, the two peaks at 7.0 ppm and 2.8 ppm are assigned to the P3HT backbone proton at position 4 and the α -methylene protons of the hexyl chains, respectively. For specifically the tolyl-initiated sample, we can use the ratio of integrations of the hexyl chain protons to the tolyl methyl protons, enabling an NMR-measure of number average molecular weight, M_n . From this ratio, it was determined that the P3HT block has $M_n = 15$ kg/mol. NMR also allows quantification of the regioregularity of P3HT.^[42] Our material shows an absence of regiodefekt peaks, and thus presents 100% regioregularity. After deprotection of TMS end-functional group with TBAF, an α -tolyl- ω -pentynyl-P3HT chain was obtained, indicated by the appearance of a singlet signal at 3.52 ppm attributed to terminal alkyne proton, as indexed by the

arrow. For P3HT-*b*-POEM copolymer, not only does the spectrum contain both functionalities from the two precursor homopolymers, the simultaneous appearance of triazole ring signal at 7.47 ppm formed by cycloaddition and disappearance of terminal alkyne signal also indicate the successful click reaction.

Figure 5.1(b) shows GPC traces of the homopolymer P3HT and POEM (DP 124), as well as the resulting block copolymer. GPC is based on correlating the hydrodynamic volume of the randomly coiled polymer chains with polymer molecular weight. For the flexible POEM homopolymer, the M_n determined by GPC is 23.5 kg/mol with \mathcal{D} 1.15. However, conjugated polymers such as P3HT adopt a more rod-like conformation in solution compared to coil-like polystyrene standards and therefore the GPC results tend to overestimate. The molecular weight of P3HT homopolymer analyzed by GPC exhibited molar masses of 18.5 kg/mol and 17.5 kg/mol for P3HT-TMS and P3HT-alkyne, respectively, with monomodal molar mass distributions and \mathcal{D} close to 1.2. As GPC results are referential with respect to polystyrene standards, the molecular weight of the P3HT block is determined using NMR, as described above. Upon CuAAC “click” reaction, the GPC trace of the block copolymer indicates a shift to shorter retention time, which corresponds to a larger molecular weight, indicating the formation of the block copolymer. The polymer continues to show a quasi-monomodal distribution peak with a tiny shoulder peak attributed to any remaining P3HT homopolymer, which is difficult to completely remove.

Further confirmation of the “click” reaction success was obtained from FTIR as shown in **Figure 5.2**. The characteristic vibrational band of alkyne group in P3HT homopolymer shows up at 3310 cm^{-1} as a tiny absorption indicating successful deprotection of TMS groups. The tiny absorption is due to the small ratio of alkyne group compared to the long polymer chain. For α -azido-POEM, the end-functional group was proved by coexistence of ester bond stretching and azido group

stretching at 1740 and 2100 cm^{-1} respectively. Upon “click” reaction, the total absence of alkyne specific absorption indicates the complete consumption of alkyne-P3HT while the complete disappearance of azido specific absorption indicates successful removal of all excess α -azido-POEM. Moreover, the typical strong absorption of carboxylic group also confirms the incorporation of POEM block into the copolymer system.

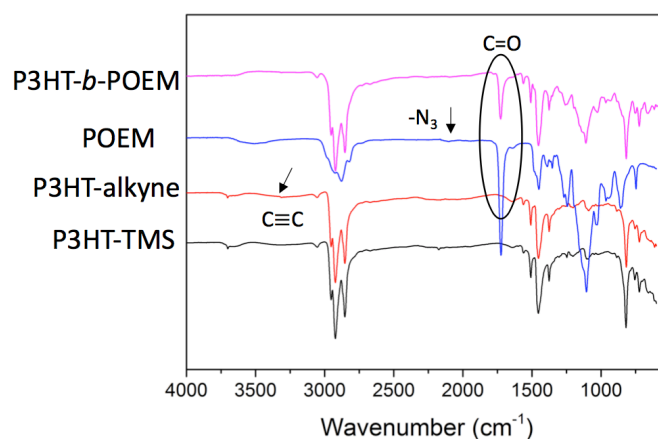


Figure 5.2 FTIR spectra of P3HT and POEM homopolymers and P3HT-*b*-POEM copolymer.

5.3.2 Structural control of P3HT-*b*-POEM via addition of LiTFSI

A combination of grazing incidence small-angle and wide-angle X-ray scattering (GISAXS and GIWAXS) was employed to study the structural evolution of P3HT-*b*-POEM upon the addition of the ionic dopant LiTFSI. The coupling P3HT with POEM block not only introduces additional functionalities but also helps to improve the solution processability of the materials due to the high solubility of POEM in various types of solvents. AFM images of P3HT-*b*-POEM-LiTFSI thin film in Figure 5.3 show smooth, featureless surface topography of all samples ($r = 0 \sim 0.20$) studied, indicative of good miscibility between P3HT-*b*-POEM and LiTFSI.

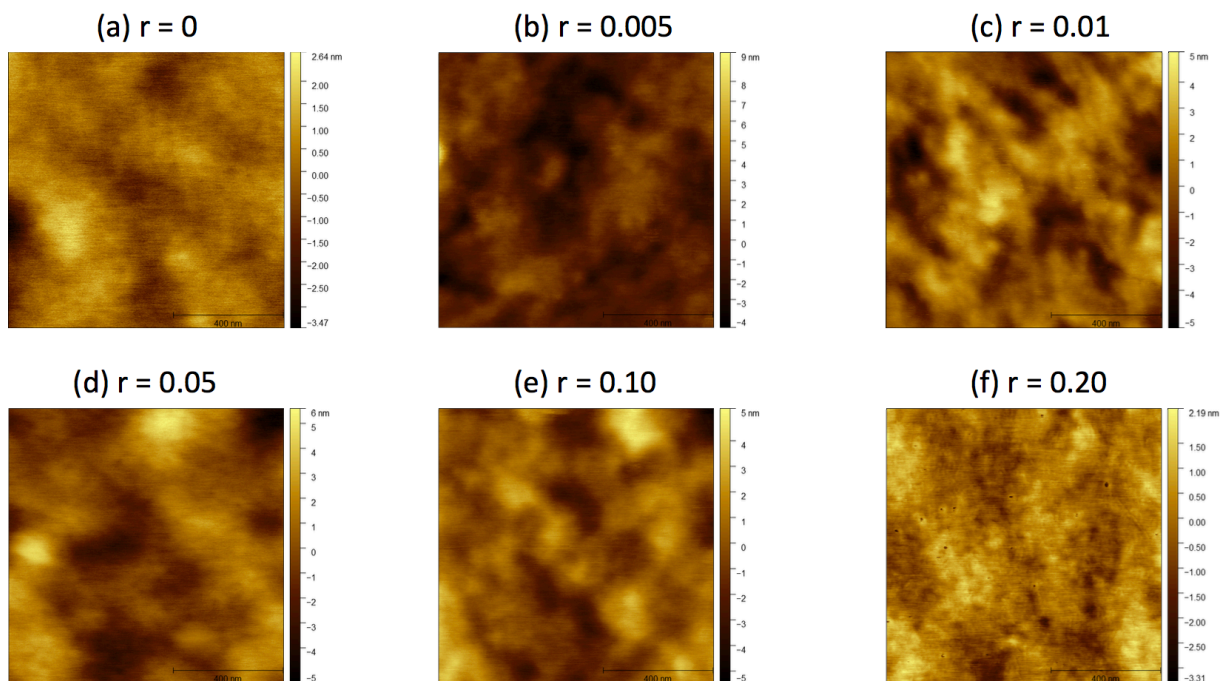


Figure 5.3 AFM phase images of P3HT-*b*-POEM-LiTFSI complex thin films at different Li⁺ blending concentrations. (a) $r = 0$, (b) $r = 0.005$, (c) $r = 0.01$, (d) $r = 0.05$, (e) $r = 0.10$, (f) $r = 0.20$.

GIWAXS measurements were performed to study the crystallite structure of the P3HT block upon addition of LiTFSI. **Figure 5.4(a)** depicts GIWAXS patterns of P3HT-*b*-POEM-LiTFSI thin film with varying LiTFSI blending ratio r at room temperature. The GIWAXS pattern of the neat sample contains diffuse scattering features of side-chain stacking peaks ($h00$) and π -stacking peak (010) both in the in-plane and out-of-plane directions, indicative of a disordered structure of the neat sample. Upon introducing LiTFSI, the GIWAXS patterns of P3HT-*b*-POEM progressively changes. In $r = 0.02$ and 0.10 samples, the intensity of both ($h00$) and (010) peaks increase, suggesting the improvement in relative degree of crystallinity by the addition of LiTFSI. In addition, we observe the ($h00$) peaks predominately in the out-of-plane direction and (010) peak predominately in the in-plane direction, which is indicative of stronger bias toward edge-on orientation of LiTFSI-blended samples. At very high salt concentration of $r = 0.20$, the structure

is still more ordered than the neat sample but there appears additional background scattering which could originate from excess amounts of LiTFSI. Such improvement of molecular order by the addition of ionic dopant has been reported in the literature^[43] and also shown in our previous works on glycolate side chain-bearing polythiophene derivatives^[44] and an oligothiophene-based liquid crystal.^[24] We can conclude here that the P3HT block in this block copolymer exhibits an “edge-on” orientation (shown in **Figure 5.4(d)**) with π -stacking distance (featured by (010) peak) 0.39 nm between P3HT backbone parallel to substrate and lamellae distance (featured by (h00) peaks) 1.6 nm of P3HT side chain spacing perpendicular to substrate.

Furthermore, horizontal and vertical linecuts, featuring π -stacking peaks (010) and side-chain stacking peaks (h00) respectively of the GIWAXS patterns were also analyzed to provide more quantitative comparison between different samples. For the horizontal linecut, the (010) peak shifts to higher q , indicative of the reduction in the π -stacking distance. Below, we will show that this observation is due to electronic doping effect of LiTFSI, leading to the formation of polaron that reduces the π -stacking distance.^[45] For the vertical linecut, the intensity of the side-chain stacking (h00) peak increases upon addition of LiTFSI while the peak position remains almost unchanged. Since GIWAXS measurement is only sensitive to crystallite domain, this observation suggests that LiTFSI either stays in the amorphous domain of P3HT or in the POEM domain. This is in contrast to electrochemical doping^[46] or chemical mixing of ion with conducting polymers^[44] where ions are found to partially infiltrate into the crystallite domains of the samples. Overall, we show that addition of the ionic dopant is a strong method to control the structure of P3HT-*b*-POEM, which will have direct influence on electronic conductivity of the materials.

Figure 5.4(b) depicts GISAXS profiles of P3HT-*b*-POEM-LiTFSI thin films at different LiTFSI concentrations $r = [\text{Li}^+]/[\text{EO}]$ where EO is the number of repeated ethylene oxide units in POEM

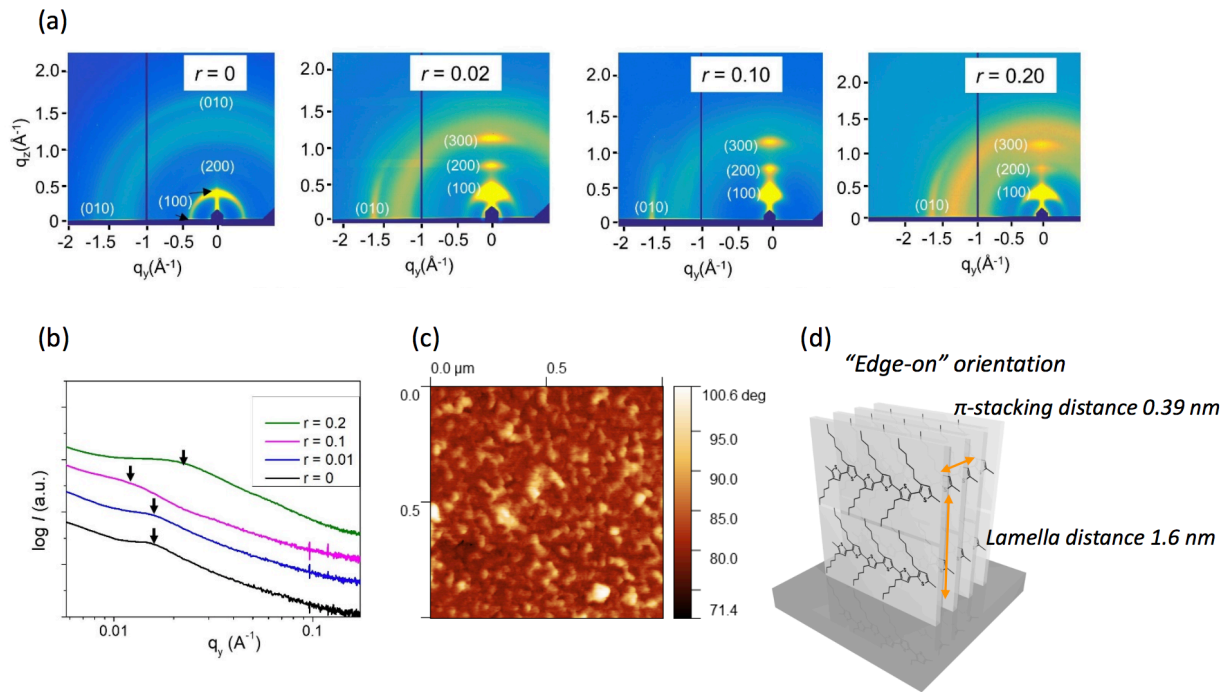


Figure 5.4 (a) Representative GIWAXS patterns of P3HT-*b*-POEM thin films at different LiTFSI blending ratios $r = [\text{Li}^+]/[\text{OEM}]$. (b) GISAXS horizontal linecuts of different P3HT-*b*-POEM-LiTFSI thin film samples. (c) AFM phase image of pristine P3HT-*b*-POEM thin film spin-coated on a piece of silicon wafer. (d) the “Edge-on” orientation of P3HT block in P3HT-*b*-POEM.

block. The GISAXS profile of the neat sample ($r = 0$) only shows a single broad peak near $q = 0.015 \text{ \AA}^{-1}$ which corresponds to a domain spacing L_0 of ca. 42 nm. Upon adding LiTFSI, the domain spacing increases to ca. 49 nm at $r = 0.1$ but unexpectedly reduces to ca. 31 nm at $r = 0.2$. Such weak, featureless GISAXS profile is indicative of rather weak phase separation in conjugated block copolymers. Such phenomenon was also proved by the AFM images of pristine P3HT-*b*-POEM thin film (shown in **Figure 5.4(c)**) in which the P3HT fibrils are immersed in the amorphous POEM matrix instead of forming well-defined phase separation. This is because the strong crystallization of the conjugated block which dominates over microphase separation between incompatible blocks as well-documented in literature.^[47,48]

5.3.3 Improved molecular order and induced electronic doping of P3HT-*b*-POEM by the addition of LiTFSI

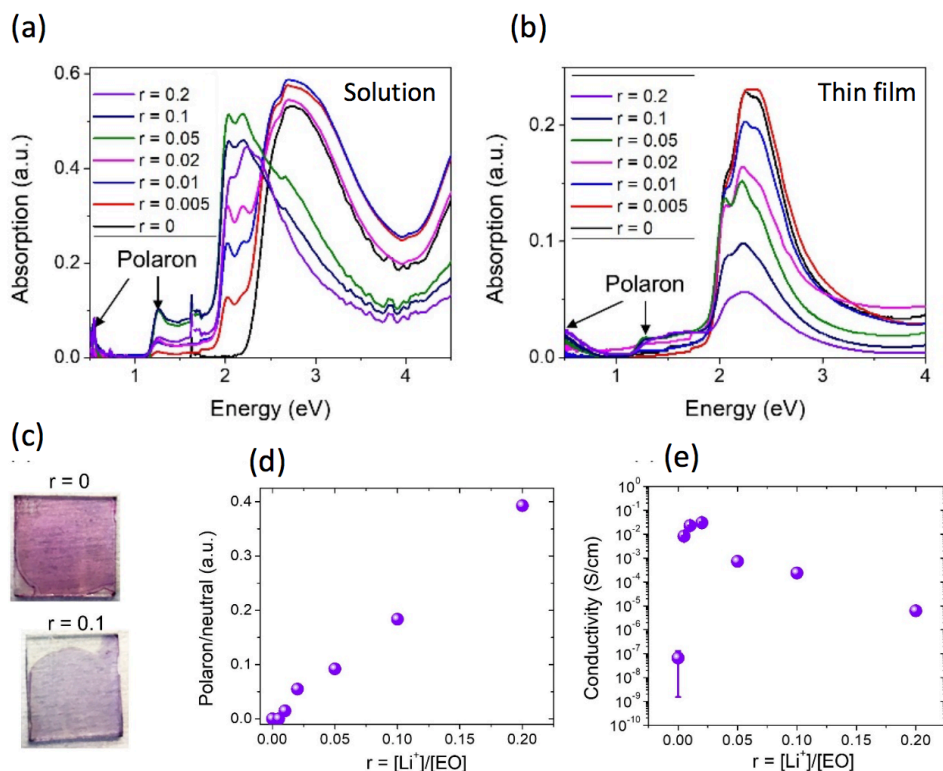


Figure 5.5 Raw UV-vis absorption spectra of P3HT-*b*-POEM-LiTFSI in (a) solution and (b) thin films. (c) Optical images of P3HT-*b*-POEM thin films without LiTFSI (top) and blended with LiTFSI at concentration $r = 0.1$ (bottom). (d) Ratio between the polaron and neutral peak intensity extracted from UV-vis absorption spectra from thin film sample. (e) Electronic conductivity of P3HT-*b*-POEM thin film as a function of LiTFSI blending ratio.

To look into the origin of enhanced molecular order in P3HT-*b*-POEM by LiTFSI, the interaction of P3HT-*b*-POEM with LiTFSI in both solution and thin film states were studied using UV-vis absorption spectroscopy as shown in **Figure 5.5**(a) and (b) respectively. In **Figure 5.5**(a), a single broad absorption peak near 3 eV was observed corresponding to the absorption of disordered amorphous P3HT as expected. Upon blending with LiTFSI, we observe the appearance of the

aggregate shoulders near 2 eV whose relative intensity increases with LiTFSI concentration from $r = 0$ to 0.05 but decreases at higher value of r . Similarly, the relative intensity of the aggregates shoulder in P3HT-*b*-POEM thin film in **Figure 5.5(b)** also increases till $r = 0.05$ before being suppressed at high LiTFSI concentration. Such observation indicates the formation of π -stacked aggregates in solution upon adding LiTFSI, which provides nucleated crystallites/aggregates for crystal growth and directly translates to higher order in solid state samples after spin-casting from solutions. In addition to the formation of aggregates in solution, the introduction of LiTFSI also leads to formation of polaron, indicative of electrical doping of P3HT-*b*-POEM. This is evidenced by the appearance of the polaron absorption peak near 1.2 eV both in solution and thin film state, as indicated by the black arrows. This is a surprising observation since LiTFSI is a redox-inactive. Here, we suspect that the formation of charged conjugated segments in solution provides attractive forces between adjacent chains which promotes the formation of aggregates, similar to observation in mixed solution of conjugated polymer with molecular dopant.^[20] It is important to note that in our experiments we used acetonitrile to dissolve LiTFSI prior to mixing with P3HT-*b*-POEM solution. Since AN is a poor solvent for P3HT, it is also possible to promote aggregation.^[49] To distinguish the effect of acetonitrile and LiTFSI, a controlled experiment was performed in which the P3HT-*b*-POEM is blended with only acetonitrile and doesn't show as much induced aggregation compared to the one with LiTFSI. We thus conclude that the improvement in P3HT-*b*-POEM molecular order originates from the combination of the solubility factor of acetonitrile and the doping effect of LiTFSI.

The electronic doping effect of LiTFSI is quite novel and calls for further investigation. Shown in **Figure 5.5(c)** are the optical images of P3HT-*b*-POEM thin film before and after blending with LiTFSI at concentration $r = 0.1$. It is evident that the addition of LiTFSI results in color bleaching

of P3HT-*b*-POEM, as a result of electrical doping effect of LiTFSI. Moreover, the ratio of the polaron peak intensity near 0.5 eV and neutral peak intensity near 2.3 eV is termed the polaron/neutral ratio and was also calculated as done in prior studies.^[22,50] This polaron/neutral ratio shown in **Figure 5.5(d)** can be used to qualitatively describe the doping level of P3HT-*b*-POEM by LiTFSI. Upon increasing LiTFSI concentration, the polaron/neutral ratio is found to monotonically increase, suggesting the increase in doping level. Room temperature electronic conductivity plot in **Figure 5.5(e)** shows clear effect of LiTFSI doping on electrical performance of P3HT-*b*-POEM. The electronic conductivity of P3HT-*b*-POEM increases by more than 5 orders of magnitude from $(6.5 \pm 5) \times 10^{-8}$ S/cm in neat sample to $(3 \pm 0.2) \times 10^{-2}$ S/cm in $r = 0.02$ samples before dropping to ca. 6.2×10^{-5} S/cm in $r = 0.2$ sample. We attribute the drop of conductivity at high salt concentrations to the disordered structure induced by excessive amount of LiTFSI.

Here, it is worth mentioning that the use of LiTFSI or other redox-inactive salts to improve electrical performance of organic semiconductors have been reported in literature.^[6,24,43,51–53] The enhanced electrical performance in such cases has been attributed to factors such as changes in dielectric constant or molecular order caused by the addition of ionic dopants. To the best of our knowledge, our result was the first report of chemical doping of conjugated polymer by using a redox-inactive salt, which might have important implication for the field of molecular doping. It is also important to note that such chemical doping phenomenon was not observed when blending P3HT-*b*-PEO or just P3HT homopolymer with LiTFSI,^[51] suggesting the important role of the POEM block. A complete understanding of the underlying mechanism for LiTFSI doping in P3HT-*b*-POEM will require probing local nano-scale distribution of ions, using different type of salts and different chemistry of non-conducting blocks, which will be a subject of investigation in future studies.

5.3.4 Further improvement of electrical performance via doping with F4TCNQ vapor

Even though LiTFSI has been shown to electronically dope P3HT-*b*-POEM, the resulting electronic conductivity is relatively low due to the level of doping judged by the weak intensity of the polaron peak. Further doping the materials with the molecular dopant 2,3,5,6-tetrafluoro-7,7,8,8-tetracyanoquinodimethane (F4TCNQ) is necessary to optimize electrical performance of P3HT-*b*-POEM-LiTFSI systems. Sequential doping is employed to introduce F4TCNQ into P3HT-*b*-POEM-LiTFSI thin film via vapor deposition. This method has been shown to lead to homogenous doping through the thickness of the thin film as well as minimal disruption of the underlying self-assembled structure, thus enabling investigation of the influence of LiTFSI on structure and electrical performance of P3HT-*b*-POEM.^[18,23,24,54]

UV-vis measurement was employed again to study the degree of doping of F4TCNQ on P3HT-*b*-POEM-LiTFSI samples at different LiTFSI concentrations. We note that for all of our samples, the optimum doping time was found to be near 5 min where the UV-vis absorption spectra remained unchanged and electrical conductivity saturates. Shown in **Figure 5.6(a)** are absorption spectra of P3HT-*b*-POEM-LiTFSI samples after doping with F4TCNQ at the optimum time of 5 min. F4TCNQ doping leads to the suppression of the main absorption peak near 2.3 eV alongside with the appearance of the F4TCNQ anion peaks near 1.4 and 1.6 eV, polaron peak near 0.5 eV and F4TCNQ neutral peak near 3.5 eV, consistent with integer charge transfer doping mechanism between P3HT block and F4TCNQ as expected.^[22] To quantify the degree of F4TCNQ doping, we show in **Figure 5.6(b)** the polaron/neutral peak intensity ratio. The addition of LiTFSI results in a positive impact on doping efficiency, evident by the increase in the polaron/neutral ratio with increasing LiTFSI concentration. The doping efficiency is highest in $r = 0.2$ sample despite its

highly disordered structure inferred from UV-vis measurement, suggesting that the degree of order is not the major factor affecting doping efficiency in the P3HT-*b*-POEM system. However, it remains difficult to identify the separate contribution from LiTFSI- and F4TCNQ-doping at this moment.

The electronic conductivity of the F4TCNQ-doped samples was also measured as a function of F4TCNQ doping time shown in **Figure 5.6(c)**. Upon exposing the samples to F4TCNQ vapor, the electronic conductivity of the samples quickly rises and saturates after 2 – 5 min. The maximum conductivity for each F4TCNQ-doped P3HT-*b*-POEM-LiTFSI sample is plotted in **Figure 5.6(d)** as a function of LiTFSI concentration. Despite that the conductivity of the neat $r = 0$ sample is 0.61 ± 0.10 S/cm, more than an order of magnitude lower than that of P3HT homopolymer of 14.7 ± 1.7 S/cm, which is attribute to the disordered morphology of P3HT-*b*-POEM inferred from GIWAXS measurement and the presence of POEM block that inhibits transport, the maximum conductivity quickly rises upon introducing LiTFSI and reaches the highest value of 31.6 ± 1.8 S/cm at $r = 0.02$. This value represents an effective conductivity of ca. 75 S/cm (normalized to P3HT volume fraction) which surpasses the conductivity of P3HT homopolymer and demonstrates one of the highest conductivities reported for F4TCNQ doped P3HT systems. The improvement in electrical performance by addition of small amount of LiTFSI could originate from (i) improved molecular order, (ii) the presence of carrier concentration induced by LiTFSI doping, (iii) increase in doping efficiency, or a combination of more than one factor. For $r > 0.02$, the conductivity monotonically decreases with increasing LiTFSI concentration. Since the doping efficiency still increases with r (Figure 5.6(b)), the drop of conductivity at high value of r is likely caused by the reduce in charge carrier mobility evident by the disordered structure probed by UV-vis measurement.

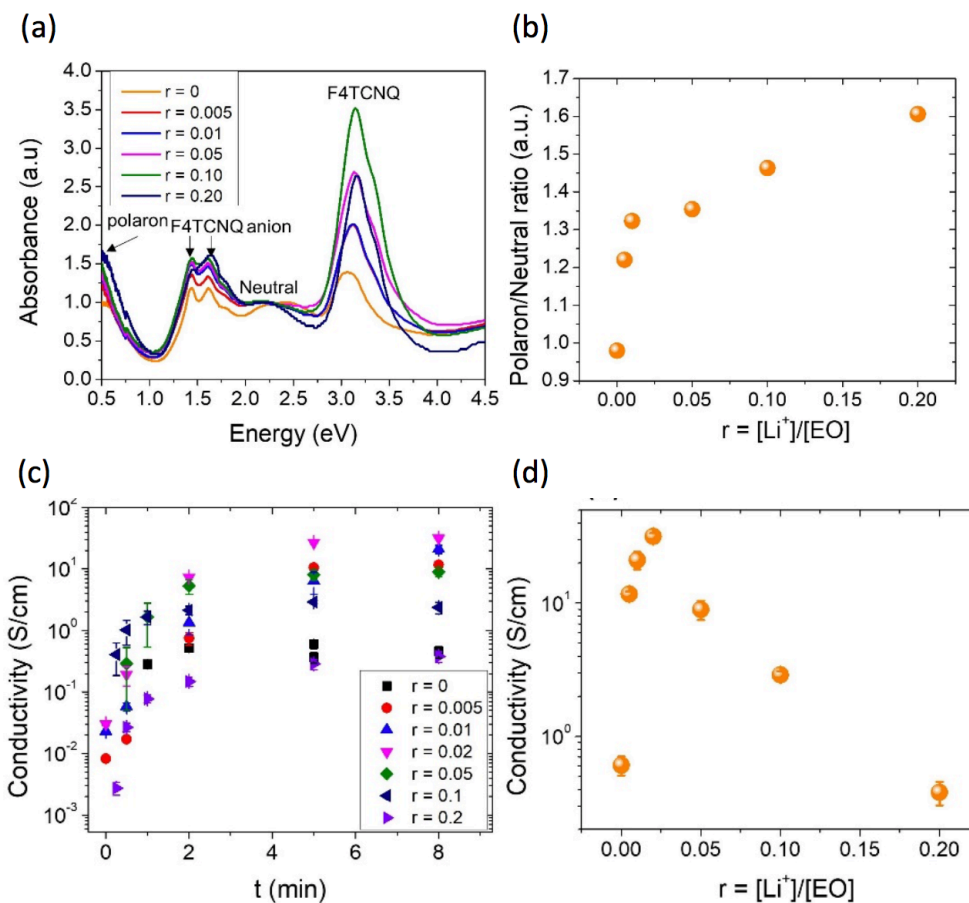


Figure 5.6 (a) UV-vis absorption spectra of different P3HT-*b*-POEM-LiTFSI sample at optimum F4TCNQ doping condition. (b) Ratio of polaron/neutral peak intensity extracted from (a). (c) Electronic conductivity of different P3HT-*b*-POEM-LiTFSI samples as a function of F4TCNQ vapor doping time. (d) Maximum conductivity of each F4TCNQ-doped P3HT-*b*-POEM-LiTFSI samples.

5.4 Conclusions

In conclusion, a conjugated block copolymer P3HT-*b*-POEM was synthesized via CuAAC “click” reaction, in which the rigid P3HT block exhibits promising electronic conductivity while the POEM block provides not only flexibility and solubility, but also potential ionic conductivity due to the side chain ethylene oxide units charged with Li^+ . Although our material doesn’t seem qualified for mixed ionic electronic conductivity due to suppressed microphase separation

resulting from high crystallinity of P3HT block, we did succeed in studying the structural morphology and electronic conductivity characteristics with a variety of methods.

We explored how co-processing the block copolymer P3HT-*b*-POEM with the ionic dopant LiTFSI improved its structure and thermoelectric performance. Overall, co-processing P3HT-*b*-POEM with LiTFSI solution led to a marked enhancement in molecular order probed by both GIWAXS and UV-vis absorption spectroscopy before dropping at higher LiTFSI concentration. We attributed this improvement to the interaction between P3HT-*b*-POEM chain in solution, leading to the formation of aggregates in solution thus resulted in highly order P3HT-*b*-POEM-LiTFSI samples in thin film state. In addition, blending P3HT-*b*-POEM with LiTFSI also resulted in electrical doping of P3HT-*b*-POEM, leading to more than 5 orders of magnitude increase in electronic conductivity. Due to the increase in molecular order, F4TCNQ-vapor doped P3HT-*b*-POEM-LiTFSI sample yielded the highest electrical conductivity around 31 S/cm at $r = 0.02$, which ca. 50 time as high as the neat sample. Our results demonstrated that co-processing conjugated polymer with ionic dopants is a powerful strategy to control morphology and thermoelectric performance for lightweight and low-cost organic thermoelectric modules.

REFERENCES

- [1] F. S. Bates, *Science* **1991**, *251*, 898.
- [2] C. R. Craley, R. Zhang, T. Kowalewski, R. D. McCullough, M. C. Stefan, *Macromol. Rapid Commun.* **2009**, *30*, 11.
- [3] M. C. Iovu, M. Jeffries-EL, E. E. Sheina, J. R. Cooper, R. D. McCullough, *Polymer* **2005**, *46*, 8582.
- [4] M. C. Iovu, C. R. Craley, M. Jeffries-EL, A. B. Krankowski, R. Zhang, T. Kowalewski, R. D. McCullough, *Macromolecules* **2007**, *40*, 4733.
- [5] M. C. Iovu, R. Zhang, J. R. Cooper, D. M. Smilgies, A. E. Javier, E. E. Sheina, T. Kowalewski, R. D. McCullough, *Macromol. Rapid Commun.* **2007**, *28*, 1816.
- [6] X. Liu, K. S. Jeong, B. P. Williams, K. Vakhshouri, C. Guo, K. Han, E. D. Gomez, Q. Wang, J. B. Asbury, *Journal of Physical Chemistry B* **2013**, *117*, 15866.
- [7] W. Han, M. Byun, Z. Lin, *J. Mater. Chem.* **2011**, *21*, 16968.
- [8] Y. J. Lee, S. H. Kim, H. Yang, M. Jang, S. S. Hwang, H. S. Lee, K.-Y. Baek, *J. Phys. Chem. C* **2011**, *115*, 4228.
- [9] S. K. Patra, R. Ahmed, G. R. Whittell, D. J. Lunn, E. L. Dunphy, M. A. Winnik, I. Manners, *J. Am. Chem. Soc.* **2011**, *133*, 8842.
- [10] J. Li, X. Li, D. Ni, J. Wang, G. Tu, J. Zhu, *J. Appl. Polym. Sci.* **2014**, *131*, 41186.
- [11] C.-L. Liu, C.-H. Lin, C.-C. Kuo, S.-T. Lin, W.-C. Chen, *Progress in Polymer Science* **2011**, *36*, 603.
- [12] A. Loiudice, A. Rizzo, M. Biasiucci, G. Gigli, *The Journal of Physical Chemistry Letters* **2012**, *3*, 1908.
- [13] Y. Zhang, H. Zhou, J. Seifert, L. Ying, A. Mikhailovsky, A. J. Heeger, G. C. Bazan, T.-Q. Nguyen, *Advanced materials (Deerfield Beach, Fla.)* **2013**, *25*, 7038.
- [14] H. Yan, J. G. Manion, M. Yuan, F. P. García de Arquer, G. R. McKeown, S. Beaupré, M. Leclerc, E. H. Sargent, D. S. Seferos, *Advanced Materials* **2016**, *28*, 6491.
- [15] G. Lu, J. Blakesley, S. Himmelberger, P. Pingel, J. Frisch, I. Lieberwirth, I. Salzmann, M. Oehzelt, R. Di Pietro, A. Salleo, N. Koch, D. Neher, *Nature communications* **2013**, *4*, 1588.
- [16] B. Lussem, C. M. Keum, D. Kasemann, B. Naab, Z. Bao, K. Leo, *Chemical Reviews* **2016**, *116*, 13714.
- [17] I. E. Jacobs, A. J. Moulé, *Advanced Materials* **2017**, *29*, 1.
- [18] K. Kang, S. Watanabe, K. Broch, A. Sepe, A. Brown, I. Nasrallah, M. Nikolka, Z. Fei, M. Heeney, D. Matsumoto, K. Marumoto, H. Tanaka, S. Kuroda, H. Sirringhaus, *Nature Materials* **2016**, *15*, 896.
- [19] J. D. Roehling, J. Li, G. Zhang, M. P. Augustine, *Journal of Materials Chemistry C* **2016**, *4*, 3454.
- [20] D. T. Scholes, S. A. Hawks, P. Y. Yee, H. Wu, J. R. Lindemuth, S. H. Tolbert, B. J. Schwartz, *Journal of Physical Chemistry Letters* **2015**, *6*, 4786.
- [21] S. N. Patel, A. E. Javier, K. M. Beers, J. A. Pople, V. Ho, R. A. Segalman, N. P. Balsara, *Nano Letters* **2012**, *12*, 4901.
- [22] E. Lim, K. A. Peterson, G. M. Su, M. L. Chabynyc, *Chemistry of Materials* **2018**, *30*, 998.
- [23] J. Hynynen, D. Kiefer, L. Yu, R. Kroon, R. Munir, A. Amassian, M. Kemerink, C. Müller, *Macromolecules* **2017**, *50*, 8140.
- [24] B. X. Dong, Z. Liu, M. Misra, J. Strzalka, J. Niklas, O. Poluektov, F. A. Escobedo, C. K. Ober, P. F. Nealey, S. N. Patel, *ACS Nano* **2019**, *13*, 7665–7675.

- [25] J. Gao, B. W. Stein, A. K. Thomas, J. A. Garcia, J. Yang, M. L. Kirk, J. K. Grey, *Journal of Physical Chemistry C* **2015**, *119*, 16396.
- [26] I. Salzmann, G. Heimel, M. Oehzelt, S. Winkler, N. Koch, *Accounts of Chemical Research* **2016**, *49*, 370.
- [27] A. Saha, T. K. Paira, M. Biswas, S. Jana, S. Banerjee, T. K. Mandal, *J. Polym. Sci., Part A: Polym. Chem.* **2015**, *53*, 2313.
- [28] H. A. Bronstein, C. K. Luscombe, *J. Am. Chem. Soc.* **2009**, *131*, 12894.
- [29] C. R. Snyder, J. S. Henry, D. M. DeLongchamp, *Macromolecules* **2011**, *44*, 7088.
- [30] D. C. Coffey, D. S. Ginger, *Nature Mater* **2006**, *5*, 735.
- [31] H. Sirringhaus, P. J. Brown, R. H. Friend, M. M. Nielsen, K. Bechgaard, B. M. W. Langeveld-Voss, A. J. H. Spiering, R. A. J. Janssen, E. W. Meijer, P. Herwig, D. M. de Leeuw, *Nature* **1999**, *401*, 685.
- [32] R. Mauer, M. Kastler, F. Laquai, *Adv. Funct. Mater.* **2010**, *20*, 2085.
- [33] Y. Lee, K.-I. Fukukawa, J. Bang, C. J. Hawker, J. K. Kim, *J. Polym. Sci. A Polym. Chem.* **2008**, *46*, 8200.
- [34] J. Liu, E. Sheina, T. Kowalewski, R. D. McCullough, *Angew. Chem. Int. Ed.* **2002**, *41*, 329.
- [35] C. P. Radano, O. A. Scherman, N. Stingelin-Stutzmann, C. Müller, D. W. Breiby, P. Smith, R. A. J. Janssen, E. W. Meijer, *J. Am. Chem. Soc.* **2005**, *127*, 12502.
- [36] C.-A. Dai, W.-C. Yen, Y.-H. Lee, C.-C. Ho, W.-F. Su, *J. Am. Chem. Soc.* **2007**, *129*, 11036.
- [37] H. Lim, K.-T. Huang, W.-F. Su, C.-Y. Chao, *J. Polym. Sci. A Polym. Chem.* **2010**, *48*, 3311.
- [38] T. Higashihara, K. Ohshimizu, A. Hirao, M. Ueda, *Macromolecules* **2008**, *41*, 9505.
- [39] Y. Tao, B. McCulloch, S. Kim, R. A. Segalman, *Soft Matter* **2009**, *5*, 4219.
- [40] M. Urien, H. Erothu, E. Cloutet, R. C. Hiorns, L. Vignau, H. Cramail, *Macromolecules* **2008**, *41*, 7033.
- [41] A. Saha, T. K. Paira, M. Biswas, S. Jana, S. Banerjee, T. K. Mandal, *J. Polym. Sci., Part A: Polym. Chem.* **2015**, *53*, 2313.
- [42] R. D. McCullough, *Adv. Mater.* **1998**, *10*, 93.
- [43] H. Luo, C. Yu, Z. Liu, G. Zhang, H. Geng, Y. Yi, K. Broch, Y. Hu, A. Sadhanala, L. Jiang, P. Qi, Z. Cai, H. Sirringhaus, D. Zhang, *Science Advances* **2016**, *2*, 1.
- [44] B. X. Dong, C. Nowak, J. W. Onorato, J. Strzalka, F. A. Escobedo, C. K. Luscombe, P. F. Nealey, S. N. Patel, *Chemistry of Materials* **2019**, *31*, 1418.
- [45] W. Liu, L. Müller, S. Ma, S. Barlow, S. R. Marder, W. Kowalsky, A. Köhn, R. Lovrincic, *The Journal of Physical Chemistry C* **2018**, *122*, 27983.
- [46] E. M. Thomas, M. A. Brady, H. Nakayama, B. C. Popere, R. A. Segalman, M. L. Chabinyc, *Adv. Funct. Mater.* **2018**, *28*, 1803687.
- [47] J. P. Coote, J. S. Kim, B. Lee, J. Han, B. J. Kim, G. E. Stein, *Macromolecules* **2018**, *51*, 9276.
- [48] J. S. Kim, Y. Kim, H. J. Kim, H. J. Kim, H. Yang, Y. S. Jung, G. E. Stein, B. J. Kim, *Macromolecules* **2017**, *50*, 1902.
- [49] B. G. Kim, M. S. Kim, J. Kim, *ACS Nano* **2010**, *4*, 2160.
- [50] J. Hynynen, D. Kiefer, C. Müller, *RSC Advances* **2018**, *8*, 1593.
- [51] S. N. Patel, A. E. Javier, G. M. Stone, S. A. Mullin, N. P. Balsara, *ACS Nano* **2012**, *6*, 1589.

- [52] H. J. Snaith, M. Grätzel, *Applied Physics Letters* **2006**, 89.
- [53] B. A. Gregg, S. G. Chen, H. M. Branz, *Applied Physics Letters* **2004**, 84, 1707.
- [54] S. N. Patel, A. M. Glaudell, K. A. Peterson, E. M. Thomas, K. A. O'Hara, E. Lim, M. L. Chabinyc, *Science Advances* **2017**, 3, e1700434.

Chapter Six: Paired Ionic-Electronic Conduction in Regioregularity (RR)-Controlled Self-Assembled P3HT-POEM Rod-Coil Block Copolymers

6.1 Introduction

The importance of conductivity pathways for effective charge transport between adjacent conjugated polymer chains leads to interest in high crystallinity and well-ordered intermolecular assembly when considering materials for producing efficient electronic devices.^[1,2] On the other hand, excessive crystallization of conjugated polymers has an adverse effect on their processability and mechanical stability, which lead to poor solubility and brittleness respectively, making it difficult to produce a uniform film with cost-effective solution processing techniques and could even limit their application. The idea of a conjugated block copolymer, as mentioned in the prior chapter, could mitigate geometric constraints, provide more flexibility^[3] and modify the solubility^[4,5] by introducing a flexible coil block in addition to a rigid conjugated block. P3HT, as one of the most studied conjugated polymers,^[6] has attracted interest in the synthesis of block copolymers in which its unique opto-electronic properties are combined with self-assembly into nanostructures with a number of complex morphologies. There have been numerous examples of block copolymers involving P3HT such as P3HT-*b*-PAA,^[7,8] P3HT-*b*-P2VP,^[9–11] P3HT-*b*-P4VP,^[12–14] P3HT-*b*-PEO^[15,16] and others. Specially in the P3HT-*b*-PEO copolymer, the coil blocks have additional functions aside from providing phase-separation. In fact, the incorporation of a p-type semiconductor and an ionic conductor allows for application in electrochemical energy storage devices which requires both ionic and electronic transport.^[16] For example, it can be used as a polymer electrolyte for lithium batteries, serving as both binder and charge transporter.

In conventional coil-coil block copolymers where the self-assembly behavior is driven by phase-separation of random coil blocks, various equilibrium morphologies can be tuned by adjusting the

volume fraction of each block, the Flory-Huggins interaction parameter, χ , and the degree of polymerization. In rod-coil block copolymers, the stiffness asymmetry and topological disparity between the two blocks require the introduction of two more parameters: the Maier-Saupe interaction strength characterizing the alignment interaction between rod blocks, and geometrical asymmetry which is defined as the ratio between the coil radius of gyration and the rod length.^[17] Therefore, self-assembly is controlled by competition between phase-segregation driven by Flory-Huggins enthalpic interactions and strong crystallization driven by intermolecular interactions of conjugated chains.^[2]

Tuning the RR of conjugated polymers has become an important means to modify and optimize their thermal and optical performances. Kim et al.^[1,2] has demonstrated that decrease of RR caused distortion of the packing structures and subsequently lowered the degree of crystallinity. Electrical performance was reduced though the lower RR P3HTs showed great improvement with respect to the mechanical properties such as decreased tensile modulus and high elongation for mechanical stability. In order to achieve mixed ionic-electronic conducting functions from conjugated block polymers, well-ordered phase separation is required for the formation of co-continuous phase as confined charge transport channels for ions and electronic charge carriers. To this end, we managed to suppress the crystallinity of the P3HT block by synthesizing a series of P3HTs with varying regioregularities (RR).

A PEOMEMA block with higher density of ethylene oxide units in the side chains was also synthesized via ATRP and the final diblock copolymer was produced with the same “click” reaction. A higher ethylene oxide density of PEOMEMA block rendered the block copolymer more hydrophilic and required more complicated purification methods. The subsequent phase morphology and self-assembly behavior of block copolymers with varying RR values and volume

fractions were studied by AFM, TEM and exhibited short-range order. Moreover, intrinsically charged coil block such as poly(sodium 4-styrenesulfonate) (PSS) and poly(4-vinylpyridine) (P4VP) were also synthesized via ATRP and RAFT respectively as a comparison with intrinsically non-charged POEM. Currently this project is still ongoing and more intriguing results will come out soon.

6.2 Experimental Section

6.2.1 Materials

3-Hexylthiophene, N-bromosuccinimide (NBS) were purchased from AK Scientific, Inc. Sodium 4-vinylbenzenesulfonate, 4-vinylpyridine, 2,2'-bipyridyl (bpy), copper (I) bromide (Cu(I)Br), copper (I) iodide (Cu(I)I), *N,N,N',N'',N''*-pentamethyldiethylenetriamine (PMDETA), tetrakis(triphenylphosphine)palladium(0) (Pd(PPh₃)₄), 2-isopropoxy-4,4,5,5-tetramethyl-1,3,2-dioxaborolane, isopropylmagnesium chloride lithium chloride complex solution (*i*-PrMgCl LiCl, 1.3 M in THF), ethynylmagnesium bromide solution (0.5 M in THF), triethylamine (TEA), 4-dimethylaminopyridine (DMAP), *N,N'*-dicyclohexylcarbodiimide (DCC), azobisisobutyronitrile (AIBN), poly(ethylene glycol) methyl ether methacrylate (average $M_n \sim 300$) were purchased from Sigma-Aldrich. 2-(((Dodecylthio)carbonothioyl)thio)-2-methylpropanoic acid was purchased from AmBeed. Organic solvents such as acetone, hexane, ethyl acetate (EtOAc), methanol (MeOH), anhydrous dichloromethane (CH₂Cl₂), ethanol (EtOH), tetrahydrofuran (THF), and chloroform (CHCl₃) were purchased from Fisher and VWR. 1,2-dimethoxyethane (DME) was purchase from Honeywell. NBS was recrystallized with water and stored in fridge prior to use. THF was freshly distilled with sodium and benzophenone under a N₂ atmosphere prior to use. Poly(ethylene glycol)methyl ether methacrylate (average $M_n \sim 300$) monomer was made inhibitor-

free and stored at -20 °C freezer before polymerization. 4-Vinylbenzenesulfonate was distilled and stored at -20 °C freezer before polymerization.

6.2.2 Characterizations

6.2.2.1 Nuclear magnetic resonance (NMR)

¹H and ¹³C NMR spectra were recorded on a Mercury 300, a Varian INOVA 400, a Bruker AV 500 spectrometers at room temperature. Chemical shifts were quoted relative to the residual protons of the deuterated solvents CDCl₃ ($\delta = 7.26$ for ¹H and $\delta = 77.36$ for ¹³C). The multiplicity was characterized by the following abbreviations: s-singlet, d-doublet, t-triplet, q-quartet, m-multiplet.

6.2.2.2 Gel Permeation Chromatography (GPC)

GPC was performed on a Waters ambient-temperature GPC instrument equipped with a Waters 410 differential refractive index detector and a Waters 486 UV-Vis detector. GPC was performed at a flow rate of 1.0 mL/min with THF or DMF with 0.05 M LiBr as the eluent at 40 °C and the elution times were converted to molecular weights using a calibration curve based on low dispersity polystyrene (PS) standards.

6.2.2.3 Transmission electron microscope (TEM)

TEM was performed on a 120 kV field emission FEI T12 Spirit TEM equipped with an LaB6 filament, a SIS Megaview III CCD camera, and a STEM dark field and bright field detector. Polymer samples were drop-casted on carbon grids and stained by RuO₄ aqueous solution.

6.2.2.4 Atomic force microscope (AFM)

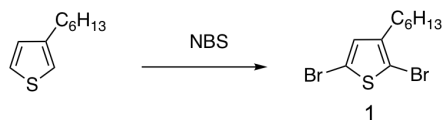
AFM measurements were performed on an Asylum MFP-3D atomic force microscope using the tapping (AC) mode. Polymer samples were spin-coated on silicon wafers from chloroform solutions followed by thermal annealing.

6.2.2.5 UV-vis spectroscopy

UV-vis measurements were conducted on a Shimadzu UV-Vis-NIR Spectrometer with absorption range from 200-700 nm. For solution state measurement, polymer samples were dissolved in dry THF or dispersed in MeOH at concentration of 1 mg/mL.

6.2.3 Synthetic procedures

6.2.3.1 Synthesis of regioregularity (RR)-controlled P3HT



Scheme 6.1 Synthetic procedure of 3-hexylthiophene monomer.

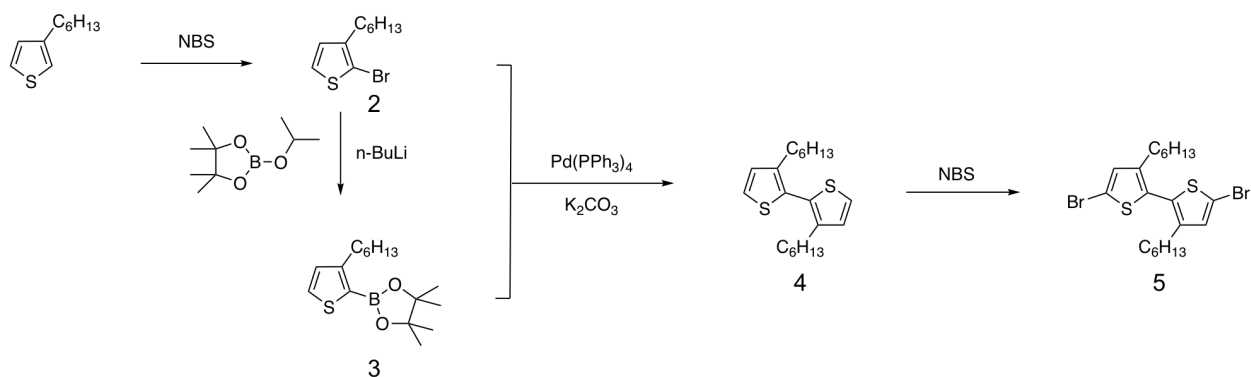
Synthesis of 2,5-dibromo-3-hexylthiophene (1)

3-hexylthiophene (1.0 eq, 25 mmol) was dissolved in 50 mL THF in a round-bottom flask and cooled down to 0°C. NBS (2.6 eq, 65 mmol) was added portionwise to the flask in 30 min. The reaction mixture was stirred at 0°C for another 30 min followed by room temperature overnight. The reaction was quenched by NaOH solution and extracted with EtOAc (30 mL × 3). The organic layer was then washed with water (30 mL × 3) followed by dried over MgSO₄ and concentrated.

The crude product was purified by column chromatography with hexane as eluent to get the final product as colorless liquid in 90% yield.

^1H NMR (300MHz, CDCl_3 , δ): 6.78 (s, 1H; Th H), 2.51 (t, $J=9$ Hz, 2H; CH_2), 1.54 (quintet, $J=6$ Hz, 2H; CH_2), 1.30 (m, 6H; $(\text{CH}_2)_3$), 0.90 (t, $J=6$ Hz, 3H; CH_3).

^{13}C NMR (300MHz, CDCl_3 , δ): 142.99, 130.95, 110.33, 107.95, 31.61, 29.59, 28.83, 22.62, 14.13.



Scheme 6.2 Synthetic procedures of head-to-head (H-H) linked 3-hexylthiophene dimer.

Synthesis of 2-bromo-3-hexylthiophene (2)

3-hexylthiophene (1.0 eq, 25 mmol) was dissolved in 50 mL THF in a round-bottom flask and cooled down to 0°C . NBS (1.05 eq, 26.25 mmol) was added portionwise to the flask in 30 min. The reaction mixture was stirred at 0°C for another 30 min followed by room temperature overnight. The reaction was quenched by NaOH solution and extracted with EtOAc ($30\text{ mL} \times 3$). The organic layer was then washed with water ($30\text{ mL} \times 3$) followed by dried over MgSO_4 and concentrated. The crude product was purified by column chromatography with hexane as eluent to give **2** as colorless liquid in 96 % yield.

^1H NMR (300MHz, CDCl_3 , δ): 7.19 (d, $J=6\text{Hz}$, 1H; Th H), 6.80 (d, $J=6\text{Hz}$, 1H; Th H), 2.56 (t, $J=7.56\text{Hz}$, 2H; Th- $\underline{\text{CH}_2}$), 1.57 (m, 2H; Th- CH_2 - $\underline{\text{CH}_2}$), 1.31 (m, 6H; $(\text{CH}_2)_3$), 0.89 (t, $J=6\text{Hz}$, 3H; CH_3).

Synthesis of 2-(3-hexylthiophen-2-yl)-4,4,5,5-tetramethyl-1,3,2-dioxaborolane (**3**)

2 (1.0 eq, 10mmol) and 2-isopropoxy-4,4,5,5-tetramethyl-1,3,2-dioxaborolane (2.0 eq, 20 mol) were mixed with 20 mL anhydrous THF in a dry flask. The reaction mixture was purged with Argon for 30 min and then cooled down to $-78\text{ }^\circ\text{C}$ with acetone/dry ice bath. $n\text{-BuLi}$ (1.2 eq, 12 mmol) was slowly added to the reaction mixture at $-78\text{ }^\circ\text{C}$ followed by warmed up to room temperature and stirred overnight. The reaction was then quenched by cold water and extracted with EtOAc (40 mL \times 3). The organic layer was washed with water (30 mL \times 3) followed by dried over MgSO_4 and concentrated via Rotavap. The crude product was purified by column chromatography with hexane/EtOAc (20:1, v/v) as eluent to give **3** as slight yellow liquid in 79% yield.

^1H NMR (300MHz, CDCl_3 , δ): 7.49 (d, $J=6\text{ Hz}$, 1H; Th H), 7.02 (d, $J=6\text{ Hz}$, 1H; Th H), 2.88 (t, $J=6\text{Hz}$, 2H; Th- $\underline{\text{CH}_2}$), 1.57 (m, 2H; Th- CH_2 - $\underline{\text{CH}_2}$), 1.33 (s, 12H; CH_3), 1.30 (m, 6H; $(\text{CH}_2)_3$), 0.88 (t, $J=6\text{Hz}$, 3H; Th- $(\text{CH}_2)_5$ - $\underline{\text{CH}_3}$).

Synthesis of 3,3'-dihexyl-2,2'-bithiophene (**4**)

To a dry 3-neck flask equipped with a condenser and a stir bar was added **2** (1.0 eq, 5 mmol), **3** (1.2 eq, 6 mmol), and K_2CO_3 (3.0 eq, 15 mmol). The flask was purged with Argon for 30 min followed by addition of $\text{Pd}(\text{PPh}_3)_4$ (0.01 eq, 0.05 mmol). Meanwhile to another round bottom flask was added mixed solvent of DME/ H_2O (40 mL + 10 mL). The solvent was purged with Argon for

30 min followed by canula transferred to the 3-neck flask. The reaction mixture was refluxed at 85 °C overnight. The crude product was extracted with EtOAc (30 mL × 3), washed with water (30 mL × 3), dried over MgSO₄, and purified by column chromatography with pure hexane as eluent to give **4** as colorless liquid in 95% yield.

¹H NMR (300MHz, CDCl₃, δ): 7.29 (d, J=6Hz, 2H; Th H), 6.97 (d, J=6Hz, 2H; Th H), 2.49 (t, J=6Hz, 4H, Th-CH₂), 1.54 (m, 4H; Th-CH₂-CH₂), 1.24 (m, 12H; (CH₂)₃), 0.85 (t, J=6Hz, 6H; CH₃).

Synthesis of 5,5'-dibromo-3,3'-dihexyl-2,2'-bithiophene (**5**)

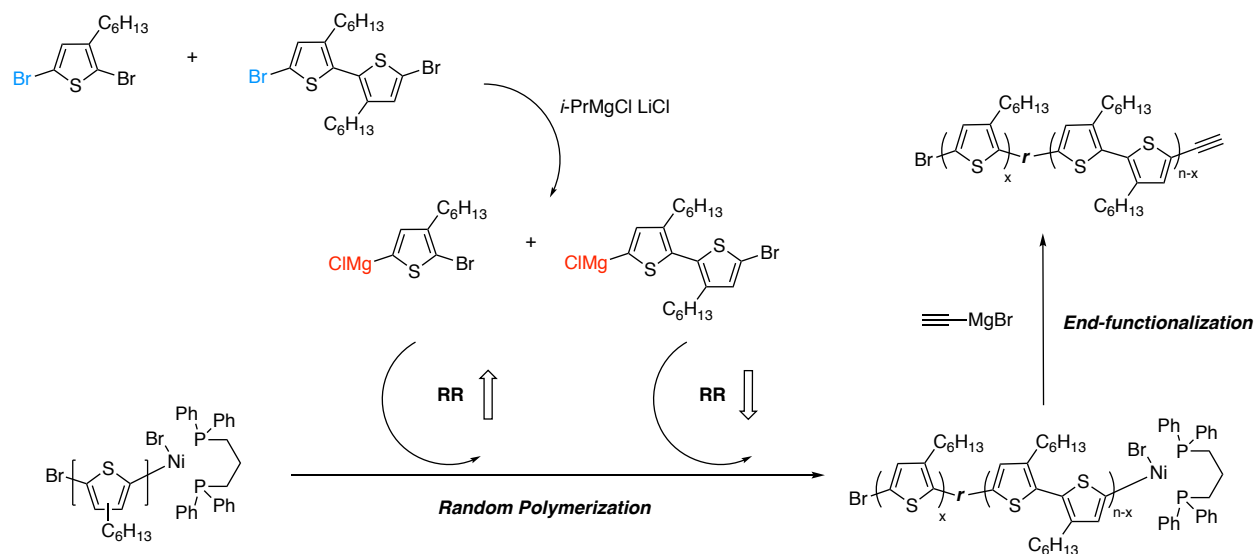
3,3'-dihexyl-2,2'-bithiophene (1.0 eq, 4 mmol) was dissolved in 50 mL THF in a round-bottom flask and cooled down to 0°C in cold ice bath. NBS (2.8 eq, 11.2 mmol) was added portionwise to the flask in 30 min. The reaction mixture was stirred at 0°C for another 30 min followed by room temperature overnight. The reaction was quenched by NaOH solution and extracted with EtOAc (30 mL × 3). The organic layer was then washed with water (30 mL × 3) followed by dried over MgSO₄ and concentrated. The crude product was purified by column chromatography with hexane as eluent to give **5** as colorless liquid in 84 % yield.

¹H NMR (300MHz, CDCl₃, δ): 6.91 (s, 2H; Th H), 2.43 (t, J=6Hz, 4H; Th-CH₂), 1.49 (quintet, J=6Hz, 4H; Th-CH₂-CH₂), 1.24 (m, 12H; (CH₂)₃), 0.86 (t, J=6Hz, 6H; CH₃).

Synthesis of RR-controlled P3HT homopolymer

1 and **5** (at different ratios) were dissolved in 20 mL anhydrous THF under Argon atmosphere. Isopropylmagnesium chloride-lithium chloride complex solution (0.98 eq of the total amount of monomer and dimer) was then added in one shot while the solution was vigorously stirred at 0 °C. After 30min, the reaction mixture was warmed up to room temperature and kept stirred for another

2h. A Ni(dppp)Cl₂ (0.02 eq of the total amount of monomer and dimer) suspension in dry THF was added in one shot to initiate the polymerization. After reacting at room temperature for 15 min, ethynylmagnesium bromide solution (0.4 eq of the total amount of monomer and dimer) was added in one shot and stirred for the last 5 min to terminate and end-functionalize the polymerization. The polymers were precipitated in large amount of cold methanol and collected via centrifuge. The polymers were purified by being dissolved in CHCl₃, filtered, and reprecipitated in MeOH for three times. The final product was further purified with hexane to remove low molecular weight oligomers followed by drying under vacuum and stored in -20 °C freezer before use.

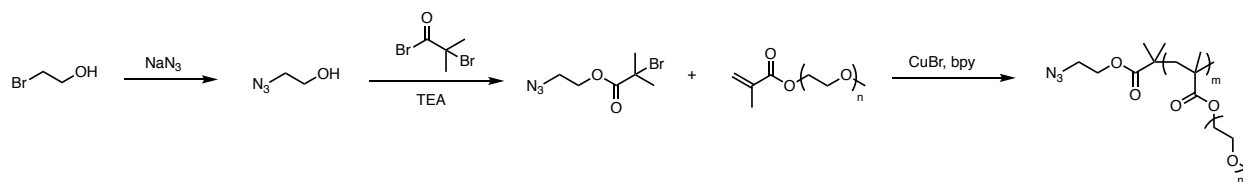


Scheme 6.3 synthetic procedures of RR-controlled P3HT homopolymer.

6.2.3.2 Synthesis of α -azido-PEOMEMA via ATRP

In this chapter, a methacrylate monomer with longer PEO units on the side chain was chosen to provide more ionic conducting characteristics to the final block copolymer. The synthesis remained the same with last chapter where 2-azidoethyl 2-bromoisobutyrate was used as initiator

and polymers of varying molecular weights were synthesized by adjusting the monomer: initiator ratios. The synthetic procedures and polymer molecular weights were shown in **Scheme 6.4** and **Table 6.1** respectively.



Scheme 6.4 Synthetic procedure of α -azido-PEOMEMA.

Table 6.1 Molecular weight of azido-PEOMEMA characterized by GPC

$[M]_0/[I]_0$	M_n (g/mol)	M_w (g/mol)	\bar{D}	DP
50:1	15.1 k	17.8 k	1.17	50
80:1	22.0 k	26.5 k	1.20	72
100:1	29.7 k	37.2 k	1.25	98
150:1	35.1 k	45.1 k	1.28	116
200:1	57.5 k	75.8 k	1.32	191

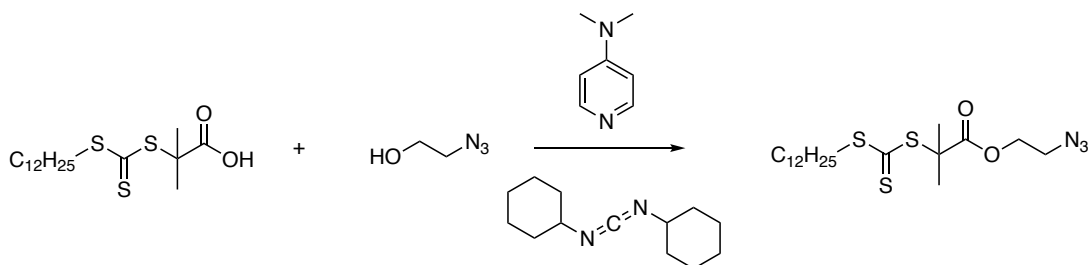
6.2.3.3 Synthesis of azido-P4VP via Reversible addition-fragmentation chain-transfer polymerization (RAFT)

Synthesis of azido-end-functionalized RAFT chain transfer agent (CTA- N_3)

The chain transfer agent was synthesized following previous procedures.^[18] 2-azidoethanol (2.0 eq, 4 mmol), DMAP (0.5 eq, 1 mmol), and 2-(((dodecyl-thio)carbonothioyl)thio)-2-methyl propanoic acid (1.0 eq, 2 mmol) were dissolved in anhydrous CH_2Cl_2 and stirred for 5 min. DCC (1.0 eq, 2 mmol) was dissolved in 20 mL CH_2Cl_2 and added to the mixture dropwise. The reaction was stirred for overnight. After completion of reaction, the precipitate was filtered and CH_2Cl_2

was evaporated, the crude product was purified by column chromatography with hexane: EtOAc = 16:1 (v/v) as eluent to give the final product as yellow oil in 75.5 % yield.

$^1\text{H NMR}$ (CDCl_3 , 500 MHz, δ): 4.27 (t, $J=5.1\text{Hz}$, 2H; CH_2), 3.45 (t, $J=5.05\text{Hz}$, 2H; CH_2), 3.28 (t, $J=7.45\text{Hz}$, 2H; CH_2), 1.72 (s, 6H; 2CH_3), 1.25 (m, 20H; $(\text{CH}_2)_{10}$), 0.88 (t, $J=6.92\text{Hz}$, 3H; CH_3).



Scheme 6.5 Synthetic procedure of RAFT chain transfer agent

Synthesis of poly(4-vinylpyridine) (P4VP) via RAFT

To a round-bottom flask was charged AIBN (0.2 eq, 0.04 mmol), 4-vinylpyridine (100 eq, 20 mmol), CTA- N_3 (1.0 eq, 0.2 mmol) dissolved in 2.15 mL anhydrous toluene. The mixture was purged with Argon for 20 min and stirred at 80 °C for 15 h when the solution became gel. The crude product was then dissolved in CHCl_3 , concentrated followed by precipitated in large amount of ether to give 2.02 g white solid.

6.2.3.4 Synthesis of poly(sodium 4-vinylbenzenesulfonate) (PSS) via ATRP

The synthetic procedure of PSS via ATRP was similar to that of PEOMEMA. To a Schlenk flask was charged Cu(I)Br (0.0326 g, 0.22 mmol) and 2,2'-bipyridyl (0.0688 g, 0.44 mmol). The solids were degassed and refilled with Argon for five cycles. In another round-bottom flask ABIB initiator (0.052 g, 0.22 mmol), sodium 4-vinylbenzenesulfonate monomer (4.5532 g, 22 mmol) were dissolved in mixed solvent of water and MeOH (15 mL + 15 mL) by sonication and bubbled with

Argon for 30 min. The solution was canula transferred to the Schlenk flask and stirred at room temperature for 22 h under Argon. After the completion of polymerization, the reaction mixture was diluted in 20 mL EtOH and passed through a short column of neutral Al₂O₃ to remove remaining copper catalyst. The crude product was concentrated and further purified via dialysis in 10K MWCO membrane in H₂O/MeOH bath for 24 h. The final product was obtained via freezing drying. The molecular weight and Đ were not characterized as the water GPC is not available.

6.3 Results and discussions

6.3.1 Synthesis of regioregularity (RR)-controlled P3HT block with alkyne end-functionalization

A series of P3HT homopolymers were synthesized via modified Grignard metathesis (GRIM) with varying RR values achieved by adjusting the ratio between thiophene monomers and H-H coupled bithiophene dimers while maintaining the same equivalent of Ni(dppp)Cl₂ catalyst following previous procedures.^[19] The RR values were determined by ¹H NMR calculated by the ratio between the integration of peaks at δ 2.78, representing head-to-tail (H-T) bonding and δ 2.54, representing head-to-head (H-H) bonding, respectively. The larger the integration of H-H linkage, the lower the RR values. P3HT with RR values of 96, 84, 80, 76 and 68% were produced (see **Figure 6.1(a)**). The UV-vis spectra of P3HT with varying RR values in THF solution were also obtained and shown in **Figure 6.1(c)** in which the typical absorption peak of P3HT exhibited an evident blue-shift upon reduced RR values as the increasing amount of H-H bonding disrupted backbone packing. The alkyne end-functional group can be easily achieved by *in-situ* end-capping of the active chain end with ethynylmagnesium bromide at room temperature, which simultaneously functionalized and quenched the polymerization. Following precipitation from

methanol, the materials were isolated by filtration or centrifugation. Despite the fact that sequential Soxhlet extractions are usually considered to be the standard protocol^[20] for P3HT purification, it has been proved by several groups that, due to the sensitivity and instability of the terminated alkyne groups, alkyne-functionalized P3HT undergoes alkyne-alkyne homocoupling after being subjected to Soxhlet extraction,^[21] due to either residual metal catalyst^[8,12] or increased temperature during hot extraction. Therefore, instead of Soxhlet extraction, an alternative procedure consisting of subsequent dissolution of the P3HT-alkyne in CHCl₃, filtration, and multiple precipitations in MeOH at room temperature was used. The product was then washed successively with hexane under sonication at room temperature and the supernatant decanted in order to remove the low molecular weight thiophene oligomer, yielding a monomodal alkyne-functionalized P3HT homopolymer as shown in **Figure 6.1(b)**. However, the samples remain vulnerable if stored at room temperature. Thermally-initiated homocoupling was proved by the gradual growth of a high molecular weight peak as shown in **Figure 6.1(d)**, indicated by the arrow, which corresponds to nearly twice the molecular weight of the bulk P3HT product determined by GPC. In order to avoid homocoupling and safely store samples for a longer time, they were kept under N₂ atmosphere in -20 °C freezer. The characterization results of different P3HT homopolymers are shown in **Table 6.2**. Note that since GPC is based on correlating the hydrodynamic volume of the randomly coiled polymer chains with polymer molecular weight and it tends to overestimate molecular weight of conjugated polymer systems, the number average molecular weight M_n of P3HT was not accurate and was further corrected based on the relationship of the molecular weight calculated by MALDI and GPC.^[22]

UV-Vis spectroscopy was employed to study the assembly behavior of the P3HT block. As shown in **Figure 6.1(c)**, all samples were dissolved in THF and tested in solution state. An evident blue

shift of the maximum absorption peak, characteristic of P3HT absorption, was observed from 451 nm to 431 nm as the RR value decreases from 94 % to 68%, suggesting that low regioregularity impairs the intermolecular packing of P3HT and leads to a larger π - π^* bandgap.

Table 6.2 Characteristics of RR-controlled P3HT blocks

Monomer:dimer	RR	M _n	Đ	Corrected M _n	DP
—	96	9.74 k	1.09	5.25 k	31
8.08	84	11.8 k	1.14	6.21 k	37
6.12	80	11.6 k	1.11	6.10 k	36
5.00	76	13.3 k	1.20	6.75 k	40
4.66	68	15.6 k	1.18	7.50 k	44

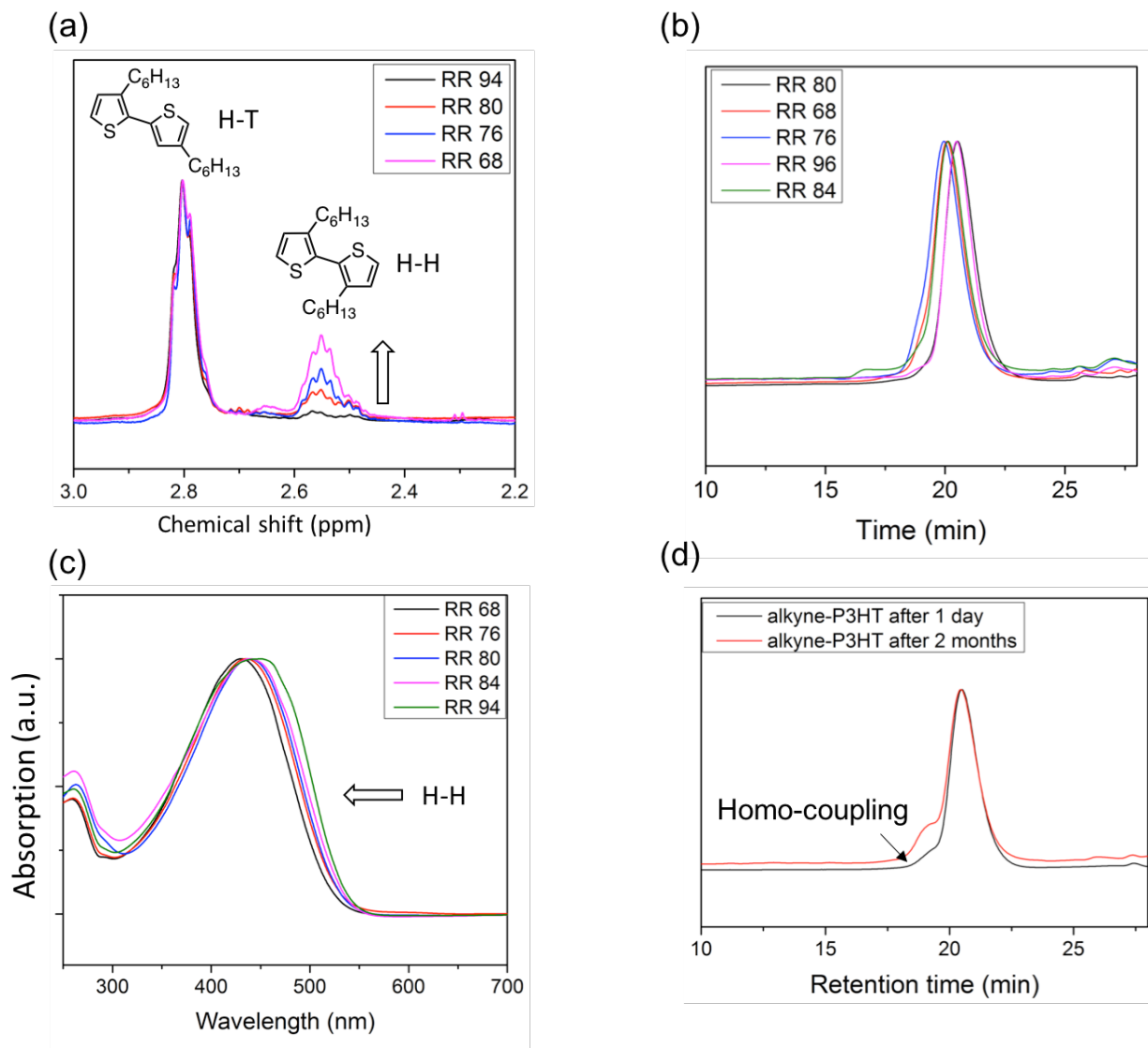


Figure 6.1 Characterizations of RR-controlled P3HT-alkyne homopolymer: (a) normalized ^1H 500MHz NMR spectra of P3HT-alkyne with varying RR. (b) GPC traces of different P3HT-alkyne polymers; (c) UV-vis spectra of P3HT-alkyne polymers dissolved in THF. (d) homo-coupling of P3HT-alkyne after storing at room temperature for 2 months.

6.3.2 Synthesis and purification of P3HT-*b*-PEOMEMA copolymer

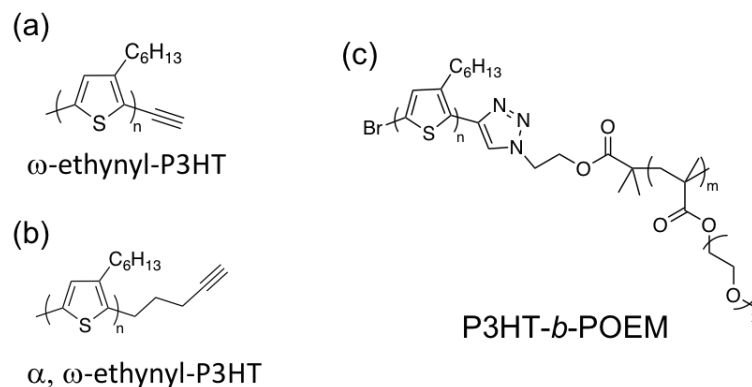


Figure 6.2 Structures of (a) ω -ethynyl-P3HT, (b) α, ω -ethynyl-P3HT, and (c) P3HT-*b*-PEOMEMA.

Subsequently, a series of N₃-PEOMEMA with narrow Đ (1.1-1.3) was synthesized by ATRP with α -azido initiator and Cu(I)Br/bpy as catalyst-ligand complex. Here the poly(ethylene oxide)methyl ether methacrylate was chosen for the following two reasons: first, it carries more ethylene oxide units (4~5) per molecule which imparts higher incorporation of Li ions; second, the longer PEO chains render the polymer more hydrophilic and less compatible with P3HT block, which could further enhance phase separation of the block copolymers. Different chain lengths of PEOMEMA were designed in order to investigate the phase behavior of P3HT-*b*-PEOMEMA copolymers as a function of volume fractions of P3HT. The RR-controlled P3HT-alkyne and N₃-POEM were then coupled by CuAAC “click” reaction and yielded P3HT-*b*-PEOMEMA copolymers with different RR and $f_{(P3HT)}$ values.

The purification process of P3HT-*b*-PEOMEMA is much more difficult compared to that of P3HT-*b*-POEM with only two ethylene oxide units in side chain. When MeOH was used to precipitate the final product of block copolymer and wash off the excess PEOMEMA, not only did we observe significant product loss from the dark purple supernatant after precipitation and filtration

indicating that there was P3HT-*b*-PEOMEMA copolymer dissolved or dispersed in MeOH since MeOH is a poor solvent for P3HT homopolymer. Therefore, both fractions were collected for characterization. Moreover, bimodal peaks corresponding to the target diblock copolymer and the precursor P3HT homopolymer were detected by RI and UV detectors in the GPC traces for both the precipitate and supernatant fraction, indicative of residue P3HT homopolymer that was not completely consumed. Listed below in **Table 6.3** are the characteristics of P3HT-*b*-PEOMEMA with varying RR values and block ratios that have been synthesized to date. Their GPC traces with both UV and RI detectors are shown in **Figure 6.3**.

Table 6.3 Characteristics of P3HT-*b*-PEOMEMA copolymers

No	M_n (P3HT)*	RR (P3HT)	DP (P3HT)	DP (PEOMEMA)	$f_{(P3HT)}$
(a)	6.25 k	94	38	72	0.35
(b)	6.10 k	80	36	50	0.42
(c)	6.10 k	80	36	72	0.33
(d)	7.50 k	68	44	72	0.38

*The M_n of P3HT is corrected by GPC-MALDI relationship, the unit is g/mol.

As shown in **Figure 6.3(a)**, both the precipitate and supernatant fraction of the P3HT-*b*-PEOMEMA copolymer were collected for GPC measurement (indexed as bottom and top, respectively) in comparison with the P3HT and PEOMEMA precursor homopolymers. The success of the “click” reaction between the two blocks was monitored by a shift of polymer peaks to shorter retention time which corresponds to higher molecular weight detected by both RI and UV detectors, whereas the bottom sample was also detected a “shoulder” peak indicating remaining homopolymer resulted from incomplete consumption or purification. The UV-detected

trace gives us a clearer depiction of the composition of each fraction in which the main peak overlap, indicating that the two fractions consist of the same components. In addition, the remaining P3HT block was detected and indicated by the yellow circle as PEOMEMA block is not UV-active. This is quite unusual as P3HT homopolymer is insoluble in MeOH and therefore

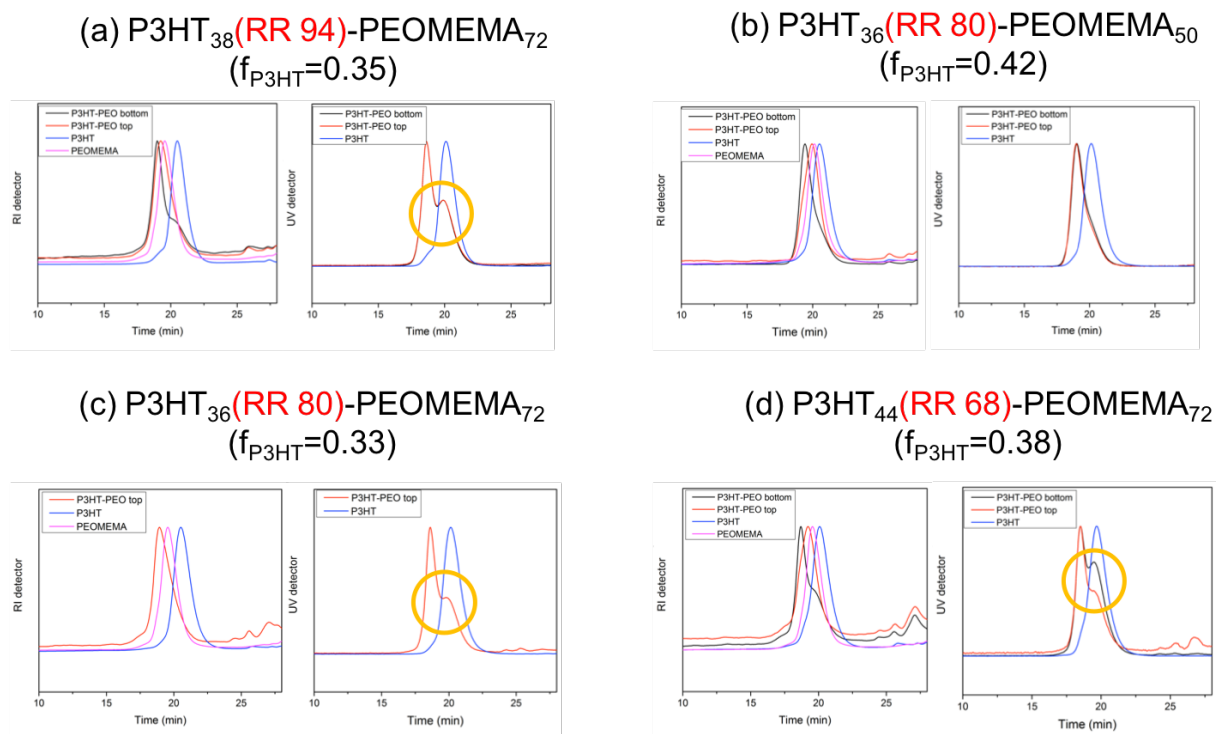


Figure 6.3 GPC traces of P3HT-*b*-PEOMEMA with varying RR values and block ratios detected by RI (left) and UV (right) detectors: (a) P3HT₃₈ (RR 94%)-*b*-PEOMEMA₇₂, (b) P3HT₃₆ (RR 80%)-*b*-PEOMEMA₅₀, (c) P3HT₃₆ (RR 80%)-*b*-PEOMEMA₇₂, (d) P3HT₄₄ (RR 68%)-*b*-PEOMEMA₇₂.

unlikely to appear in the top layer. Similar results were also observed for sample (c) and (d). Noted that in **Figure 6.3(c)** almost no precipitate was left after successive washing with MeOH while there was P3HT remained in the supernatant. Such phenomenon was attributed to a variety of factors, including the reactivity of P3HT-alkyne, the solubility and self-assembly behavior of

P3HT-*b*-PEOMEMA copolymers, and so on. The only perfectly clean sample is P3HT₃₆ (*RR* 80%)-*b*-PEOMEMA₅₀ without any P3HT homopolymer detected by either RI or UV detector.

Let's discuss the reactivity of P3HT-alkyne first. Due to easier synthetic procedure, in this chapter an ω -ethynyl-P3HT was synthesized in which the C \equiv C triple bond was directly linked to the P3HT polymer chain by introduction of ethynylmagnesium bromide at the end of polymerization which simultaneously arrested chain growth and resulted in end-functionalization. The incorporation of the ethynyl terminal groups is identified as a singlet signal appearing at 3.52 ppm by ¹H NMR shown in **Figure 6.4**. The P3HT block is available for the next cycloaddition reaction step without further protection or deprotection. However, it could be anticipated that this ω -ethynyl-P3HT (structure shown in **Figure 6.2(a)**) is not very reactive with respect to azido coupling due to the ethynyl conjugation with P3HT that constrains its reactivity both electronically and sterically, compared to α,ω -ethynyl-P3HT (structure shown in **Figure 6.2(b)**) which has an alkyl spacer between delocalized bonds.^[23] The steric factors and electronic effects also play a role in the success of this click chemistry.^[24] There have been experimental results reporting that electron-withdrawing substituents on the alkyne accelerate Cu^I-catalyzed alkyne-azide coupling by facilitating the formation of a metallocycle^[25] whereas in ω -ethynyl-P3HT the π -conjugated structure presents electron-giving effect to the alkyne group. On the other hand, Thelakkat et al.^[15] also proposed that the residual P3HT could arise from incomplete end-group functionalization.

The amphiphilicity and self-assembly behavior of the block copolymers also play an important role. Generally, MeOH is considered to be a selective solvent for PEOMEMA while P3HT shows very poor solubility. In previous chapter, MeOH was used to precipitate and purify the P3HT-*b*-PEOM copolymer in which the π - π stacking of P3HT is stronger due to relatively large molecular

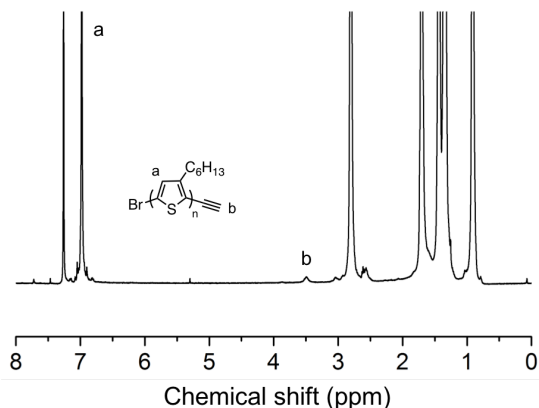


Figure 6.4 ^1H NMR of ω -ethynyl-P3HT

weight and therefore dominant in the P3HT-*b*-POEM system. In P3HT-*b*-PEOMEMA, however, the length of P3HT block is shorter while the PEOMEMA block possesses longer chain length as well as higher ethylene oxide density, endowing more hydrophilicity to the block copolymer. As a consequence, the strong amphiphilic character makes the copolymer soluble in a wide range of solvents, including not only neutral solvents such as THF, but also selective solvents such as MeOH. Different colors are observed depending on the type of solvent, for example, orange for THF and purple for MeOH, as shown in **Figure 6.5(a)**, in which the optical properties of P3HT are influenced by intrachain and interchain interactions of the materials.^[21] There have been extensive studies about solvent-induced self-assemblies and morphological behaviors of amphiphilic P3HT-*b*-PEO copolymers which are comparable to our systems.^[26,27] The subtle balance between microphase separation of copolymer and π - π stacking of conjugated block determines the phase structures and can be controlled by solvents of different selectivity. Moreover, the relatively longer PEOMEMA block could also form a micellar structure encircling the remaining P3HT homopolymer.^[27]

UV-Vis spectroscopy was conducted on P3HT-*b*-PEOMEMA solutions in both THF and MeOH,

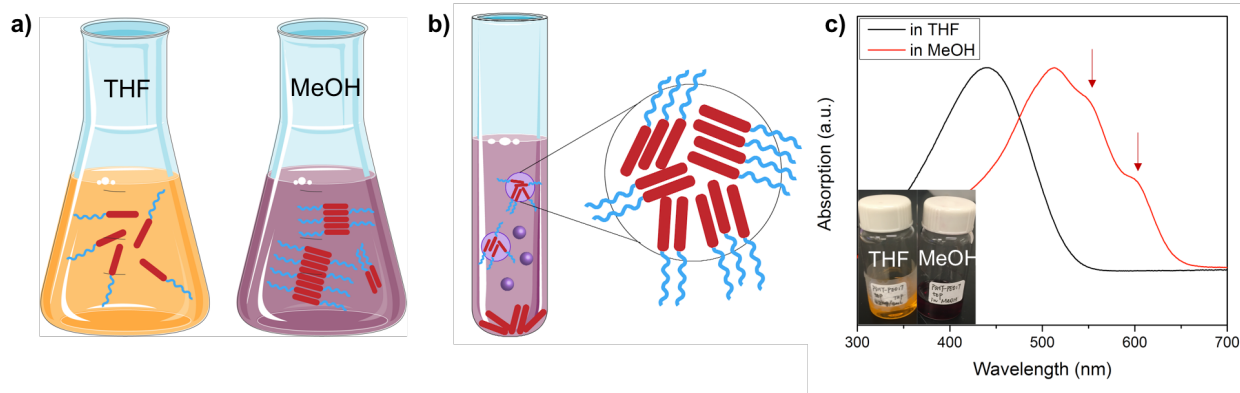


Figure 6.5 (a) P3HT-*b*-PEOMEMA copolymer dissolved or dispersed in THF (left) and MeOH (right). (b) Schematic representation of P3HT-*b*-PEOMEMA copolymer in supernatant layer and P3HT homopolymer precipitated out. (c) UV-vis absorption spectra of P3HT₃₆ (RR 80%)-*b*-PEOMEMA₇₂ in THF and MeOH at a concentration of 1 mg/mL.

with the latter coming from the centrifuge supernatant during the purification step. In the good solvent THF, the solution displayed an orange color with UV-vis absorption maximum λ_{\max} appearing at 421 nm, characteristic of the intrachain π - π^* absorption of P3HT block, suggesting that the block copolymer is fully dissolved in THF and the incorporation of PEOMEMA coil block doesn't affect the conformation of the conjugated block. As expected, the PEOMEMA block doesn't contribute to the absorption spectra between 300-700 nm. While in MeOH, a transparent solution was obtained where a significant bathochromic shift from 421 to 510 nm was observed, indicative of the increased planarity of packed P3HT-*b*-PEOMEMA chains in the assemblies.^[28,29] The appearance of two vibronic or "shoulder" peaks, as indicated by the arrows in **Figure 6.5(c)**, was attributed to the strong interchain π - π interaction associated with the formation of P3HT aggregates^[30] as shown in the scheme of **Figure 6.5(a)**. It has been claimed that in selective solvent such as MeOH, the P3HT-*b*-PEOMEMA copolymers are able to form stable core-shell micellar aggregates^[31,32] when the PEO fraction is larger than 31 wt%. The PEOMEMA corona stabilizes and solubilizes the aggregates in MeOH and as a consequence precipitation is prevented.

The most effective way for removing residual P3HT homopolymer so far was put forward by Thelakkat et al.^[15] who adopted Soxhlet extraction method with MeOH to remove the excess PEO while minimizing the product loss. However, he also admitted that among all the methods he had tried, including Soxhlet extraction, reprecipitation or even column chromatography, none could lead to a complete removal of P3HT homopolymer even though the residue had been decreased dramatically. Here we came up with another purification method involving ultrasonication and centrifugation with MeOH, given that the amphiphilic nature of block copolymer renders better solubility in MeOH. Our purification method was carried out at room temperature to reduce possible thermal damage to the product, compared to Soxhlet extraction which required high temperature refluxing. The crude product was first passed through a short column of neutral alumina to remove residue copper catalyst followed by precipitation in cold ether to remove excess amounts of PEOMEMA block from the reaction. Then the crude product was further purified with repeated dispersion in methanol under ultrasonication for 30min followed by centrifugation at 4200 rpm for 15 min until the supernatant became light and clear. Ultrasonication was quite necessary in this procedure as polymer chains could be frozen and locked in an unfavorable conformation upon addition of large amounts of poor solvent, which may result in P3HT homopolymer locked into the interior of a core-shell structure. Ultrasonic treatment thus facilitated polymer interaction with solvent molecules and presumably led to decreased chain entanglement. By repeating those procedures several times, most of P3HT-*b*-PEOMEMA could be extracted with MeOH and separated via centrifugation. The solution was then concentrated and reprecipitated from ether to give the final product as a dark purple solid.

6.3.3 Self-assembly and phase separation of RR-controlled P3HT-*b*-PEOMEMA

At the beginning of this chapter we talked about different factors that determine the formation of rod-coil block copolymer self-assembly. Due to decreased RR values, the rigidity and crystallinity of the P3HT block is impaired, leading to lower electronic conductivity while in the meantime the microphase separation between P3HT and PEOMEMA could result in well-ordered co-continuous phases for mixed ionic/electronic conductivity. This phenomenon is defined as the “crystallinity-conductivity trade-off”. The RR effect on phase-separation morphology of P3HT-*b*-PEOMEMA copolymers is further investigated by AFM and TEM, as shown in **Figure 6.6**. Two samples consisting of the same RR value for the P3HT block but different volume fractions, $f_{(P3HT)}$, were studied. The bulk polymer samples were prepared by spin-coating from chloroform solutions and thermally annealed at 130 °C overnight for AFM measurement. Disordered fibril-like structures were observed for both samples (shown in **Figure 6.6**(a), (b), (d) and (e)), similar to the morphology of P3HT homopolymer, irrespective of $f_{(P3HT)}$ values. Despite the reduction of RR value (80%), the morphology of P3HT-*b*-PEOMEMA is still dominated by the crystallization of P3HT, which inhibited its self-assembling into ordered nanostructures. The result suggested that 80%-RR P3HT block is not good enough. For TEM measurement, the samples were prepared by drop-casting from chloroform solutions and stained with RuO₄ aqueous solution for a couple of hours at room temperature. Both TEM samples exhibited some short-range ordered patterns with contrast difference between P3HT and PEOMEMA blocks, which could be treated as a starting point for phase separation. **Figure 6.6**(e) exhibited qualitatively increased domain spacing compared to **Figure 6.6**(c) due to the extended length of PEOMEMA block which induces better phase separation. For future investigation, P3HT with even lower RR value as well as larger volume fraction will be the focus of study.

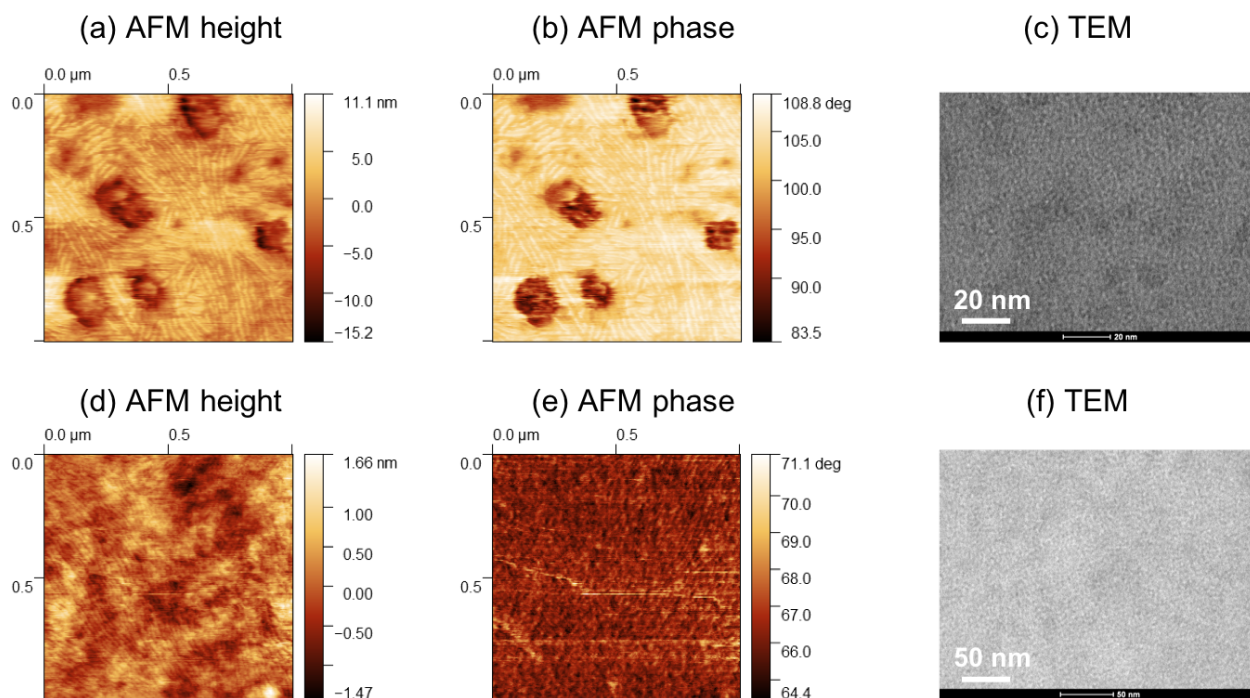


Figure 6.6 Phase separation of P3HT₃₆ (*RR 80%*)-*b*-PEOMEMA₅₀: (a) AFM height image, (b) AFM phase image, (c) TEM image. Phase separation of P3HT₃₆ (*RR 80%*)-*b*-PEOMEMA₇₂: (d) AFM height image, (e) AFM phase image, (f) TEM image.

6.4 Conclusions

In summary, we succeeded in tuning the morphology of P3HT-*b*-PEOMEMA copolymer through control of P3HT regioregularity and block volume ratios in order to induce well-ordered phase separation for the formation of a co-continuous phase for simultaneous transport of ions and electronic charge carriers. A series of block copolymers were synthesized via “click” reaction. Incomplete consumption of P3HT precursor homopolymer cannot be eliminated from the copolymer product and was attributed to (1) low reactivity of ω -ethynyl-P3HT in which the alkyne group was directly attached to P3HT backbone and (2) micelle phases formed by amphiphilic P3HT-*b*-PEOMEMA copolymers trapping residue P3HT inside. It has been demonstrated that when *RR* is high, crystallization of the conjugated block dominates over microphase separation of

block copolymer while when RR is low, the block copolymer can self-assemble into the highly ordered nanostructures at thermal equilibrium. Short-range ordered phase separation was detected by AFM and TEM with RR 80% block copolymer samples. In future work, more copolymer samples with lower RR values, higher molecular weight and varying block ratios will be investigated using GISAXS and an optimal condition for the “crystallinity-conductivity trade-off” will be achieved. What’s more, intrinsically charged polymers such as PSS and P4VP were synthesized with azido-end-group functionalization ready for following production of block copolymer. Their structures and conducting characteristics will also be studied.

REFERENCES

- [1] J.-S. Kim, Y. Kim, H.-J. Kim, H. J. Kim, H. Yang, Y. S. Jung, G. E. Stein, B. J. Kim, *Macromolecules* **2017**, *50*, 1902.
- [2] J.-S. Kim, J. Han, Y. Kim, H. Park, J. P. Coote, G. E. Stein, B. J. Kim, *Macromolecules* **2018**, *51*, 4077.
- [3] W. Han, M. Byun, Z. Lin, *J. Mater. Chem.* **2011**, *21*, 16968.
- [4] Y. J. Lee, S. H. Kim, H. Yang, M. Jang, S. S. Hwang, H. S. Lee, K.-Y. Baek, *J. Phys. Chem. C* **2011**, *115*, 4228.
- [5] S. K. Patra, R. Ahmed, G. R. Whittell, D. J. Lunn, E. L. Dunphy, M. A. Winnik, I. Manners, *J. Am. Chem. Soc.* **2011**, *133*, 8842.
- [6] H. Sirringhaus, *Science* **1998**, *280*, 1741.
- [7] C. R. Craley, R. Zhang, T. Kowalewski, R. D. McCullough, M. C. Stefan, *Macromol. Rapid Commun.* **2009**, *30*, 11.
- [8] Z. Li, R. J. Ono, Z.-Q. Wu, C. W. Bielawski, *Chem. Commun.* **2011**, *47*, 197.
- [9] Y.-H. Lee, W.-C. Yen, W.-F. Su, C.-A. Dai, *Soft Matter* **2011**, *7*, 10429.
- [10] J. Gwyther, J. B. Gilroy, P. A. Rugar, D. J. Lunn, E. Kynaston, S. K. Patra, G. R. Whittell, M. A. Winnik, I. Manners, *Chem. Eur. J.* **2013**, *19*, 9186.
- [11] Y.-J. Kim, C.-H. Cho, K. Paek, M. Jo, M. Park, N.-E. Lee, Y. Kim, B. J. Kim, E. Lee, *J. Am. Chem. Soc.* **2014**, *136*, 2767.
- [12] R. H. Lohwasser, M. Thelakkat, *Macromolecules* **2012**, *45*, 3070.
- [13] V. Gernigon, P. L  v  que, F. Richard, N. Leclerc, C. Brochon, C. H. Braun, S. Ludwigs, D. V. Anokhin, D. A. Ivanov, G. Hadziioannou, T. Heiser, *Macromolecules* **2013**, *46*, 8824.
- [14] K. Yuan, F. Li, L. Chen, H. Wang, Y. Chen, *J. Mater. Chem. A* **2013**, *1*, 10881.
- [15] P. M. Reichstein, S. G  drich, G. Papastavrou, M. Thelakkat, *Macromolecules* **2016**, *49*, 5484.
- [16] A. E. Javier, S. N. Patel, D. T. Hallinan, V. Srinivasan, N. P. Balsara, *Angewandte Chemie International Edition* **2011**, *50*, 9848.
- [17] M. He, F. Qiu, Z. Lin, *J. Mater. Chem.* **2011**, *21*, 17039.
- [18] A. Vora, K. Singh, D. C. Webster, *Polymer* **2009**, *50*, 2768.
- [19] J.-S. Kim, J.-H. Kim, W. Lee, H. Yu, H. J. Kim, I. Song, M. Shin, J. H. Oh, U. Jeong, T.-S. Kim, B. J. Kim, *Macromolecules* **2015**, *48*, 4339.
- [20] M. Jeffries-El, G. Sauv  , R. D. McCullough, *Macromolecules* **2005**, *38*, 10346.
- [21] H. Yang, H. Xia, G. Wang, J. Peng, F. Qiu, *Journal of Polymer Science Part A: Polymer Chemistry* **2012**, *50*, 5060.
- [22] J. Liu, R. S. Loewe, R. D. McCullough, *Macromolecules* **1999**, *32*, 5777.
- [23] M. Urien, H. Erothu, E. Cloutet, R. C. Hiorns, L. Vignau, H. Cramail, *Macromolecules* **2008**, *41*, 7033.
- [24] C. W. Torn  e, C. Christensen, M. Meldal, *J. Org. Chem.* **2002**, *67*, 3057.
- [25] J. P. Collman, N. K. Devaraj, C. E. D. Chidsey, *Langmuir* **2004**, *20*, 1051.
- [26] J. Li, X. Li, D. Ni, J. Wang, G. Tu, J. Zhu, *J. Appl. Polym. Sci.* **2014**, *131*, 41186.
- [27] M. G. Mohamed, C.-C. Cheng, Y.-C. Lin, C.-W. Huang, F.-H. Lu, F.-C. Chang, S.-W. Kuo, *RSC Adv.* **2014**, *4*, 21830.
- [28] J. B. Gilroy, D. J. Lunn, S. K. Patra, G. R. Whittell, M. A. Winnik, I. Manners, *Macromolecules* **2012**, *45*, 5806.
- [29] L. Li, G. Lu, X. Yang, *J. Mater. Chem.* **2008**, *18*, 1984.

- [30] E. Lee, B. Hammer, J.-K. Kim, Z. Page, T. Emrick, R. C. Hayward, *J. Am. Chem. Soc.* **2011**, *133*, 10390.
- [31] S.-W. Kuo, H.-F. Lee, C.-F. Huang, C.-J. Huang, F.-C. Chang, *J. Polym. Sci. A Polym. Chem.* **2008**, *46*, 3108.
- [32] C.-A. Dai, W.-C. Yen, Y.-H. Lee, C.-C. Ho, W.-F. Su, *J. Am. Chem. Soc.* **2007**, *129*, 11036.

Chapter Seven: Conclusions

MIECs have shown great potential for applications in energy production, energy storage, sensors, electrochromic devices, or even robot materials which combine sensing, actuation, computation, or communication capabilities. In order to enable rational design, and long-term improvements in MIEC performance, the relationship between molecular structure, morphology, and conducting properties needs to be understood. In this dissertation, an iterative combination of simulation and experiments was established for the study of newly-synthesized materials through collaboration with Prof. Escobedo's group from Cornell University (simulation) and Prof. Nealey's & Patel's groups from the University of Chicago (characterizations).

In an early chapter of the dissertation, computational studies identified a smectic liquid crystal (LC) with ionically conducting planes which exhibited excellent conductivity comparable or superior to previously reported MIEC LCs. Furthermore, the same molecule was predicted to have strong electronic conductivity and experiment proved that it spontaneously formed parallel electronic and ionic conduction paths of high conductivity in thin films. Computation was used to explain how Li-salts, added to enable ionic conductivity, enhanced the electronic conductivity through structure control. Finally, computational studies showed that varying lengths of PEO segments in the ternary facial amphiphilic structure led to morphology evolution from a lamellar to a cylindrical phase as well as the existence of different ion transport mechanisms.

In a subsequent chapter, we described a concerted effort using computationally-led materials research to identify, synthesize and characterize a new π -conjugated LC 4T/PEO₄ with high ionic conductivity. Using molecular dynamics (MD) simulation, Dr. Mayank Misra examined the self-assembly structures and thermal stabilities of 4T/PEO_{*n*} for different *n* in order to choose the best chemical structure for synthesis. All-atom simulations were performed to construct self-assembled

structures with good conductivity and indicated that all 4T/PEO n compounds adopted a smectic morphology in which both ionic and electronic conduction pathways exist and that the LC thermal stability was strongly related to the length of PEO segments with melting points ranging from 127 °C to 37 °C for $n = 3$ to 6. Increasing the volume fraction of PEO thus has a negative impact on the thermal stability of 4T/PEO n . In light of these results, 4T/PEO4 was predicted to be the best candidate for synthesis with a good balance between transport characteristics and thermal stability. An experimental thermal transition near 100 °C matched the melting temperature of 107 °C predicted by MD simulation. The self-assembled structure and ion conduction characteristics of 4T/PEO4 in thin film configuration were characterized by Dr. Ban Xuan Dong. At a LiTFSI concentration $r = 0.05$, the maximum achieved conductivity measured by interdigitated electrode (IDE) is 5.2×10^{-4} S/cm at 70 °C, which is superior to those reported for prior nanosegregated ionic LCs. Upon heating near the transition temperature of *ca.* 100 °C we observed a significant loss of smectic order together with a pronounced drop in ionic conductivity. Additional simulation from Dr. Misra showed that through π - π interaction, the 4T units in 4T/PEO4 arrange in herringbone patterns below the transition temperature. At temperatures higher than the transition temperature the 4T units melted leading to a loss of smectic order. Our combined experimental results thus have led to the discovery of a new smectic liquid crystal with significant ionic conductivity and great potential for use in MIEC studies.

In the same chapter, we also showed that F4TCNQ-doped 4T/PEO4 possessed high electronic conductivity in the presence and absence of LiTFSI. A sequential doping method was employed in which F4TCNQ infiltrated 4T/PEO4 thin film sample through vapor deposition and the conductivity was measured as a function of F4TCNQ exposure time. The optimum electronic transport was realized at the intermediate Li⁺ concentration $r = 0.1$ where the 4T/PEO4 structure

become more crystalline and the maximum electronic conductivity of $3.1 \times 10^{-3} \pm 5 \times 10^{-5}$ S/cm was achieved. Our experimental results indicated that electronic transport in mixed conduction materials could unexpectedly be modulated by the presence of an ionic transport component and simultaneous ionic/electronic conductivity was captured. We demonstrate that by utilizing the ease of synthesis, straightforward self-assembly, and computational simplicity, LCs could be used as material testbeds to understand mixed conduction behavior of soft materials in general.

In a following chapter, we discussed how self-assembly with greater complexity can open new perspectives for sophisticated functional materials. The experimental and simulation results from facial polyphiles revealed that the combination of more than two incompatible segments and the adoption of anisotropic molecular shape can help to stabilize some complex LC phases. A prototype of T-shaped 5T/PEOn/Alkyl is then proposed, consisting of three incompatible segments. Using MD simulation with a coarse-grained (CG) model, Yangyang Sun investigated the phase behavior of 5T/PEOn/Alkyl molecules. By varying the length of the PEO lateral chain and alkyl segments, different ordered phases were found. 5T/PEO3/decyl with a relatively shorter PEO chain was found to form a lamellar phase in which the alkyl segment itself formed one layer, and the thiophene and PEO segments together formed another adjacent layer where the PEO segments formed small clusters scattered in the thiophene packing structure. 5T/PEO10/hexyl with a relatively longer PEO chains was found to form a continuous columnar phase, which can potentially be beneficial for ion transport. To confirm the predicted ordered phase of 5T/PEOn/Alkyl and their ion transport functionality, I synthesized a series of 5T/PEOn/Alkyl molecules with varying lengths of PEO chains (PEO3, PEO4, and PEO10). Their self-assembled structures were characterized by GIWAXS at room temperature and agreed quite well with all-atom simulation results. Ionic conductivity as a function of temperature was characterized with

discontinuous decrease in the vicinity of phase transition observed, suggesting a different ion transport mechanism from 4T/PEO4 while more simulation results is in need to further explore the fundamental theory.

Finally, the knowledge and experience from LC was applied to large dimension rod-coil P3HT-*b*-POEM copolymer. We found out that all-regioregular P3HT block resulted in high crystallinity which suppressed microphase separation between blocks and rendered very weak ionic conductivity. The incorporation of LiTFSI not only led to a marked enhancement in molecular order through the formation of aggregates, but also resulted in electronic doping of P3HT-*b*-POEM, leading to more than 5 orders of magnitude increase in electronic conductivity. F4TCNQ-vapor doped P3HT-*b*-POEM-LiTFSI sample yielded a highest electrical conductivity around 31 S/cm at $r = 0.02$. In order to achieve mixed conductivity, however, a “crystallinity-conductivity” trade-off is defined in which the regioregularity of P3HT and block ratios are varied to enable well-ordered phase separation for the formation of co-continuous domains for mixed charge transport. An optimal condition is our goal.

In summary, our research progress for this project depends intimately on iterative feedback cycles between experiment and simulation. Simulation actively guides experiments by probing the viability and initial promise of new candidate molecules, narrowing the search for appropriate candidates. Through a feedback cycle, experiments guided simulation when interesting, previously unexplored behavior was identified. The ability to access atomic-level information provided by simulation is invaluable to experiments and continues the cycle. These newly discovered materials show improved properties over existing materials and offer new avenues we hope to explore. For future study, new building blocks will be investigated for ionic and electronic conductivity, such as ionic liquid component (e.g. imidazolium, ammonium, phosphonium) and fused mesogen group,

respectively. We believe that LCs containing charged ionic liquid moieties will provide better initial undoped self-assembly and serve as the ion transport phase. Ionic LCs are promising candidates for the creation of adaptive, nanostructured, anisotropic (“low-dimensional”) ion-conducting materials for molecular electronics, such as batteries, fuel cells, solar cells and capacitors. They will replace PEO components to achieve better self-aligning conduction pathways resulting from stronger electrostatic interaction between cations and anions as well as better nanosegregation between immiscible portions of the ILC. On the other hand, fused mesogenic groups provide better rigidity and increased planarity which can lead to higher efficiency of charge transport. Possible candidates include thienothiophene and its derivatives. New materials consisting of ionic liquid and thieno[3,2-b]thiophene will be synthesized and studied in order to approach improved mixed conductivity. Furthermore, we will keep searching for collaborations to apply our materials to prototype devices such as OCET devices to test their performance as biosensors.

As for the π -conjugated block copolymer, we will keep probing fundamental ionic/electronic transport in polymers to elucidate design principles of high performing mixed polymeric conductors. First, MD simulation will be employed to search for relevant chemistries for high transconductance polymers. Second, investigation on fundamental connections between polymer microstructure and conducting properties will be carried out through experiments. Finally, we will try to fabricate prototype devices to determine the role of polymer chemistries, microstructure, and ionic/electronic transport on device performance. Investigations on intrinsically charged P4VP and PSS will also be conducted apart from POEM block.